Characterization of OMVPE-Grown GaSb-Based Epilayers
Using *In Situ* Reflectance and *Ex Situ* TEM

by

Christopher J. Vineis

B.S., Materials Science and Engineering
University of Pennsylvania, 1996

Submitted to the Department of Materials Science and Engineering
in Partial Fulfillment of the Requirements for the Degree of

Doctor of Philosophy in Electronic Materials

at the

Massachusetts Institute of Technology

June 2001

Signature of Author.....
.....
Department of Materials Science and Engineering
May 4, 2001

Certified by.....
.....
Christine A. Wang
Senior Staff, MIT Lincoln Laboratory
Thesis Supervisor

Certified by.....
.....
Klavs F. Jensen
Lammot du Pont Professor of Chemical Engineering and
Professor of Materials Science and Engineering
Thesis Supervisor

Accepted by.....
.....
Harry L. Tuller
Professor of Ceramics and Electronic Materials
Chair, Departmental Committee on Graduate Students

Characterization of OMVPE-Grown GaSb-Based Epilayers
Using *In Situ* Reflectance and *Ex Situ* TEM

by

Christopher J. Vineis

Submitted to the Department of Materials Science and Engineering
on May 4, 2001 in Partial Fulfillment of the
Requirements for the Degree of Doctor of Philosophy in
Electronic Materials

ABSTRACT

The focus of this thesis was to investigate and characterize GaSb, GaInAsSb, and AlGaAsSb epilayers grown by organometallic vapor phase epitaxy (OMVPE). These epilayers were principally characterized using *in situ* spectral reflectance and *ex situ* transmission electron microscopy (TEM).

An *in situ* spectral (380-1100 nm) reflectance monitoring system was designed and fitted to the OMVPE reactor. It was determined that longer wavelengths are more useful for quantitative growth rate analysis, while shorter wavelengths are more sensitive to the GaSb substrate oxide desorption process. It was also determined that the GaInAsSb and AlGaAsSb alloy compositions could be determined accurately using *in situ* reflectance ratios. Use of the *in situ* reflectance monitor to efficiently perform necessary reactor/growth calibrations was also demonstrated.

Analytic functions were used to model the refractive indices of GaSb, AlGaAsSb, and GaInAsSb. Specifically, Adachi's Model Dielectric Function [1, 2] was curve-fit to data for GaSb between 400 and 1000 nm, and fourth-order polynomials were fit to data for GaSb and GaInAsSb between 1 and 3 μm. A linear interpolation of binary functions was used to generate a refractive index model for AlGaAsSb between 1 and 3 μm as a function of Al fraction. These models were helpful in interpreting *in situ* reflectance data, and also in designing distributed Bragg reflectors.

Phase separation in GaInAsSb was studied using TEM. A wide range of microstructures was observed, from nearly homogeneous to strongly phase separated. It was seen that in phase separated samples, the composition modulations typically created and coupled to morphological perturbations in the surface. One interesting manifestation of the phase separation was the spontaneous formation of a natural superlattice (period typically 10-30 nm) throughout the epilayer. This superlattice had two variants: one parallel to the growth surface, and one tilted with respect to the growth surface. It was

discovered that the tilted superlattice was coupled to surface undulations, which formed to relieve surface strain associated with the superlattice. A qualitative model was developed to explain the propagation of the tilted superlattice.

Thesis Supervisor: Christine A. Wang
Title: Senior Staff, MIT Lincoln Laboratory

Thesis Supervisor: Klavs F. Jensen
Title: Lammot du Pont Professor of Chemical Engineering and Professor of Materials Science and Engineering

Table of Contents

List of Figures

List of Tables

Acknowledgments

I would not have been able to accomplish this thesis without the help of numerous individuals, whose assistance I would like to acknowledge. First and foremost is my advisor, Dr. Christine Wang. Her guidance was extremely useful to me in so many areas. In addition to helping provide some general direction and focus to my thesis, Chris also taught me a tremendous amount about OMVPE growth, III-V semiconductors, and general lab practices and procedures. Her assistance in (and careful editing of!) papers and presentations was also very helpful to me. But perhaps the area where she helped me most was when I had to make big decisions – to stay at MIT for my Ph.D., and what jobs to consider upon graduation. The time she spent discussing various options with me helped a lot in making these decisions. All of these things were a tremendous aid in my professional development, and so I just want to say that I really appreciated the opportunity to work with you, Chris.

I would also like to thank my co-advisor, Professor Klavs Jensen. He was also very helpful in providing some focus to my thesis, editing papers and providing suggestions, and discussing job options with me as well as my professional development in general. His experience and insight proved very useful in numerous situations.

I greatly appreciate the assistance of my other thesis committee members as well, Professors Sam Allen and Leslie Kolodziejski. They asked the right questions which helped interpret some of my results along the way, and also provided helpful revisions to my thesis at the end.

Several people at MIT Lincoln Laboratory provided great technical assistance as well as much needed comic relief. Doug Oakley was particularly helpful over the years, since he worked closely with Chris and me. Besides his technical help in the lab – providing suggestions and assistance setting up experiments and collecting data – I greatly appreciated his pointers on my golf swing and teaching me more about fishing than I ever wanted to know! I enjoyed our lunchtime conversations that always provided a lot of laughs and relaxation, and will definitely miss those moments. Joe Chludzinski, Dan Calawa, Paul Nitishin, and Jim Caunt also provided a lot of useful technical assistance. Our group office - Dr. Jon Twichell, Dr. George Turner, Dr. David Spears, Mary Collins and Paula Jones - as well as several other members of Lincoln Laboratory, were helpful in editing my papers and presentations and ensuring that I had all the resources I needed to acquire my data. I would also like to thank Mike Manfra, Tony Napoleone, and Rich Poillucci for being excellent officemates and always providing hilarious lunchtime stories!

Mike Frongillo (brewer of the self-proclaimed world's greatest coffee!), Dr. Tony-Garratt Reed, and Libby Shaw were helpful in obtaining TEM and AFM characterization results.

I would like to thank our sponsor, the Department of Energy, for providing me with the necessary funding and resources to conduct this thesis research. I would also

like to thank Dr. William Breiland at Sandia National Laboratories for providing me with a copy of ADVISOR, his *in situ* reflectance curve-fitting software program. Also, Dr. Andrew Norman at the National Renewable Energy Laboratory provided me with useful suggestions for TEM specimen preparation and image interpretation.

I owe a lot of thanks to my friends from Syosset, U. Penn., and MIT. Without them, life would be pretty boring. This incomplete list includes James Piangozza, Ramu Venkatachalam, Felix Kuo, Adam and Sarah Durst, Rizwan Alladin, Matt and Jean Lehmann, Michelle Oh, Jane Koh, Kathy Lee, Jim Yurko, Tom Langdo, Toby Freyman, Krystyn Van Vliet, Matt Farinelli, Kevin Lee, and especially Jeeyoung Choi. Going out to bars, clubs, and restaurants in Beantown and NYC, watching sports, or just hanging out with them definitely made my time at MIT a lot more fun!

Finally, I thank my mother and father – Rose and Randy, and my sister Elizabeth. My family has always been very supportive of my efforts, and I dedicate this thesis to them.

1. Introduction

Considerable research of inorganic semiconductors over the last fifty years has resulted in a very detailed understanding of these materials, and enabled exciting devices in the fields of microelectronics and optoelectronics. Silicon is well-known as the basis of the integrated circuit industry, and more recently, with the rapidly growing interest in wireless communication and optoelectronic components, III-V semiconductors have received tremendous attention. In particular, arsenic- and phosphorous-based semiconductors, such as aluminum gallium arsenide (AlGaAs), indium gallium arsenide (InGaAs), and indium gallium arsenide phosphide (InGaAsP), are used as building blocks for telecommunications lasers and detectors. Research into nitride-based III-V semiconductors, such as indium gallium nitride (InGaN) and aluminum gallium nitride (AlGaN), has also exploded during the last several years because of the strong interest to use these materials in applications such as displays, lighting, and high-density optical information storage.

Antimonide-based III-Vs, such as gallium indium arsenide antimonide (GaInAsSb) and aluminum gallium arsenide antimonide (AlGaAsSb), have received less

focus and are not as well characterized as the previously mentioned materials. However, antimonide-based semiconductors are very important for near- and mid-infrared devices such as lasers, detectors, and thermophotovoltaics (TPVs). These devices enable applications including chemical sensing, free-space atmospheric communications, and energy conversion. In order to improve device characteristics it is important to understand the properties and behavior of the materials from which the devices are created. This thesis focused on characterization of antimonide-based semiconductors grown by organometallic vapor phase epitaxy (OMVPE). In particular, gallium antimonide (GaSb), GaInAsSb, and AlGaAsSb were studied *in situ* during growth using spectral reflectance, and *ex situ* primarily by transmission electron microscopy (TEM) and atomic force microscopy (AFM).

The GaInAsSb, AlGaAsSb, and GaSb epitaxial layers studied in this thesis were used to create TPVs. A schematic device structure is shown in Fig. 1(a). Figure 1(b) shows a bandgap versus lattice constant chart for the materials. Note that all the layers were grown lattice-matched to the GaSb substrate. Thermophotovoltaics are structurally and functionally similar to solar cells. However, the alloy composition of the GaInAsSb active base and emitter layers is such that the energy gap lies in the infrared (IR). Therefore, TPVs convert IR energy to electricity, unlike solar cells, which convert sunlight to electricity.

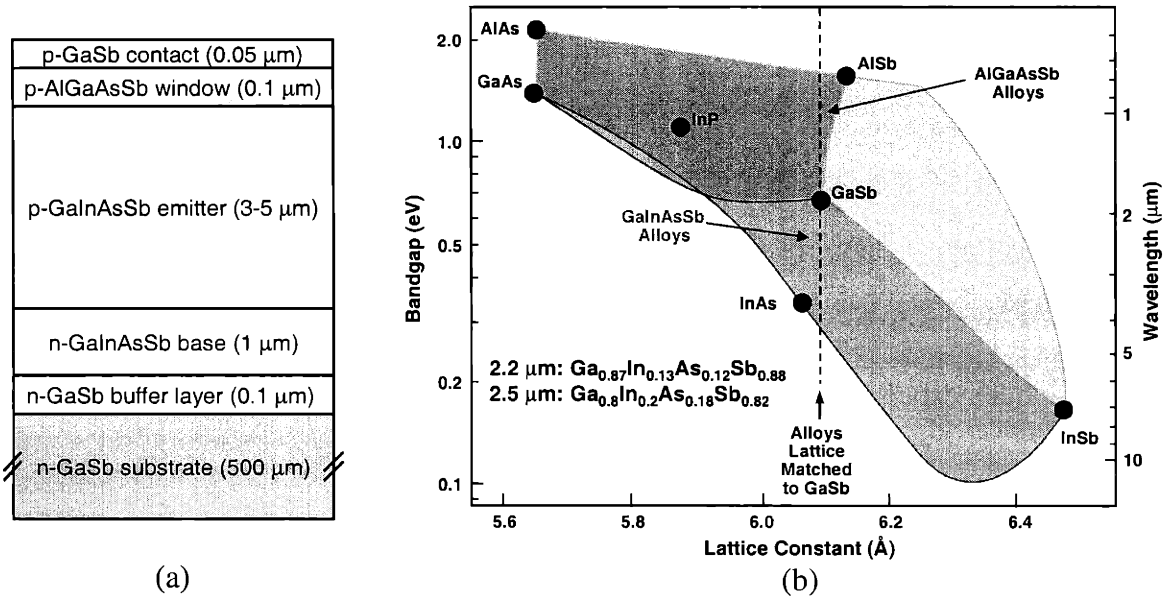

Fig. 1. A schematic diagram of a TPV cell is shown in (a), while (b) illustrates the materials on a bandgap vs. lattice constant chart.

This thesis is organized as follows. The next chapter discusses *in situ* reflectance monitoring, beginning with an overview of probe options and the reasons reflectance was chosen. The experimental setup is then illustrated in detail followed by the theory and equations for reflectance. After that the results are presented, which include the use of the *in situ* reflectance monitor to: obtain the refractive index, growth rate, and alloy composition of various epilayers; study the GaSb substrate oxide desorption process; and perform routine reactor/growth calibrations.

Chapter 3 presents models for the refractive indices of GaSb, GaInAsSb, and AlGaAsSb. Fourth-order polynomials were fit to ellipsometric data for GaSb [3] and $Ga_{0.84}In_{0.16}As_{0.14}Sb_{0.84}$ [4] in the wavelength range of 1 to 3 μm. Data for $Al_xGa_{1-x}As_ySb_{1-y}$ lattice-matched to GaSb was generated as a function of Al fraction, 'x', using a linear interpolation of binary refractive indices. Specifically, data for

$AlAs_{0.08}Sb_{0.92}$ was generated from a linear interpolation between literature data for AlAs [5] and AlSb [6]. Data for $Al_xGa_{1-x}As_ySb_{1-y}$, between 1 and 3 μm, was then generated using a linear interpolation between the data for GaSb and $AlAs_{0.08}Sb_{0.92}$. To create analytic functions of the refractive indices of GaSb, GaAs, InAs, and InSb, in the range of 200-1000 nm, Adachi's Model Dielectric Function [1, 2] was curve-fit to literature refractive index data [7, 8]. The temperature dependence of the refractive index of GaSb was approximated based on the temperature dependencies of GaAs and InSb. These refractive index models were helpful in designing distributed Bragg reflectors for enhanced TPV performance, and interpreting features seen in the *in situ* reflectance data.

Chapter 4 discusses phase separation in $Ga_{1-x}In_xAs_ySb_{1-y}$ $(0.1 < x,y < 0.2)$ epilayers. Background information about the thermodynamic driving force for phase separation is presented first. Next, a select literature review of reported phase separation in various ternary and quaternary III-V alloys is presented, followed by a review of the results of previous characterization studies of GaInAsSb epilayers. The TEM results from this thesis are then discussed, which include the effects of alloy composition, substrate miscut direction, and substrate miscut angle of the extent of phase separation in GaInAsSb. One interesting manifestation of the phase separation was the spontaneous formation of a natural superlattice throughout the epilayer. Two variants of this superlattice were observed – one parallel to the growth surface, and one tilted with respect to the growth surface. The tilted superlattice was studied in detail. A qualitative model for the propagation of this tilted superlattice is presented, which can explain both the continuity of the superlattice and the additional tilt angle of the tilted superlattice with respect to the substrate miscut angle. Finally, a framework of the thermodynamic driving

force for phase separation versus the kinetic barrier to surface diffusion is discussed and indicates the growth conditions under which the tilted variant of the superlattice was formed.

General conclusions and a summary are given in chapter 5, followed by suggestions for future work in chapter 6.

2. *In Situ* Reflectance Monitoring

2.1 Overview of *in situ* monitoring

2.1.1 Overview of epitaxial growth techniques

Thin film epitaxial growth for electronic and optoelectronic devices is typically performed by liquid phase epitaxy (LPE), molecular beam epitaxy (MBE), or organometallic vapor phase epitaxy (OMVPE). LPE is a near-equilibrium growth technique in which a single-crystal substrate is placed in contact with a supersaturated liquid melt. Atoms in the liquid phase at the liquid/solid interface continuously leave the melt and bond to the solid, growing a thin film epilayer. High growth rates can be achieved by LPE; however, it is difficult to obtain high quality interfaces between various thin film epilayers.

For devices that require atomically abrupt interfaces, such as quantum well lasers, growth by MBE or OMVPE is more suitable. In MBE, a solid source material is heated to sublime a molecular gas. Since MBE chambers are pumped to high vacuum, typically better than 10^{-9} torr, this molecular gas or molecular beam has a large mean free path

before a collision between molecules takes place. Molecules therefore diffuse uninterrupted toward a heated substrate, where they adsorb to the surface and bond to the crystal. MBE has proven capable of growing very high-purity epilayers, and is the technique by which the most atomically abrupt interfaces can be obtained. This high degree of control often results in superior device performance for devices where monolayer thickness control is critical. However, MBE is typically limited to low growth rates (~1 μm/hr), and since maintenance of high vacuum systems in general is fairly time consuming, MBE has drawbacks for high-volume manufacturing.

Growth by OMVPE is typically carried out at atmospheric or low pressure (usually from 1-780 torr). Organometallic sources are stored in bubblers and their vapors are carried to a heated substrate by an inert carrier gas, either hydrogen or nitrogen. (Hydride or halide sources can also be used; examples include arsine (AsH_3) and phosphine (PH_3).) The metal in the organometallic is the atom of interest to be incorporated in the epilayer, while the organic part is often a methyl, ethyl, or butyl group. When the organometallic precursor is close enough to the heated substrate, it undergoes "cracking" or pyrolysis, in which the covalent bonds between the metal and organic ligands are broken. Ideally, the metal atom is incorporated into the growing epilayer, while the organic group is swept out of the reactor. OMVPE growth techniques have improved over time such that very high quality epilayers and interfaces can now be created, and therefore devices grown by OMVPE often rival those grown by MBE. In addition, growth rates achievable for OMVPE can be five to ten times higher than those for MBE. As a result, OMVPE is often the growth technique of choice for high-volume manufacturing.

2.1.2 Uses of *in situ* monitoring

In situ growth monitoring is particularly useful for MBE and OMVPE. There are two primary motivations or interests for *in situ* monitoring. In research and development applications, *in situ* monitoring is the only way to gain insight into fundamental growth processes. Parameters of interest during growth include: surface chemistry / geometry / morphology; growth mode (e.g. step-flow, layer-by-layer, 3-D); gas phase chemistry; adatom incorporation pathways / mechanisms; adatom surface diffusion rates; onset of dislocation formation for lattice-mismatched epilayers; etc. This insight can take device creation from growth by trial-and-error, to growth by scientific principles. Improved material quality and device performance can result from this knowledge.

In manufacturing environments, *in situ* monitoring enables epilayer parameters of interest to be rapidly obtained, and allows observation of run-to-run variation in these parameters. Parameters of interest typically include the thickness, composition, temperature, doping level, strain, and roughness of an epilayer. Not only can *in situ* monitoring provide faster feedback on these parameters than *ex situ* measurements, but it can also be used to observe dynamically changing parameters that *ex situ* characterization cannot. For example, if the growth rate of an epilayer varied during a run, this variation could be detected by *in situ* monitoring techniques. *Ex situ* x-ray, however, would only yield an average growth rate, based on measured layer thickness and growth time.

2.1.3 Types of *in situ* monitor probes

It is obvious that no single *in situ* probe will be sensitive to all the parameters of interest listed above. However, a variety of probes exists, each sensitive to different growth parameters [9, 10]. In general, the requirements of an *in situ* probe are that it must be: sensitive to the parameter of interest; non-invasive/non-destructive; and rapid on the time scale of the process being monitored. In addition, any modifications made to a reactor to incorporate *in situ* monitoring must not disturb the epitaxial growth process. In MBE, the high-vacuum environment allows for both electronic and optical probes. Electron-based probes include reflection high-energy electron diffraction (RHEED), Auger electron spectroscopy (AES), and x-ray photoelectron spectroscopy (XPS). These *in situ* probes can be used to monitor surface reconstructions (dimers), monolayer growth oscillations, substrate oxide desorption, surface chemistry and surface bonding. Optical probes (including x-rays) are the only option for atmospheric- and low-pressure OMVPE reactors. However, such a broad range of optical probes exists that this is not a limitation. Examples of optical probes that can be used to obtain information about a wafer surface or bulk (and the features to which they are sensitive) include[9]:

- Pyrometry (calculates wafer temperature from wafer emissivity) [11, 12]
- Laser light scattering (surface roughness) [13-17]
- Specular reflectance (epilayer complex refractive index and thickness) [see below for references]
- Ellipsometry (monolayer composition control; substrate oxide desorption; surface/interface roughness) [18-22]
- Deflection of multiple parallel laser beams (epilayer stress) [23, 24]
- Surface photoabsorption (SPA—enhanced surface sensitivity; surface dimers) [25-28]
- Reflectance difference/anisotropy spectroscopy (RDS/RAS—high surface sensitivity; surface reconstructions; monolayer growth oscillations; doping levels), and [29-32]
- Grazing incidence angle x-rays (growth mode; surface morphology) [33, 34].

From these options, specular reflectance was chosen for this thesis to monitor the OMVPE growth *in situ*. The reasons this technique was chosen are as follows: first, analysis of the reflectance signal yields very useful quantitative information about an epilayer—its growth rate and complex refractive index [35-43]. These parameters are easily obtained from the reflectance because the equations governing the signal are well-known. Second, no information is needed *a priori* to analyze the reflectance signal—an especially useful feature for GaSb-based materials since the literature database of information is relatively limited. Finally, reflectance is relatively inexpensive and easy to implement compared to the other optical techniques. Specifically, the number, cost, and complexity of the various components is less than for ellipsometry, SPA, or RDS/RAS.

2.2 *In situ* reflectance setup

2.2.1 Initial setup

The initial experimental setup for the *in situ* reflectance monitor is shown in Fig. 2(a) [43]. A 5 W tungsten-halogen lamp provided a randomly-polarized broadband white light source between 400 and 3000 nm, with peak output intensity near 1000 nm. A 600 μm-core-diameter optical fiber transmitted the light from the lamp to a mirror which reflected the light onto the substrate at a near-normal incidence angle of approximately 2-3° (measured from the surface normal). A lens was placed below the mirror to focus the beam onto the substrate. The specularly reflected beam from the substrate was directed by another mirror to a receiving fiber, which transmitted the light to a commercial silicon spectrometer photodiode array (Si PDA; Control Development, Inc., Model PDA-OSC 380-1100 nm). The Si PDA had a holographic grating that

diffracted light from 380-1100 nm across a 512-element pixel array. All the PDA optics and electronics were mounted directly on a PC plug-in card. Spectra could be acquired with an integration time as short as 1 ms, although for this thesis research 1 s integration times were typically used. This integration time was long enough to yield a good signal-to-noise ratio (typically >6:1 for $Ga_{0.9}In_{0.1}As_{0.09}Sb_{0.91}$, >140:1 for $Al_{0.8}Ga_{0.2}As_{0.06}Sb_{0.94}$, where the signal is defined as the peak-to-peak amplitude of the *in situ* reflectance oscillations), and short enough compared to the fastest growth rate (1.54 nm/s for GaInAsSb, yielding an *in situ* reflectance oscillation period of ~70 s).

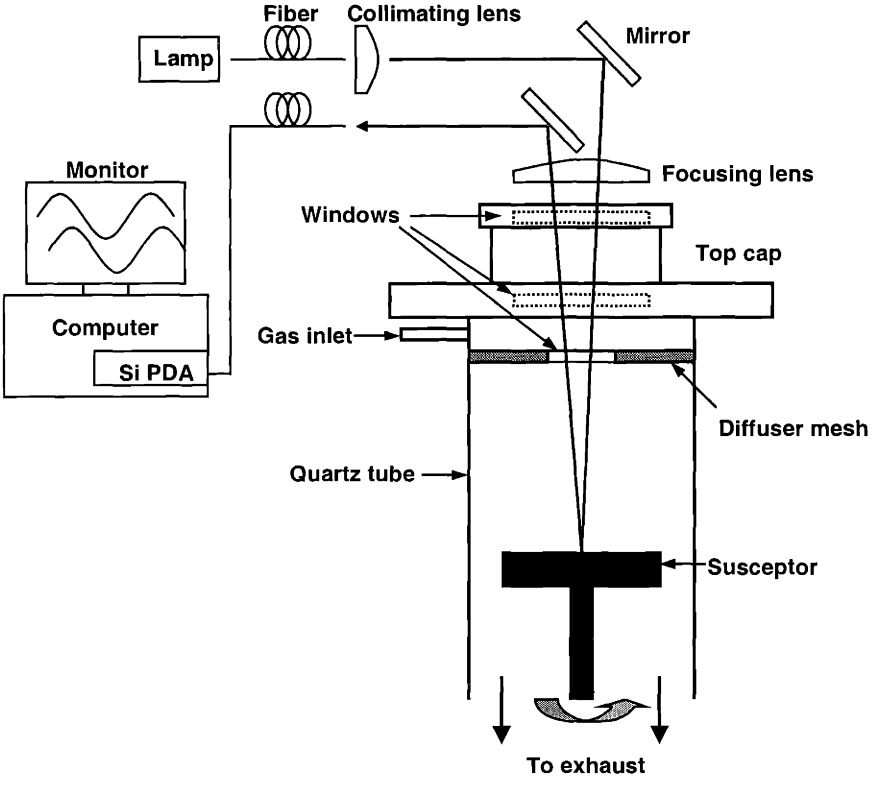

(a)

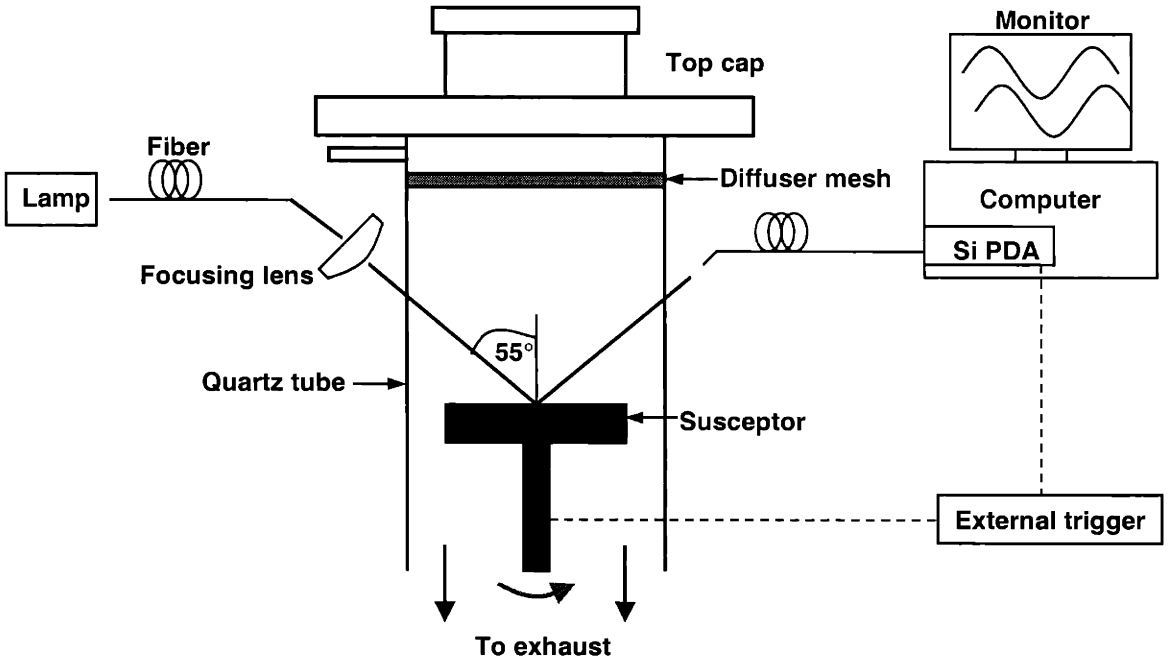

(b)

Fig. 2. Schematic diagram of (a) the initial setup and (b) the redesigned setup for the *in situ* reflectance monitor.

The organometallic sources and hydrogen carrier gas were injected into the volume just above the mesh diffuser screen as seen by the gas inlet in Fig. 2(a). The gas mixed turbulently in that volume, and then exhibited laminar flow through the reactor due to the mesh diffuser screen. In order to obtain near-normal optical access, the stainless steel top cap, inner cap (not shown), and mesh diffuser screen all had to be modified to include optical windows. These modifications were designed and completed by others prior to this thesis. Two-inch diameter windows were axially centered in the top cap and inner cap, and a one-inch diameter window was axially centered in the mesh diffuser screen.

Upon completion of the *in situ* reflectance monitor design, the standard top cap, inner cap, and diffuser screen (all without windows) were replaced with the modified designs that included windows to accommodate the reflectance monitor. After several growth runs, it was determined that these modifications affected the epitaxial growth process. Small droplet-like particles (less than 5 μm diameter) were observed scattered over the wafer surface under Nomarski interference microscopy. It is unclear what these particles were or how they formed. However, one possibility is that the window in the diffuser mesh may have caused recirculating flows in the reactor. Finite element modeling done by others prior to this thesis indicated that a 1-inch diameter obstruction in the diffuser screen would preserve laminar flow conditions, while a 2-inch diameter obstruction would cause recirculating flows beneath the obstruction [43]. Although the window in the diffuser screen was only 1 inch in diameter, with the flanges that held it in place the diameter of the total obstruction was 1.5 inches. Therefore, recirculating flows may have been present below the window and caused these growth defects.

2.2.2 Redesigned setup

Since one of the primary considerations for any *in situ* monitor is that it must not disturb or affect the epitaxial growth process, a decision was made to eliminate the near-normal optical access, return to the standard caps and mesh without windows, and redesign the *in situ* reflectance monitoring system. Fortunately, the reactor design provided extensive optical access at non-normal incidence angles. Due to the laminar gas flow and thermal profile in the reactor, during deposition the quartz tube was only coated with deposits below the susceptor. Therefore, optical access through the top half of the quartz tube (approximately 8 cm length) remained unobstructed.

The redesigned experimental setup for the *in situ* reflectance monitor is shown in Fig. 2(b). The optical fiber was re-positioned to transmit light from the lamp to a 25 mm diameter achromatic lens that focused the beam through the quartz tube and onto the wafer at an incidence angle of 55°. This angle was chosen due its easy accessibility in the reactor. The reflected beam was transmitted by the receiving fiber to the Si PDA.

During experiments using the initial setup, it was observed that a slight angular wobble of the susceptor during rotation prevented the reflected beam from remaining centered on the receiving fiber throughout the entire rotation period. This was also true for the redesigned monitor at 55°. As a result, the measured reflectance artificially oscillated at the same frequency as the wafer rotation. A beat frequency signal, related to the difference in frequency between the susceptor rotation rate and the data acquisition rate, was superimposed on the true reflectance signal [41, 43, 44]. This beat frequency signal can be eliminated if the data acquisition rate is synchronized with the rotation rate.

Synchronization can be accomplished by setting the PDA detector integration time to be some multiple of the susceptor rotation period. However, a more elegant and robust solution is the use of an external trigger system. Such a system was designed and included in the modified *in situ* reflectance setup. The design consisted of a light-emitting diode (LED) and bulk Si detector situated 180° apart at the base of the susceptor rotation shaft. This shaft was not perfectly circular at the base – there was a cutout to allow access to a thermocouple feed-through. At a particular azimuthal rotation position of the susceptor, the shaft cutout was aligned with the external triggering system such that the optical beam from the LED could reach the Si detector. A circuit was designed which then sent a TTL (+5 V) pulse to the external trigger input of the Control

Development Si PDA spectrometer. The trigger system synchronized data acquisition with the susceptor rotation, such that signal integration was always initiated at the same azimuthal rotation position of the susceptor. This completely eliminated noise associated with mechanical susceptor wobble.

The optical components chosen for the initial *in situ* reflectance monitor design were based on several designs described in the literature [35-38, 41]. *In situ* reflectance setups designed 10-15 years ago typically utilized a single wavelength laser and bulk silicon detector. As the availability of silicon detector arrays increased and the cost decreased, broadband spectral reflectance setups became more common. In all literature reports, the III-V semiconductor alloys being monitored had cutoff wavelengths of 1.5 μm or shorter (i.e. bandgaps of 0.8 eV or larger). The most commonly monitored materials included GaAs, AlAs, AlGaAs, InGaAs, InGaAsP, GaN, and AlGaN. In order for quantitative information to be extracted from an *in situ* reflectance signal, the epilayer must be sufficiently transparent at the growth temperature and at the wavelength of light used to monitor. Since silicon detector arrays have detectivity out to 1.1 μm, the materials listed above all meet this requirement. However, since the GaInAsSb alloys monitored in this thesis typically had a cutoff wavelength of 2.3 μm (bandgap of 0.54 eV), it was not clear at the outset that a silicon detector array would be suitable for *in situ* reflectance monitoring, due to the large absorption of this alloy in the silicon detector array wavelength range. Results presented later demonstrate that wavelengths longer than 700 nm are acceptable for monitoring GaInAsSb.

A comprehensive Windows-based data acquisition and display program was written in Visual Basic as part of this thesis. This program allowed the user to calibrate

the PDA spectrometer, acquire reflectance data during epitaxial growth, view the reflectance on-screen in real-time, store the data for subsequent analysis, and perform curve-fits to extract quantitative information.

Non-linear least squares regressive curve-fitting of the reflectance was accomplished by calling C++ routines compiled as a dynamic link library (DLL). This DLL was obtained from Dr. William G. Breiland at Sandia National Laboratories, and is known as ADVISOR (Analysis of Deposition using Virtual Interfaces and Spectroscopic Optical Reflectance) [36].

2.3 Theory and equations for specular reflectance

2.3.1 Basic equations†

Whenever light encounters a dielectric discontinuity, such as at the interface between two different epitaxial layers, a fraction of the light is reflected. For two homogeneous, isotropic media, with a flat planar interface between them, the complex reflection coefficient for normal incidence light is given by:

$$r_s = r_p = \frac{N_1 - N_2}{N_1 + N_2} \tag{1}$$

where r_s is the reflection coefficient of s-polarized light (electric field perpendicular to the plane of incidence), r_p is the reflection coefficient of p-polarized light (electric field parallel to the plane of incidence), and N_j is the complex refractive index of medium j. The complex refractive index has a real and an imaginary component for an absorbing medium, and is given by $N = n\text{-}i*k$, where n is the real component that relates the speed of light in vacuum to the speed of light in the medium, k is the imaginary component

dependent on the absorbance of the medium, and i is the imaginary constant. The reflectance, defined as the fraction of energy reflected at the interface relative to the incident energy, is given (at normal incidence) by:

$$R = r_s r_s^* = r_p r_p^* = |r_s|^2 = |r_p|^2 \tag{2}$$

where r_j^* is the complex conjugate of r_j. For smooth interfaces where there is no diffuse (non-specular) scattering, the fraction of incident light that is not reflected is instead refracted (transmitted) into the medium below the interface.

For non-normal incidence angles, the reflectance equations are modified as follows:

$$r_s = \frac{N_1 \cos\phi_1 - N_2 \cos\phi_2}{N_1 \cos\phi_1 + N_2 \cos\phi_2} \tag{3a}$$

$$r_p = \frac{N_2 \cos\phi_1 - N_1 \cos\phi_2}{N_2 \cos\phi_1 + N_1 \cos\phi_2} \tag{3b}$$

$$R_s = |r_s|^2 \tag{4a}$$

$$R_p = |r_p|^2 \tag{4b}$$

where ϕ_1 is the incidence angle, defined as the angle between the incident light beam and the surface normal. Snell's Law, $N_1 \sin\phi_1 = N_2 \sin\phi_2$, can be used to calculate the angle of refraction into medium 2. For absorbing media (extinction coefficient $k > 0$), the angle of refraction is complex and cannot be directly interpreted as a measurable, physical angle.

Light incident on a multilayer film stack reflects at every interface between films that have different refractive indices, as seen in Fig. 3. The vector sum of these individual reflectances determines the total reflectance measured from the stack. If the

---

† The equations in this section can be found in several different books. See for example refs. [9, 45, 46].

thickness of the topmost film in the stack is continuously increasing or decreasing (e.g. due to film deposition or etching), then the relative phase of reflectance 'A' continuously changes with respect to the phases of the underlying reflectances 'B', 'C', etc. This causes the reflectance of the stack to oscillate as a function of the topmost film thickness, with periodic constructive and destructive interference conditions causing maxima and minima in the reflectance, respectively. An example of such reflectance oscillations is shown in Fig. 4. This is a theoretical plot of reflectance vs. layer thickness at a wavelength of 750 nm, for deposition of GaInAsSb on GaSb followed by deposition of AlGaAsSb. (The refractive indices used to generate this plot were taken from data in Fig. 5.)

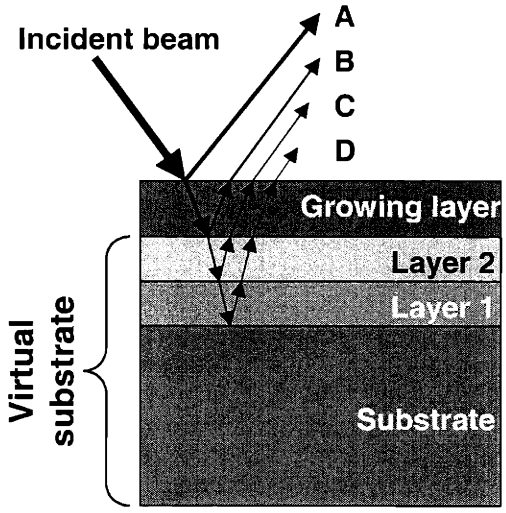

Fig. 3. Diagram illustrating light incident on a multilayer film stack. During epitaxial deposition the thickness of the growing layer continuously increases, causing constructive and destructive interference between reflectance 'A' and the underlying reflectances. This creates oscillations in the *in situ* reflectance signal, shown in Fig. 4.

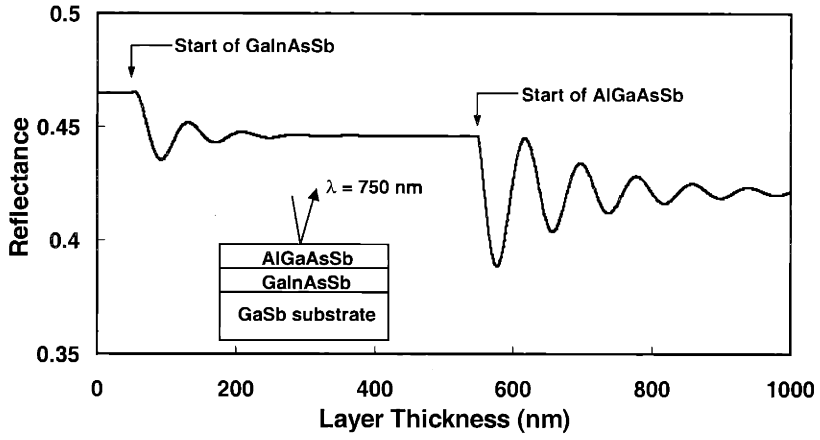

Fig. 4. Example of calculated *in situ* reflectance curve for deposition of GaInAsSb and AlGaAsSb on a GaSb substrate. The maxima and minima correspond to epilayer thicknesses that yield constructive and destructive interference conditions, respectively.

2.3.2 Matrix representation of a multilayer film stack

If the thickness and refractive index are known for each layer in a multilayer film stack, then the reflectance of the stack can be calculated (assuming all surfaces and interfaces are flat, and all films are homogeneous). A variety of techniques exist to calculate the reflectance; most rely on a matrix representation of the multilayer film stack [45, 46]. Specifically, each film can be represented by the following 2x2 matrix [45]:

$$\begin{bmatrix} \cos\beta_r & i\sin\beta_r / \eta_r \\ i\eta_r \sin\beta_r & \cos\beta_r \end{bmatrix} \tag{5}$$

where the phase shift β_r for layer r is defined by

$$\beta_r = \frac{2\pi N_r d_r \cos\phi_r}{\lambda} \tag{6}$$

and the tilted optical admittance η_r is defined by

$$\eta_r = N_r \cos\phi_r \qquad \text{(for s polarization)} \tag{7a}$$

$$\eta_r = N_r / \cos\phi_r \qquad \text{(for p polarization)} \tag{7b}$$

N_r is the complex refractive index of layer r, d_r is the thickness of layer r, ϕ_r is the propagation angle in layer r measured from the surface normal, and λ is the wavelength of the light in vacuum.

The substrate is represented by a simple 2x1 matrix:

$$\begin{bmatrix} 1 \\ \eta_{sub} \end{bmatrix} \tag{8}$$

where the tilted optical admittance of the substrate, η_{sub}, is defined similarly to equation (7) above, using the complex refractive index N_{sub} of the substrate.

The characteristic matrix of the entire assembly (films + substrate) is given by:

$$\begin{bmatrix} B \\ C \end{bmatrix} = \left(\prod_{r=1}^{q} \begin{bmatrix} \cos\beta_r & i\sin\beta_r / \eta_r \\ i\eta_r \sin\beta_r & \cos\beta_r \end{bmatrix} \right) \begin{bmatrix} 1 \\ \eta_{sub} \end{bmatrix} \tag{9}$$

where q is the total number of epilayers in the multilayer stack. It is essential to multiply the matrices in the proper order.

Once the characteristic matrix of the assembly is known, the reflectance is easily calculated as [45]:

$$R = \left(\frac{\eta_0 - \frac{C}{B}}{\eta_0 + \frac{C}{B}} \right) \left(\frac{\eta_0 - \frac{C}{B}}{\eta_0 + \frac{C}{B}} \right)^* = \left| \frac{\eta_0 - \frac{C}{B}}{\eta_0 + \frac{C}{B}} \right|^2 \tag{10}$$

where η_0 is the tilted optical admittance of the incident medium, defined as above using the complex refractive index of the incident medium (= 1 for air/vacuum). For s- or p-polarized reflectance, the appropriate tilted optical admittances are defined in eqn. (7).

During multilayer film deposition, the complex refractive index N_r and growth rate G_r of each film can be extracted from the reflectance oscillations by curve-fitting the above matrix equation to the measured reflectance. The matrix can be converted from a static calculation to one which is a function of growth time by replacing the film thickness, d_r, by the product G_r*t, where G_r is the growth rate of layer r and t is the time. As the first film is deposited, five parameters can be curve-fit for: n_{sub}, k_{sub}, n_r, k_r, and G_r. (Note that in general, n_r and k_r for any film r will be different at different wavelengths due to dispersion. However, the extracted growth rate of the film, G_r, should be constant regardless of the wavelength of light used.) Once these parameters are known, they can be substituted into the matrix equation as constants to curve-fit n, k, and G of subsequent film deposition. This technique requires that n, k, and G be curve-fit for each film as it is deposited so that these parameters can be used when curve-fitting for the subsequently deposited film. This requirement leads to forward-propagating errors and can result in highly inaccurate results [47]. If the parameters extracted for one film in the stack are inaccurate, these inaccuracies will affect the calculated parameters for all subsequent films. This situation is obviously highly undesirable.

2.3.3 Virtual interface and virtual substrate concepts

The problem of forward-propagating errors can be overcome, and the curve-fitting procedure can be greatly simplified, if the virtual substrate and virtual interface concepts are used. Developed by Urban [48] and Aspnes [49] and later refined for *in situ* reflectance by Breiland [36], these simplifications take advantage of the fact that during epitaxial growth, all films below the topmost growing film are static in time. Rather than

treating the multilayer stack in Fig. 3 by an [Ambient / Film 3 / Film 2 / Film 1 / Substrate] model, it can treated by an [Ambient / Film 3 / Effective substrate] model. Any number of films can always be lumped together and mathematically represented as one film with an effective refractive index. This simplification is mathematically exact. Note also that the interface between Film 3 and the effective substrate does not have to be associated with the actual, physical interface. Rather, a virtual interface can be defined anywhere within Film 3, such that the only some top portion of Film 3 is analyzed, and the lower portion of Film 3 is lumped into the effective substrate [36]. This means that if growth conditions such as the growth rate are dynamically changing during film growth, this variation can be measured by the *in situ* reflectance by analyzing different time segments of the growth of Film 3.

Once the stack is reduced to an [Ambient / Film 3 / Effective substrate] model, data analysis is straightforward. The normal-incidence reflectance equation governing such a system is well-known and given by [36]:

$$r(t) = \frac{r_\infty + r_i \exp(\frac{-i4\pi NGt}{\lambda})}{1 + r_\infty r_i \exp(\frac{-i4\pi NGt}{\lambda})} \tag{11a}$$

$$R(t) = r(t)r^*(t) = |r(t)|^2 \tag{11b}$$

As before, N is the complex refractive index and G is the growth rate of the epilayer, λ is the wavelength of the light in vacuum, and t is the growth time. r_∞ represents the reflection coefficient of an infinitely thick film of the epilayer, and is given by the standard equation $(1-N)/(1+N)$. r_i is the reflection coefficient at the virtual interface,

between the epilayer and the virtual substrate, and is given by $(N\text{-}N_{VS})/(N+N_{VS})$, where N_{VS} is the complex refractive index of the effective or virtual substrate.

Equation (11b) can be curve-fit to *in situ* reflectance data using a non-linear, least-squares regressive routine to extract five variables: n_{VS}, k_{VS}, n_{film}, k_{film}, and G [36]. The values n_{VS} and k_{VS} for the virtual substrate are usually not of interest because they do not represent a single, homogeneous film. However, the values n_{film} and k_{film} for the film are useful because they are a function of the alloy composition. Although the relationship between alloy composition and refractive index is rarely known theoretically (especially at growth temperatures!), it can be determined experimentally. The growth rate is obviously useful because the properties of thin film devices are very dependent on the various film thicknesses.

Equation (11) above is for normal-incidence reflectance. The equation for oblique-incidence reflectance is similar but slightly more complicated [50].

2.3.4 Requirements of *in situ* reflectance signal to obtain *n*, *k*, and *G*

In order to achieve a successful curve fit, the reflectance data must meet a few requirements [36]. First, at least five data points must be present if all five parameters (n_{VS}, k_{VS}, n_{film}, k_{film}, and G) are unknown and must be fit as variables. Second, at least one extremum (minimum or maximum) and one inflection point must be present in the reflectance signal to enable the curve-fitting routine to determine amplitude, phase, and frequency information. The most accurate curve-fits are usually obtained if at least one or two signal oscillations are included in the data set. Each oscillation period represents a phase change of 2π in the reflectance. The phase is given by $(4*\pi*n*d)/\lambda$, where λ is the

wavelength of light in vacuum, n is the real part of the refractive index (at the wavelength λ), and d is the film thickness. Setting this equation equal to 2π, and plugging in typical values of $\lambda = 633$ nm and $n = 5$ (approximation for GaSb at 633 nm at 550 °C), yields $d = \lambda/(2*n) = 63$ nm. This means that films must be grown at least 63 nm thick under typical conditions in order to accurately curve-fit the reflectance data and extract n, k, and G.

Finally, accurate curve-fits require that the absolute reflectance is known. Each epilayer can be fit for three parameters (n, k, and G) since the reflectance signal has three independent features that are a function of different pairs of these parameters. These features are: the frequency of the oscillations (dependent on n and G), the exponential decay of the amplitude of the oscillations (dependent on k and G), and the mean value of the absolute reflectance towards which the signal is decaying (dependent on n and k). There is a high correlation between the parameters n and G which can only be broken if the absolute reflectance is known [36]. Otherwise, only optical growth rates ($n*G$ product) can be determined, as opposed to actual, physical film growth rates (G).

2.4 Experimental results from *in situ* reflectance

2.4.1 Overview of experimental results

The next few sections present various experimental results obtained from the *in situ* reflectance. The most commonly reported use of *in situ* reflectance in the literature is to determine n, k, and G for thin-film epilayers. This capability was the initial driving force for selecting reflectance from among the various *in situ* optical probes. Results of this type of measurement are presented in section 2.4.2, after the experimental growth

conditions are listed in section 2.4.1.1. During the course of the thesis, it was observed that the *in situ* reflectance is useful for more than just determining n, k, and G, however. This probe is also sensitive to: substrate oxide desorption [51]; a loss of source material; the minimum V/III ratio; and minimum organometallic source pre-flow times for equilibration. Examples in sections 2.4.3 to 2.4.6 will highlight the ability of *in situ* reflectance to provide rapid diagnostics of these routine and non-routine occurrences in epitaxial growth. The capability to detect errors during an epitaxial growth run is a particularly powerful feature of *in situ* probes. *In situ* monitoring detects when an error occurred, and provides insight into the cause of the error. Both of these capabilities are difficult to achieve with *ex situ* characterization. More details are provided in the following sections.

2.4.1.1 OMVPE experimental growth conditions

The OMVPE growth was performed by Dr. Christine Wang, and was carried out in a vertical, rotating-disk reactor, operated at 150 torr. Hydrogen carrier gas was flowed at a rate of 10 slpm. All-organometallic sources were used, including triethylgallium (TEGa), trimethylantimony (TMSb), solution trimethylindium (TMIn), tertiarybutylarsine (TBAs), and tritertiarybutylaluminum (TTBAl). Dimethylzinc (DMZn) was used as a p-dopant, and diethyltellurium (DETe) as an n-dopant. The growth temperature was varied from 525 to 575 °C, the V/III ratio was typically between 1 and 2, and the GaSb substrates were oriented (001) miscut 2° or 6° toward the (101), the (-1-11)A, or the (1-11)B. Growth rates for the GaInAsSb, AlGaAsSb, and GaSb epilayers were typically 5 μm/hour, 1 μm/hour, and 1 μm/hour, respectively.

2.4.2 Experimental results on obtaining *n*, *k*, and *G* of an epilayer from *in situ* reflectance

If the reflectance signal meets the criteria mentioned in section 2.3.4, then values of n, k, and G (at the growth temperature) can be extracted for an epilayer. Several examples of such n and k data obtained under the initial (near-normal incidence) *in situ* reflectance monitor are shown in Fig. 5 [43].

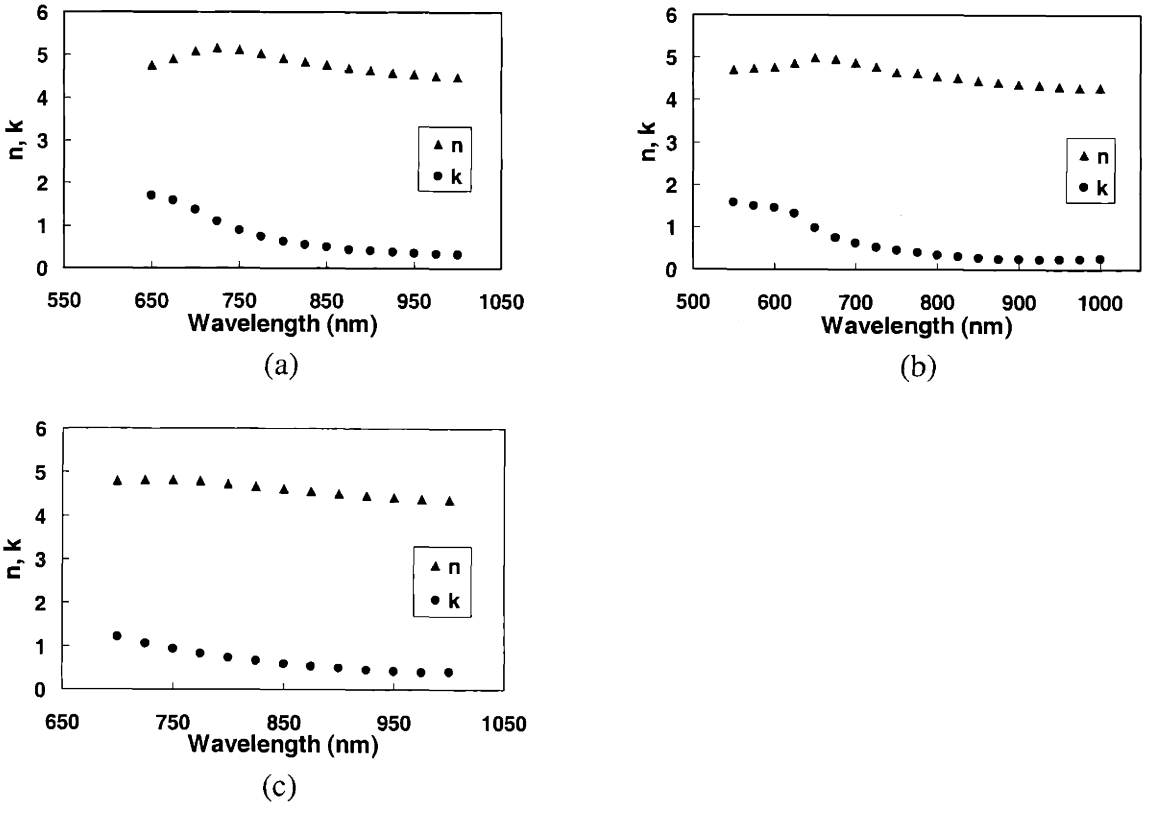

Fig. 5. Refractive indices obtained from *in situ* reflectance data for (a) GaSb at 525 °C, (b) $Al_{0.2}Ga_{0.8}As_{0.02}Sb_{0.98}$ at 550 °C, and (c) $Ga_{0.83}In_{0.17}As_{0.16}Sb_{0.84}$ at 525 °C.

Note that values of n, k, and G can only be extracted at wavelengths longer than 700 nm for $Ga_{0.83}In_{0.17}As_{0.16}Sb_{0.84}$ grown at 525 °C. (Epilayer composition was determined from high-resolution x-ray diffraction (HRXRD) splitting of ω-2Θ scans, the peak emission in 300 K photoluminescence spectra, and the energy gap dependence on composition.) This is because optical absorption in this alloy at wavelengths shorter than 700 nm is so high that less than one full oscillation is present in the reflectance signal, and the curve-fitting routine fails to converge.

In order to calibrate the reflectance system to measure absolute reflectance, under the initial setup an aluminum mirror was used as a reference calibration standard. The spectral reflectance of the mirror from 380-1100 nm was measured *ex situ* using a Cary 5E Spectrophotometer, accurate to better than 1%. This known reflectance spectrum was then used to calibrate the arbitrary units of the *in situ* Si PDA spectrometer. The accuracy of the *in situ* absolute reflectance measurements using this calibration technique was limited to about 4%. The reason for the limited accuracy was the way the optical components were mounted in the initial setup. Since the substrates are loaded into and out of the reactor by removing the top and inner cap (the diffuser screen is attached to the inner cap), it was necessary to mount the optical mirrors and lens on an optical breadboard, which was in turn mounted on rails that straddled the top cap. This enabled the optical components to slide out of the way to allow the top cap to be removed for wafer loading and unloading, and to slide back in place above the top cap window to enable *in situ* optical monitoring. However, the top cap, inner cap, and optical breadboard had some mechanical "play" in their exact positioning. As a result, it was not possible to relocate these parts to exactly the same position every time wafers were

loaded and unloaded. Therefore, the position of the parts when *in situ* measurements were being taken was not exactly the same position as when the mirror was loaded into the reactor to calibrate the reflectance. This slight misalignment probably accounted for the 4% accuracy limitation.

An error in the absolute reflectance of 4% results in roughly a 4% error in the extracted values of n, k, and G. Unfortunately, there is no available literature data to compare to the extracted values of n and k shown in Fig. 5. However, the extracted growth rates can be compared to growth rates determined by standard *ex situ* x-ray diffraction methods. Epitaxial layer thickness was determined within ± 2% by HRXRD, using software based on the Takagi-Taupin solution to dynamical x-ray diffraction. This layer thickness is directly related to the epilayer growth rate by the simple formula Film Thickness = Growth Rate * Growth Time. Film thicknesses determined from the *in situ* reflectance were 234.0 nm ± 10.0 nm for the GaInAsSb layer, 273.0 nm ± 11.0 nm for the AlGaAsSb layer, and 360.0 nm ± 14.4 nm for the GaSb layer. These values agreed well with thicknesses determined *ex situ* by HRXRD: 231.0 nm ± 4.6 nm for the GaInAsSb layer, 263.2 nm ± 5.3 nm for the AlGaAsSb layer, and 369.5 nm ± 7.4 nm for the GaSb layer. Dividing the *in situ* reflectance film thicknesses by the appropriate growth times yielded the following growth rates: 1.17 nm/s for $Ga_{0.83}In_{0.17}As_{0.16}Sb_{0.84}$ at 525 °C, 0.273 nm/s for $Al_{0.2}Ga_{0.8}As_{0.02}Sb_{0.98}$ at 550 °C, and 0.24 nm/s for GaSb at 525 °C.

Values for n, k, and G were also extracted from *in situ* reflectance obtained using the modified setup at a 55° incidence angle. Since the ADVISOR curve-fitting routine assumed a setup using a normal incidence angle (0°), there was some inaccuracy associated with this in the extracted values of n, k, and G. Simulations were run in order

to determine the magnitude of this error. Using typical n and k values displayed in Fig. 5 and standard reflectance equations, simulated curves of reflectance vs. epilayer growth time were generated for randomly-polarized light at an incidence angle of 55°. These simulated curves were then loaded into ADVISOR and curve fit. For $Ga_{0.83}In_{0.17}As_{0.16}Sb_{0.84}$ grown on GaSb at 550 °C, the following parameters were used as input for a 1000 nm wavelength: $N_{GaInAsSb}$ = 4.365-i*0.413, N_{GaSb} = 4.512-i*0.346, and G = 1.550 nm/s. The ADVISOR curve-fit values were $N_{GaInAsSb}$ = 4.287-I*0.421 and G = 1.551 nm/s. This gives errors of –1.8% for n, +1.9% for k, and +0.06% for G. (Note that if the simulated data were generated at an incidence angle of 0° instead of 55°, the exact input values were correctly returned, as expected.) At a wavelength of 700 nm, the following input values were used: $N_{GaInAsSb}$ = 4.798-i*1.212, N_{GaSb} = 5.061-i*1.380, and G = 1.550 nm/s. The extracted values from the curve-fit were $N_{GaInAsSb}$ = 4.624-i*1.202 and G = 1.588 nm/s, giving errors of –3.6% for n, -0.8% for k, and +2.5% for G.

For $Al_{0.81}Ga_{0.19}AsSb$ grown on GaSb at 550 °C, the following parameters were used as input for λ = 1000 nm: $N_{AlGaAsSb}$ = 3.880-i*0.120, N_{GaSb} = 4.512-i*0.346, and G = 0.180 nm/s. (The AlGaAsSb refractive index was obtained from *in situ* data not shown in Fig. 5). The ADVISOR curve-fit values were $N_{AlGaAsSb}$ = 3.877-i*0.126 and G = 0.176 nm/s, yielding errors of –0.08% for n, +5% for k, and –2.22% for G.

It is fairly surprising that the error due to assuming a 0° incidence angle (when in fact a 55° incidence angle was used) is less than 5% for any parameter. However, there are two reasons for this fortunate result. First, as the simulated curves in Fig. 6 show, the reflectance for randomly-polarized light remains about the same (within 2%) for the range of incidence angles from 0-68°. This is because the s-polarized reflectance is

increasing, while the p-polarized reflectance is decreasing in this incidence angle range. The two trends cancel out for randomly-polarized light, providing a fairly constant reflectance. The Fig. 6 calculations are for GaSb at a wavelength of 1000 nm at 300 K, but the trend is the same for all the III-Vs and growth temperatures examined in this thesis. Thus, changing the incidence angle from 0° to 55° introduces less than 2% error in the value of the absolute reflectance, provided randomly-polarized light is used.

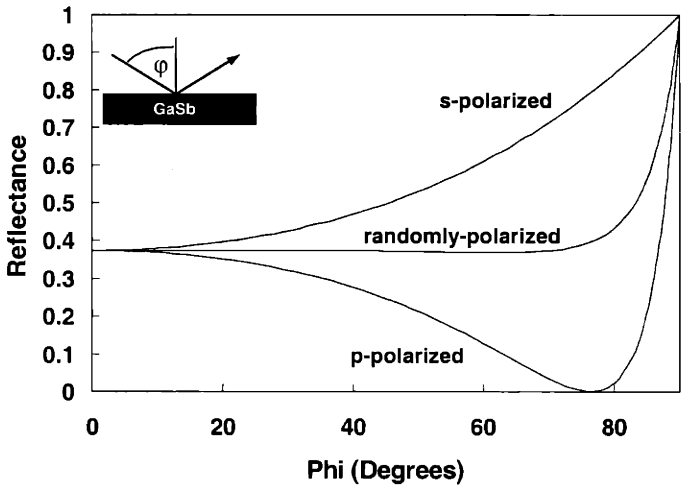

Fig. 6. Reflectance of GaSb at 300 K as a function of incidence angle (phi) and polarization. Notice that the randomly-polarized reflectance remains relatively constant over a wide range of incidence angles.

The second effect that minimizes the error of curve-fitting data obtained at a 55° incidence angle is the angle of refraction. By Snell's Law, it can be determined that the approximate angle of refraction into the epilayers is about 10° (since $N_1 = 1$, $N_2 \approx 4.6$ at 550 °C, and $\varphi_1 = 55°$). This means that in the epilayers, the light is propagating at approximately near-normal incidence. Also, the physical path length traveled by the light

is only increased by 1.5% for an angle of 10° compared to 0°, using simple geometrical calculations. Therefore, the calculated growth rate won't be substantially affected by this increase in physical path length.

Data obtained using randomly-polarized light at an incidence angle of 55° can therefore be fairly accurately curve-fit by software that assumes an incidence angle of 0°, especially at λ = 1000 nm. However, for the most accurate results, curve-fitting software should take into account the angle of incidence. This capability is available using AADVISOR 2.0 [50].

Experimental results from the redesigned setup at 55° comparing the growth rates determined by *in situ* reflectance at 1000 nm and *ex situ* x-ray are given in Table I. The growth rates determined by *in situ* reflectance were consistently lower than those from *ex situ* x-ray. Under the redesigned setup, the starting reflectance of the GaSb substrate was used to calibrate to units of absolute reflectance. A mirror was not used to perform this calibration for two reasons. First, a mirror standard whose randomly-polarized reflectance was accurately known at a 55° incidence angle from 380-1100 nm was not available. Second, it was observed that substrates did not always sit exactly the same on the susceptor. Any tilt difference between the seating of a mirror standard and the substrate yielded inaccuracies in calibrating absolute reflectance. Therefore, it was decided to simply use the starting reflectance of the GaSb substrate as the calibration.

Table I. Comparison of Epitaxial Growth Rates Determined by *in situ* Reflectance and *ex situ* X-ray		
Layer	***In situ* growth rate (@ 1000 nm)**	***Ex situ* x-ray growth rate**
GaSb	0.266 nm/s	0.294 nm/s
GaInAsSb	1.376	1.520
AlGaAsSb	0.167	0.184

However, the reflectance value assumed for GaSb ($R_{GaSb} = 0.371$ at 25 °C at $\lambda = 1000$ nm at a 55° incidence angle) to perform the calibration to absolute reflectance units was obviously too high, since the extracted growth rates were too low. (A 2 nm-thick oxide was assumed present on the GaSb surface. The reflectance value is barely affected by the starting oxide thickness at $\lambda = 1000$ nm under the experimental setup, however. Calculations indicate that the reflectance only decreases from 0.372 for a clean, oxide-free GaSb surface to 0.370 for a surface with a 6 nm-thick oxide.) Using the growth rates from the x-ray data, the starting reflectance of the GaSb substrate at 25 °C at a 55° incidence angle was properly calibrated to $R_{GaSb} = 0.335$ at $\lambda = 1000$ nm. This starting reflectance was a lot lower than expected based on ellipsometric data (see sec. 3.2.2). One possible explanation for this result is the polarization state of the light incident on the substrate. If the light was not randomly polarized as assumed, but rather was partially polarized with 41% s polarization and 59% p polarization, this would explain the lower-than-expected GaSb reflectance. It is possible that the randomly-polarized lamp output became partially polarized after transmission through the OMVPE reactor quartz tube, since the transmission coefficients are different for s- and p-polarized light. In addition, the quartz itself and the optical fiber may partially polarize the light.

However, the exact origin of the discrepancy between the expected reflectance (0.371) and the apparent, actual reflectance (0.335) is still unclear.

Some slight variation in the starting reflectance was observed from substrate to substrate. Therefore, a more accurate calibration than the starting reflectance of the substrate is the high temperature reflectance of the GaSb buffer layer grown on the substrate. At 1000 nm at 550 °C this value is $R_{GaSb} = 0.393$, based on calibration of the *in situ* reflectance growth rates to *ex situ* x-ray growth rates. Similarly, $R_{GaSb} = 0.383$ at 1000 nm at 525 °C. This calibration yielded highly accurate, reproducible results.

One of the most common uses of an *in situ* reflectance monitor is to provide growth rate calibrations before a growth run series [36]. In order to calibrate the growth rate of various epilayers before a series of runs, it is fairly time consuming (and wasteful) to grow a series of individual epilayer films and curve-fit each growth rate using *ex situ* x-ray diffraction. Instead, it is far quicker to do one growth run that contains all the epilayers of interest, and curve fit the growth rate of each layer in that run from the *in situ* reflectance data. An example of such a run is shown in Fig. 7. All parameters of interest can be varied during this run, including temperature and alloy composition. As long as each epilayer has sufficient dielectric contrast with the underlying layers in the film stack to provide reflectance oscillations, each growth rate can be curve-fit using the virtual interface model described above.

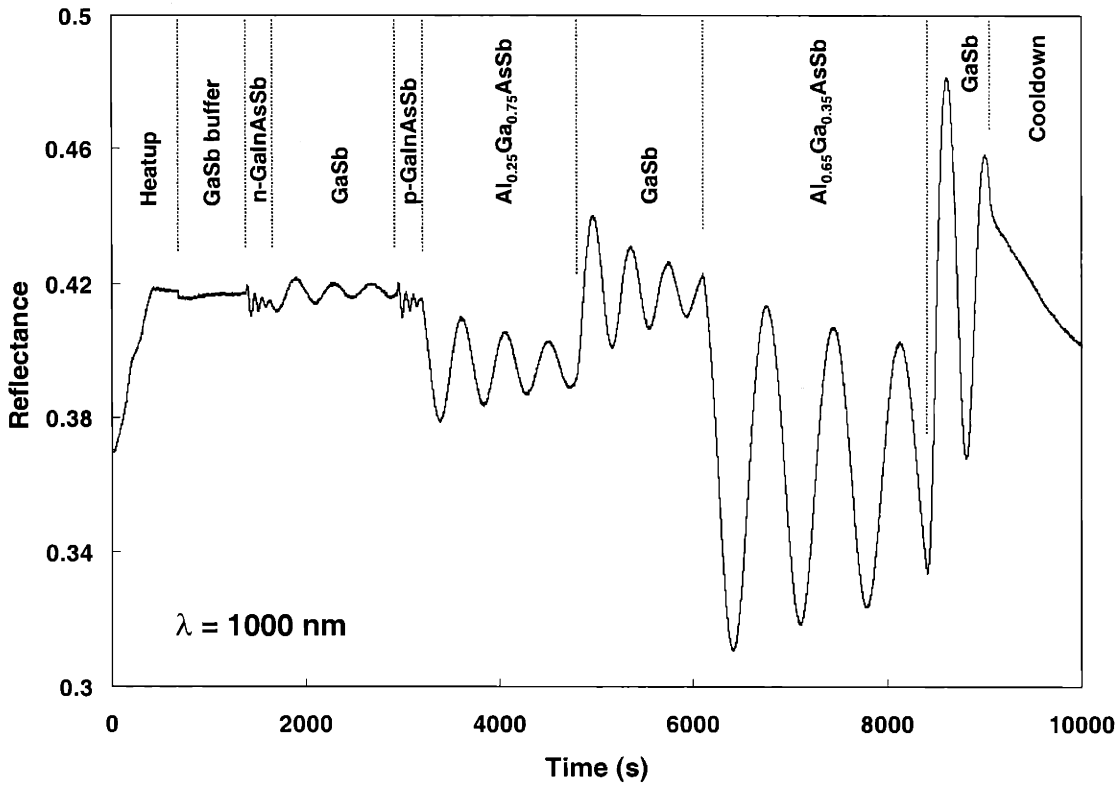

Fig. 7. *In situ* reflectance at 1000 nm obtained during a single growth rate calibration run. The growth rate of each layer can be determined from this data, which is much faster than the normal technique of growing separate layers and determining the growth rate of each from *ex situ* x-ray.

Once growth rate and other necessary calibrations have been completed, device structures can be grown. Figure 8(a) shows the typical *in situ* reflectance at $\lambda = 1000$ nm obtained during growth of a TPV device. The first 720 seconds were heat-up of the GaSb substrate from 25 to 550 °C. Features seen in the reflectance during the heat-up are associated with substrate oxide desorption and are discussed in more detail in section 2.6 below. The next 500 s were growth of an n-doped GaSb buffer layer. After that, from 1225 to 2025 s, the n-$Ga_{0.83}In_{0.17}As_{0.16}Sb_{0.84}$ base layer was grown. Then the p-$Ga_{0.83}In_{0.17}As_{0.16}Sb_{0.84}$ emitter layer was grown from 2025 to 5025 s, followed by the

$Al_{0.2}Ga_{0.8}As_{0.02}Sb_{0.98}$ window layer from 5027 to 5105 s, and finally the p-GaSb contact layer from 5105 to 5275 s. Cool-down began at 5275 s. Note that the reflectance remained constant from the n-doped GaInAsSb base layer to the p-doped GaInAsSb emitter layer, indicating that the *in situ* reflectance was not sensitive to doping at λ = 1000 nm and a doping level of ~$2x10^{18}$ cm^{-3}.

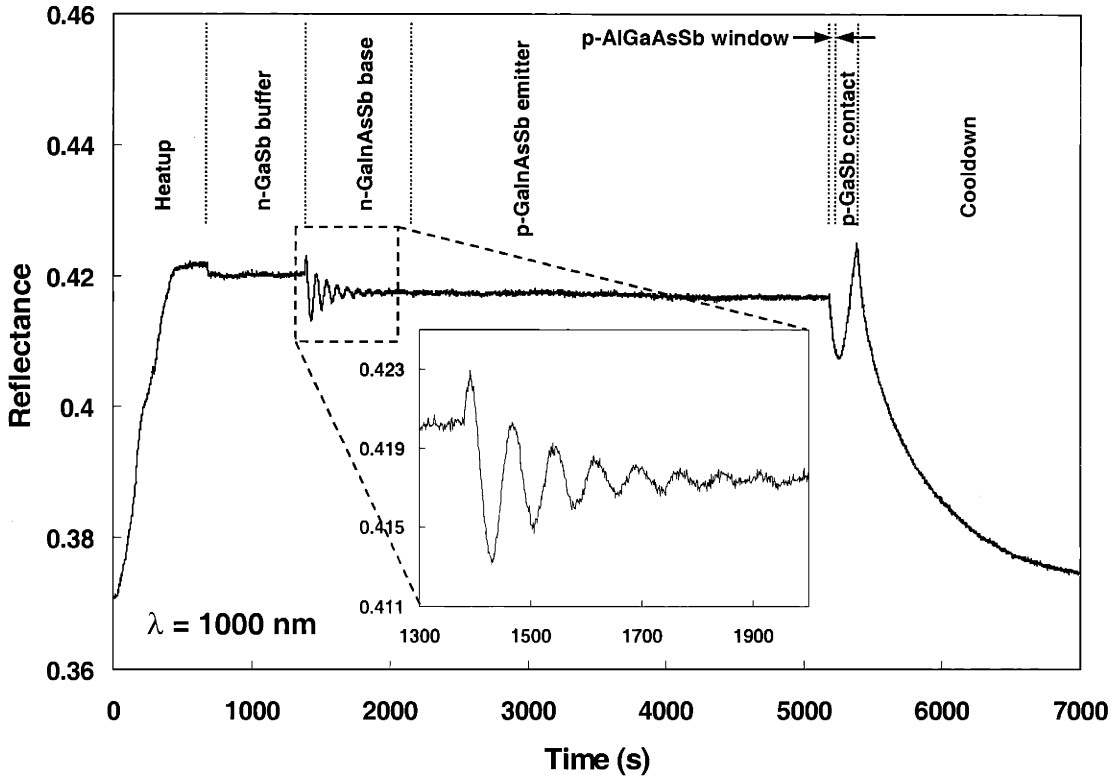

(a)

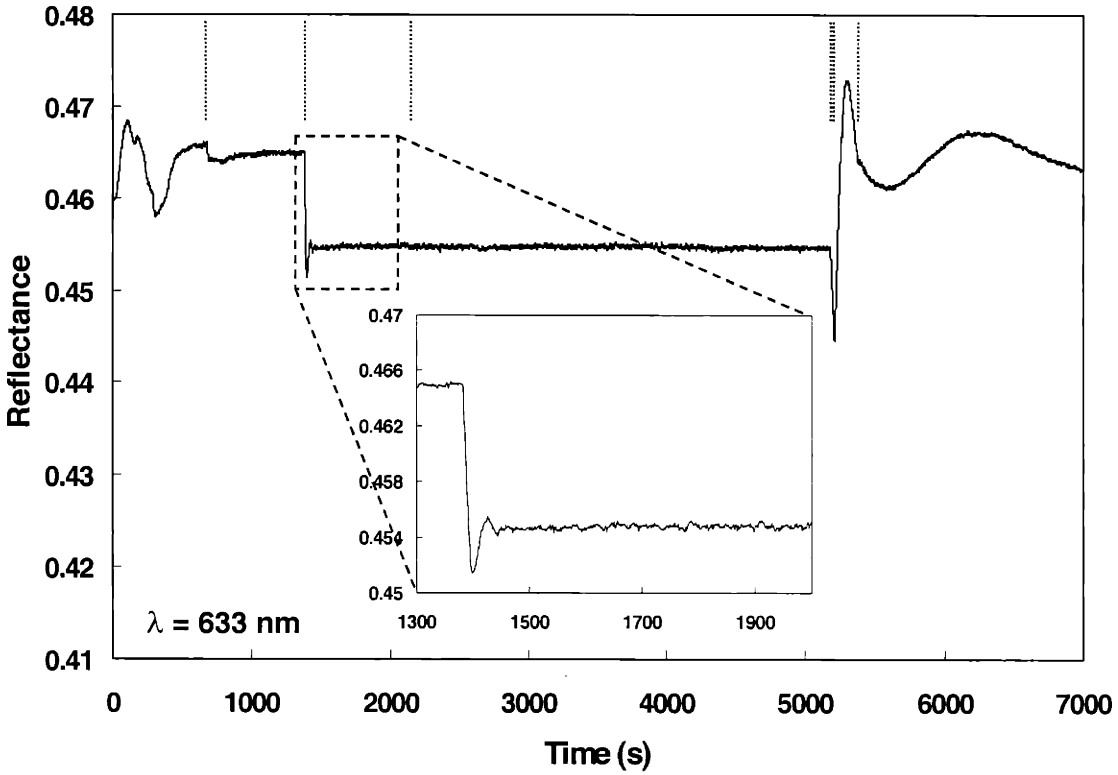

(b)

Fig. 8. *In situ* reflectance at (a) 1000 nm and (b) 633 nm obtained during a TPV growth run. Since there was not much refractive index contrast between the n-GaInAsSb base and n-GaSb buffer layers, the amplitude of the n-GaInAsSb-base reflectance oscillations was fairly small. In addition, the oscillations rapidly dampened at 633 nm due to high absorption.

Since the n-$Ga_{0.83}In_{0.17}As_{0.16}Sb_{0.84}$ layer was mostly GaSb, there was not much refractive index contrast between the n-GaInAsSb base layer and the n-GaSb buffer layer (Δn ~ 0.14). As a result, the amplitude of the reflectance oscillations was quite small, as seen in the inset in Fig. 8(a). This is especially evident in Fig. 7, where the amplitude of the oscillations of the AlGaAsSb layers was far larger, due to a large refractive index difference between $Al_{0.65}Ga_{0.35}As_{0.05}Sb_{0.95}$ and GaSb (Δn ~ 0.55). It was important to minimize noise in the reflectance signal because the signal level (oscillation amplitude)

was so low for GaInAsSb layers on GaSb. In this work it was found that the external trigger system mentioned above was an essential part of reducing noise.

Since absorption was high in GaInAsSb at 1000 nm at 550 °C ($k \sim 0.4$), the reflectance oscillations quickly dampened and died out. Only about 6-7 oscillations can be clearly seen in the inset. However, these oscillations were more than sufficient for accurate curve-fitting of n, k, and G. This was not the case for *in situ* reflectance obtained at 633 nm, shown in Fig. 8(b). This reflectance, taken during the same TPV run as the reflectance in Fig. 8(a), shows the very high absorption of GaInAsSb at 633 nm ($k > 1.5$). In this case, the inset shows that the reflectance oscillations dampened out before even one full oscillation was complete. Therefore, the curve-fitting routine was unable to converge and determine values of n, k, and G at 633 nm.

2.4.2.1 Semi-quantitative analysis: use of reflectance ratios to determine alloy composition

As discussed above, values of n and k at the growth temperature can be extracted for an epilayer from *in situ* reflectance oscillations. These values are usually not directly of interest because they are at elevated temperatures. They are only indirectly of interest in that they can be correlated with the alloy composition. However, for this purpose, it is actually much easier to use reflectance ratios, rather than curve-fits to reflectance oscillations. Specifically, the ratio of the *in situ* reflectance of GaInAsSb to that of GaSb can be correlated to the 300 K photoluminescence (PL) peak of the GaInAsSb epilayer within an accuracy of 1%. This is true over the entire range of growth temperatures (525-575 °C) and alloy compositions (GaInAsSb 300 K PL peaks from 1.9 to 2.5 μm) studied in this thesis. This is very useful since the use of a ratio eliminates the need for absolute

reflectance calibrations: any arbitrary units can be used for the reflectance, as long as these units scale linearly with the absolute reflectance. In addition, any wavelength of light can be used to obtain this ratio – even highly-absorbed wavelengths that do not yield growth oscillations. In fact, fewer oscillations are preferable because it is the ratio of the baseline reflectance toward which the oscillations are decaying that is required. Therefore, the quicker the oscillations dampen out, the quicker the baseline reflectance of the GaInAsSb epilayer can be measured. In practice, it is preferable to use the ratio at a wavelength of 700 nm. This wavelength is the most sensitive because it is near the E_1 peak of GaSb (see chapter 3) at 550 °C, and therefore has the largest reflectance difference between GaSb and GaInAsSb (in the wavelength range of the Si spectrometer). Finally, this technique is very accurate because it uses ratios, which inherently have higher precision than single measurements.

The results of this technique are demonstrated in Fig. 9(a). The value along the horizontal axis is the ratio of the baseline reflectance of a GaInAsSb epilayer to that of the GaSb buffer layer in the same run, taken at 700 nm. The baseline reflectance is the value for a bulk layer, which is the value toward which the reflectance oscillations dampen. For example, in Fig. 8(b) (which is at a wavelength of 633 nm), the baseline reflectance of the GaInAsSb epilayer is about 0.455, and that of the GaSb buffer layer is about 0.465. Therefore, the ratio would be 0.455/0.465 = 0.979. (Again, it is emphasized that this ratio does not require the use of absolute reflectance values – arbitrary units can be used.) The vertical axis is the 300 K PL peak wavelength in units of nm. Results for more than 20 samples have been plotted and are seen to fall along a straight line.

The equation for this line is:

$$300\text{ K PL peak wavelength (nm)} = -16649*m + 18285 \qquad (12a)$$

where m is the reflectance ratio at a wavelength of 700 nm. Note that this ratio is essentially independent of the growth temperature between 525 and 575 °C. It is seen from Fig. 9(a) that the 300 K PL peak wavelength can be determined within 1% accuracy across the entire range of alloy compositions of interest for TPV devices using the reflectance ratio of GaInAsSb to GaSb, and the equation above.

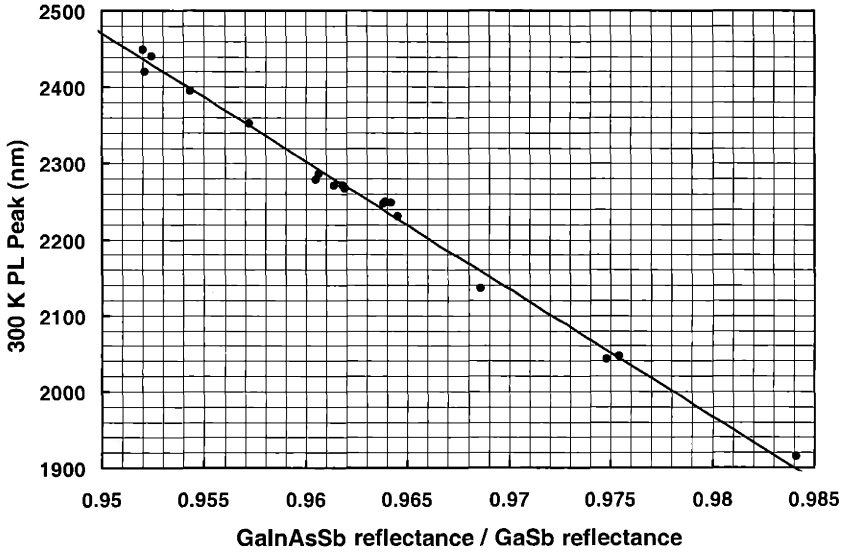

(a)

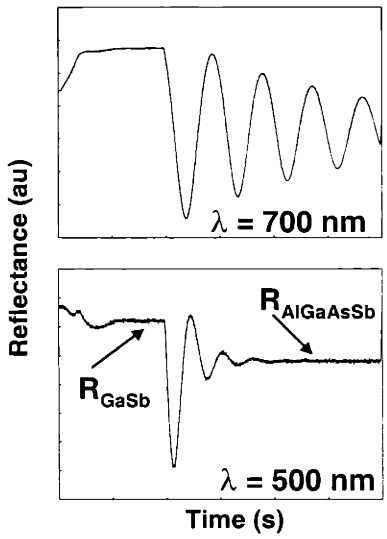

(b)

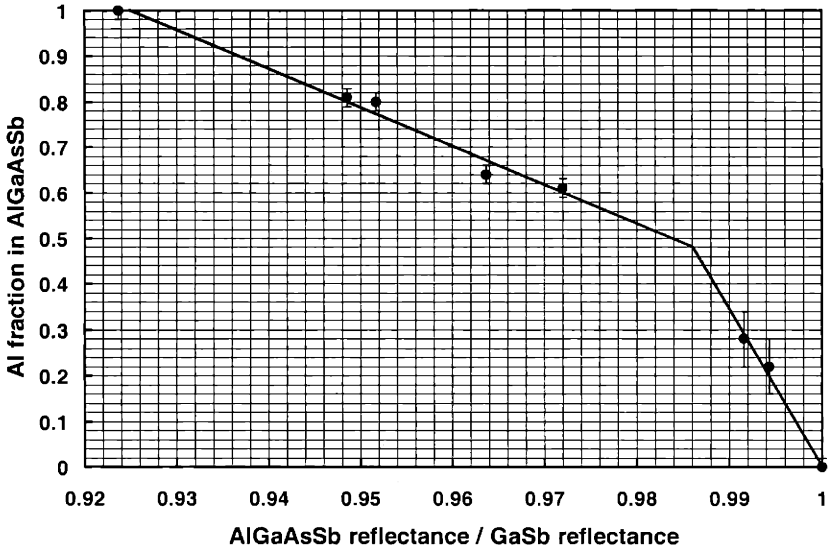

(c)

Fig. 9. Plots illustrating the use of *in situ* reflectance ratios to accurately determine alloy composition. In (a) the 300 K photoluminescence peak wavelength of GaInAsSb is plotted as a function of the *in situ* reflectance ratio between GaInAsSb and GaSb, while in (c) the Al fraction in AlGaAsSb (as determined by Rutherford backscattering) is similarly plotted as a function of the *in situ* reflectance ratio between AlGaAsSb and GaSb. (b) *In situ* reflectance of $Al_{0.81}Ga_{0.19}AsSb$ grown at 550 °C on GaSb illustrating the higher optical absorption at λ = 500 nm vs. λ = 700 nm. The baseline reflectance of AlGaAsSb is more easily obtained at λ = 500 nm for thin epilayers.

The room temperature PL peak wavelength of the GaInAsSb base and emitter layers is a very important parameter for TPV devices. Therefore, the ability of the *in situ* reflectance to determine this value accurately is a very useful feature. Feedback time from *in situ* reflectance data is obviously much faster than that from *ex situ* PL; therefore, using this feature saves time during composition calibrations.

A similar correlation between a reflectance ratio and the composition of AlGaAsSb epilayers was obtained. In this case, the reflectance ratio of AlGaAsSb to GaSb at a wavelength of 500 nm was used. This ratio is more sensitive at 700 nm as with GaInAsSb; however, the AlGaAsSb reflectance oscillations do not dampen out quickly at 700 nm (since the layer is less absorbing than GaInAsSb) and it is therefore difficult to determine the baseline reflectance of thin layers using 700 nm. The oscillations dampen much quicker at 500 nm; therefore, the baseline reflectance can be measured more quickly. This is shown in Fig. 9(b), which compares *in situ* reflectance at $\lambda = 700$ nm and $\lambda = 500$ nm for $Al_{0.81}Ga_{0.19}AsSb$ grown at 550 °C. Figure 9(c) plots the fraction "x" of Al in $Al_xGa_{1-x}As_ySb_{1-y}$ versus the baseline reflectance ratio of AlGaAsSb to the GaSb buffer layer at a wavelength of 500 nm. (The As/Sb fractions are fixed by lattice-matching conditions to the GaSb substrate.) The actual fraction of Al in the epilayer was determined using *ex situ* Rutherford backscattering (performed by Charles Evans & Associates). The equations are given by:

$$\text{Al fraction 'x'} = -8.428*m + 8.795 \qquad (m < 0.986) \qquad (12b)$$

$$\text{Al fraction 'x'} = -34.149*m + 34.155 \qquad (m > 0.986) \qquad (12c)$$

where m is again the *in situ* reflectance ratio. There is a kink in the data, and therefore two equations, because of the transition between a direct and indirect bandgap. At 25 °C, $Al_xGa_{1-x}As_ySb_{1-y}$ $(0 < x < 0.45)$ has a direct bandgap, while $Al_xGa_{1-x}As_ySb_{1-y}$

($0.45 < x < 1$) has an indirect bandgap[†] [52-54]. The *in situ* reflectance ratio data suggested a crossover from direct to indirect gap at a slightly higher Al fraction of $x = 0.48$, rather than $x = 0.45$, which may be related [53] to the higher temperature of this data (550 °C) compared to the reported data (25 °C). Because of this crossover, the data between $0 < x < 0.48$ has one slope, related to the slope of the direct bandgap E_Γ versus Al fraction, while the data between $0.48 < x < 1$ has another slope, related to the indirect bandgap E_X.

2.4.3 Use of *in situ* reflectance to monitor GaSb substrate oxide desorption

2.4.3.1 Introduction and background

High-quality epitaxial crystal growth requires a clean, oxide-free starting substrate surface. Oxide desorption is routinely monitored using reflection high-energy electron diffraction (RHEED) in molecular beam epitaxy. However, RHEED and other electron-based *in situ* probes require a high vacuum environment, and therefore cannot be utilized in atmospheric- or low-pressure epitaxial systems. Very few reports exist in the literature on the use of *in situ* optical probes to monitor substrate oxide desorption. Pidduck *et al.* [13, 55-59] and Lavoie *et al.* [14, 60, 61] have reported the use of *in situ* laser light scattering to monitor Si and GaAs oxide desorption in MBE, while more recently Allwood *et al.* [28, 62-65] have used p-polarized reflectance at Brewster's angle to monitor oxide desorption of GaAs, InSb, and GaSb substrates in atmospheric-pressure OMVPE. It is of particular interest to monitor oxide desorption from GaSb substrates

[†] For complete accuracy, $Al_xGa_{1-x}As_ySb_{1-y}$ has a direct transition to the Γ point for ($0<x<0.2$), an indirect transition to the L point for ($0.2<x<0.45$), and an indirect transition to the X point for ($0.45<x<1$).

because these substrates have been difficult to prepare for epitaxy. Various preparation recipes exist in the literature, and groups have had varied success growing on etched or epi-ready substrates.

Although there are no reported studies of monitoring substrate oxide desorption *in situ* using randomly-polarized reflectance, data obtained during this thesis work suggested that such *in situ* reflectance is sensitive to the oxide desorption process. In particular, three observations led to this conclusion. First, features observed in the *in situ* reflectance during substrate heat-up were not present during substrate cool-down, indicating that the substrate was not the same before and after heat-up. This is illustrated in Fig. 10(a), which shows *in situ* reflectance at 500 nm of an epi-ready substrate (loaded into the OMVPE reactor as-received, with no additional treatment) heated from 25 to 550 °C (heating started at 20 s), held at 550 °C, and then cooled back to 25 °C (cooling started at 1840 s). Note the different features seen during heat-up compared to cool-down. Second, the difference between heat-up and cool-down is less for etched substrates than for epi-ready substrates. This is seen in Fig. 10(b), which shows *in situ* reflectance at 500 nm of an etched GaSb substrate. Compared to Fig. 10(a), the heat-up and cool-down are more similar in Fig. 10(b). (The etch procedure for this substrate was an initial solvent rinse in hot trichloroethylene, acetone, and 2-propanol, followed by a 5 minute etch in HCl, followed by a final rinse in 2-propanol. More details on the etch procedure are discussed below.) Finally, the form or shape of the cool-down curve agrees well with theoretical calculations, whereas the heat-up curve differs from theoretical expectations. Figure 10(c) illustrates theoretical heat-up and cool-down

---

However, the Γ and L bands are nearly identical between $0<x<0.45$; therefore, the L band can be excluded from the above analysis for simplicity with very little loss in accuracy.

curves for GaSb at 500 nm that can be compared to Figs. 10(a) and (b). These theoretical curves were generated from an analytical model of the refractive index of GaSb as a function of temperature, which is discussed in detail in section 3.3.2.

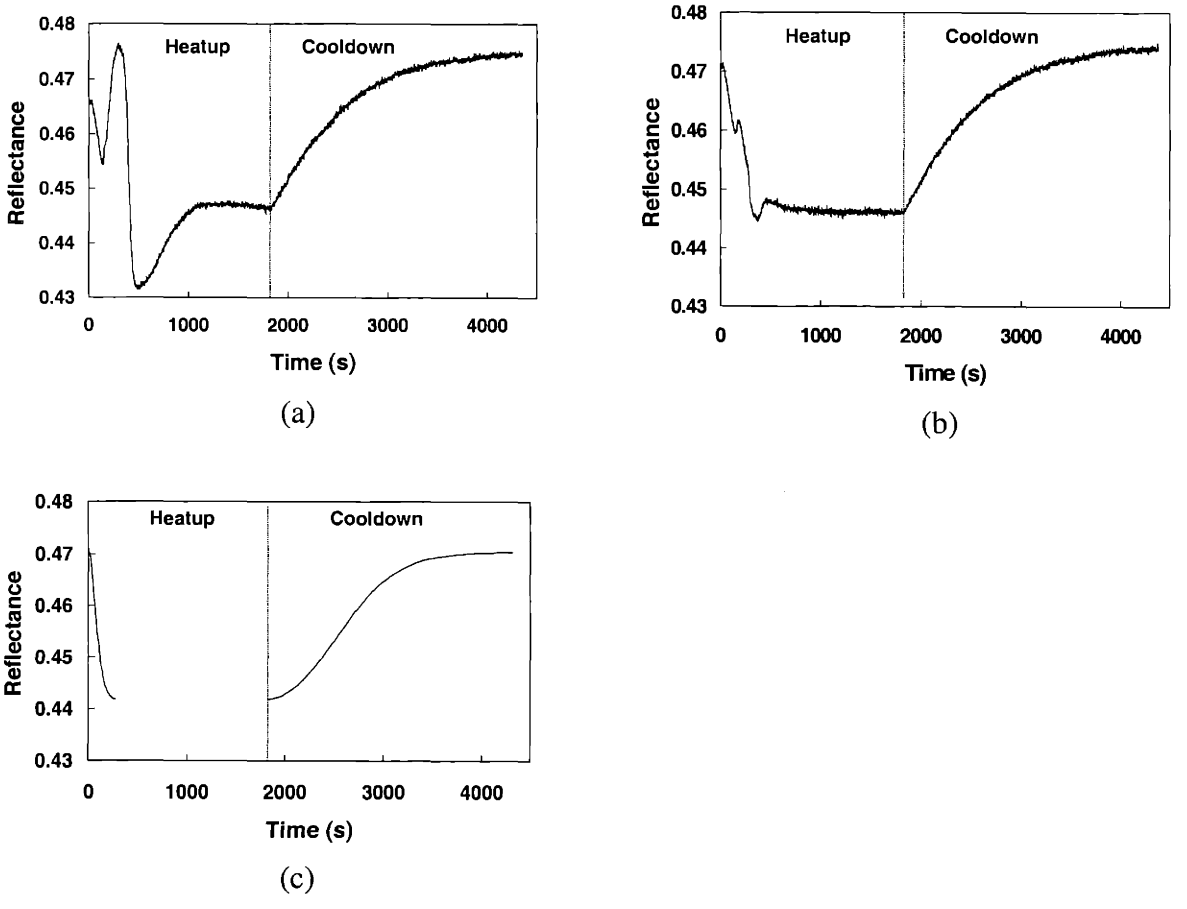

Fig. 10. *In situ* reflectance at 500 nm of the heatup and cooldown of (a) an epi-ready GaSb substrate and (b) an HCl-etched GaSb substrate. The curves in (c) are calculations based on the temperature-dependent refractive index model given in section 3.3.2.

These three observations taken together suggest that some film is present on the surface of the GaSb substrate when it is loaded into the OMVPE reactor, that this film desorbs during substrate heat-up, and is therefore not present in either the cool-down or

the theoretical heat-up/cool-down curves (which are for clean GaSb). This film is most likely the substrate oxide.

Based on these observations, a more detailed study of the substrate oxide desorption was undertaken. *In situ* reflectance and *ex situ* atomic force microscopy (AFM) were used to characterize GaSb substrates that received different preparation procedures, to determine which substrate preparation technique yielded the least amount of oxide and highest-quality surface most suitable for epitaxial growth.

2.4.3.2 Experimental conditions

The GaSb substrates used for this study were Te-doped n-type greater than $1x10^{17}$ cm^{-3}, and were (001) misoriented 2° toward (101). Substrates were used either as-received epi-ready, or were degreased in solvents, etched in acid and rinsed before loading into the reactor. All substrates not used epi-ready were degreased. The solvent degrease consisted of hot trichloroethylene, followed by acetone and then 2-propanol. The etch procedure was 5 min of agitation in HCl. This was followed by an additional 30 s etch in Br_2-HCl-HNO_3-CH_3COOH in certain cases for comparison [66]. Substrates were then rinsed ten times in one of three different solutions: 2-propanol, methanol, or deionized water (DI H_2O), and blown dry with N_2. After the substrates were loaded into the reactor, they were heated to 525, 550, or 575 °C in a H_2 carrier gas at a flow rate of 10 slpm at 150 Torr. The heating rate during the initial part of the heat-up was 1.8 °C/s. Total time for heat-up and anneal was varied between 600 s and 1800 s. In some experiments, GaSb was deposited after the anneal, using a triethylgallium (TEGa) flow rate of 1 sccm and trimethylantimony (TMSb) flow rate of 1.5 sccm.

In situ reflectance data was obtained using the redesigned setup, at an incidence angle of 55°. Substrates were rotated at 40 rpm, and a signal integration time of 1 second was used. The surface morphology of substrates was measured by *ex situ* AFM (Digital Instruments, Nanoscope IIIA) operated in tapping mode. Etched Si cantilevers with a nominal tip radius of 5 to 10 nm and a sidewall angle of 10° were used. Samples were typically scanned at 2 lines per second with 512 points per line.

2.4.3.3 Experimental results

In situ reflectance during heating of four different GaSb substrates is shown in Fig. 11. Figure 11(a) is the reflectance at a wavelength of 500 nm, (b) is at 633 nm, and (c) is at 1000 nm. The epi-ready substrate in Fig. 11 was loaded into the reactor and heated with no pre-growth surface treatment (i.e. as-received). The HCl-etched substrate was degreased in solvents, etched in HCl and rinsed in 2-propanol before loading into the reactor. The HCl/BrAc-etched substrate received a similar treatment, although it was etched for 30 s in Br_2-HCl-HNO_3-CH_3COOH to remove GaSb following the HCl etch. Heating began at 25 s, and the temperature was stable at 550 °C by 460 s. To obtain the oxide-free curve a substrate was heated to 550 °C, cooled to 30 °C, and re-heated to 550 °C. Since the substrate remained in the reactor in a H_2 ambient during cooling and subsequent re-heating, it is expected that the surface was oxide-free during re-heating.

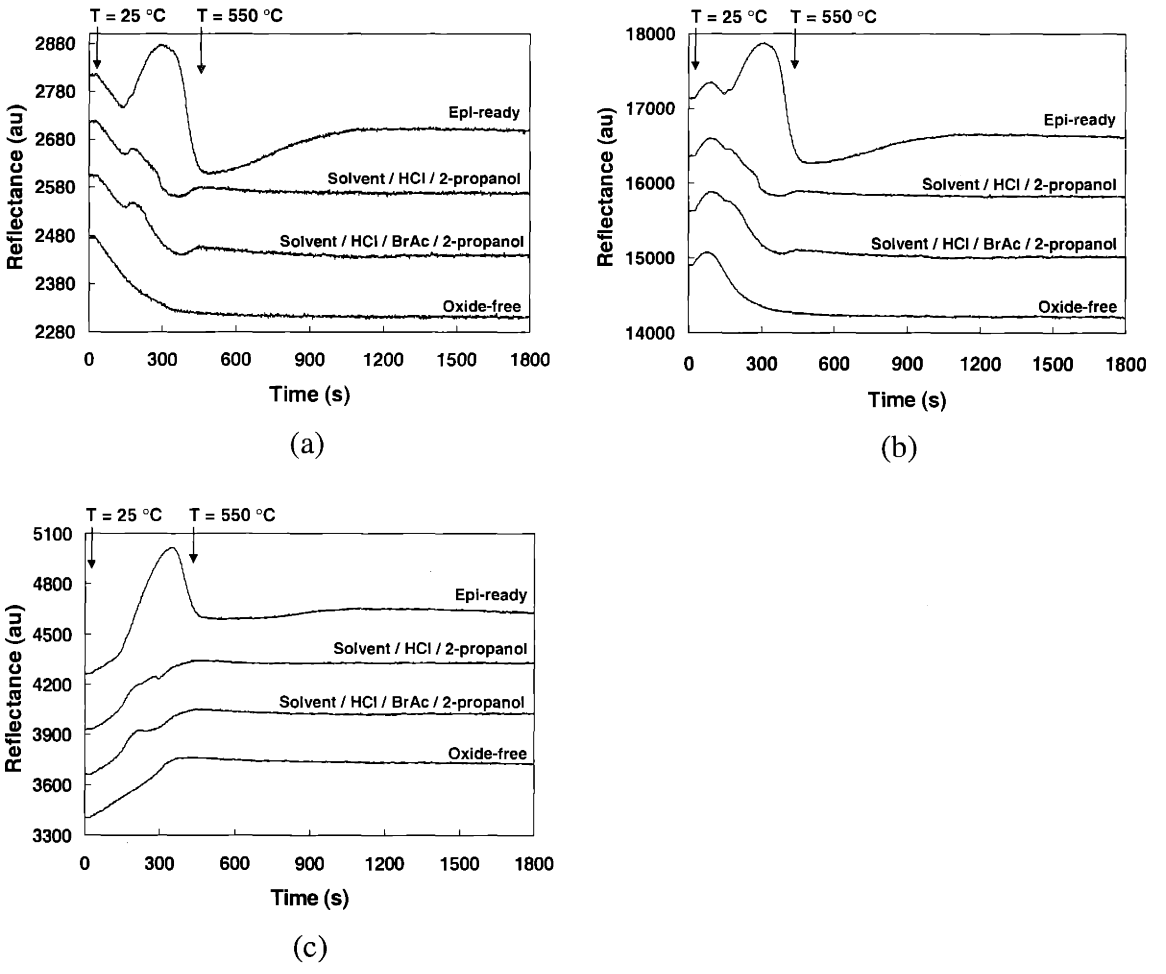

Fig. 11. *In situ* reflectance at: (a) 500 nm, (b) 633 nm, and (c) 1000 nm, during GaSb substrate heatup and oxide desorption comparing the effect of various etch procedures.

The reflectance of the epi-ready substrate displayed a much larger deviation from the oxide-free substrate during heating than did the etched substrates. In addition, the reflectance of the epi-ready substrate took a longer time (1200 s) to equilibrate than the etched substrates (600 s). These differences were due to different substrate oxide thicknesses. *Ex situ* ellipsometry indicated that the approximate oxide thickness on the epi-ready substrate was 5-6 nm, while it was 1-2 nm on the etched ones. Also note that the *in situ* reflectance was similar for the HCl-etched and the HCl/BrAc-etched

substrates. This suggests that the additional BrAc etch may be an unnecessary step. Eliminating the BrAc etch step is desirable for several reasons: it eliminates handling of bromine; it saves time in the etch procedure; and it eliminates a step that potentially roughens the GaSb surface. It is known that BrAc etches GaSb; however, this etch usually does not leave a planar surface, but rather can roughen the surface. This roughness is undesirable since it may promote phase separation (see section 4.4.3.2 for an example of how roughness/strain can promote phase separation), and degrade device performance through non-planar interfaces.

Figure 12 shows AFM images of two GaSb surfaces annealed at 550 °C. The substrate in Fig. 12(a) was loaded into the reactor and heated for 1200 s with no pre-growth surface treatment (i.e. epi-ready). The substrate in Fig. 12(b) was degreased in solvents, etched in HCl, rinsed in 2-propanol and also heated for 1200 s. A substrate which received an additional 30 s etch in BrAc following the HCl etch appeared the same as that in Fig. 12(b). The epi-ready surface exhibited a random texture (root-mean-square (RMS) roughness ~ 0.33 nm), while the etched substrates (RMS roughness ~ 0.20 nm) were mainly vicinal with mono- and bi-layer steps. Note that the surface morphology was similar for the substrates etched in HCl or HCl/BrAc. This result confirmed the *in situ* reflectance data that suggested that the additional etch in BrAc was an unnecessary step for oxide removal.

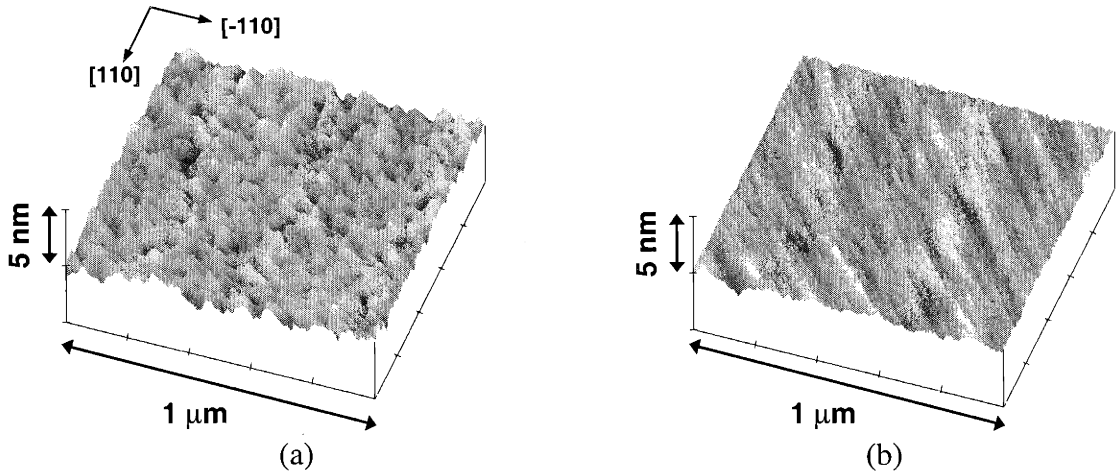

Fig. 12. AFM images of annealed (a) epi-ready and (b) HCl-etched substrates. A substrate which received an additional 30 s etch in BrAc following the HCl etch appeared the same as (b). The etched surfaces were suitable for step-flow growth, while the annealed epi-ready surface was rougher and did not indicate the step structure.

It is also apparent from Fig. 12 that the annealed etched surfaces were more suitable for step-flow growth than was the annealed epi-ready surface. To confirm this, GaSb epilayers were grown on epi-ready and etched substrates. The AFM image shown in Fig. 13(a) indicates that the 0.18 μm-thick epilayer grown on the epi-ready substrate was rougher (RMS roughness ~ 0.60 nm) than the underlying substrate itself. This suggests that growth on the epi-ready substrate occurred in an undesirable growth mode that caused continual surface roughening during deposition. However, epitaxial growth on the etched substrates (Figs. 13(b) and (c)) remained vicinal with the same RMS roughness as the underlying substrates, indicating that growth on these substrates occurred in the preferred step-flow mode.

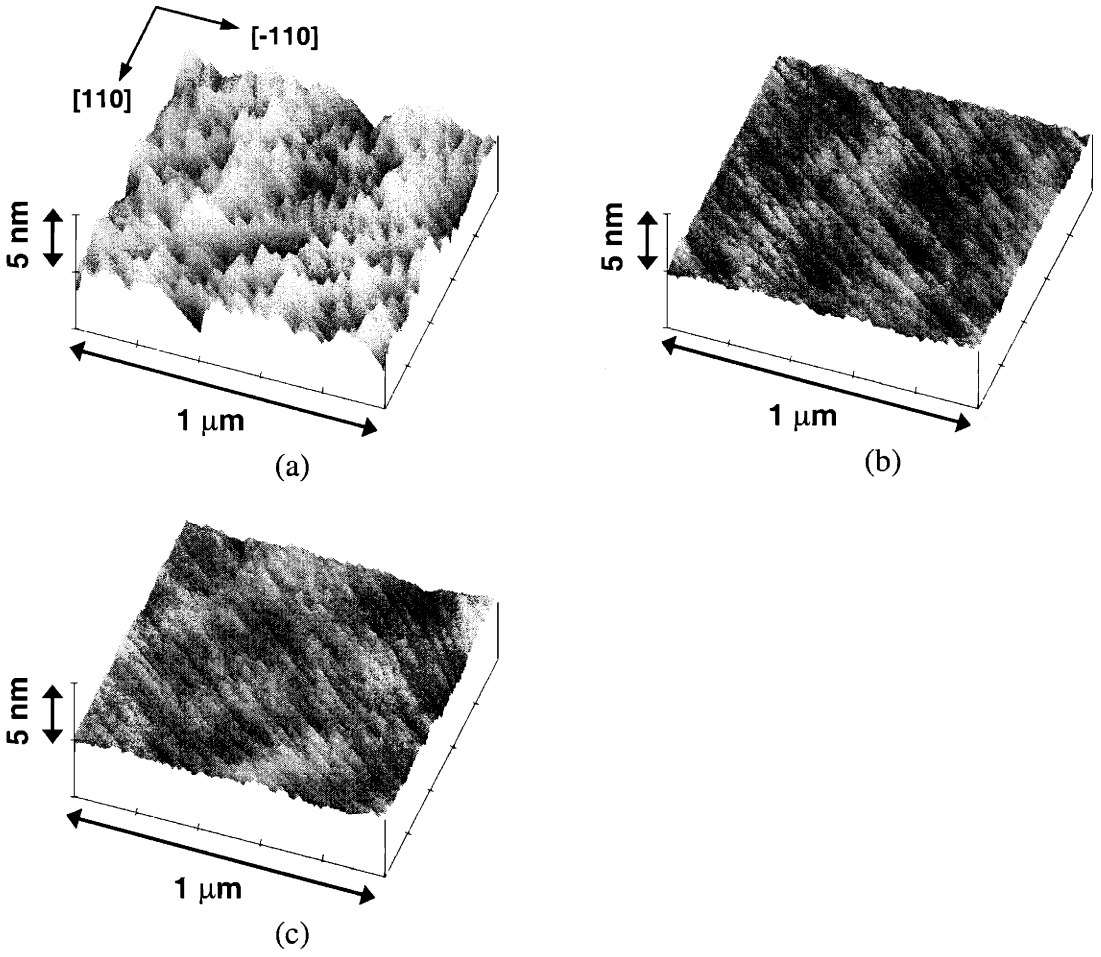

Fig. 13. AFM images of epitaxial GaSb grown on annealed (a) epi-ready, (b) HCl-etched, and (c) HCl-/BrAc-etched substrate surfaces. The epitaxial GaSb grown on the etched substrates had the same RMS roughness as the underlying substrates due to step-flow growth, while the epitaxial GaSb grown on the epi-ready substrate was rougher than the annealed substrate surface.

For substrates that were etched only in HCl, the effect of the post-etch rinse on oxide formation was also investigated. Figure 14 shows the *in situ* reflectance at 500 nm from substrates that were post-etch rinsed ten times in: (a) DI H_2O, (b) methanol, (c) 2-propanol followed by a 10 min exposure to atmosphere under a clean hood, or (d) 2-propanol. The substrates were typically in the rinse liquid for about 120 s, and were subsequently loaded into a N_2-purged glove box. Substrates were then transferred into

the reactor within 150 s (except for curve (c)). Since curve (d) exhibited the least deviation from the reflectance measured for an oxide-free substrate (see Fig. 11), these results suggest that a 2-propanol rinse and minimal exposure to air develops the least oxide formation.

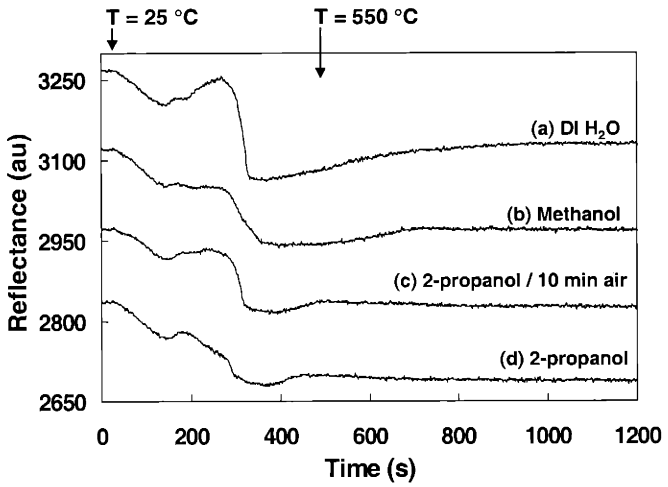

Fig. 14. *In situ* reflectance at 500 nm illustrating the effect of the post-etch rinse on the substrate oxide. The substrates were solvent-rinsed and HCl-etched before being rinsed in (a) deionized water, (b) methanol, (c) 2-propanol followed by a 10 min air exposure, or (d) 2-propanol.

Ex situ AFM images shown in Fig. 15 are in agreement with this conclusion. Figures 15 (a), (b), and (c) correspond to the substrates shown in Figs. 14 (a), (b), and (d). Note that while all three surfaces were essentially vicinal, those rinsed in DI H_2O or methanol exhibited slight pitting. In addition, the substrates rinsed in DI H_2O or methanol took longer to equilibrate than the one rinsed in 2-propanol. The surface rinsed in 2-propanol was equilibrated after a 600 s anneal, while those rinsed in DI H_2O or methanol require an 1800 s anneal to equilibrate. These results indicate that a post-etch

rinse in 2-propanol is the most suitable for high-quality epitaxial growth. It is known that water accelerates the formation of oxide on GaSb, and this is clearly seen in the *in situ* reflectance of Fig. 14. Therefore, exposure to water should be avoided during GaSb substrate preparation.

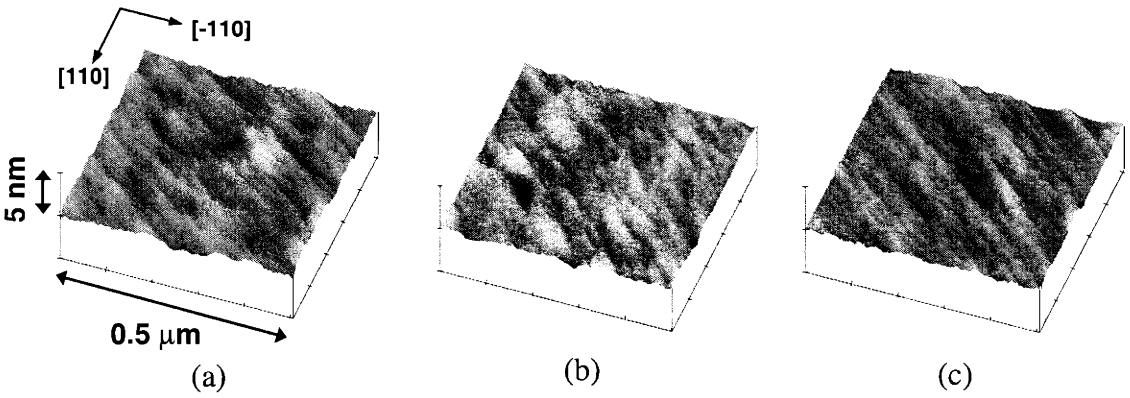

Fig. 15. AFM images illustrating the effect of the post-etch rinse on substrate surface morphology. The substrates were solvent-rinsed and HCl-etched before being rinsed in (a) deionized water, (b) methanol, or (c) 2-propanol.

The effect of anneal temperature on oxide desorption and surface morphology was also studied. HCl-etched substrates were rinsed in 2-propanol and then heated for 720 s to either 525 or 575 °C. As seen in Figs. 16(a) and (b), the surface morphology of these samples was similar to that of the sample heated to 550 °C (shown in Fig. 12(b)), indicating that under these preparation conditions the annealed substrate surface is relatively insensitive to anneal temperature.

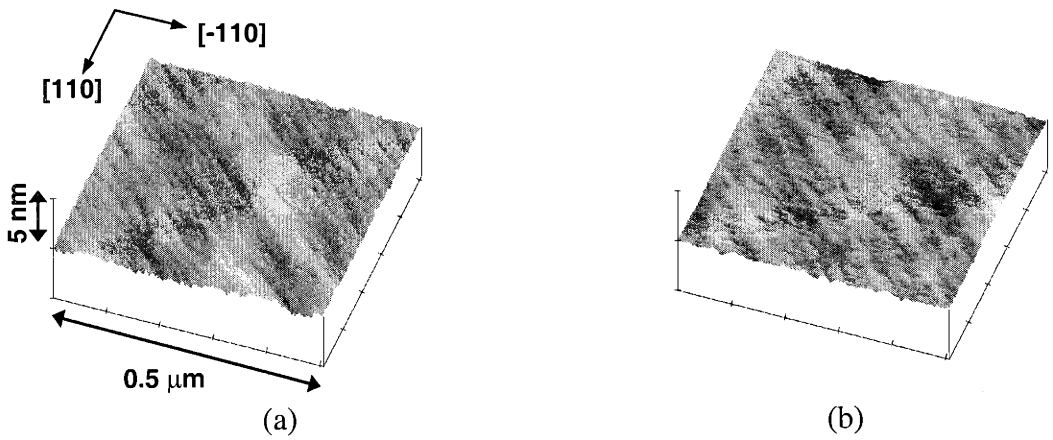

Fig. 16. AFM images of solvent-rinsed, HCl-etched, 2-propanol-rinsed substrates annealed at (a) 525 °C and (b) 575 °C. Both surfaces were vicinal and appeared similar.

It was also found that the anneal time, which ranged from 600-1800 s, had no significant effect on the reflectance and surface morphology of HCl-etched, 2-propanol-rinsed substrates. Epi-ready substrates, however, were more sensitive to anneal time. AFM images of 0.18 μm-thick epitaxial GaSb grown on epi-ready GaSb shown in Fig. 17 indicated that epi-ready surfaces heated for 1200 s (Fig. 17(b)) or longer were smoother than those annealed for only 900 s (Fig. 17(a)). This surface smoothing might explain the continually increasing reflectance from 900 to 1200 s shown in Fig. 11. However, it should be pointed out that even with total anneal times of 1800 s, the epi-ready surface never achieved the vicinal nature of annealed etched substrates.

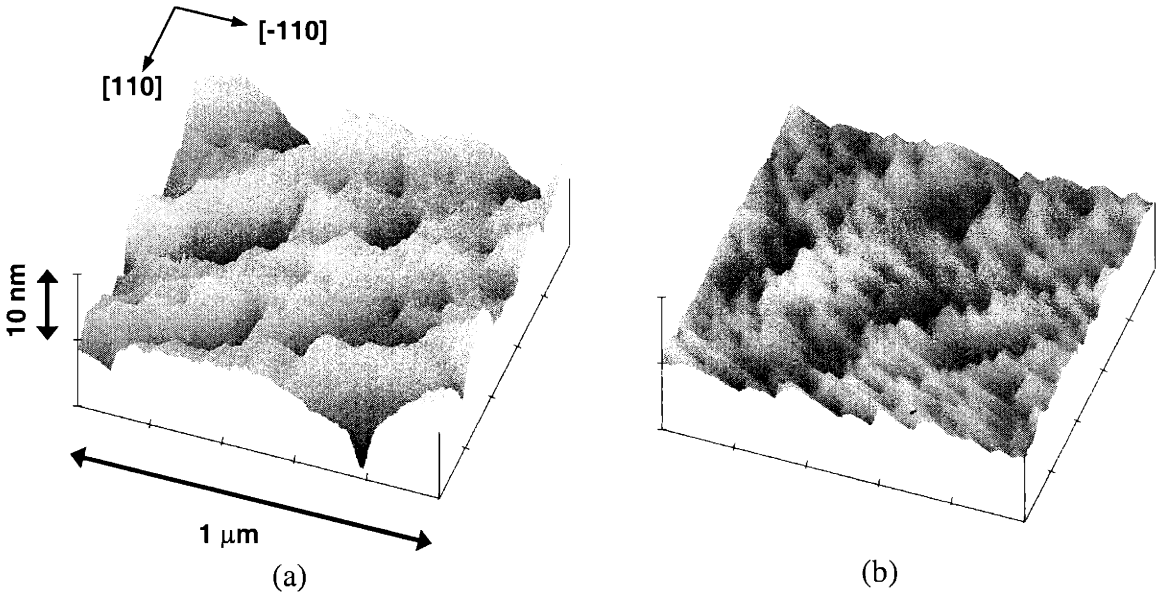

Fig. 17. AFM images of epitaxial GaSb grown on epi-ready substrates that had been annealed for (a) 900 s and (b) 1200 s. The surface was much smoother after the longer anneal time.

The effect of TMSb flow during substrate heating was investigated for HCl-etched (Fig. 18(a)) and epi-ready (Fig. 18(b)) substrates. TMSb at a flow rate of 1.5 sccm was introduced into the reactor when the substrate temperature reached 330 °C (200 s). Features related to the oxide desorption process seen in the *in situ* reflectance data occurred at lower temperatures with TMSb flow, suggesting that oxide desorption kinetics may have increased with TMSb flow. The effect was more noticeable for epi-ready substrates than for etched substrates. However, for both substrates, AFM images were similar for substrates annealed with and without TMSb flow, with substrates annealed under TMSb flow having a tendency to be slightly rougher than those annealed without TMSb flow. This roughness might be associated with excess antimony on the surface, and it is possible that under different TMSb flow rates results could differ.

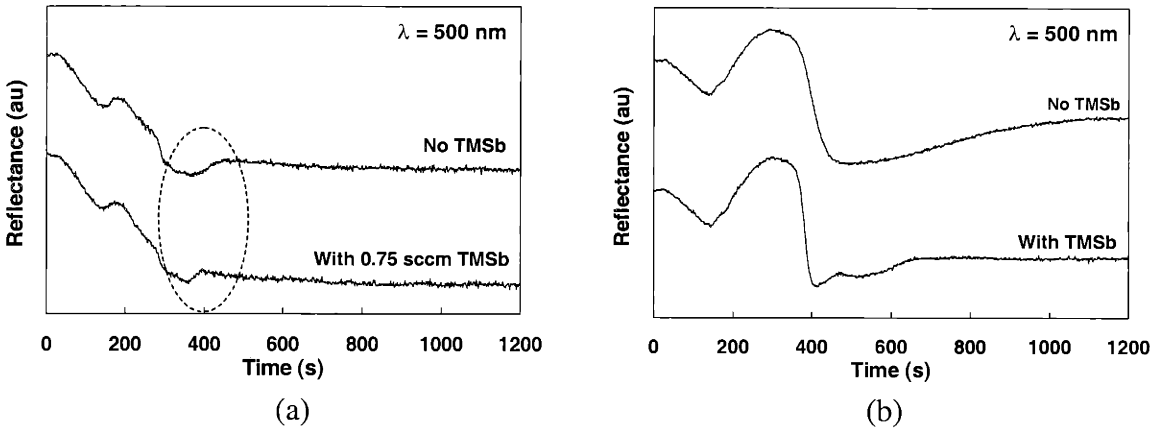

Fig. 18. *In situ* reflectance at 500 nm illustrating the effect of trimethylantimony (TMSb) flow on oxide desorption during substrate heatup for (a) HCl-etched and (b) epi-ready substrates.

2.4.3.4 Discussion of oxide desorption features seen in *in situ* reflectance

The differences observed in the reflectance spectra from the various GaSb substrate preparation methods can be explained by considering previously reported studies [67-71] on the native oxide of GaSb. The oxide is primarily composed of Sb_2O_3 and Ga_2O_3, with respective free energies of formation at 25 °C of -150 and -239 kcal/mol [68]. Since Sb_2O_3 is metastable in contact with GaSb, the following reaction takes place:

$$Sb_2O_3 + 2GaSb \rightarrow Ga_2O_3 + 4Sb \qquad (13)$$

with a free energy change of –68.5 kcal/mol [69, 71]. It has been reported that this reaction takes place significantly at temperatures above 200 °C [72]. It has also been reported that Sb_2O_3 and Ga_2O_3 begin to desorb at approximately 340 °C and 500 °C, respectively [72-74]. Therefore, the following reactions are likely to occur during heating of a GaSb substrate with a native oxide: reaction of Sb_2O_3 and GaSb to form Ga_2O_3 and elemental Sb; desorption of Sb_2O_3; and desorption of Ga_2O_3.

These previously reported temperatures correlate well with features observed in the *in situ* reflectance, as shown in Fig. 19. In this figure, the reflectance of the sample from Fig. 14(c) is shown at 633 nm along with the reflectance of an oxide-free substrate. (This wavelength was chosen because it most clearly displays the onset of various features in the oxide desorption process.) Note that the two reflectance curves have not been offset; therefore, their relative reflectance contains valuable information. In particular, the starting reflectances indicate that the presence of an oxide reduces the reflectance of a GaSb substrate, in agreement with theoretical calculations using randomly-polarized light at a 55° incidence angle. Therefore, if the oxide simply desorbed during substrate heating with no other reactions taking place, then the reflectance of the surface with the oxide could never be higher than that without the oxide. However, at 220 °C the reflectance of the substrate with the oxide increases above that of the oxide-free surface, which implies that a third phase must be present on the surface, in addition to the GaSb and oxides. This third phase might be the elemental Sb produced by reaction (13) above.

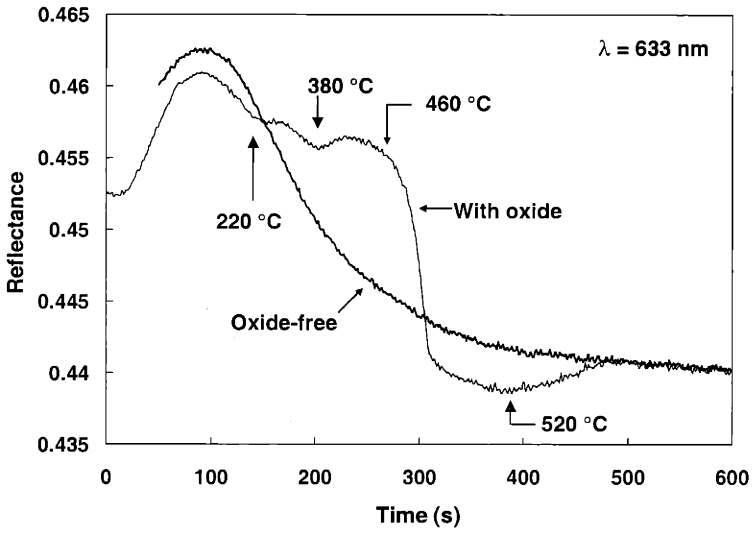

Fig. 19. Features seen in the *in situ* reflectance at 633 nm during substrate oxide desorption. An oxide-free-substrate heatup is also plotted for comparison.

At 380 °C, the reflectance of the surface with the oxide increases again, which is probably due to desorption of Sb_2O_3. This increase is more prominent than the increase shown for the HCl-etched substrate in Fig. 11(b). This difference can be explained by the relative amount of Sb_2O_3 present on these two substrates. Since HCl etches Sb_2O_3 [75], it is expected that an etched GaSb substrate loaded directly into the reactor will contain less Sb_2O_3 than one that has been etched and intentionally exposed to air. For substrates that are etched and loaded directly into the reactor, all of the Sb_2O_3 probably reacts with the GaSb before the sample reaches 380 °C. Therefore, no Sb_2O_3 is left on these surfaces to desorb at 380 °C, and no peak is seen at 380 °C in the reflectance of such a substrate. However, the substrate associated with the reflectance in Fig. 19 was exposed to atmosphere for 10 min before loading into the reactor, and therefore would have more Sb_2O_3 present on the surface.

The next feature seen in the reflectance in Fig. 19 is a sudden drop at 460 °C (280 s). The magnitude of the reflectance drop was observed from different runs to be proportional to the expected amount of elemental Sb produced by reaction (13). Therefore, this drop is possibly due to desorption of the elemental Sb. This sharp drop continues until about 315 s, at which point the reflectance is below that of the oxide-free surface. The lower reflectance is due to the remaining Ga_2O_3. At 520 °C (380 s), the reflectance increases again, which is probably due to desorption of Ga_2O_3. Once the oxide is completely removed (485 s), the reflectance matches that of the oxide-free surface.

Based on the above interpretation, a proposed explanation for the rougher surface of the annealed epi-ready substrate compared to the etched substrate is that the epi-ready substrate is roughened by consumption of GaSb from reaction (13). Since an epi-ready substrate contains approximately five times more Sb_2O_3 than an HCl-etched substrate, reaction (13) suggests that more GaSb is consumed during the heating of an epi-ready substrate than an etched substrate. The roughness of the epi-ready substrate is not due to incomplete oxide desorption, since the substrate reheat (not shown) indicated a clean, oxide-free surface.

2.4.3.5 Summary of *in situ* reflectance monitoring of substrate oxide desorption

In situ reflectance has been used as a valuable tool for observing oxide desorption from GaSb substrates. Information in the literature about the native oxide on GaSb was used to interpret features seen in the reflectance during substrate heating. Based on *in situ* reflectance and *ex situ* AFM of annealed surfaces and subsequent epitaxial growth,

the following substrate preparation procedure is recommended for reproducible, high quality epitaxial growth on GaSb:

1. Solvent rinse (hot trichloroethylene, acetone, 2-propanol)
2. Etch/agitate for 5 min in concentrated HCl
3. Rinse ten times in 2-propanol; blow dry with N_2
4. Heat to any temperature from 525-575 °C in a H_2 ambient for at least 600 s

2.4.4 Detecting a loss of source material

It is often difficult to determine when an organometallic bubbler will run out of source material. Although deposition software typically tracks grams of usage, this calculation is not highly reliable—bubblers often have shorter or longer lifetimes than expected based on calculated usage. During a growth run it is useful to know if source material runs out, so that the run can be stopped. This minimizes wasted time and other source materials. *In situ* reflectance is capable of detecting a loss of source material, as seen in Fig. 20. In this figure, an etched GaSb substrate was heated from 25 °C to 550 °C (t = 23-623 s) and GaInAsSb was deposited (t = 623-2133 s). Cooldown began at t = 2133 s. The reflectance is shown at 500 and 1000 nm. Notice that the reflectance signal dropped significantly for both wavelengths during growth of the GaInAsSb layer. During growth of a normal GaInAsSb layer, the reflectance should remain level as seen in Fig. 8. However, in the run shown in Fig. 20, the surface rapidly developed facets due to a loss of triethylgallium. These facets greatly increased diffuse (scattered) reflectance, causing the specular reflectance to decrease rapidly. Shorter wavelengths were more sensitive to these facets; therefore, the reflectance dropped earlier for 500 nm than for 1000 nm.

Although these facets are easily observed by eye or Nomarski microscopy once the wafer is removed from the reactor, it is useful to detect them *in situ* because of the time and economic savings gained from terminating an unsuccessful run.

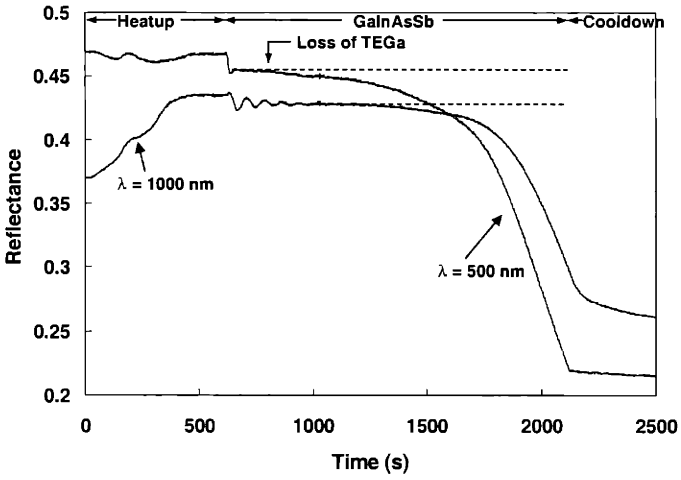

Fig. 20. *In situ* reflectance at 500 and 1000 nm demonstrating the sensitivity of the reflectance to a loss of organometallic source material during a run.

2.4.5 Determining the minimum V/III ratio by *in situ* reflectance

The sensitivity of *in situ* reflectance to surface facets and other defects is also useful to determine the minimum V/III ratio for high-quality surface morphology. The V/III ratio is the partial pressure ratio of group V sources to group III sources in the gas phase. Unlike arsenides and phosphides, which are typically grown at high V/III ratios, antimonides must be grown in a restricted range of low V/III ratios due to the low vapor pressure of antimony. Typical V/III ratios for antimonide-based materials are between 1 and 2 [76-78]. If the V/III ratio is too high, surface facets develop. If it is too low, then metal droplets form as the surface becomes metal rich. Changes in the V/III ratio as

slight as 10% (e.g. from 1.2 to 1.3), can make the difference between a high-quality surface morphology and one degraded by facets or metal droplets. Whenever source materials are replaced, calibration runs are required to determine the new minimum V/III ratio. This calibration process can be simplified using *in situ* reflectance monitoring. Instead of conducting multiple runs, each at slightly different V/III ratios, and examining the surface morphology of each wafer *ex situ*, all V/III ratios can be examined *in situ* in one run using reflectance.

Figure 21 shows an example of how this can be accomplished. Starting at a V/III ratio slightly less than 2, a series of layers can be grown at successively decreased V/III ratios until the surface becomes metal rich, causing the reflectance to drop significantly. In Fig. 21, the initial GaSb epilayer was grown at a V/III ratio of 1.9, from t = 680-860 s. Then, epilayers were grown at V/III ratios of 1.8 (t = 920-1100 s), 1.7 (t = 1160-1340 s), 1.6 (t = 1400-1580 s), and 1.5 (t = 1640-1830 s). The reflectance clearly dropped significantly at t = 1670 s, suggesting that at a V/III ratio of 1.5 the surface had become metal rich. The minimum V/III ratio for those particular sources, therefore, was 1.6. The use of *in situ* reflectance monitoring greatly simplifies this calibration procedure.

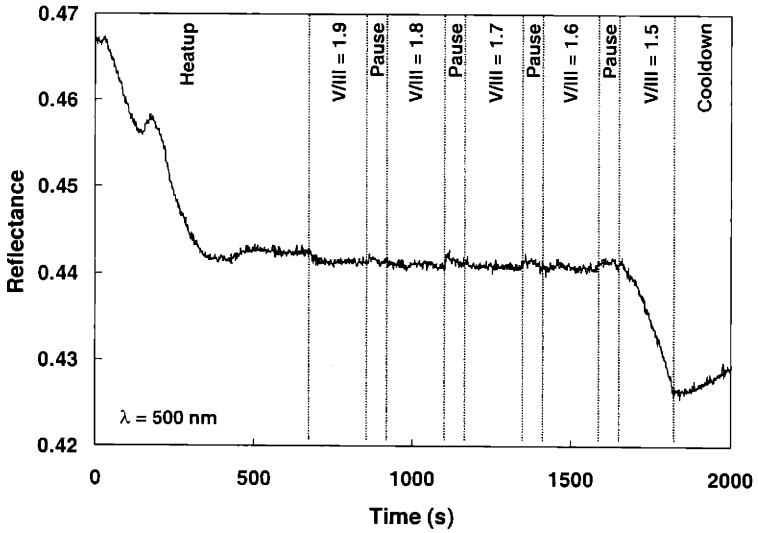

Fig. 21. Use of *in situ* reflectance at 500 nm for easy calibration of minimum V/III ratio.

2.4.6 Determining minimum source pre-flow time for equilibration

In situ monitoring is a powerful diagnostic tool that can detect if something went wrong during a growth run and exactly when the error occurred. It is also usually helpful in determining what caused the problem. An example of this is shown in Fig. 22(a). This *in situ* reflectance at 633 nm was taken during the growth of a distributed Bragg reflector (DBR) stack, consisting of alternating layers of AlGaAsSb and GaSb. The first 3 periods are shown in Fig. 22(a). Notice that the two minima in the reflectance of the first quarter-wave AlGaAsSb epilayer occurred at lower reflectances than those of the two subsequent quarter-wave AlGaAsSb layers. This suggests that the composition of the first quarter-wave AlGaAsSb layer was different than the composition of the subsequent AlGaAsSb layers. Since the reflectance dipped lowest for the first layer, the first AlGaAsSb layer must have had a lower refractive index (n) than the other layers. A quick, qualitative

assessment of the composition suggests that this first layer must have incorporated more Al than the other layers, since AlSb has a lower refractive index than GaSb at 633 nm at 550 °C. (Quantitative analysis of this *in situ* reflectance corroborates that the first AlGaAsSb layer had more Al than the other layers, since it had a lower n and lower k.) The reason for the increased Al incorporation was that insufficient pre-flow time was given for the TEGa source to equilibrate by deposition of the first AlGaAsSb layer. Since TEGa flowed continually during growth of the DBR, it equilibrated in time for the remaining AlGaAsSb layers, yielding the appropriate composition. In a subsequent run, shown in Fig. 22(b), this problem was fixed by increasing the TEGa preflow time and rate. In this figure, it is seen that the AlGaAsSb minima occurred at similar reflectances for all 3 quarter-wave layers, indicating similar compositions for all 3 epilayers. (Note that the targeted quarter-wave thicknesses and compositions were different for the DBRs in Figs. 22(a) and (b); therefore, the *in situ* reflectance curves are not exactly the same.)

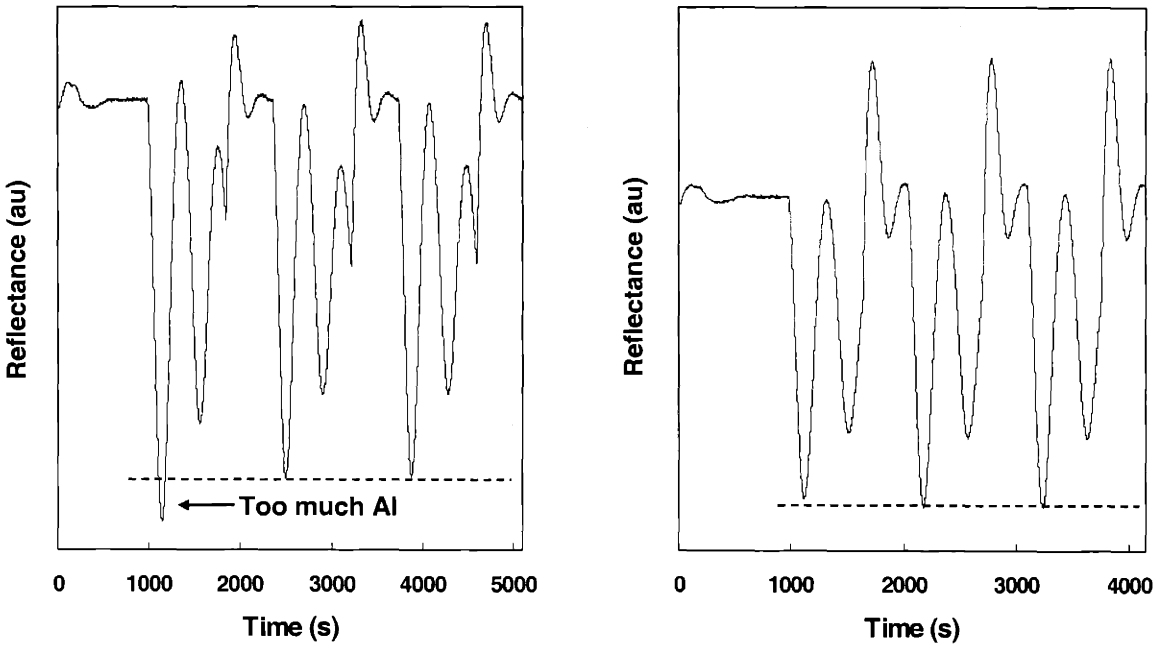

Fig. 22. *In situ* reflectance at 633 nm used to determine the minimum source preflow time required for equilibration. The triethylgallium (TEGa) source had not equilibrated in time for growth of the first quarter-wave AlGaAsSb layer in (a), while increased preflow time solved the problem as shown in (b).

The usefulness of *in situ* reflectance monitoring is highlighted by this example. It is unlikely that any *ex situ* diagnostics would have determined that something was wrong with the DBR stack. Even if a problem were detected, it would be extremely difficult using *ex situ* diagnostics to determine in which epilayer the problem had occurred, and more specifically what had gone wrong. All of these issues were easily detected, interpreted, and corrected using *in situ* reflectance monitoring.

2.5 Summary of *in situ* reflectance monitoring

Results from this thesis have shown that *in situ* spectral reflectance is very useful for monitoring GaSb-based III-Vs grown by organometallic vapor phase epitaxy. In particular, quantitative analysis of *in situ* reflectance was used to extract the refractive index (n and k) and growth rate of various epilayers. The growth rate determined *in situ* using $\lambda = 1000$ nm compared very favorably to that determined using standard *ex situ* high-resolution x-ray diffraction techniques, once the absolute reflectance was properly calibrated. Semi-quantitative analysis was used to correlate *in situ* reflectance ratios to the 300 K photoluminescence peak of GaInAsSb (using $\lambda = 700$ nm) and alloy composition of AlGaAsSb (using $\lambda = 500$ nm). Qualitative analysis of the *in situ* reflectance data also provided insight into various growth processes. For the first time, randomly-polarized *in situ* reflectance was used to study substrate oxide desorption. It was demonstrated that the reflectance (particularly at $\lambda = 500$ and $\lambda = 633$ nm) is very sensitive to the GaSb oxide desorption process, and can detect the effect of various etch and post-etch treatments. A substrate preparation procedure for high-quality epitaxial growth was recommended based on results from the *in situ* reflectance and *ex situ* atomic force microscopy. In addition, the reflectance was also used to detect a loss of source material during a growth run; the minimum V/III ratio for good surface morphology; and incorrect epilayer composition due to insufficient pre-flow time for one source material.

These examples taken together demonstrate the power of—and variety of uses for—*in situ* reflectance monitoring, as a characterization tool of GaSb-based materials.

3. Modeling Optical Constants of Antimonide-Based Materials

3.1 Introduction

The basic optical properties of a material are governed by its complex refractive index, given as [9, 45, 46]:

$$N = n\text{-i}*k \tag{14}$$

where n is the real part and k is the imaginary part of the refractive index. The real part, n, is the ratio of the speed of light in vacuum to the speed of light in the medium:

$$n = c_0/c \tag{15}$$

where c_0 is the speed of light in vacuum. The imaginary part, k, is also known as the extinction coefficient and describes optical absorption in the medium, since the absorption coefficient is $\alpha = 4\pi k/\lambda$.

The refractive index is related to the dielectric constant, ε, given by:

$$\varepsilon = \varepsilon_1\text{-i}*\varepsilon_2 \tag{16}$$

where ε_1 is the real part and ε_2 is the imaginary part. The relationship between the refractive index and dielectric constant is given by:

$$\varepsilon = N^2 \tag{17}$$

The individual real and imaginary components are given by:

$$\varepsilon_1 = n^2 - k^2 \tag{18a}$$

$$\varepsilon_2 = 2nk \tag{18b}$$

$$n = \frac{\sqrt{\varepsilon_1^2 + \varepsilon_2^2} + \varepsilon_1}{2} \tag{19a}$$

$$k = \frac{\sqrt{\varepsilon_1^2 + \varepsilon_2^2} - \varepsilon_1}{2} \tag{19b}$$

These components (n, k, ε_1, and ε_2) are all real, positive numbers.

Knowledge of these optical constants is necessary to design optoelectronic devices, since these parameters determine how light propagates through a device. Simulation of *in situ* reflectance also requires these parameters, and this knowledge can help interpretation of features seen in the *in situ* reflectance signal. It is therefore of interest to determine the refractive index values.

3.2 Analytic models of optical constants

3.2.1 Introduction

The term "constant" in optical constant or dielectric constant is actually a misnomer, since both n and k are strong functions of wavelength in certain regions of the electromagnetic spectrum. This phenomenon is referred to as dispersion. The refractive index is also a function of temperature, pressure, and other variables. In many simple

calculations, a look-up table containing tabulated values of refractive index vs. wavelength is all that is required. However, an analytic function of the refractive index is often desirable because it enables more complex models of optical properties, and provides better interpolation of parameters in regions where no data exist. Various such analytic functions exist, and are described in the following two sections. Section 3.2.2 provides functional representations of the refractive index at energies below the fundamental bandgap, while section 3.2.3 discusses a highly accurate model for the refractive index at energies above the bandgap. In both sections, these models are applied to the binaries and quaternaries studied in this thesis.

3.2.2 Analytic functions at energies below the fundamental bandgap

At energies below the fundamental bandgap of a material, the refractive index is not a strong function of wavelength and therefore can be modeled quite accurately using fairly simple models. Two well-known models are the Herzberger and Sellmeier dispersion formulas [6]. The Herzberger formula models the refractive index as:

$$n = A + \frac{B}{\lambda^2 - 0.028} + \frac{C}{\left(\lambda^2 - 0.028\right)^2} + D\lambda^2 + E\lambda^4 \tag{20}$$

where λ is the wavelength in microns. The coefficients A, B, C, D, and E are constants to be determined by regressively curve-fitting the equation to data. The Sellmeier equation is:

$$n^2 = \varepsilon + \frac{A}{\lambda^2} + \frac{B\lambda_1^2}{\lambda^2 - \lambda_1^2} \tag{21}$$

where A and B are constants to be determined, ε is the static dielectric constant, and λ_1 is the wavelength of the fundamental bandgap in microns.

In many cases, the dispersion can also be modeled using a simple polynomial equation. A second-order function typically gives good qualitative agreement with the data, while a third- or fourth-order function can be used to achieve higher accuracy. Due to their simplicity and high accuracy, polynomial equations were used in this thesis to provide analytic models of the refractive index at energies below the bandgap.

For thermophotovoltaic devices that have a cutoff wavelength of 2.3 μm, it is of interest to know the optical properties in the wavelength range of 1-3 μm. However, at room temperature, the fundamental bandgap of most of the materials characterized in this thesis is in this energy range. Therefore, in order to still have simple polynomial analytic models for the refractive index in this energy range, the model must be broken into two equations: one curve for data between the bandgap and 3 μm, and another curve for data between 1 μm and the bandgap. Although the data between 1 μm and the bandgap represents refractive index values at energies above the bandgap, the polynomial equations can still be used to successfully model the data. This is because the refractive index lineshape remains simple enough to use polynomial models until energies above the E_1 critical point. At higher energies, the lineshapes become too complicated to model using simple polynomial equations, and the model presented in section 3.2.3 must be used. The E_1 energy gap occurs at wavelengths shorter than 1 μm for all the materials examined in this thesis; therefore, the data between 1 μm and the fundamental bandgap can be modeled with polynomials. In addition, the imaginary part of the refractive index, k, can be modeled effectively between 1 μm and the fundamental bandgap using a cubic equation for the materials in this thesis. Wavelengths shorter than 1 μm require using the model presented in section 3.2.3.

For GaSb, which has a room temperature fundamental bandgap of 0.72 eV (1.72 μm) [79], the following equations were used:

$$n_{GaSb}(\lambda) = A \cdot \lambda^3 + B \cdot \lambda^2 + C \cdot \lambda + D \qquad (1000 < \lambda < 1720 \text{ nm}) \qquad (22a)$$

$$A = -0.38002 \cdot 10^{-9}$$
$$B = 0.20920 \cdot 10^{-5}$$
$$C = -0.0037272$$
$$D = 6.1686$$

$$n_{GaSb}(\lambda) = E \cdot \lambda^4 + F \cdot \lambda^3 + G \cdot \lambda^2 + H \cdot \lambda + I \qquad (1720 \text{ nm} < \lambda < 3000 \text{ nm}) \qquad (22b)$$

$$E = 0.21450 \cdot 10^{-12}$$
$$F = -0.21361 \cdot 10^{-8}$$
$$G = 0.79745 \cdot 10^{-5}$$
$$H = -0.013310$$
$$I = 12.308$$

$$k_{GaSb}(\lambda) = J \cdot \lambda^3 + K \cdot \lambda^2 + L \cdot \lambda + M \qquad (1000 < \lambda < 1819 \text{ nm}) \qquad (22c)$$

$$J = -0.55542 \cdot 10^{-9}$$
$$K = 0.21181 \cdot 10^{-5}$$
$$L = -0.0028524$$
$$M = 1.5234$$

$$k_{GaSb}(\lambda) = 0 \qquad (\lambda > 1819 \text{ nm}) \qquad (22d)$$

The constants were determined using a regressive curve-fit to experimental n and k data obtained by Munoz *et al.*[†] [3] . The equations (solid lines) and data (points) are plotted in Fig. 23(a). The fit is very good over the entire wavelength range.

[†] I would like to thank Munoz et al. for supplying me with a spreadsheet form of the data.

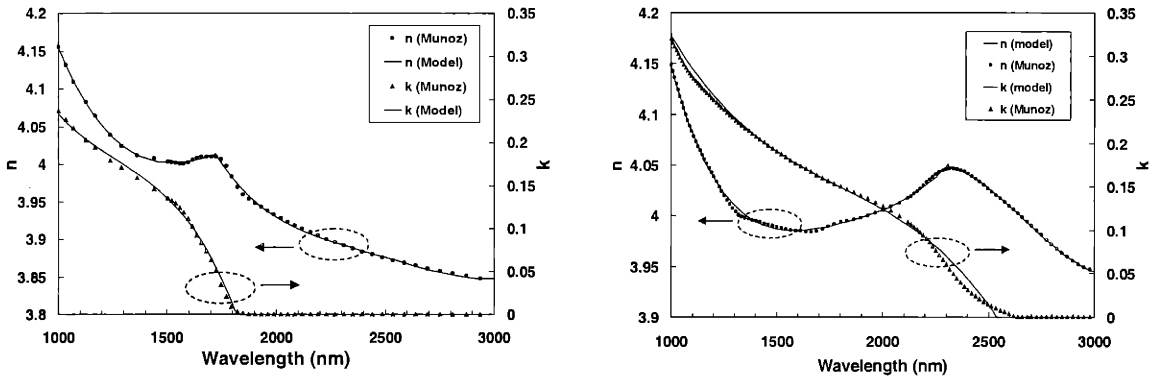

Fig. 23. Refractive index data (circles, triangles) and polynomial curve-fits (lines) to data for: (a) GaSb and (b) $Ga_{0.84}In_{0.16}As_{0.14}Sb_{0.86}$.

$Ga_{0.84}In_{0.16}As_{0.14}Sb_{0.86}$ was also measured experimentally by Munoz *et al.* [4]. The curve-fit to this data yielded the following equations:

$$n_{\mathrm{GaInAsSb}}(\lambda) = A\cdot\lambda^4 + B\cdot\lambda^3 + C\cdot\lambda^2 + D\cdot\lambda + E \qquad (1000 < \lambda < 2310\ \mathrm{nm}) \qquad (23a)$$

$$A = 0.285454\cdot10^{-12}$$
$$B = -0.2117264\cdot10^{-8}$$
$$C = 0.5961718\cdot10^{-5}$$
$$D = -0.00748765$$
$$E = 7.50528$$

$$n_{\mathrm{GaInAsSb}}(\lambda) = F\cdot\lambda^3 + G\cdot\lambda^2 + H\cdot\lambda + I \qquad (2310 < \lambda < 3000\ \mathrm{nm}) \qquad (23b)$$

$$F = 0.371588\cdot10^{-9}$$
$$G = -0.297584\cdot10^{-5}$$
$$H = 0.0077491$$
$$I = -2.5526$$

$$k_{\mathrm{GaInAsSb}}(\lambda) = J\cdot\lambda^3 + K\cdot\lambda^2 + L\cdot\lambda + M \qquad (1000 < \lambda < 2530\ \mathrm{nm}) \qquad (23c)$$

$$J = -0.144262\cdot10^{-9}$$
$$K = 0.780496\cdot10^{-6}$$
$$L = -0.0015311$$
$$M = 1.2182$$

$$k_{\mathrm{GaInAsSb}}(\lambda) = 0 \qquad (\lambda > 2530\ \mathrm{nm}) \qquad (23d)$$

These results are plotted in Fig. 23(b). Again, it is seen that an excellent curve-fit was achieved.

For $Al_xGa_{1-x}As_ySb_{1-y}$ lattice matched to GaSb, there are no reported experimental values of n and k between 1 and 3 μm for the complete range of x and y between 0 and 1. Alibert *et al.* [80] have reported values for $Al_xGa_{1-x}As_ySb_{1-y}$ ($0 < x < 0.51$) between 0.83 and 2.5 μm, while Di Lernia *et al.* [54] have characterized $Al_xGa_{1-x}Sb$ ($0 < x < 0.5$) between 0.25 and 0.89 μm. However, linear interpolation of data for the constituent binaries can be used to create a data set for the quaternary. It is seen in Fig. 1(b) that the AlGaAsSb alloy compositions lattice-matched to GaSb lie on a tie-line between GaSb and $AlAs_{0.08}Sb_{0.92}$. (The AlAsSb composition was determined using a simple lever rule between the two binaries, AlAs and AlSb.) The equation for GaSb was given above; the equation for $AlAs_{0.08}Sb_{0.92}$ can be generated by curve-fitting a polynomial to a data set for which $n_{AlAs0.08Sb0.92} = 0.92*n_{AlSb} + 0.08*n_{AlAs}$. Literature data were used for AlAs [5] and AlSb [6]. The equation for $AlAs_{0.08}Sb_{0.92}$ is then:

$$n_{AlAs(0.08)Sb(0.92)}(\lambda) = A\cdot\lambda^4 + B\cdot\lambda^3 + C\cdot\lambda^2 + D\cdot\lambda + E \quad (1000 < \lambda < 3000 \text{ nm}) \quad (24a)$$

$$A = 0.443572\cdot10^{-13}$$
$$B = -0.404344\cdot10^{-9}$$
$$C = 0.137986\cdot10^{-5}$$
$$D = -0.00213213$$
$$E = 4.49384$$

$$k_{AlAs(0.08)Sb(0.92)}(\lambda) = 0 \quad (\lambda > 1000 \text{ nm}) \quad (24b)$$

Data for $Al_xGa_{1-x}As_ySb_{1-y}$ can be generated by:

$$n_{Al(x)Ga(1-x)As(y)Sb(1-y)} = (1-x)*n_{GaSb} + x*n_{AlAs(0.08)Sb(0.92)} \quad (24c)$$

This assumes that a linear interpolation is appropriate – that there is no refractive index bowing parameter between the binary GaSb and ternary $AlAs_{0.08}Sb_{0.92}$. This is a

reasonable assumption based on models and data in the literature that indicate very little bowing [52, 53]. If there were significant bowing between GaSb and $AlAs_{0.08}Sb_{0.92}$, the only effect would be that the variable 'x' in eqn. (24c) would serve only as a fitting parameter, and not as a true composition.

3.2.3 Analytic function at energies above the fundamental bandgap (Model Dielectric Function)

The above-bandgap refractive index for GaSb at 300 K [3] is plotted in Fig. 24. Note that both n and k are strong functions of energy in this range. Due to this large dispersion, a more complicated function is required to represent n and k at these energies. The most successful such model was developed by Adachi, and is known as the Model Dielectric Function (MDF) [1, 2, 81, 82].

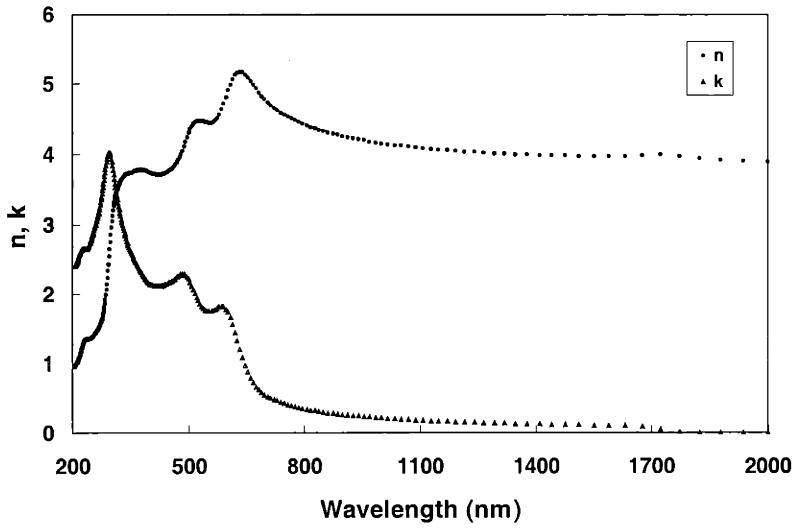

Fig. 24. Above-bandgap refractive index for GaSb. Note the strong dispersion below 800 nm.

The basis of the MDF is that the complex dielectric function, ε, is strongly connected with the electronic energy band structure of a material. The optical joint density of states is large for electronic transitions near critical points (CPs) in the Brillouin Zone. This occurs for electrons with a momentum wavevector, $\boldsymbol{k}$, such that the conduction and valence band slopes are the same at that wavevector, or both the conduction and valence bands simultaneously have slopes equal to zero. When one of these conditions is met, a CP is defined. Figure 25 shows a plot of the energy band structure of GaSb, with the various CPs or interband transitions labeled. The fundamental bandgap is called E_0, and represents an electronic transition from the highest valence band to the lowest conduction band at the Γ point. There is also a spin-orbit split interaction at this point, called $E_0+\Delta_0$, where Δ_0 represents the splitting energy between the highest valence band and the lower-lying spin-orbit split valence band. In the energy range of interest, from 1-6 eV (207-1240 nm), there are several other CPs, including E_1, $E_1+\Delta_1$, E_2, E_L (an indirect transition from the valence band at the Γ point to a minimum in the conduction band near the L point), and excitons at the E_1 and $E_1+\Delta_1$ transitions.

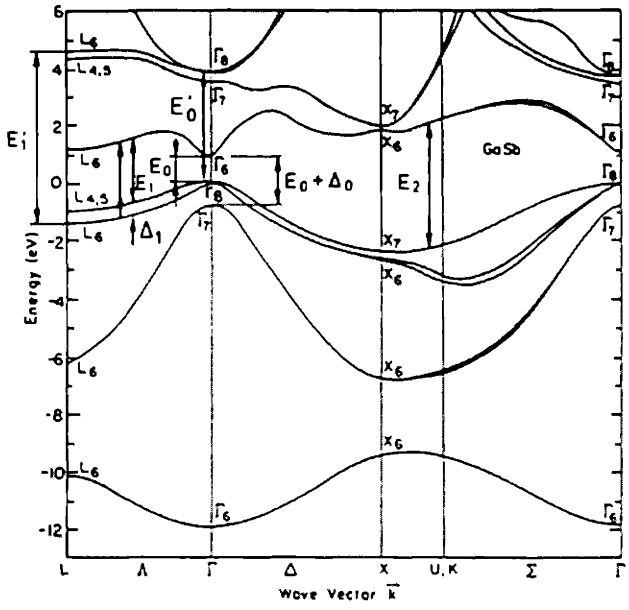

Fig. 25. Energy band structure of GaSb, indicating interband critical points. From ref. [79].

In the MDF, a function is given to describe the lineshape of the interband transition at each CP. The total dielectric function is given by simple addition of each of these individual CP terms. Each critical point interaction is described by three principal variables: the energy at which the CP occurs (i.e. the bandgap energy); the oscillator strength of the interaction at this CP; and a lifetime or broadening term for this interaction. Although this means that the overall function for the dielectric constant contains many parameters, the function itself is conceptually straightforward and provides the most accurate, physical representation of the dielectric constant.

For each CP, the energy of the interaction is often known experimentally from derivative spectroscopic ellipsometry data. This parameter can then be taken as a constant. The oscillator strength and broadening of each CP can be calculated from first

principles calculations; however, in practice, it is usually much easier to simply determine these parameters from a regressive curve-fit of the dielectric function to experimental dielectric constant data (typically from ellipsometry). Literature reports have shown that in many cases the values determined for the oscillator strength and lifetime from a curve-fit to data are fairly close to those calculated from first principles, thereby confirming the validity and physical accurateness of the MDF.

The E_0 and $E_0+\Delta_0$ transitions are of the 3-D M_0 type [1]. This type of transition has a lineshape given by:

$$\varepsilon(\omega) = \frac{A\left\{ f(\chi_0) + 0.5\left(\frac{E_0}{E_0 + \Delta_0} \right)^{1.5} f(\chi_{SO}) \right\}}{E_0^{1.5}} \tag{25a}$$

with

$$f(\chi_0) = \frac{2 - (1+\chi_0)^{0.5} - (1-\chi_0)^{0.5}}{\chi_0^2} \tag{25b}$$

$$f(\chi_{S0}) = \frac{2 - (1+\chi_{S0})^{0.5} - (1-\chi_{S0})^{0.5}}{\chi_{S0}^2} \tag{25c}$$

$$\chi_0 = \frac{\hbar\omega + i\Gamma_0}{E_0} \tag{25d}$$

$$\chi_{S0} = \frac{\hbar\omega + i\Gamma_0}{E_0 + \Delta_0} \tag{25e}$$

(Note: equations (25b) and (25c) are given incorrectly in ref. [1]. They are given correctly here.) As mentioned above, E_0 is the energy (in eV) of the fundamental bandgap, while Δ_0 is the spin split-off energy. The parameter A is the interaction strength parameter (units of $eV^{1.5}$), which was used as a fitting parameter in this thesis, but can be

calculated from first principles as: $4/3*(1.5\mu_0)^{1.5}P^2$, where μ_0 is the reduced mass of the valence band and P is the momentum matrix element. Γ_0 is the broadening parameter of the transition in eV units, while $\hbar\omega$ is the optical energy in eV, related to the wavelength of light by: $\hbar\omega$(eV) = 1240/λ (μm).

The E_1 and $E_1+\Delta_1$ transitions are of the 3-D M_1 type, but can be approximated as 2-D minima M_0 since the longitudinal effective mass is much larger than the transverse masses [1]. The contributions of these CPs to the dielectric function is given by:

$$\varepsilon(\omega) = \frac{-B_1 \ln\left(1-\chi_{1d}^2\right)}{\chi_{1d}^2} - \frac{B_2 \ln\left(1-\chi_{1sd}^2\right)}{\chi_{1sd}^2} \tag{26a}$$

where

$$\chi_{1d} = \frac{\hbar\omega + i\Gamma_1}{E_1} \tag{26b}$$

$$\chi_{1sd} = \frac{\hbar\omega + i\Gamma_1}{E_1 + \Delta_1} \tag{26c}$$

B_1 and B_2 represent the strengths of the transitions at E_1 and $E_1+\Delta_1$, respectively, while Γ_1 is the broadening parameter.

The nature of the E_2 transition is more complicated because it does not correspond to a single, well-defined CP. Therefore, its lineshape is best represented by a damped harmonic oscillator function [1]:

$$\varepsilon(\omega) = \frac{C}{\left(1-\chi_2^2\right) - i\chi_2\gamma_{E2}} \tag{27a}$$

where

$$\chi_2 = \frac{\hbar\omega}{E_2} \tag{27b}$$

As before, C is the oscillation strength parameter, while γ_{E2} is the lifetime broadening parameter.

Indirect bandgap transitions are represented by a second-order process, given by [1]:

$$\varepsilon(\omega)=\frac{2D}{\pi}\left\{-\frac{\left(E_g^{ID}\right)^2}{\left(\hbar\omega+\mathrm{i}\Gamma_{ID}\right)^2}\ln\left(\frac{E_c}{E_g^{ID}}\right)+0.5\left(1+\frac{E_g^{ID}}{\hbar\omega+\mathrm{i}\Gamma_{ID}}\right)^2\ln\left(\frac{\hbar\omega+\mathrm{i}\Gamma_{ID}+E_c}{\hbar\omega+\mathrm{i}\Gamma_{ID}+E_g^{ID}}\right)+0.5\left(1-\frac{E_g^{ID}}{\hbar\omega+\mathrm{i}\Gamma_{ID}}\right)^2\ln\left(\frac{\hbar\omega+\mathrm{i}\Gamma_{ID}-E_c}{\hbar\omega+\mathrm{i}\Gamma_{ID}-E_g^{ID}}\right)\right\} \tag{28}$$

where D is the interaction strength parameter, Γ_{ID} is the lifetime broadening parameter, E_g^{ID} is the energy of the indirect bandgap, and E_C is a cutoff energy necessary to limit the non-physical extension of the parabolic bands to infinite energies.

Finally, excitonic effects can modify interband electronic transitions. Excitons are known to have a strong effect near the E_1 and $E_1+\Delta_1$ transitions [82]. The form of these 2-D Wannier-type excitons can be described by a Lorentzian lineshape:

$$\varepsilon(\omega)=\frac{B_{1x}}{E_1-\hbar\omega-\mathrm{i}\Gamma_{\mathrm{exc}}}+\frac{B_{2x}}{E_1+\Delta_1-\hbar\omega-i\Gamma_{\mathrm{exc}}} \tag{29}$$

where B_{1x} and B_{2x} are the interaction strength parameters of excitons at the E_1 and $E_1+\Delta_1$ transitions, respectively, and Γ_{exc} is the broadening parameter. For simplicity it has been assumed that the excitons occur at the same energy as the direct E_1 and $E_1+\Delta_1$ transitions, although in reality they occur at slightly lower energies.

The effect of higher energy CPs can be simply included as a constant ($\varepsilon_{1\infty}$) in the 1-6 eV energy range of ε_1, since these CPs have minimal dispersion in this energy range. It is not necessary to include this constant in the function for ε_2, since these higher order transitions have little or no effect on ε_2 because their magnitude decays strongly to zero

as lower energies are approached. The dielectric function is obtained by summing each of the individual lineshapes described above. Both the real (ε_1) and imaginary (ε_2) components of the dielectric constant are contained in this function, and are simply given by $\varepsilon_1 = \mathrm{Re}(\varepsilon) + \varepsilon_{1\infty}$ and $\varepsilon_2 = \mathrm{Im}(\varepsilon)$, where Re() and Im() represent the real and imaginary parts of the function. By curve-fitting the function for ε_2 to experimentally measured data, values for the various interaction strengths and lifetime parameters can be determined. These constants are the same for ε_1, since ε_2 and ε_1 are inter-related by the well-known Kramers-Kronig relation [1]. In addition, once ε_2 and ε_1 are known, other optical properties (such as n, k, absorption, reflectance, etc.) can easily be calculated.

In one of his initial papers [2], Adachi presented results of curve-fits to various binary alloys. In particular, the binaries GaSb, GaAs, InAs, and InSb are of interest because they are the binaries from which GaInAsSb is comprised. Figures 26(a)-(d) shows the results of Adachi's curve-fits to these binaries at 300 K. Although the general lineshape of the data is very well captured by the MDF in these plots, there is some discrepancy between the absolute values of the data and the model. This first paper did not include the effects of excitons at the E_1 and $E_1+\Delta_1$ transitions, which are fairly important.

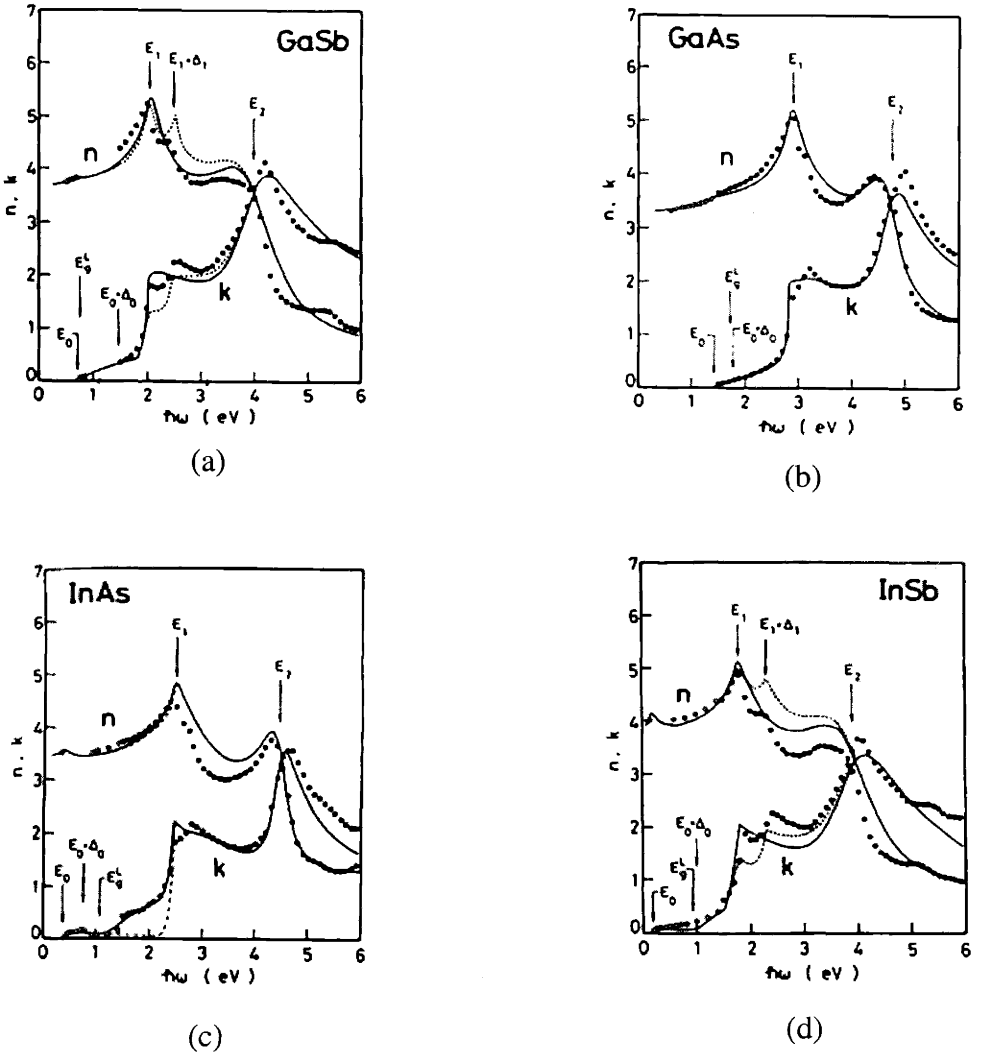

Fig. 26. Refractive index data and Adachi's Model Dielectric Function curve-fits to (a) GaSb, (b) GaAs, (c) InAs, and (d) InSb. From ref. [2].

To improve upon Adachi's initial results, a more comprehensive model including all of the CPs was generated for this thesis and curve-fit to data. The results of this model are compared to data in Figs. 27(a)-(d). Note the excellent agreement between the data and model. The parameters used in the model are listed in Table II. The energy of

each bandgap was taken from literature values [2, 79, 83-87], while the other parameters were determined from curve-fitting the function to literature data [7, 8].

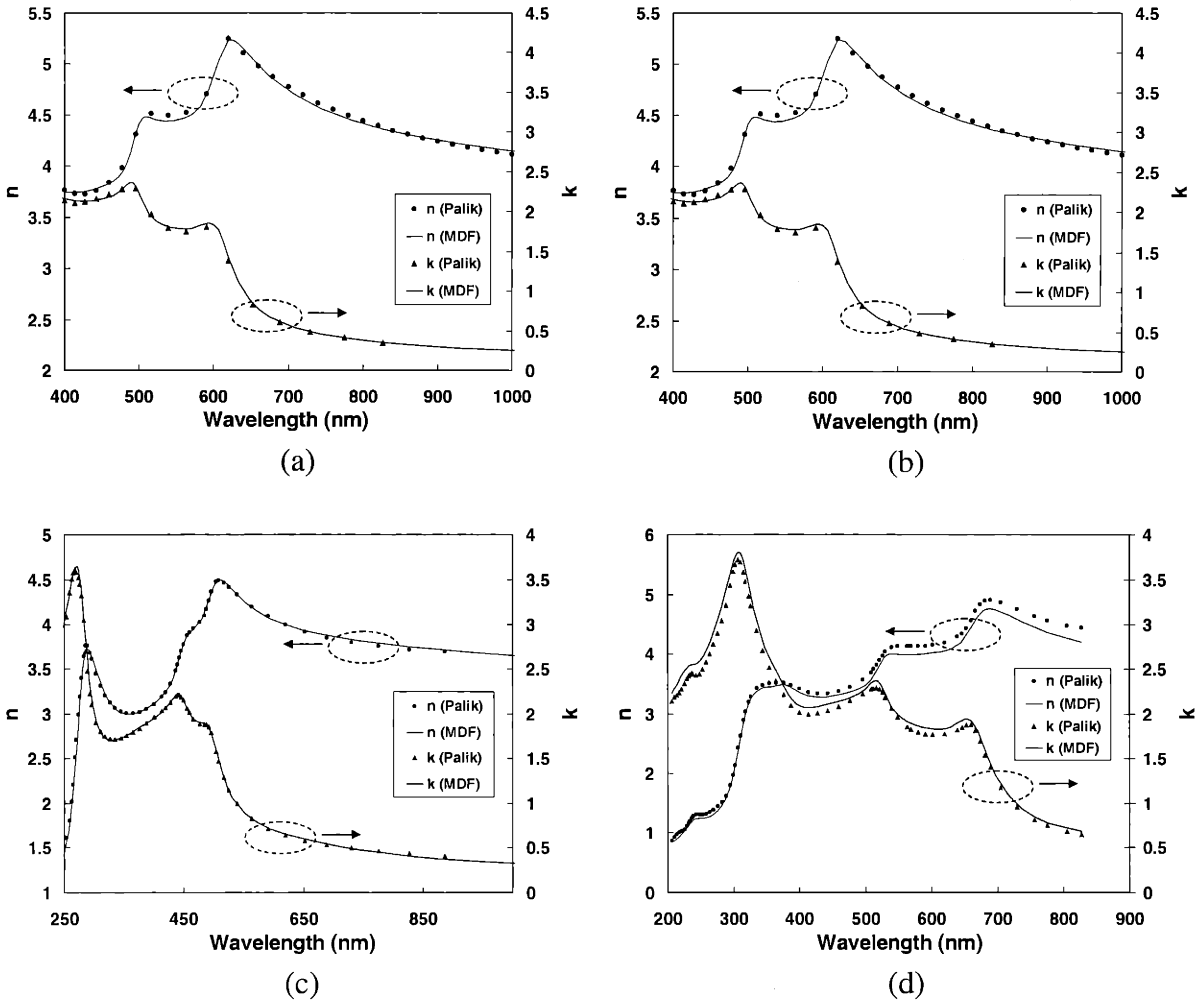

Fig. 27. Refractive index data and improved MDF fit to (a) GaSb, (b) GaAs, (c) InAs, and (d) InSb.

Table II. Parameters used in MDF Analytic Model of Binary Refractive Indices				
Parameter	**GaSb**	**GaAs**	**InSb**	**InAs**
E_0	0.72	1.42	0.18	0.36
$E_0+\Delta_0$	1.47	1.77	0.99	0.76
A	1.48	2.632	3.89	2.06
Γ_0	0.05	0.1	0.15	0.2
E_1	2.05	2.9	1.86	2.5
$E_1+\Delta_1$	2.49	3.13	2.37	2.78
B_1	6.12	4.31	6.96	5.61
B_2	1.2	1.32	1.35	0.07
Γ_1	0.15	0.04	0.25	0.16
E_2	4.0	4.8	3.92	4.46
C_{E2}	5.11	1.904	1.47	2.16
γ_{E2}	0.3	0.117	0.134	0.13
$E_{0'}$		4.45	3.35	
$C_{E0'}$		0.809	0.335	
$\gamma_{E0'}$		0.115	0.127	
$E_{0'}+\Delta_{0'}$			3.65	
$C_{E0'+\Delta0'}$			0.906	
$\gamma_{E0'+\Delta0'}$			0.165	
$E_{1'}$			5.24	
$C_{E1'}$			0.202	
$\gamma_{E1'}$			0.157	
E_g^{ID}	1.0	1.73		1.07
E_c	2.05	2.9		2.5
D	4.92	26.86		14.54
Γ_{ID}	0.1	0.05		0.1
B_{1x}	0.68	.732	0.618	0.578
B_{2x}	0.4	.388	0.326	0.363
Γ_{exc}	0.09	0.1	0.093	0.119
$\varepsilon_{1\infty}$	0.5	1	0	1.5

The temperature dependence of the dielectric constant can be included in the above model by making each parameter a temperature-dependent term. The temperature dependence of the various energy gaps is known to follow Varshni's equation, an empirical function given by [88]:

$$E_g(T) = E_g(0) - \frac{\alpha T^2}{T + \beta} \tag{30}$$

where $E_g(0)$ is the energy of the bandgap at 0 K, T is the temperature in degrees Kelvin, and α and β are constants. This function can be curve-fit to experimentally measured data. Zollner *et al.* have determined the following equations for GaSb [79]:

$$E_0(T) = 0.812 - \frac{0.00042 \cdot T^2}{T + 140} \tag{31a}$$

$$[E_0 + \Delta_0](T) = 1.552 - \frac{0.00042 \cdot T^2}{T + 140} \tag{31b}$$

$$E_1(T) = 2.186 - \frac{0.00068 \cdot T^2}{T + 147} \tag{31c}$$

$$[E_1 + \Delta_1](T) = 2.621 - \frac{0.00067 \cdot T^2}{T + 176} \tag{31d}$$

$$E_2(T) = 4.32 - \frac{0.0009 \cdot T^2}{T + 376} \tag{31e}$$

The oscillator strengths and broadening factors are usually either independent of temperature or have a linear dependence on temperature above a certain temperature. For this thesis, it was of interest to know the temperature dependence of the dielectric constant for GaSb between 25 and 575 °C. If an experimental set of data for ε_2 (or k) existed at 575 °C in the energy range of 1-6 eV, it would be straightforward to curve fit the MDF to this data and thereby determine the temperature dependence of the oscillator strengths and broadening parameters. Unfortunately, no reports of such data exist in the literature. Reports on the temperature dependence of oscillator strengths and broadening parameters do exist, however, for InSb [84, 89] and GaAs [85, 86]. These results can be used to make an approximate guess at the parameters for GaSb. Although the results will

not be exact, the basic features of the dielectric constant as a function of temperature should be fairly well predicted. Using the InSb and GaAs results as guidelines, the following relationships were approximated for GaSb:

$$A = 2.23 - 0.0025*T \quad (32a)$$
$$\Gamma_1 = 0.111 + 0.00013*T \quad (32b)$$
$$C = 3.79 + 0.0044*T \quad (32c)$$
$$\gamma_2 = 0.186 + 0.00038*T \quad (32d)$$
$$\Gamma_{exc} = 0.052 + 0.00013*T \quad (32e)$$

The other parameters listed in Table II remained constants. Using the above equations, the dielectric constant for GaSb can now be expressed as an analytic function of energy and temperature. The results as a function of energy were presented above in Fig. 27(a). The results as a function of temperature are discussed below in section 3.3.3.

3.3 Examples illustrating the use of analytic functions for the refractive index

The optical constant functions presented in sections 3.2.2 and 3.2.3 are all sufficiently accurate to model various optical responses of the materials studied in this thesis. The following subsections demonstrate two examples of how these models were used as part of this thesis work. In particular, they were used to predict the reflectance of various distributed Bragg reflector (DBR) stacks (and back out parameters from the measured reflectance of these stacks); and predict the temperature dependence of the reflectance of a GaSb substrate. The first application, the DBR, was helpful in interpreting *ex situ* reflectance measurements, while the other application was very useful in interpreting features seen in the *in situ* reflectance signal during growth runs.

3.3.1 Distributed Bragg reflectors (DBRs)

3.3.1.1 Interest in DBRs for TPVs and DBR basics

The device performance of thermophotovoltaic and photovoltaic cells often improves when back surface reflectors are used. These reflectors enhance performance for two primary reasons. First, not all incident light is absorbed during the first pass through the cell. These wasted photons decrease internal quantum efficiency because they are not converted to electronic carriers. A reflector at the back surface of the cell gives these photons a second pass through the cell, and therefore increases the quantum efficiency of the cell. Second, photogenerated carriers can recombine before they are removed from the device. This recombination also decreases the quantum efficiency. If the light generated by recombination is given a second pass through the cell by a back surface reflector, it increases the quantum efficiency. This "photon-recycling" manifests itself as an increase in the measured minority carrier lifetime. This increase is artificial, since the inherent carrier lifetime is not actually affected by the reflector. However, the experimentally observed time between the incident light pulse and the decay of photogenerated carriers is increased by the reflector, thereby causing an increase in the measured lifetime.

One technique to create a back surface reflector is to epitaxially grow a DBR stack on the substrate before growing the device. This technique has the benefit that the entire device structure—active layers plus back surface reflector—can be grown in one epitaxial growth run, minimizing process complexity. A DBR stack is simply a series of alternating high- and low-refractive-index epilayers, which creates a very high reflectance at a particular wavelength [45]. The reflectance at each interface in the stack is a function of the refractive index difference between the high- and low-index layers.

By increasing the refractive index difference, the reflectance is increased. In addition, the reflectance of the stack is a maximum when the individual reflectances from each interface are all in phase. This is guaranteed by making the thickness of each epilayer a so-called "quarter-wave" thick. The thickness, t, is then given by $t = \lambda/(4n)$, where λ is the center wavelength of the DBR stack, and n is the real part of the refractive index at that wavelength. A pair of high- and low-index layers taken together is called a period. As the number of periods is increased, the maximum reflectance at the center wavelength increases monotonically. However, the bandwidth of the high-reflectance zone simultaneously decreases. (This can be a positive or a negative depending on the intended application. For this application it is a drawback.)

The maximum reflectance at the center wavelength of the DBR stack as a function of the number of periods, p, in the stack is given by [45]:

$$R = \left(\frac{1 - \left(\frac{n_H}{n_L} \right)^{2 \cdot p} \left(\frac{n_H^2}{n_S} \right)}{1 + \left(\frac{n_H}{n_L} \right)^{2 \cdot p} \left(\frac{n_H^2}{n_S} \right)} \right)^2 \tag{33}$$

where n_H, n_L, and n_S are the refractive indices of the high-index layer, low-index layer, and substrate, respectively. The maximum reflectance is obtained with the high-index layer outermost at both sides of the stack; thus the number of layers in the stack is $(2p+1)$. This equation assumes that each layer in the stack is a quarter-wave thick.

Since the TPV device is epitaxially grown on top of the DBR stack, it is important that the materials used for the DBR be lattice-matched to the GaSb substrate. Otherwise, dislocations can propagate into the TPV and decrease device performance. In addition, the refractive index contrast between the high- and low-index layers used for the DBR

stack should be as large as possible. The larger this spread, the fewer the layers needed in the stack to achieve a high reflectance. Fortunately, two materials exist which are lattice-matched to GaSb and have a fairly large refractive index difference: GaSb and $Al_xGa_{1-x}As_ySb_{1-y}$.

As an example, consider a hypothetical DBR centered at 2.2 μm using alternating layers of GaSb and $Al_{0.5}Ga_{0.5}As_{0.04}Sb_{0.96}$. (The As and Sb concentrations are fixed by lattice-matching conditions to the GaSb substrate.) Using the model in section 3.2.2, the refractive index at 2.2 μm of GaSb is 3.902 and $Al_{0.5}Ga_{0.5}AsSb$ is 3.559. The quarter-wave thickness is therefore 141.0 nm for GaSb and 154.5 nm for $Al_{0.5}Ga_{0.5}AsSb$. The maximum reflectance as a function of the number of periods in the DBR is plotted in Fig. 28(a), based on eqn. (33) above.

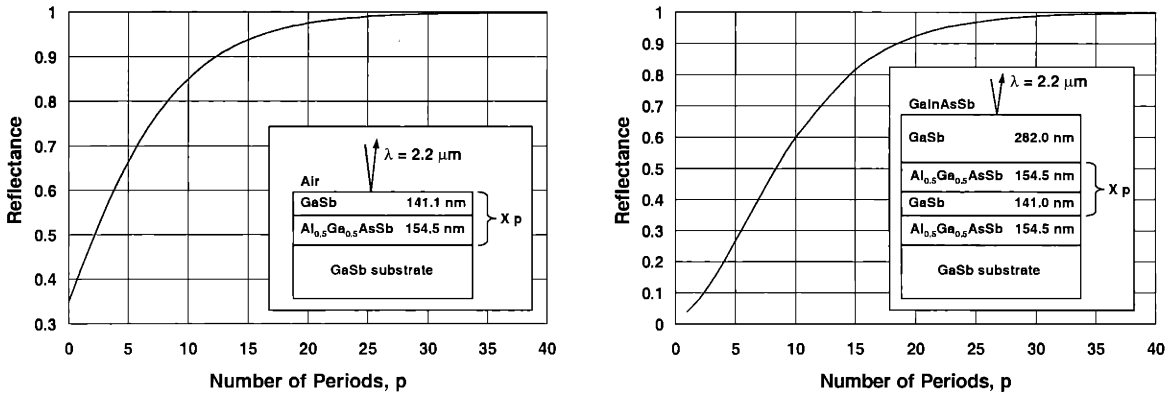

Fig. 28. Calculated reflectance at the center wavelength (2.2 μm) of a DBR as a function of the number of periods for (a) a DBR structure in air and (b) a DBR structure in a TPV.

In an actual device, this is not the reflectance that will be seen by photons, however. This is because the incident medium for photons going into the DBR stack will

not be air, but rather will be the GaSb buffer layer (or n-GaInAsSb base layer). In a 2.3 μm-cutoff-wavelength TPV device without a DBR stack, the reflectance at the GaInAsSb/GaSb interface is extremely low (< 10% between 1 and 3 μm) since there is very little refractive index difference between GaInAsSb and GaSb. However, with the DBR stack, the reflectance can be substantially increased. The maximum effective device reflectance as a function of periods is plotted in Fig. 28(b). The structure is:

[GaInAsSb | half-wave GaSb | {quarter-wave $Al_{0.5}Ga_{0.5}AsSb$ | quarter-wave GaSb}^{n} | quarter-wave $Al_{0.5}Ga_{0.5}AsSb$ | GaSb substrate]

and is shown schematically in the figure. In order to deposit GaInAsSb on GaSb, rather than on AlGaAsSb, the half-wave GaSb layer is inserted. This half-wave layer acts as an absentee layer at 2.2 μm and therefore maximizes reflectance between the GaInAsSb epilayer and the topmost quarter-wave AlGaAsSb layer.

Several experimentally obtained results of various DBR stacks are now discussed, comparing the measured reflectance with that calculated using the refractive index models of section 3.2.2 above.

3.3.1.2 Comparisons of measured and calculated reflectances for various DBRs

Example 1. 5-period DBR nominally centered at 2.4 μm using GaSb/$Al_{0.64}Ga_{0.36}AsSb$

The initial DBR was targeted to have a center wavelength at 2.4 μm, using alternating epilayers of GaSb ($n = 3.884$ at $\lambda = 2.4$ μm) and $Al_{0.64}Ga_{0.36}As_{0.05}Sb_{0.95}$ ($n = 3.451$ at $\lambda = 2.4$ μm, using eqn (24c) above). (The AlGaAsSb alloy composition was determined using the *in situ* reflectance ratio at $\lambda = 500$ nm, not shown here, and eqn. (12b) above.) A 5-period stack was grown, with the following targeted structure:

[{154.5 nm GaSb | 173.9 nm $Al_{0.64}Ga_{0.36}AsSb$ }^{5} | GaSb buffer layer | GaSb substrate]

The *in situ* reflectance of this growth is shown at $\lambda = 1000$ nm in Fig. 29. The *ex situ* reflectance is plotted in Fig. 30(a) as a function of wavelength. This reflectance was measured using a Cary 5E UV-Vis-NIR spectrophotometer. Also plotted in Fig. 30(a) is the predicted reflectance using the models presented in section 3.2.2, with the thicknesses and composition given above. Although the shape of the measured reflectance spectrum is similar to the calculated spectrum, the feature locations are slightly shifted in wavelength and intensity. This suggests that the actual epilayer thicknesses and/or AlGaAsSb composition are different than the targeted values.

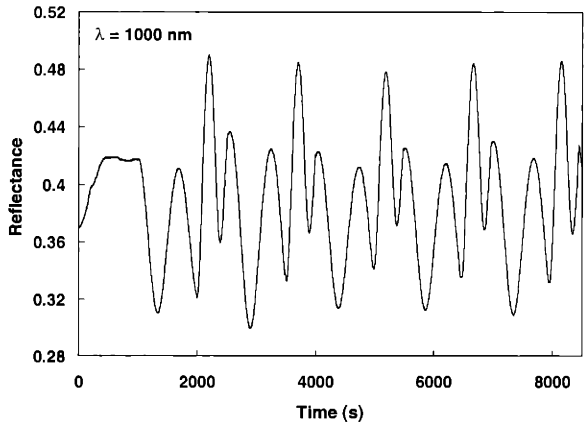

Fig. 29. *In situ* reflectance at 1000 nm of a 5-period DBR targeted to have a center wavelength at 2.4 μm.

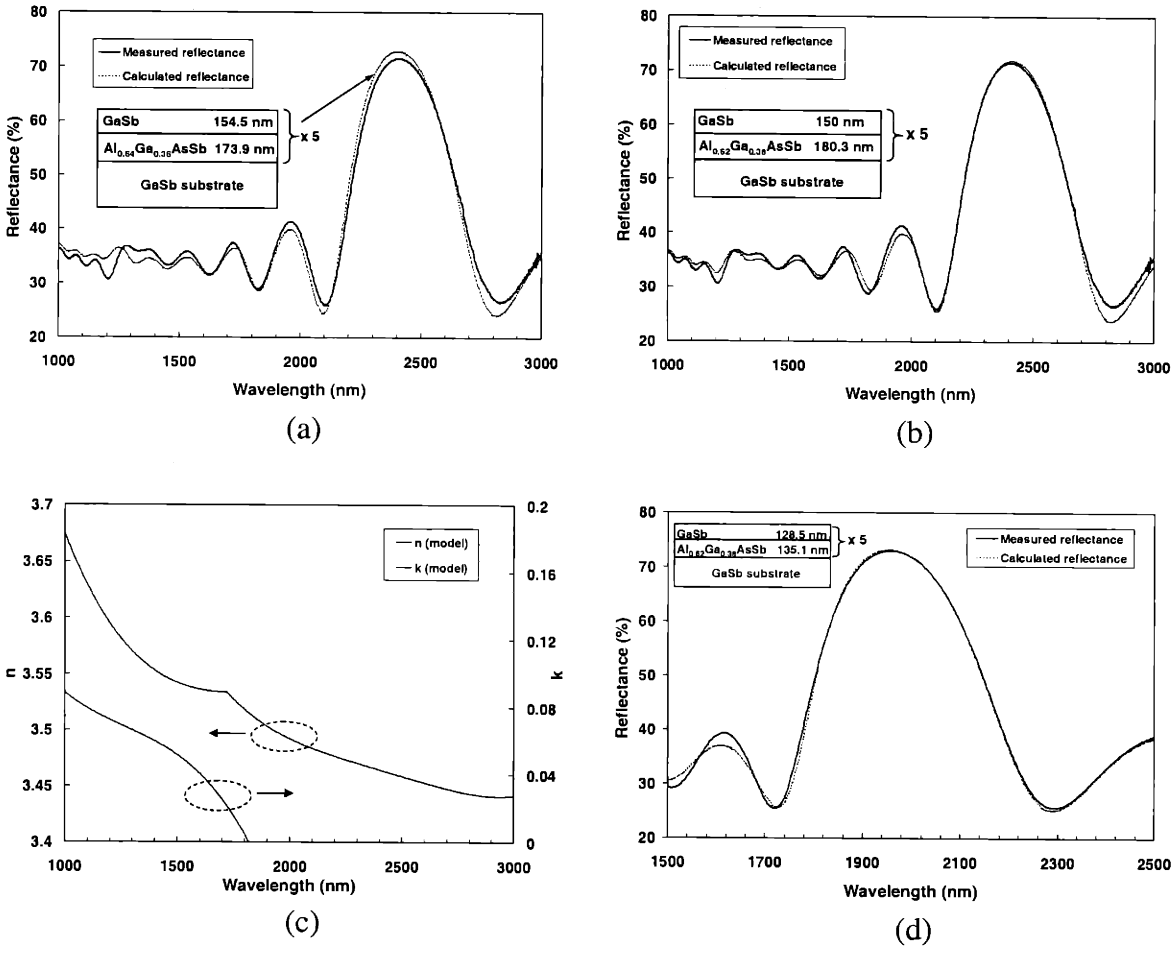

Fig. 30. (a) *Ex situ* reflectance spectrum of 5-period DBR and initial calculated spectrum based on targeted epilayer thicknesses and composition. (b) Improved fit to measured data. (c) Calculated refractive index used for $Al_{0.62}Ga_{0.38}AsSb$ epilayer in DBR in (b). (d) *Ex situ* reflectance and fit for a different 5-period DBR, using the same $Al_{0.62}Ga_{0.38}AsSb$ alloy composition.

Figure 30(b) shows the same measured reflectance with a calculated spectrum based on the following parameters: AlGaAsSb composition = $Al_{0.62}Ga_{0.38}AsSb$, GaSb thickness = 150 nm, and $Al_{0.62}Ga_{0.38}AsSb$ thickness = 180.3 nm. The fit is improved over the entire wavelength range. To obtain the parameters for this fit, first the "composition" of the AlGaAsSb epilayer was determined using the *ex situ* reflectance spectrum as follows: since the refractive index of GaSb at 2.4 μm is 3.884, the refractive index of the

AlGaAsSb layer must have been 3.471 to achieve the measured maximum reflectance of 71.5% at 2.4 μm for a 5-period DBR stack (see eqn. (33) above). Using the model for the refractive index of AlGaAsSb given above indicated an Al "composition" of 62%, yielding $Al_{0.62}Ga_{0.38}AsSb$. The difference between the Al fraction determined by the *in situ* reflectance/RBS calibration (0.64) and that determined by the $Al_xGa_{1-x}AsSb$ refractive index model (0.62) is probably within the noise of the experimental data, but may also be related to a slight bowing of the $Al_xGa_{1-x}AsSb$ refractive index with composition not taken into account in the model.

The thickness of each film was determined next using a regressive curve-fit of the calculated DBR reflectance to the *ex situ* measured reflectance over the entire 1000-3000 nm wavelength range. The curve-fit was performed using the IMD optical modeling software package (Version 4.1, © 1997-1998 David L. Windt, Bell Laboratories). The refractive indices of each layer were fixed by eqns. (22) and (24), so the only adjustable parameters in the fit were the two thicknesses. The curve-fit yielded thicknesses of 150.0 nm for the GaSb epilayers and 180.3 nm for the $Al_{0.62}Ga_{0.38}AsSb$ epilayers. These values are very close to those determined from curve-fits to the *in situ* reflectance shown in Fig. 29, which yielded growth rates of 0.2982 nm/s for the GaSb layers and 0.1890 nm/s for the $Al_{0.62}Ga_{0.38}AsSb$ epilayers. Since the growth times of the layers were 500 and 970 s, respectively, this yielded film thicknesses of 149.1 and 183.3 nm for the GaSb and $Al_{0.62}Ga_{0.38}AsSb$ layers, respectively.

The generated refractive index for $Al_{0.62}Ga_{0.38}AsSb$ based on eqn. (24) is plotted in Fig. 30(c). These values agree very well with results from other models reported in the literature [52, 80, 90]. The generated values are not totally accurate, however, because

they predict an incorrect bandgap at $\lambda \sim 1800$ nm for $Al_{0.62}Ga_{0.38}AsSb$ (due to the influence of GaSb in the model). The actual bandgap of this alloy is less than 1000 nm [52]. This simplification does not cause a major problem though. It only introduces a minor amount of artificial dispersion near 1800 nm for n, and the artificial non-zero k values between 1800 nm and the true bandgap of $Al_{0.62}Ga_{0.38}AsSb$ ($E_x \sim 880$ nm, $E_0 \sim$ 760 nm [52]) have only minimal impact on optical property calculations since $k << n$ in this wavelength range. For the highest accuracy, though, the calculated DBR reflectance shown in Fig. 30(b) assumed that $k = 0$ for $1000 < \lambda < 3000$ nm, rather than the non-zero values shown in Fig. 30(c).

Example 2. 5-period DBR nominally centered at 2.0 μm using GaSb/$Al_{0.64}Ga_{0.36}AsSb$

A 5-period DBR stack was also grown at a nominal center wavelength of 2.0 μm. The same $Al_{0.62}Ga_{0.38}AsSb$ composition was used for the modeling as in the previous example. The targeted quarter-wave thicknesses were 127.3 nm for GaSb ($n = 3.929$ at 2.0 μm) and 143.2 nm for $Al_{0.62}Ga_{0.38}AsSb$ ($n = 3.492$ at 2.0 μm). The measured and calculated reflectance of this stack is shown in Fig. 30(d). The thickness of each epilayer used for the calculated reflectance was determined by a curve-fit to the *ex situ* measured reflectance spectrum between 1.5 and 2.5 μm, using IMD as mentioned in Example 1 above. The best curve-fit yielded thicknesses of 128.5 nm and 135.1 nm for the GaSb and $Al_{0.62}Ga_{0.38}AsSb$ epilayers, respectively. These values are again similar to those determined from a curve-fit to the *in situ* reflectance for this DBR (not shown here), which indicated film thicknesses of 126.5 nm for GaSb (growth rate = 0.2861 nm/s, growth time = 442 s) and 140.2 nm for $Al_{0.62}Ga_{0.38}AsSb$ (growth rate = 0.1891 nm/s,

growth time = 742 s). The calculated reflectance spectrum agrees well with the measured spectrum, which had a center wavelength of 1.956 μm, slightly off from the targeted 2.0 μm.

Example 3. 10-period DBR nominally centered at 2.2 μm using GaSb/$Al_{0.81}Ga_{0.19}AsSb$

To increase the reflectance of the DBR, a 10-period structure using alternating GaSb/$Al_{0.81}Ga_{0.19}AsSb$ layers was grown. (This AlGaAsSb composition was determined as in Example 1 using the *in situ* reflectance ratio at $\lambda = 500$ nm and eqn. (12b)). The targeted center wavelength was 2.2 μm. The targeted epilayer thicknesses were 141.0 nm for GaSb ($n = 3.902$) and 164.4 nm for $Al_{0.81}Ga_{0.19}AsSb$ ($n = 3.346$). The measured and calculated reflectances are shown in Fig. 31(a). To generate the calculated spectrum, the refractive index of $Al_{0.81}Ga_{0.19}AsSb$ was calculated from eqn. (24c) and is shown in Fig. 31(b). Again, the model inaccurately included non-zero values for k between 1000 and 1820 nm, so these values were set to zero before calculating the reflectance spectra shown in Figs. 31(a) and (c).

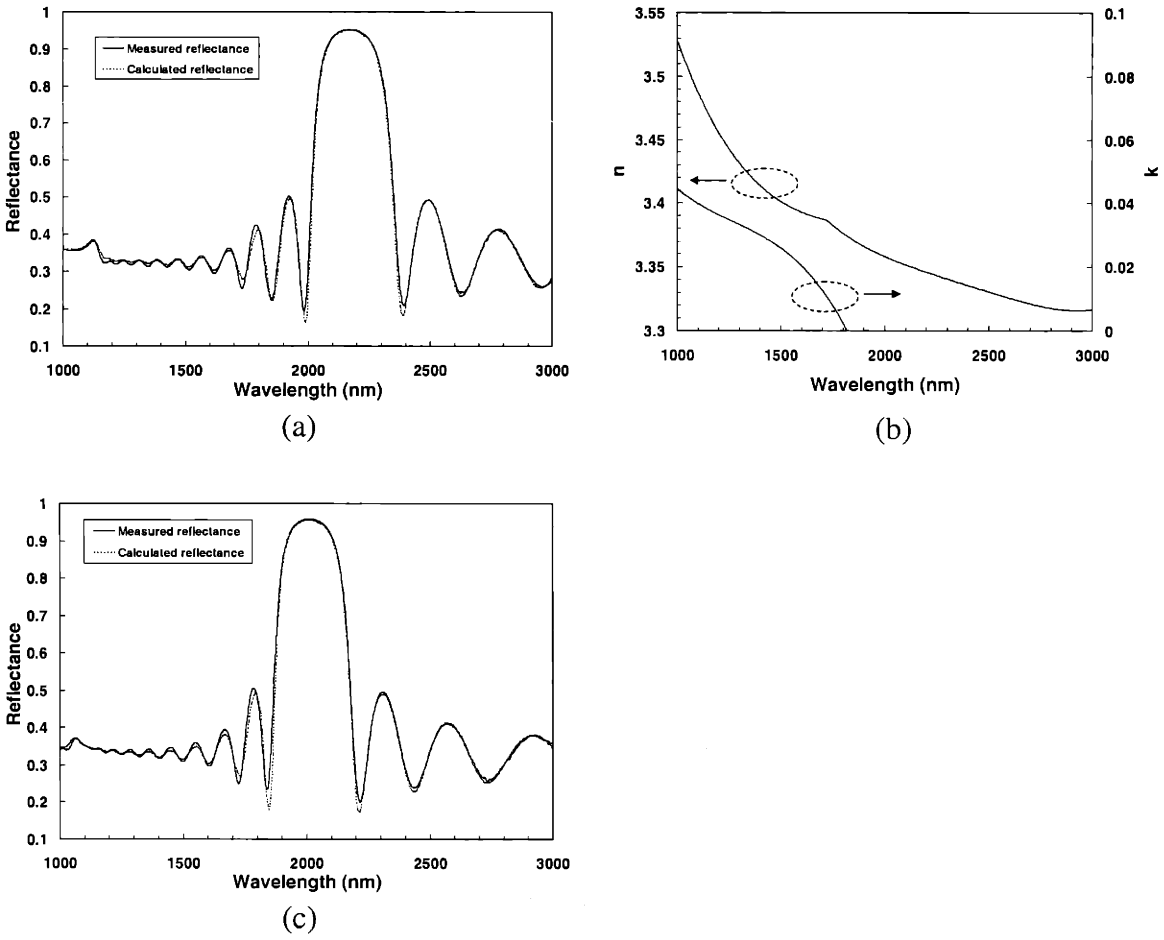

Fig. 31. Measured and calculated reflectance spectra for 10-period DBRs centered at (a) 2.2 μm and (c) 2.0 μm. The calculated refractive index for the $Al_{0.81}Ga_{0.19}AsSb$ epilayer is shown in (b).

Next, the epilayer thicknesses were determined using a regressive curve-fit of the calculated DBR reflectance spectrum to that measured experimentally.[†] The epilayer thicknesses determined from this curve-fit, 143.0 nm for the GaSb epilayers and

157.0 nm for the $Al_{0.81}Ga_{0.19}AsSb$ epilayers, agreed almost exactly with those determined by a curve-fit to the *in situ* reflectance data (not shown): 142.3 nm and 157.0 nm for the GaSb and $Al_{0.81}Ga_{0.19}AsSb$ epilayers, respectively.

Example 4. 10-period DBR nominally centered at 2.0 μm using GaSb/$Al_{0.81}Ga_{0.19}AsSb$

A 10-period DBR similar to that of Example 3 was also grown, but with a targeted center wavelength at 2.0 μm. The measured and calculated reflectance spectra are plotted in Fig. 31(c). Again, a composition of $Al_{0.81}Ga_{0.19}AsSb$ was used for the refractive index model, and the values of k were set to zero. The targeted thicknesses for this DBR were 127.3 and 148.9 nm for GaSb and $Al_{0.81}Ga_{0.19}AsSb$, respectively. The thicknesses determined from a regressive curve-fit of the calculated DBR reflectance spectrum to the measured data were 126.7 and 151.4 nm for GaSb and $Al_{0.81}Ga_{0.19}AsSb$, respectively. These values are very close to those determined from a curve-fit to the *in situ* reflectance (not shown): 125.5 and 152.9 nm, respectively.

These four examples illustrate that not only can the analytic models of the optical constants be used to predict device optical properties, which is helpful in device design, but can also be used to calculate actual epilayer parameters (such as thickness) by curve-fitting to experimental data. The latter use is especially helpful when used to compare to calculations from *in situ* measurements.

[†] The wafer size of the samples shown in Figs. 31(a) and (c) was too small to be measured *ex situ* using the Cary 5E UV-Vis-NIR spectrophotometer. The spectral reflectance of these samples was instead measured using a PerkinElmer spectrophotometer (Model Lambda 9). Unlike the Cary system, which inherently measures the absolute reflectance without using a calibration standard, the PerkinElmer system required a Au calibration standard to obtain absolute reflectance. However, the calibration was determined to be slightly off based on a comparison of another sample measured on both the Cary and PerkinElmer units.

3.3.2 Temperature dependence of GaSb reflectance

A comparison between the calculated and measured reflectance of GaSb as a function of temperature was shown for 500 nm in Fig. 10. The calculated reflectance was generated using the temperature-dependent model of section 3.2.2, for randomly-polarized light at a 55° incidence angle. The following temperature vs. time relationships were used to simulate the OMVPE reactor heat-up and cool-down:

$$T(t) = 1.9*t + 298 \qquad \text{(Heat-up)} \qquad (34a)$$

$$T(t) = 525*\exp(-t/650) + 298 \qquad \text{(cool-down)} \qquad (34b)$$

where T is in degrees K and t is in seconds. Equation (34b) very closely approximates the actual exponential cool-down of the reactor. Equation (34a), however, is only accurate from room temperature to about thirty degrees below the final temperature. The $T(t)$ curve during the final portion of heating, from thirty degrees below the final temperature to the final temperature, is sub-linear as the actual temperature asymptotically approaches the target temperature. Therefore, the theoretical heat-up curve is compressed on the time scale compared to the actual heat-up curve, whereas the theoretical cool-down curve closely mirrors the actual cool-down curve.

Additional examples comparing the theoretical and actual temperature dependence of the reflectance of GaSb are shown in Fig. 32. The theoretical heat-up and cool-down of GaSb from 25 to 550 °C at 633, 750, and 1000 nm is compared to actual reflectance data obtained during oxide-free GaSb substrate re-heats. (More information about the oxide-free data is given in section 2.4.3.3.) It is seen that while the absolute

---

The measured reflectance from the PerkinElmer unit was slightly too high; therefore, the measured data in Examples 3 and 4 was scaled by a factor of 0.982 based on the comparison sample measured on both units.

reflectance values do not exactly match between the theoretical and actual data, the general shape and features of the actual data are faithfully predicted by the theoretical curves. As mentioned in section 3.2.2, since the exact temperature dependence is unknown for several parameters in the MDF model of GaSb, it is not expected that the temperature-dependent function will predict the actual temperature dependence with a high degree of accuracy. However, the approximations used for the temperature dependencies clearly yield a reasonable model. In particular, the model was helpful in discovering that the reflectance was sensitive to GaSb substrate oxide desorption (discussed in section 2.4.3). Whereas the theoretical and actual cool-down reflectance curves were extremely similar in all cases, the actual heat-up curves had additional features to those seen in the theoretical heat-up curves. The theoretical model was helpful in identifying which features seen in the actual reflectance of the heat-up of a GaSb substrate with an oxide were due to the oxide, and which were simply due to energy-band shifts with temperature.

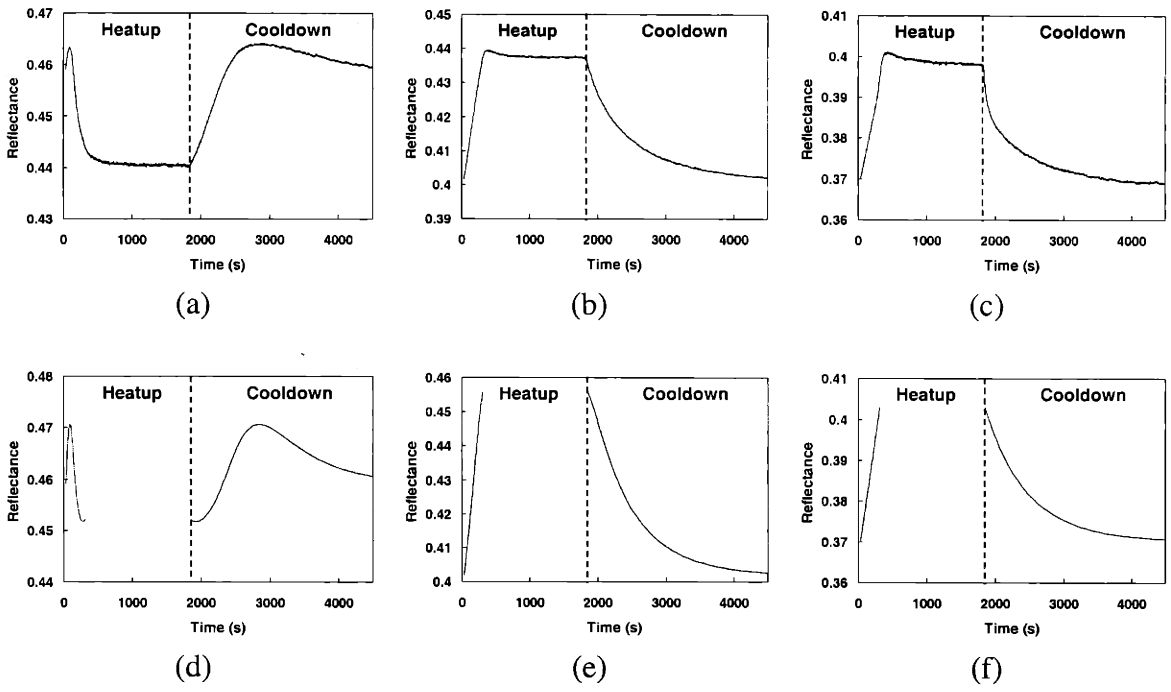

Fig. 32. Comparison of oxide-free heatup and cooldown *in situ* reflectance data at (a) 633 nm, (b) 750 nm, and (c) 1000 nm, with calculated curves at (d) 633 nm, (e) 750 nm, and (f) 1000 nm obtained using the temperature-dependent refractive index model discussed in this section.

3.4 Summary of optical constant modeling

In order to better interpret and predict *in situ* and *ex situ* optical properties, analytic functions were developed for various binaries and quaternaries studied in this thesis. In particular, the refractive indices of GaSb, $Ga_{0.84}In_{0.16}As_{0.14}Sb_{0.86}$, $AlAs_{0.08}Sb_{0.92}$, and $Al_xGa_{1-x}As_ySb_{1-y}$ were modeled from 1-3 μm using polynomial equations. These functions were useful in modeling GaSb/$Al_xGa_{1-x}As_ySb_{1-y}$ DBR stacks grown for TPV devices. Based on *ex situ* reflectance spectra of the DBRs, the actual thicknesses of the high- and low-index layers were determined using the model and compared to the targeted thicknesses and those determined from *in situ* reflectance. In addition, it was

seen that the actual Al fraction in the $Al_xGa_{1-x}As_ySb_{1-y}$ epilayer determined from the RBS calibration of eqn. (12b) could be directly used in the linear interpolation model of eqn. (24c) to generate a refractive index for the $Al_xGa_{1-x}As_ySb_{1-y}$ epilayer. This indicates that there is almost no bowing between the refractive index values of GaSb and $AlAs_{0.08}Sb_{0.92}$ as a function of composition, in agreement with other literature models and data [52, 53].

In addition, the refractive indices of GaSb, GaAs, InSb, and InAs were modeled between 1.5 and 5 eV (827 to 248 nm) using Adachi's model dielectric function. By including more critical points in the curve-fit, more accurate functions for these binaries were generated than those presented in Adachi's initial paper. An approximate temperature dependence of the refractive index of GaSb was generated using values in the literature for GaAs and InSb as guidelines. Although the predicted and actual absolute reflectance did not match exactly, the overall temperature-dependent features seen in actual data were very well captured in the model.

4. Phase Separation in GaInAsSb

$Ga_{1-x}In_xAs_ySb_{1-y}$ alloys lattice-matched to GaSb can have room temperature (RT) bandgaps between 1.7 and 4.1 μm, and are therefore of interest for mid-infrared devices. In particular, the $Ga_{1-x}In_xAs_ySb_{1-y}$ alloys studied in this thesis had compositions ranging from $Ga_{0.90}In_{0.10}As_{0.09}Sb_{0.91}$ to $Ga_{0.80}In_{0.20}As_{0.17}Sb_{0.83}$, corresponding to RT photoluminescence (PL) peaks from 2.080 to 2.485 μm. It is widely reported that ternary and quaternary III-V alloys grown by LPE, MBE, and OMVPE can exhibit phase separation and/or atomic ordering. Since $Ga_{1-x}In_xAs_ySb_{1-y}$ alloys with ($0.1 < x < 0.2$, $0.09 < y < 0.17$) lie in or near calculated and observed bulk miscibility gaps [91-95], these alloys may also exhibit phase separation. Phase separation will affect device performance and is therefore of interest to study.

This chapter is organized as follows. Section 4.1 provides an overview of phase separation thermodynamics and kinetics, including an explanation of calculated bulk miscibility gaps and the limitation of extending these calculations to kinetically-limited OMVPE growth. Section 4.2 gives a select literature review of transmission electron microscopy (TEM) studies of phase separation in various III-V ternary and quaternary

alloys. These results provide a base with which the TEM results from this thesis can be compared. Section 4.3 presents results from previous characterization studies of GaInAsSb, conducted by others prior to this thesis. These results include PL, x-ray, atomic force microscopy (AFM), and some initial TEM studies. The TEM results from this thesis work are then presented and discussed in section 4.4. The microstructure of GaInAsSb was studied as a function of alloy composition, substrate orientation, and growth temperature. A wide range of microstructures was observed, and the extent of inhomogeneity (likely due to phase separation) correlated well with previously reported results from other characterization techniques. In addition, it was seen that GaInAsSb epilayers also phase separated to form two different variants of a natural superlattice. A qualitative model was developed to explain the formation of one of the variants (the tilted superlattice). A framework of thermodynamic driving forces for phase separation vs. kinetic barriers to surface diffusion was also developed and used to map out various samples. This framework provided insight into the conditions under which a sample would exhibit a tilted superlattice. A chapter summary is then given in section 4.5.

4.1 Overview of phase separation thermodynamics and kinetics

4.1.1 Calculating phase maps for bulk alloys

When two or more elements are mixed together, the free energy of the alloy is determined by the free energy of the pure endpoint components, and the free energy of mixing. The free energy of mixing is given by [96]:

$$\Delta G^{M} = \Delta H^{M} - T\Delta S^{M} \tag{35}$$

In the regular solution model, the enthalpy (ΔH^M) and entropy (ΔS^M) of mixing for a binary alloy A_xB_{1-x} are:

$$\Delta H^M = x(1-x)\Omega \tag{36a}$$

$$\Delta S^M = -R[x\ln(x) + (1-x)\ln(1-x)] \tag{36b}$$

where R is the universal gas constant and Ω is the interaction parameter. In the quasi-chemical model, the interaction parameter is given by:

$$\Omega = ZN_A[H_{AB} - 0.5*(H_{AA} + H_{BB})] \tag{37}$$

where Z is the number of nearest-neighbor bonds, N_A is Avogadro's number, and H_{XY} is the energy of a bond between atoms X and Y, dependent on chemical interactions. For solutions with $\Omega = 0$, the system has an equal preference for AB bonds and AA/BB bonds. In these solutions the atoms will be completely randomly arranged, at all temperatures. When $\Omega < 0$, AB bonds are preferred to AA and BB bonds; therefore, the system has a thermodynamic driving force to atomically order. On the other hand, when $\Omega > 0$, AA and BB bonds are preferred to AB bonds. In this case, the system has a driving force to cluster or phase separate. Note that both clustering and ordering decrease system entropy, and therefore are only preferred at lower temperatures where the enthalpy term in eqn. (35) is dominant over the entropy term. Above a certain temperature, termed the critical temperature, the importance of entropy removes the thermodynamic driving force for clustering or ordering, and atoms will be randomly arranged.

The quasi-chemical model mentioned above relies on several assumptions, one of which is that only nearest-neighbor interactions need to be considered. Another assumption is that the bond energies are derived principally from chemical, not strain,

interactions. These assumptions are not generally valid for pseudo-binary III-V semiconductor alloys due to the nature of the crystal structure. Pseudo-binary III-V alloys are ternaries of the form $A_xB_{1-x}C$ or AC_yD_{1-y}. For those of the form $A_xB_{1-x}C$, the A and B atoms are group III elements that intermix on one FCC sublattice of the zincblende crystal structure, while atom C is a group V element that completely occupies the other FCC sublattice. Notice that in this case, the process of ordering or phase separation refers to the arrangement of the A and B atoms with respect to one another on one FCC sublattice. As the A and B atoms rearrange themselves, neither the first nearest neighbors nor the number of AC and BC bonds changes. Specifically, for any given arrangement of A and B atoms on the group III sublattice, all A atoms have only C atoms as their first nearest neighbors, and all B atoms also have only C atoms as their first nearest neighbors. Furthermore, there is no way to change the relative number of AC and BC bonds simply by rearrangement of A and B atoms; the relative number of bonds can only be changed by changing the overall composition, x. Therefore, for a pseudo-binary alloy, there are only two changes as a result of ordering or phase separation: second nearest neighbors, and strain. Atomic ordering results in all atoms and their second nearest neighbors being unlike in nature (i.e. all A atoms have B atoms as their second nearest neighbor and vice versa), while phase separation tends to create like second nearest neighbors. Furthermore, if the alloy lattice constant is a function of composition because the endpoint binaries AC and BC have different lattice constants, then phase separation creates regions of different lattice size, resulting in inherent strain energy due to the coherent interface between the various regions. Thus, factors other than first nearest-

neighbor interactions need to be considered for these alloys and the quasi-chemical model is therefore not appropriate for estimating Ω values for pseudo-binaries.

One widely utilized model for estimating Ω for pseudo-binaries is the Delta Lattice Parameter (DLP) model, developed by Stringfellow [97-101]. Examination of pseudo-binary III-V semiconductor alloys indicated that Ω is a function of the lattice parameter difference between AC and BC. This resulted in the following equations [101]:

$$\Omega^s = 4K\left[-\left(\frac{a_{AC}+a_{BC}}{2}\right)^{-2.5} + 0.5*(a_{AC}^{-2.5}+a_{BC}^{-2.5})\right] \tag{38a}$$

$$\approx 99K\frac{(a_{AC}-a_{BC})^2}{(a_{AC}+a_{BC})^{4.5}} \tag{38b}$$

where K is a constant empirically determined to be $1.15*10^7$ cal mol^{-1} Å$^{2.5}$, and a_{XY} is the lattice constant of binary XY in Å. The enthalpy of atomization, or bond energy, is given as:

$$\Delta H^{at} = Ka_0^{-2.5} \tag{39}$$

where a_0 is the average lattice constant of the alloy, given by Vegard's Law. This model is able to accurately calculate the interaction parameter Ω (typically 2000-4000 cal/mol) for nearly all III-V pseudo-binary alloys, with a standard deviation from experimental data of only 412 cal/mol—on the order of the range of the experimental results for any given system.

For a quaternary alloy of the form $A_xB_{1-x}C_yD_{1-y}$ (like $Ga_{1-x}In_xAs_ySb_{1-y}$), where the A and B atoms are group III elements that mix on one FCC sublattice while the C and D

atoms are group V elements that mix on the other FCC sublattice, the resulting Gibbs free energy per mole of the solid given by the DLP model is [98]:

$$G^S = -Ka_0^{-2.5} + RT[x\ln(x) + (1-x)\ln(1-x) + y\ln(y) + (1-y)\ln(1-y)] \quad (40)$$

The first term is due to the enthalpy of the solid while the second term is due to the configurational entropy, assuming a random distribution of A and B on one sublattice and C and D on the other. The lattice parameter for the alloy is given by Vegard's law as:

$$a_0 = (x)(y)a_{AC} + (x)(1-y)a_{AD} + (1-x)(y)a_{BC} + (1-x)(1-y)a_{BD} \quad (41)$$

Note that in these alloys, a rearrangement of atoms on the group III and group V sublattices changes both the first and second nearest neighbors and therefore the relative number of AC, AD, BC, and BD bonds, unlike in the pseudo-binary case above, where atom rearrangement only affected second nearest neighbors. Therefore, ordering and phase separation affect both chemical and strain interactions for $A_xB_{1-x}C_yD_{1-y}$ quaternary alloys.

The DLP model predicts a positive interaction parameter (Ω) for all III-V pseudo-binary and quaternary semiconductor alloys, indicating the presence of a miscibility gap in the solid phase for all these alloys. Given the Gibbs free energy of the solid at a particular temperature, eqn. (40) above, the binodal and spinodal phase boundaries can be calculated at that temperature. Alloy compositions located within the spinodal phase boundary are unstable and undergo phase separation by spinodal decomposition—a process with no energy barrier. Compositions located between the binode and spinode are metastable, and undergo phase separation by the kinetically-limited process of nucleation and growth. Compositions outside the binode are completely stable as a homogeneous alloy, at the given temperature. For material that has phase separated, the

resulting compositions at equilibrium of the two different phases are given by the binode, with the relative amounts of each phase determined by the lever rule.

The spinodal phase boundary is determined by setting the second derivatives of the free energy vs. composition curve to zero. Compositions are unstable (i.e. inside the spinodal region) if [99]:

$$\left(\frac{\partial^2 G}{\partial x^2}\right)\left(\frac{\partial^2 G}{\partial y^2}\right)-\left(\frac{\partial^2 G}{\partial x \partial y}\right)<0 \tag{42}$$

The individual second derivatives are given by [99]:

$$\frac{\partial^2 G}{\partial x^2}=N_V\left[\frac{RT}{x(1-x)}-\frac{8.75K\Delta a_A^2}{a_0^{4.5}}\right] \tag{43a}$$

$$\frac{\partial^2 G}{\partial y^2}=N_V\left[\frac{RT}{y(1-y)}-\frac{8.75K\Delta a_C^2}{a_0^{4.5}}\right] \tag{43b}$$

$$\frac{\partial^2 G}{\partial x \partial y}=N_V\left[\frac{2.5KD}{a_0^{3.5}}-\frac{8.75K\Delta a_A \Delta a_C}{a_0^{4.5}}\right] \tag{43c}$$

where N_V is the moles/volume, T is the temperature in Kelvin, and x and y are the compositions for $Ga_{1-x}In_xAs_ySb_{1-y}$. (Note: eqn. (43c) is given incorrectly in ref. [99] - it is missing the first term inside the square brackets.) Additionally,

$$D = a_{InAs} - a_{GaAs} - a_{InSb} + a_{GaSb} \tag{44a}$$

$$\Delta a_A = 0.5*(a_{InSb} - a_{GaSb} + a_{InAs} - a_{GaAs}) + D(y - 0.5) \tag{44b}$$

$$\Delta a_C = 0.5*(a_{GaAs} - a_{GaSb} + a_{InAs} - a_{InSb}) + D(x - 0.5) \tag{44c}$$

By setting eqn. (42) to zero, a spinodal isotherm can be calculated and plotted on a quaternary map, as shown in Fig. 33 (from ref. [93]). In this map, each corner of the

square is a pure binary, each side of the square is a ternary (pseudo-binary), and any point inside the square represents a quaternary alloy composition. Furthermore, all alloy compositions inside a given spinodal isotherm are (theoretically) unstable at the temperature of the isotherm, while all alloy compositions outside the isotherm are metastable or stable at that temperature. The range of unstable compositions decreases as the temperature increases. This is due to the increasing importance of entropy at higher temperatures, which decreases the thermodynamic driving force for phase separation.

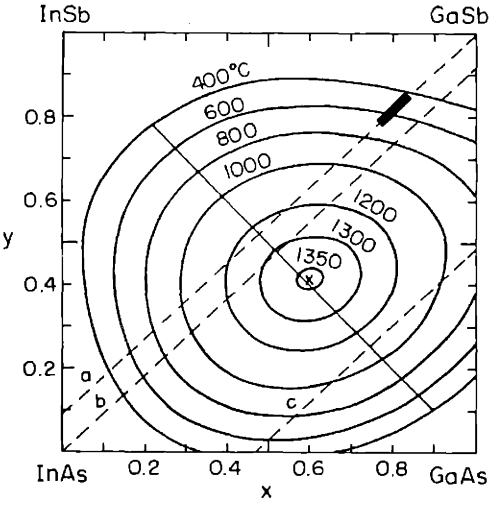

Fig. 33. Spinodal map for GaInAsSb, from ref. [93]. The alloy compositions of interest for TPVs are indicated by the thick black line. These compositions lie in or near a calculated spinodal boundary for growth between 525 and 575 °C.

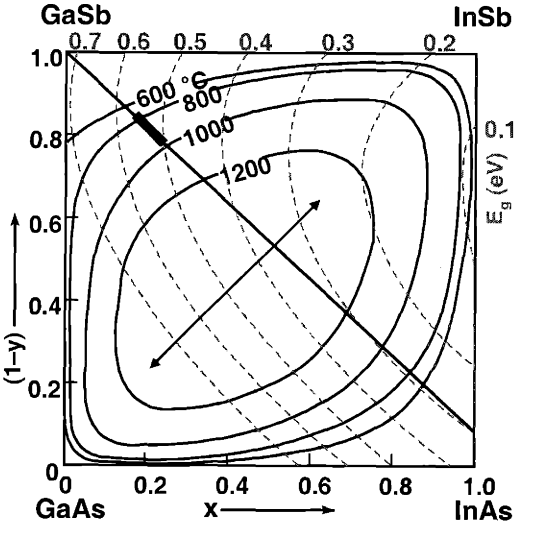

Fig. 34. Binodal map for GaInAsSb, from ref. [92]. The alloy compositions of interest for TPVs lie entirely inside a calculated bulk miscibility gap for growth between 525 and 575 °C. The tie line indicates phase separation into GaAs- and InSb-rich regions.

Figure 34 shows a quaternary map with binodal isotherms (from ref. [92]). The equations to calculate the binodes are more complicated than those for the spinodes and

will not be included here. However, they can be found in ref. [100]. Compositions inside a given binodal isotherm are metastable at that temperature and would be expected to phase separate by nucleation and growth, while compositions outside the isotherm are completely stable at that temperature. Also shown on Fig. 34 are an iso-lattice-constant line indicating GaInAsSb alloy compositions that are lattice-matched to GaSb, and iso-energy-gap lines, indicating the room temperature bandgaps of various alloy compositions. The particular range of alloy compositions of interest for thermophotovoltaic cells are those lattice-matched to GaSb substrates, lying between 0.5 and 0.6 eV. At 0.5 eV, the alloy composition is given approximately by $Ga_{0.80}In_{0.20}As_{0.17}Sb_{0.83}$, while at 0.6 eV the alloy composition is $Ga_{0.90}In_{0.10}As_{0.09}Sb_{0.91}$. These compositions were determined by the equation for the room temperature energy gap of the quaternary alloy [91]:

$$E_g = 0.726 - 0.961x - 0.501y + 0.08xy + 0.415x^2 + 1.2y^2 + 0.021x^2y - 0.62xy^2 \qquad (45a)$$

and the equation required for lattice-matching the quaternary to the GaSb substrate:

$$y = \frac{0.867x}{1 - 0.048x} \qquad (\approx 0.9x, \text{ for small } x) \qquad (45b)$$

These figures indicate that the GaInAsSb alloy compositions of interest for TPV devices tend to lie in metastable or unstable regions that could phase separate at the growth temperature (typically 525-575 °C).

4.1.2 Limitations of above bulk calculations for OMVPE growth

Although the above phase maps for bulk layers serve as useful guides, it is unlikely that they will accurately predict the microstructures of epilayers grown by OMVPE. This is because these maps are calculated using certain assumptions that are not generally valid for OMVPE growth. The primary limitation is that the calculations

are for the thermodynamic equilibrium state. However, OMVPE is a kinetically-limited growth technique [101], and it is therefore unlikely that the resulting microstructure will be that of the equilibrium state. This limitation arises specifically because the above maps implicitly assume that bulk diffusion occurs; however, bulk diffusion rates are negligibly low under typical OMVPE growth temperatures and times. It is generally believed that atoms situated more than 2-3 monolayers below the growing surface are frozen into the bulk; therefore, diffusion only occurs at or very near the growing surface when atoms are first deposited from the vapor. As a result, the microstructure of an epilayer will not generally be the preferred equilibrium for the bulk. Instead, the microstructure will be determined by the thermodynamics of where adatoms prefer to be located on the surface (i.e. randomly situated, ordered, or clustered), and the kinetics that dictate the extent to which the thermodynamic preference is achieved (i.e. growth rate, growth temperature, substrate orientation, etc.)

In addition, the above calculations only take chemical interactions into account. However, strain interactions should also be considered. This is relatively straightforward for bulk samples, but very difficult for epilayers. For bulk samples, Cahn calculated [102-104] that whenever the lattice constant is a function of composition, phase separation creates strain fields in a solid that tend to stabilize the alloy against phase separation because these fields are an energy penalty. The spinodal region calculated without including the effects of strain energy is referred to as the chemical spinodal, while that determined by including strain energy effects is called the coherent spinodal. For bulk samples where bulk diffusion can take place, the effects of strain can easily be included in the model for spinodal decomposition [96]. The calculated coherent spinodal

for a bulk sample always lies entirely within the chemical spinodal because strain energy tends to oppose phase separation in the system and stabilizes the homogenous alloy.

Unfortunately, it is not as straightforward to include the effect of strain on phase separation in an epilayer as it is in a bulk sample. Not only must strain fields between the coherent phases be considered, but the strain of these phases due to lattice-mismatch with the substrate must also be included.[†] An additional complication to including strain effects is that epilayers more effectively relieve strain than bulk samples, due to their free surface. Various theoretical and experimental studies demonstrate that free surfaces can form ripples or undulations to relax strain [106-108]. This capability suggests that strain fields may be less effective at opposing phase separation in epilayers than in bulk samples. Several authors have attempted to calculate phase maps or critical temperatures for epilayers including strain effects [107, 109-112]. However, in almost all cases, these calculations are not directly applicable to OMVPE growth because they are for the equilibrium microstructure, which implicitly requires bulk diffusion.

4.2 Review of literature on TEM studies of epitaxial phase separation

As mentioned in section 4.1.1, the DLP model predicts a miscibility gap for all ternary and quaternary III-V semiconductor alloys. Starting in the late 1970s, numerous research groups conducted detailed investigations of phase separation in various III-V ternaries and quaternaries. These studies relied principally on TEM images of alloy microstructures, although in many cases additional insight was gained from PL, x-ray,

and energy dispersive x-ray (EDX) measurements. TEM was the primary technique used to study phase separation because it provides a direct view of the microstructure of a material. Contrast seen in a TEM image arises from strain fields or chemical modulations in the sample, depending on the 2-beam conditions selected [113]. In addition, the transmission electron diffraction (TED) pattern is sensitive to certain features in a microstructure, such as atomic ordering and stacking faults.

These studies found evidence for phase separation in alloys such as InGaP [114-118], InGaAs [119, 120], AlGaAs [121-123], AlGaN [124], InGaN [125, 126], GaAsN [127], InPSb [128, 129], InAlAs [130-132], InAsSb [133, 134], GaAsSb [134, 135], InGaAsP [105, 136-142], and AlInGaP [143-145]. This section will provide a select review of these studies. This is not a comprehensive review – the literature database of TEM studies of phase separation in III-V ternaries and quaternaries is far too extensive. Instead, the results presented in this section provide a framework with which the TEM results from this thesis, presented in section 4.4, can be compared. In particular, results from the following semiconductor alloys will now be discussed: InGaAsP, InAlAs, InAsSb, and GaAsSb.

4.2.1 InGaAsP

The semiconductor alloy InGaAsP is of great technological importance as the basis for telecommunications devices in the energy range of 1.3 to 1.55 μm. Many research groups studied this material system extensively in the 1980s and 1990s because of strong commercial interest. To study the microstructure of InGaAsP, most groups examined plan-view (PV) and <110>-type cross-section (x-sec) TEM images. Results

---

† This substrate-induced strain has been observed to minimize phase separation, an effect called "lattice-

varied depending on the growth technique used. Furthermore, image interpretation was widely controversial. The major source of controversy is illustrated in Fig. 35. Figure 35(a) shows a PV TEM image from ref. [138] of InGaAsP grown lattice-matched to (001) InP by liquid phase epitaxy (LPE). A fine-scale speckle contrast on the order of 10-15 nm is observed. When the diffraction vector is changed to (040) or (400) (Figs. 35(b) and (c)), it is seen that the fine-scale speckle consists of two modulated structures running along orthogonal <100> directions. A lower magnification image in Fig. 35(d) shows the same layer, but now a "basket-weave" contrast pattern on the order of 150 nm is discernible. Figure 36 shows a typical x-sec TEM image. Notice the strong contrast running parallel to the growth direction (vertical striations). The lateral length scale of this feature is the same as the fine-scale structure seen in Figs. 35(a)-(c).

latching" or "lattice-pulling" [105]. Lattice-latching stabilizes a homogeneous alloy that is lattice-matched to the substrate, opposing a phase-separated alloy with phases lattice-mismatched to the substrate.

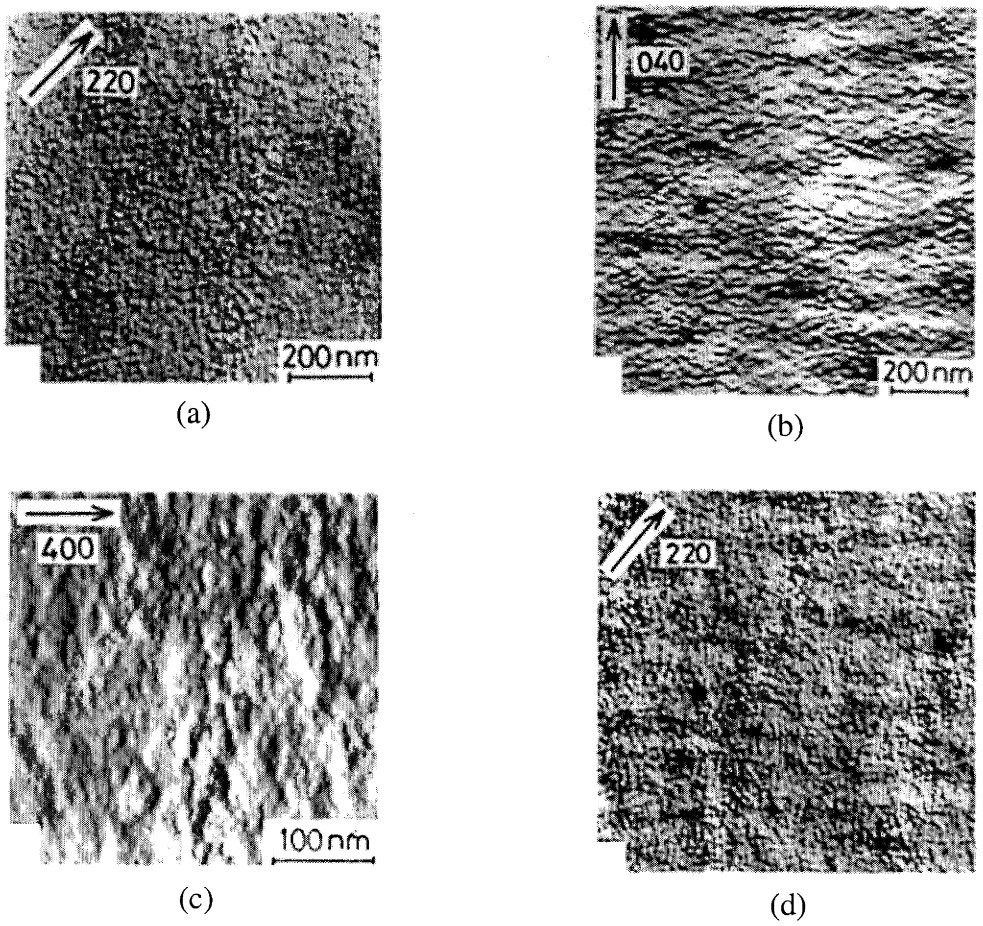

Fig. 35. PV TEM images of InGaAsP, illustrating: (a)-(c) the fine-scale speckle contrast and (d) the coarse-contrast basket-weave pattern. From ref. [138].

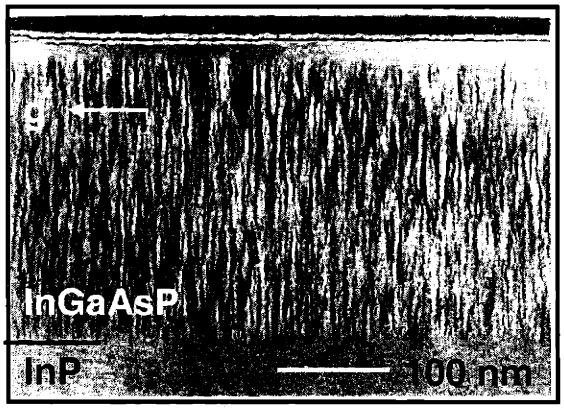

Fig. 36. Cross-section TEM image of InGaAsP, indicating spinodal-like contrast (vertical striations). From ref. [141].

These features were typically seen in all InGaAsP alloys grown by LPE with compositions inside the miscibility gap. The microstructures obtained from growth by MBE or OMVPE were somewhat different. Plan-view TEM images of InGaAsP epilayers grown by MBE exhibited the coarse contrast basket-weave pattern in some cases but not in others. In addition, the fine-scale structure was anisotropic, and it ran along one of the two <110> directions, as shown in Fig. 37 (from ref. [146]). The contrast seen in orthogonal <110> x-sec TEM images for these MBE-grown samples was similar to that shown in Fig. 36, although the lateral length scale of the vertical striations exhibited an anisotropy in agreement with the anisotropy of the features seen in the PV TEM image shown in Fig. 37. This anisotropy is likely due to the anisotropy of dimer reconstructions present on the epilayer surface during MBE growth, which run along a <110> direction and create an anisotropy in surface diffusivity. It is unlikely that such reconstructions are present on the surface during LPE growth; thus, the fine- and coarse-scale structure is instead present along both elastically-soft <100> directions in Figs. 35(a)-(d).

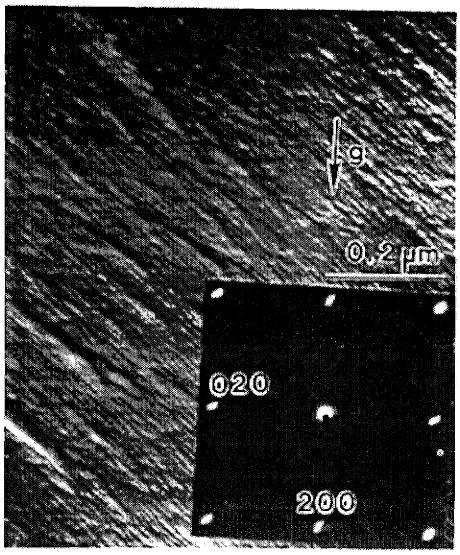

Fig. 37. Plan-view TEM image of MBE-grown InGaAsP, indicating anisotropy of surface features. From ref. [146].

The controversy in the literature surrounded the interpretation and origin of these contrast features. It was generally accepted that the features were somehow related to phase separation in the samples, since these features were only present for alloy compositions grown inside the calculated miscibility gap. In addition, samples with these features exhibited broad FWHM x-ray peaks, indicative of a spread in lattice constants, which would occur in a phase separated alloy. It was also generally accepted that the coarse-contrast basket-weave feature could not be due to bulk phase separation, since bulk diffusivities during epitaxial growth are far too low to achieve composition modulations on the order of 150 nm. The disagreements arose around which length scale seen in the TEM images was associated with a composition modulation, and at what stage the phase separation occurred during growth. Some groups suggested that the

basket-weave feature was due to spinodal decomposition that occurred by surface diffusion during epilayer growth, while the fine-scale contrast was due to phase separation occurring in the bulk during growth or sample cooling. However, another group argued that the fine-scale contrast could not be due to bulk diffusion. They pointed out that phase separation by bulk diffusion should also result in composition modulation along the growth direction, since strain in that direction is easily relaxed by the epilayer. However, x-sec TEM images (i.e. Fig. 36) do not reveal any composition modulation along the growth direction; only in the plane of growth. Therefore, they argued that the fine-scale speckle represented composition modulation occurring by surface spinodal decomposition during epilayer growth, while the basket-weave feature was simply a mechanism by which the thin TEM sample could relieve the strain associated with the fine-scale composition modulation, and therefore an artifact. Glas [147] suggested that the coarse-contrast basket-weave was associated with composition modulation on the order of 1-2 atomic percent (as measured by EDX), while the fine-scale contrast was due to static atomic displacements and random alloy variations.

A comprehensive study by LaPierre *et al.* [141] of MBE-grown material strongly suggested that the fine-scale structure is due to surface spinodal decomposition. The study examined x-sec TEM images of samples grown under different conditions. It was found that the vertical striations associated with the fine-scale speckle (i.e. Fig. 36) increased in contrast as the alloy composition went further into the miscibility gap. In addition, as the growth rate was increased, or growth temperature decreased, the striations decreased in contrast. This is consistent with an increase in the kinetic barrier to surface diffusion. Finally, since the orthogonal <110> directions are equivalent in the

bulk zincblende crystal structure, the only explanation for the anisotropy of these features along <110> directions is the anisotropy of surface reconstructions along the <110>, which implies a surface diffusion mechanism. These results taken together suggest that the fine-scale structure seen in PV TEM, and the vertical striations seen in x-sec TEM, are due to spinodal decomposition of the alloy, occurring at the surface during epitaxial growth. The origin of the basket-weave structure is still unclear, and was not examined by LaPierre *et al.* [141] since this feature was not observed in their material.

4.2.2 InAlAs

InAlAs grown by MBE or OMVPE has been reported to exhibit phase separation. Georgakilas *et al.* [132] grew InAlAs epilayers on InP substrates and found phase separation could be promoted under certain growth conditions. Phase separation took the form of vertical "slabs" in the epilayer, forming a natural lateral "superlattice" or superstructure throughout the epilayer. Plan-view TEM and AFM indicated the presence of surface undulations running along the [01-1] direction. The modulation period along the [011] direction was about 130 nm, while the length along the [01-1] direction was as much as 1 μm. The peak-to-peak height of the undulations was 20-40 nm. An [01-1] x-sec TEM image obtained using <022> 2-beam diffraction conditions indicated a self-organized lateral superlattice with a period also about 130 nm, and running along an angle of about 15° from the surface normal. The x-sec TEM image indicated that the lateral superlattice "slabs" were coupled to the surface undulations, suggesting a coupling of compositional and morphological perturbations. Such a coupling has been discussed theoretically in the literature by various authors.

Cho *et al.* [130] observed the coexistence of phase separation and ordering in InAlAs epilayers grown on InP substrates by OMVPE. Plan-view (Fig. 38(a)) and x-sec (Fig. 38(b)) TEM images indicated similar features to those seen by Georgakilas *et al.*, although on a shorter length scale. Samples grown at 565 °C exhibited composition modulations with a period of 30 nm along the [110], consisting of AlAs-rich (10-13 nm wide) and InAs-rich (15-18 nm wide) regions. Samples grown at 615 °C had a total period along the [110] direction of 50 nm, with widths of 14 and 40 nm for the AlAs- and InAs-rich regions, respectively. Samples grown at 700 °C, above the calculated critical temperature for phase separation, exhibited no such modulations. Furthermore, they found that by annealing the sample grown at 565 °C at 880 °C for 3 min the ordering was completely eliminated, but the phase separation remained.

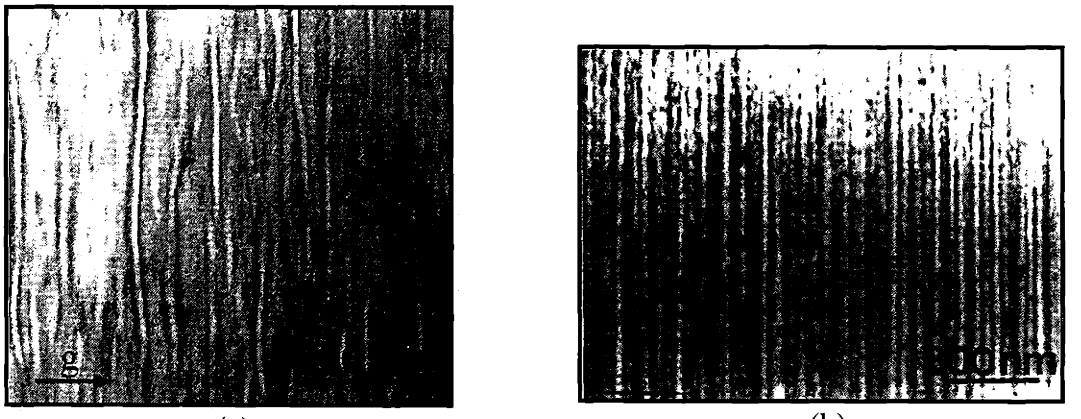

(a) (b)

Fig. 38. (a) Plan-view and (b) x-sec TEM images of InAlAs, indicating lateral phase separation throughout the epilayer. Images are from ref. [130].

Grenet *et al.* [131] studied InAlAs grown on InP by MBE at 450 °C. Since this temperature is below that reported in ref. [132] as necessary to form the natural-lateral-

superlattice phase separation, it is not surprising that Grenet only observed a fine-scale surface-spinodal-like decomposition. Interestingly, the spinodal decomposition exhibited a strong anisotropy similar to that observed above for MBE-grown InGaAsP. Both PV TEM and scanning tunneling microscopy (STM) images indicated that the spinodal decomposition had a period of 2 nm along the [110] direction and 30-50 nm along the [1-10] direction. This anisotropy is likely due to surface dimers, as with InGaAsP discussed above.

4.2.3 InAsSb

Ferguson *et al.* [133] and Norman *et al.* [134] reported that $InAs_{0.5}Sb_{0.5}$ grown on GaAs by MBE phase separated to form a natural strained-layer vertical superlattice along the [001] growth direction. A x-sec TEM image shown in Fig. 39(a) illustrates such a superlattice for a layer grown at 340 °C. Although equal fluxes of As_4 and Sb_4 were provided throughout growth of the entire epilayer, the layer phase separated to form InAs- and InSb-rich regions, with a period of 57 nm along the [001] growth direction. These platelets had lateral dimensions of 250 nm along the [110] direction and 600 nm along the [1-10] direction, exhibiting an anisotropy similar to InGaAsP and InAlAs. The <110> x-sec TED pattern of the sample (not shown) indicated that the higher order spots were split into two in the [001] direction, but not in the <110> directions. This indicated the presence of two different lattice constants perpendicular to the layer surface, but not parallel to the layer surface. The lattice constants perpendicular to the layer surface were 6.11 and 6.40 Å, corresponding to phases of $InAs_{0.69}Sb_{0.31}$ and $InAs_{0.33}Sb_{0.67}$, respectively (based on Vegard's Law). The in-plane lattice constant was 6.28 Å, corresponding to the

average alloy composition of $InAs_{0.5}Sb_{0.5}$. Microtwins and stacking faults were observed to originate and terminate at the platelet interfaces.

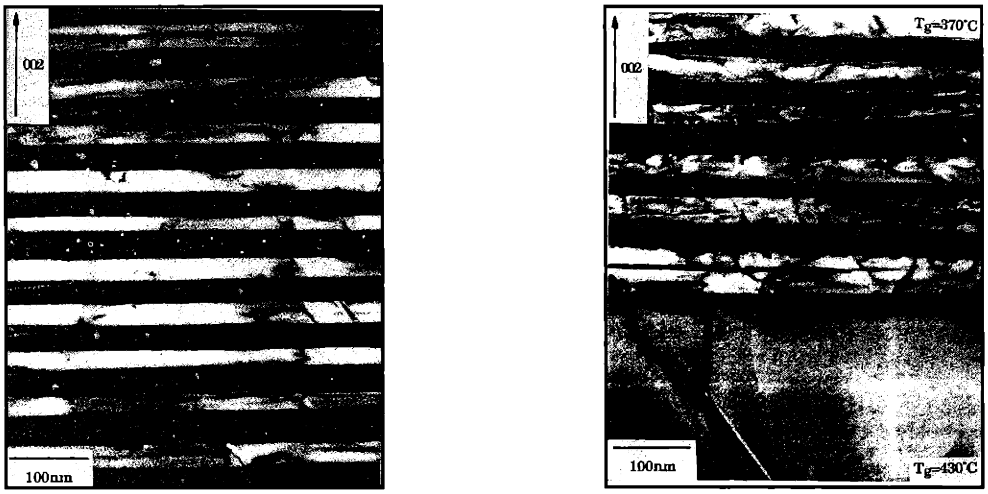

Fig. 39. X-sec TEM images of InAsSb grown at (a) 340 °C, and (b) 430 °C followed by 370 °C. Below a critical temperature, the InAsSb epilayers phase separated to form a natural vertical strained-layer superlattice in the growth direction. Images are from ref. [133].

As the growth temperature was increased, the platelet size increased, getting as large as 900 nm in the [110] direction, 2600 nm in the [1-10] direction, and 50 nm along the [001] direction (period = 100 nm) for a growth temperature of 400 °C. Figure 39(b) shows a x-sec TEM image of an $InAs_{0.5}Sb_{0.5}$ layer grown at 370 °C on top of an $InAs_{0.5}Sb_{0.5}$ layer grown at 430 °C. There are three interesting features in this image. First, the platelets that formed during growth at 370 °C are not as sharp or well-defined as those grown at 340 °C, shown in Fig 39(a). Norman *et al.* [134] subsequently found that the sharpness of the platelets could be increased by reducing the As_4 flux. Second, the platelets were completely eliminated for growth at 430 °C, and the layer appeared

homogeneous. Third, the image proves that the phase separation to form the platelets occurred at the growing surface, and not by bulk diffusion. If the platelets were formed by bulk diffusion, then the homogeneous layer grown at 430 °C should have phase separated to form platelets while the 370 °C layer was grown. That the 430 °C layer remained homogeneous indicates that the platelet formation must have occurred at the growing surface, and not by bulk diffusion. In addition, the anisotropy of the platelets in the lateral direction again suggests a surface diffusion mechanism, and not bulk diffusion, since <110> diffusivities are only anisotropic at the growth surface (due to surface dimers).

4.2.4 GaAsSb

Norman *et al.* [134] also studied $GaAs_{0.5}Sb_{0.5}$ grown on GaAs by MBE, and found that at temperatures below 500 °C it formed platelets similar to those observed for $InAs_{0.5}Sb_{0.5}$. However, the lateral size and thickness of the platelets formed in $GaAs_{0.5}Sb_{0.5}$ was much smaller than for $InAs_{0.5}Sb_{0.5}$, and the morphology was much less regular. For both the $InAs_{0.5}Sb_{0.5}$ and the $GaAs_{0.5}Sb_{0.5}$ epilayers, Norman *et al.* suggested that the phase separation may have been caused by the immiscibility of the As and Sb atoms on the growing surface, due to the miscibility gap expected at low temperatures in the As-Sb binary phase diagram.

4.3 Previous characterization studies of GaInAsSb

The discussion in section 4.1.2 illustrated the difficulties involved with accurately modeling miscibility gaps for epitaxially-grown semiconductors. However, the phase maps calculated for bulk material can be used as rough guidelines. In particular, three results of the calculations for GaInAsSb are of interest. First, since the GaSb substrate

melts at 712 °C [148], GaInAsSb epilayers cannot be grown at temperatures above the critical temperature for phase separation. Therefore, it is expected that a thermodynamic driving force for phase separation of GaInAsSb will exist during epitaxial growth. Second, as the concentrations of indium and arsenic in the GaInAsSb alloy are increased, the alloy composition goes further into the miscibility gap. Therefore, the driving force for phase separation is increased. Finally, if the GaInAsSb alloy does phase separate, it is predicted to form GaAs- and InSb-rich phases. The equilibrium microstructure for GaInAsSb alloy compositions of interest for TPV devices consists of approximately a 7:1 volume ratio of a phase slightly enriched in InSb and a phase strongly enriched in GaAs [149].

The major question that is not addressed by the phase maps is how the kinetic limitations of OMVPE growth affect the thermodynamic driving force for phase separation. Comprehensive PL, x-ray, and AFM studies by Wang [76, 150-157] conducted before and during this thesis examined the extent to which phase separation can be inhibited by varying kinetic growth parameters (such as growth temperature, growth rate, and substrate orientation). These results demonstrated the tremendous importance of growth kinetics on the extent of phase separation, and are briefly reviewed in section 4.3.1. Additional characterization results from previous studies using EDX and TEM are given in sections 4.3.2 and 4.3.3. The microstructure results obtained by TEM for this thesis are given in section 4.4, and provide great insight into the characterization results presented in this section.

4.3.1 Indirect observations of phase separation

4.3.1.1 Effect of alloy composition

Alloy composition will affect the extent of phase separation because it determines the thermodynamic driving force for phase separation. However, choice of alloy composition is usually fixed by device requirements for lattice constant and bandgap; therefore, there is not much flexibility in this parameter. Nonetheless, it is of interest to examine how the alloy properties change when the composition is varied. For TPVs, the room temperature bandgap of interest lies between 2.1 and 2.5 μm (0.59 to 0.50 eV). For alloys lattice-matched to GaSb, this results in compositions of $Ga_{0.89}In_{0.11}As_{0.09}Sb_{0.91}$ to $Ga_{0.8}In_{0.2}As_{0.18}Sb_{0.82}$ (see section 4.1.1). As the indium and arsenic contents are increased, the bandgap is decreased, and the thermodynamic driving force for phase separation is increased.

Figure 40(a) shows the 300 K and 4 K PL for $Ga_{0.88}In_{0.12}As_{0.1}Sb_{0.9}$ grown at 575 °C, on a GaSb substrate oriented (001) 2° toward (101). The 4 K full-width at half-maximum (FWHM) is about 11 meV. This narrow FWHM is indicative of a high-quality epilayer. Furthermore, the energy difference between the 4 K and 300 K PL is 71 meV, close to the expected difference of 74 meV from the Varshni equation. Figure 40(b) shows the 300 K and 4 K PL for $Ga_{0.86}In_{0.14}As_{0.12}Sb_{0.88}$, also grown at 575 °C and lattice-matched to a GaSb substrate oriented (001) 2° toward (101). The 4 K FWHM is extremely broad in this sample. This suggests an inhomogeneous alloy, with a range of compositions and associated bandgaps. In addition, the 4 K PL peak is red-shifted (i.e. at lower energy) compared to the 300 K PL peak, completely opposite to what is expected based on the energy band shift with temperature. This anomaly can also be explained by phase separation.

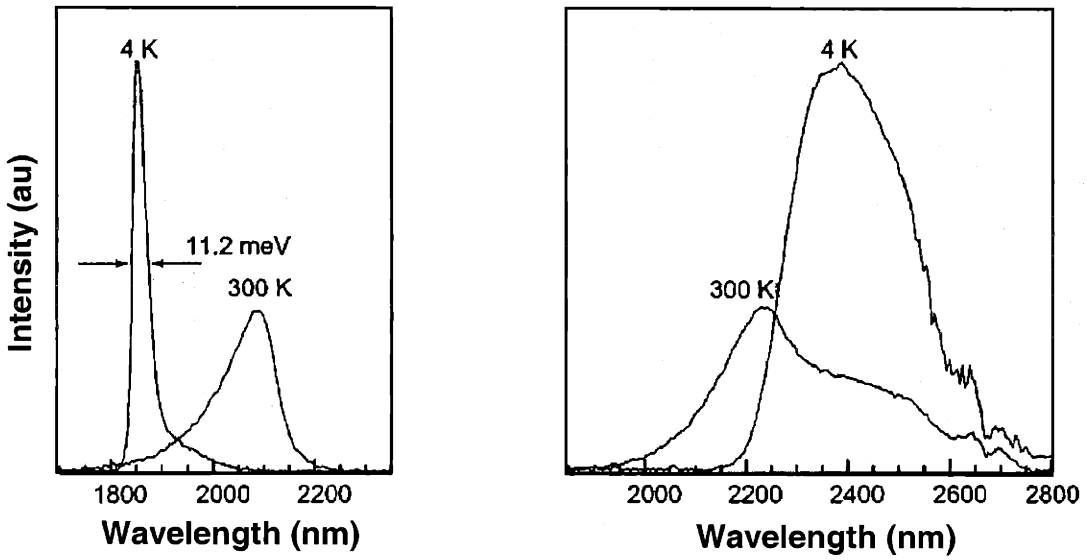

Fig. 40. 300 K and 4 K PL for: (a) $Ga_{0.88}In_{0.12}As_{0.1}Sb_{0.9}$ and (b) $Ga_{0.86}In_{0.14}As_{0.12}Sb_{0.88}$ alloys grown at 575 °C on substrates oriented (001) 2° toward (101). The PL FWHM is significantly broadened for the alloy further in the miscibility gap. From ref. [155].

Phase separation will also affect surface morphology. AFM images of the two samples discussed above are shown in Figs. 41(a) and (b). Notice that the low-indium-composition sample (Fig. 41(a)) exhibits a uniform, high-quality surface morphology. In contrast, the high-indium-composition sample, Fig. 41(b), displays a non-uniform morphology, with trenches running along the [-110] direction. This morphology is indicative of phase separation, and is discussed in more detail in section 4.3.2 below.

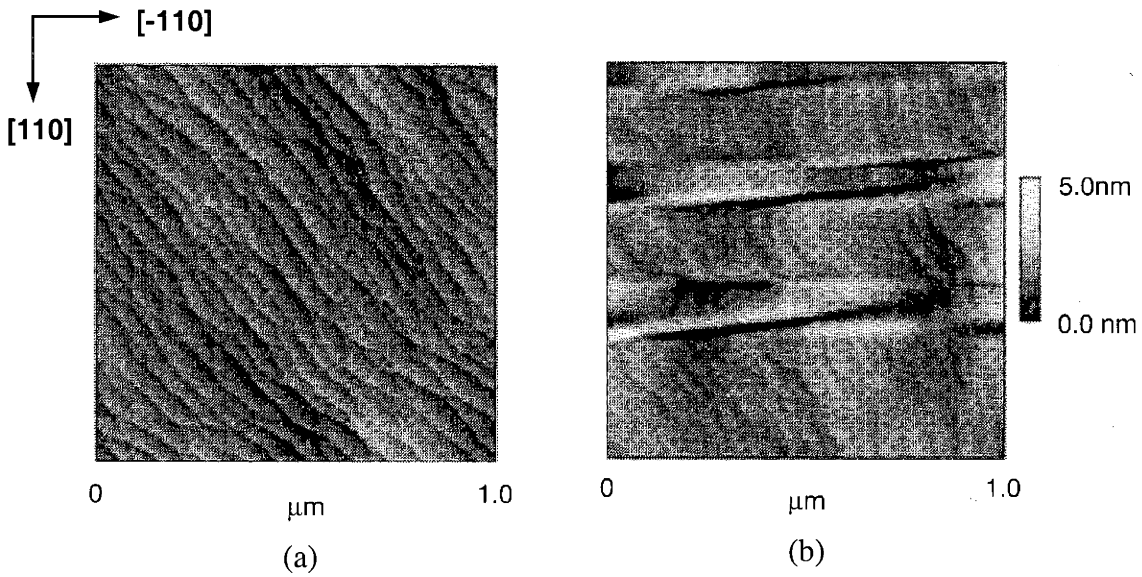

Fig. 41. AFM images of: (a) $Ga_{0.88}In_{0.12}As_{0.1}Sb_{0.9}$ and (b) $Ga_{0.86}In_{0.14}As_{0.12}Sb_{0.88}$ alloys grown at 575 °C on substrates oriented (001) 2° toward (101). The surface morphology of the sample further in the miscibility gap, (b), broke down due to phase separation. From ref. [156].

4.3.1.2 Effect of growth temperature

For a given alloy composition, the growth temperature affects both the thermodynamics and kinetics of phase separation. As the growth temperature is increased, the thermodynamic driving force for phase separation is decreased. However, the kinetics for phase separation are more favorable at higher growth temperatures, since diffusion rates are higher. Experimental results suggest that in epitaxial growth, kinetic factors are more important than thermodynamic ones; therefore, as the growth temperature is increased, the extent of phase separation is increased. This is demonstrated by the fact that regardless of which alloy composition or substrate orientation is chosen, the 4 K PL FWHM is always larger for GaInAsSb samples grown at 575 °C than at 525 °C, all other variables held constant [155, 156]. In addition, AFM images indicate that the surface morphology is more uniform and regular for samples

grown at the lower temperature. These experimental observations suggest that phase separation can be inhibited by growing the alloy at lower temperatures, which strongly underscores the importance of kinetic barriers in the kinetically-limited OMVPE growth technique.

4.3.1.3 Effect of growth rate

Wang [156] has seen that at all growth temperatures, alloy compositions, and substrate orientations, as the growth rate increases, the 4 K PL FWHM becomes narrower. This is seen in Fig. 42. The growth rate does not affect the thermodynamic driving force for phase separation. However, it greatly affects the kinetic limitations of this process. Since all diffusion during epitaxial growth is confined to the growth surface, as the growth rate is increased, the effective diffusion length (or adatom lifetime) is decreased. Each atom has less time to diffuse before the next monolayer is deposited as the growth rate is increased. These results therefore indicate the importance of kinetic effects and surface diffusion on the extent of phase separation: by using a higher growth rate, phase separation is inhibited due to kinetic limitations.

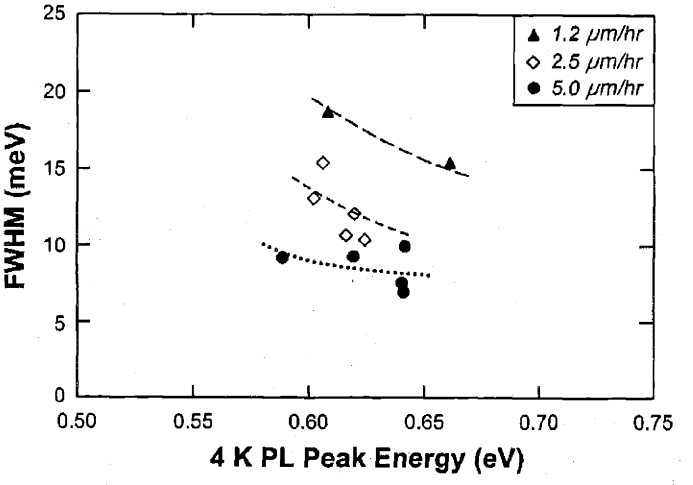

Fig. 42. 4 K PL FWHM values versus alloy composition and growth rate. Notice that as the growth rate is increased, the 4 K PL FWHM decreases, indicating the importance of kinetic barriers on limiting phase separation. From ref. [156].

4.3.1.4 Effect of substrate orientation

The choice of substrate orientation plays a major role in the extent of phase separation. For substrates that are not exactly on-orientation (e.g. (001)), both the angle and the direction of the miscut are important. When a substrate is miscut, the resulting surface has a periodic array of steps. Under the proper conditions, growth proceeds in a "step-flow" fashion, wherein all surface adatoms incorporate only at step edges, and not on terraces [101]. Step-flow growth is often desired because of the resulting high-quality surface morphology. More detail on step-flow growth is given in section 4.4.3.1.

As the angle of the miscut is increased, the density of steps increases. For step-flow growth, this decreases the adatom lifetime—the time it takes a physi- or chemisorbed atom to bond to the crystal. This should decrease the extent of phase separation, serving as a similar kinetic barrier to increasing the growth rate. The direction of the miscut is even more important. Substrates that are initially oriented (001)

can be miscut toward the (101), the (-1-11)A, or the (1-11)B direction, as shown in Fig. 43. The chemistry and bonding present on the resulting terraces and step edges is different for each direction [101]. This affects the kinetics of adatom incorporation, which affects the adatom lifetime and therefore also the extent of phase separation.

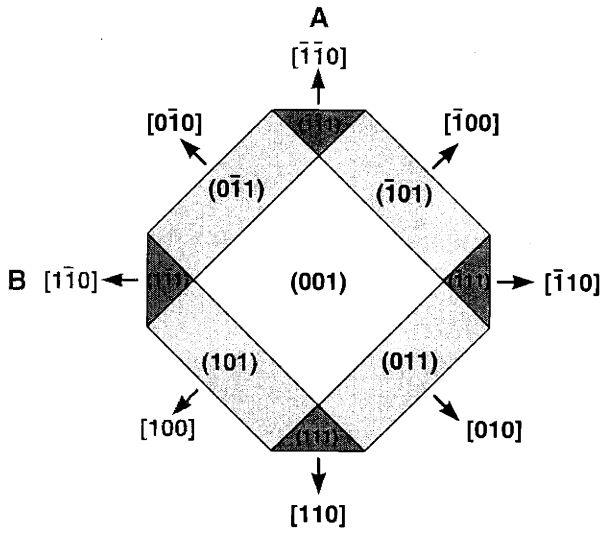

Fig. 43. Schematic illustration of the crystallographic directions for an (001)-oriented substrate. The nominally (001)-oriented boule can be intentionally miscut toward the (101), (-1-11)A, or (1-11)B plane to yield a series of evenly-spaced atomic height steps on the growth surface.

Photoluminescence, x-ray, and atomic force microscopy results from Wang all confirm that for a given miscut direction, as the angle of the miscut is increased from 2 to 6°, the homogeneity of the GaInAsSb epilayer improves. The higher the step density, the larger the kinetic barrier to the thermodynamic driving force for phase separation. For example, $Ga_{0.9}In_{0.1}As_{0.09}Sb_{0.91}$ grown at 575 °C on a substrate oriented (001) 2° toward (101) had a 4K PL FWHM of 9.3 meV, which decreased to 5.8 meV for growth on a substrate miscut 6° toward (101). Interestingly, the miscut direction is even more

important than the angle. For a given alloy composition, growth temperature, growth rate, and miscut angle, epilayers grown on GaSb substrates oriented toward the (1-11)B direction exhibit the highest uniformity, while those grown on substrates oriented toward the (101) display the least homogeneity. For example, $Ga_{0.84}In_{0.16}As_{0.14}Sb_{0.86}$ grown at 575 °C on a substrate oriented (001) 2° toward (101) had a 4 K PL FWHM of 42.0 meV. $Ga_{0.81}In_{0.19}As_{0.17}Sb_{0.83}$ grown at 575 °C on a substrate oriented (001) 2° toward (1-11)B had a far narrower 4 K PL FWHM of 13.6 meV, even though it was further into the miscibility gap.

The dramatic improvement seen in the PL FWHM simply by changing the substrate orientation strongly illustrates the importance of surface kinetics in OMVPE growth. By changing the surface morphology and chemistry through the miscut angle and direction, the bulk thermodynamics are unaffected, yet the resulting alloy properties are quite different. It is apparent from these results that adatoms preferentially incorporate at (1-11)B step edges. (1-11)B step edges therefore impose the greatest kinetic limitation to the thermodynamic driving force for phase separation. As a result, epilayers grown on substrates oriented (001) 6° toward (1-11)B exhibit the highest homogeneity and quality, while those grown on substrates oriented (001) 2° toward (101) exhibit the least homogeneity (most phase separation).

4.3.2 Direct observation of phase separation

The material characterization presented in sections 4.3.1.1-4.3.1.4 provided indirect evidence of phase separation in GaInAsSb. To summarize, as the extent of phase separation increased, the following effects were observed by Wang:

- An increase in the 4 K PL FWHM
- A decrease in the energy difference between the 4 K and 300 K PL peak wavelengths
- Increased epilayer broadening in reciprocal space x-ray maps due to tilt and strain (mosaicity)
- A decrease in surface regularity/morphology seen in AFM images

These results all suggest a range of lattice constants and bandgaps throughout the epilayer, which indirectly points to a range of alloy compositions due to phase separation.

Direct evidence of phase separation in GaInAsSb was seen using EDX analysis [154] on a sample similar to that shown in Fig. 41(b) above. Results indicated that two phases were present. One phase was slightly enriched in GaAs, on the order of a few atomic percent. The other phase was slightly enriched in InSb. Note that thermodynamic calculations discussed in section 4.1 predict phase separation into GaAs- and InSb-rich phases, in agreement with the experimental observation. The GaAs-rich phase was found to lie in the surface trench features seen in the AFM image. This is in agreement with theoretical models [158-161] of the coupling of compositional and morphological perturbations that calculate that surface strain is most effectively relieved if the smaller-lattice-constant phase lies in surface valleys, while the larger-lattice-constant phase lies in surface peaks.

4.3.3 Previous TEM studies

In collaboration with Wang, Chen *et al.* [162] used TEM to characterize GaInAsSb samples grown by Wang. For $Ga_{0.8}In_{0.2}As_{0.18}Sb_{0.82}$ grown at 525 °C on a GaSb substrate oriented (001) 6° toward (1-11)B, Chen *et al.* observed spinodal-decomposition-like contrast in [110] and [1-10] x-sec TEM images using <220> 2-beam diffraction conditions. This contrast was similar to that observed in InGaAsP samples discussed in section 4.2.1 above. Similar results were seen by Kaspi *et al.* [163].

When Chen *et al.* used <111> or <222> 2-beam conditions, a natural vertical superlattice was observed throughout the epilayer, with a period of approximately 20 nm. For the [110] x-sec image, the superlattice was tilted 10° with respect to the surface normal, as shown in Fig. 44(a). In the [1-10] x-sec image, the superlattice appeared parallel to the surface normal, also seen in Fig. 44(a). A schematic diagram of the microstructure is shown in Fig. 44(b). Interestingly, the superlattice was oriented 10° off the surface normal, even though the substrate miscut angle was only 6° off the surface normal.

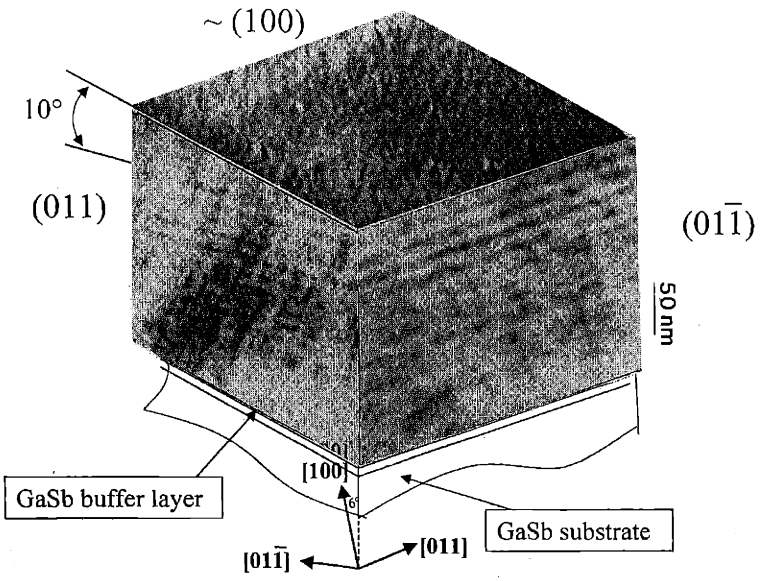

(a)

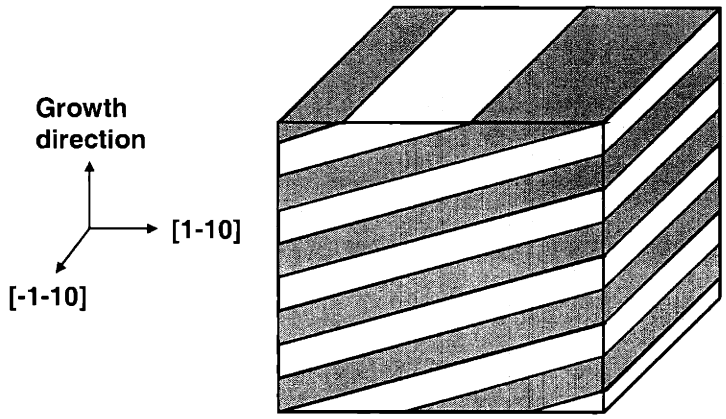

(b)

Fig. 44. X-sec TEM images from ref. [162] illustrating the tilted natural superlattice in GaInAsSb for (a) <110> and <1-10> cross-sections and (100) plan-view. A schematic diagram of the microstructure is shown in (b).

This "tilted"[†] natural vertical superlattice was initially observed by Wang using field-emission scanning electron microscopy (FE-SEM), prior to the TEM investigation [164]. Figure 45(a) shows a [110] x-sec FE-SEM image of the sample shown in Fig. 44(a). The sample received a brief stain etch before imaging in the FE-SEM. The tilted superlattice is clearly observed throughout the epilayer, with a period of 20 nm and a tilt angle of 10°. The orthogonal x-sec image (not shown here) displayed a parallel superlattice, identical to that shown in Fig. 44(a) above.

[†] Note that the atomic planes associated with this superlattice are not physically or crystallographically tilted with respect to the substrate. The word "tilted" refers to the fact that the propagation of the superlattice (with respect to the surface normal; i.e., growth direction) occurred at a larger angle than the propagation of the surface steps. In this particular case, the additional tilt angle was 10°-6° = 4°.

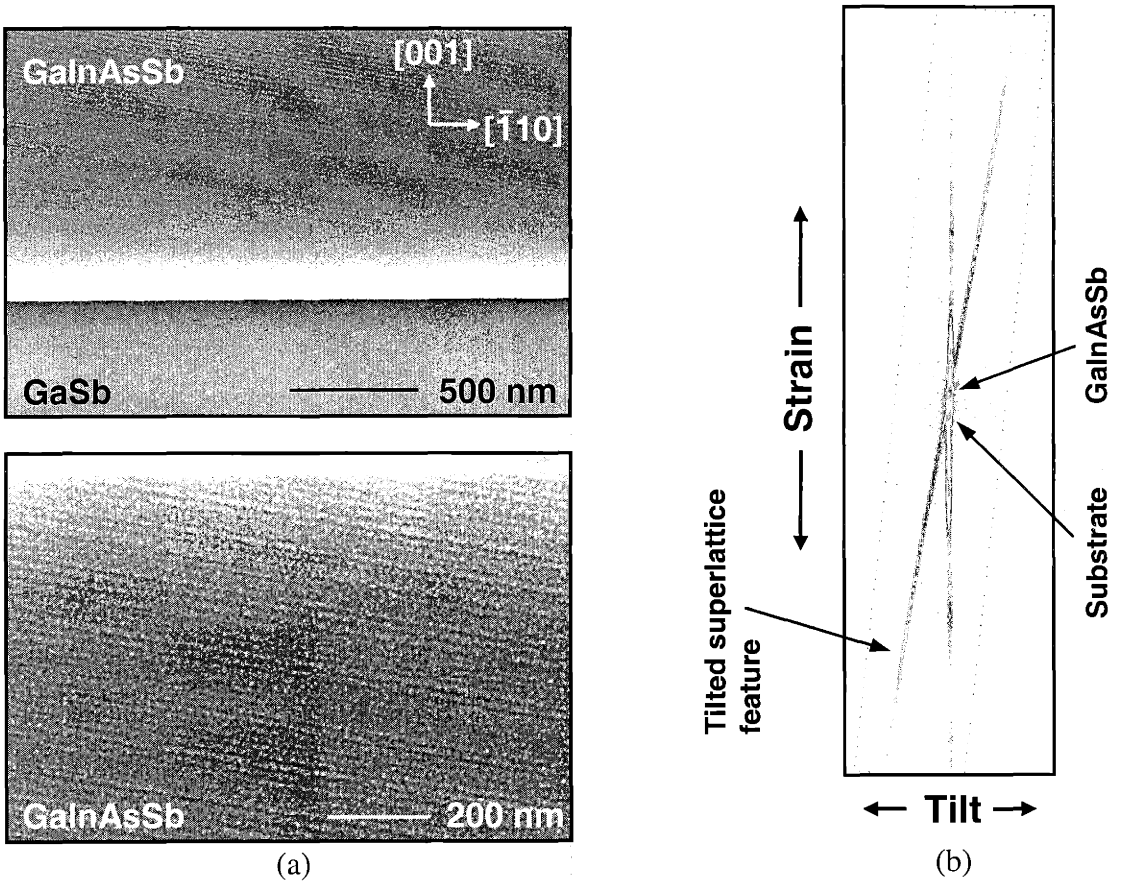

Fig. 45. (a) X-sec FE-SEM image of the tilted superlattice (upper panel shows substrate and GaInAsSb epilayer, lower panel shows only GaInAsSb at a higher magnification). (b) Reciprocal space x-ray map indicating the presence of the tilted superlattice.

The tilted superlattice was also observed by Wang using reciprocal space x-ray mapping [164]. Figure 45(b) shows a RSXRM of the sample discussed above. The vertical axis indicates strain, while the horizontal axis indicates epilayer tilt. A striation is clearly observed running through the epilayer peak in the plot, at an angle of 10° with respect to the diffraction intensity running along the vertical (strain) axis. If the period of the superlattice were perfectly well-defined, with no variation, then that striation would be replaced with well-defined spots or peaks in the RSXRM, at the reciprocal space

locations corresponding to the superlattice period. However, since there was some variation in the period, the spots were smeared out to form a striation, indicating a range of periods. It should be noted that the appearance of the relative intensities in the RSXRM image is somewhat misleading (since the image has not been reproduced as a color plot). Although it appears that the diffraction intensity associated with the tilted superlattice is very strong, in fact it is some 3 orders of magnitude less than the diffraction intensity from the epilayer peak itself. This indicates that the microstructural feature associated with the tilted superlattice does not have a large amplitude.

Since this superlattice feature was detectable by TEM, FE-SEM (after a brief stain etch), and RSXRM, it was clearly not an artifact of one particular sample preparation or characterization technique. It is in fact a real feature in the microstructure, and is likely a composition modulation in the GaInAsSb epilayer. There are very few reported observations in the epitaxial literature of phase separation in the form of self-organized vertical superlattices [114, 122, 133, 134, 165, 166], particularly superlattices with an additional tilt angle with respect to the substrate miscut [121, 144, 162]. In addition, a composition modulation that self-organizes to form a natural superlattice throughout the epilayer will clearly impact device properties, such as dark current, open-circuit voltage, and minority carrier lifetime. Therefore, it was decided to further investigate the natural superlattice formation in GaInAsSb as part of this thesis. These results are presented in section 4.4.3 below.

4.4 TEM study of phase separation in GaInAsSb

4.4.1 Microstructure results from this thesis

The PL, AFM, and x-ray results obtained by Wang and presented in the previous section indicated a range of homogeneity for GaInAsSb epilayers grown under different conditions. To gain insight into this range of characterization results, TEM (JEOL, Model 200CX, 200 kV) was used to study the microstructures of various GaInAsSb epilayers. Specifically, this thesis studied the effects of alloy composition, substrate miscut direction, substrate miscut angle, and growth temperature on the GaInAsSb microstructure. In some cases, AFM was used to correlate the microstructure with the surface morphology. The results are presented in this section and discussed in the next section. Note that all GaInAsSb epilayers were grown lattice-matched to the GaSb substrate. Table III lists the samples presented in this section. Unless otherwise specified, all TEM images presented in this section were obtained using a $\mathbf{g} = \langle 220 \rangle$ 2-beam diffraction condition. The TEM specimen preparation procedure is discussed in Appendix A.

Table III. List of GaInAsSb Samples					
Sample #	**Run #**	**Growth Temp**	**300 K PL Peak Wavelength**	**Substrate Miscut Angle**	**Substrate Miscut Direction**
1	98-873	525 °C	2.090 μm	6°	(1-11)B
2	98-874	525	2.485	6°	(1-11)B
3	99-51B	575	2.082	6°	(1-11)B
4	98-967B	575	2.314	6°	(1-11)B
5	99-55A	575	2.088	2°	(1-11)B
6	00-216	575	2.441	2°	(1-11)B
7	99-54A	575	2.080	2°	(-1-11)A
8	99-63A	575	2.291	2°	(-1-11)A
9	00-211	575	2.444	2°	(-1-11)A
10	99-54B	575	2.088	2°	(101)
11	98-952	575	2.235	2°	(101)
12	00-217	575	2.450	2°	(101)
13	99-56B	575	2.076	4°	(1-11)B
14	99-63B	575	2.260	6°	(101)

4.4.1.1 Effect of alloy composition on GaInAsSb microstructure

Five different comparisons studying the effect of GaInAsSb alloy composition on its microstructure are presented in this section. In each case, all other variables were held constant.

Figures 46(a) and (b) compare two samples grown at 525 °C on substrates oriented (001) 6° toward (1-11)B. Both TEM micrographs are bright-field (BF), <110> x-sec images, oriented so that the growth direction ((001) 6° toward (1-11)B) is straight up (indicated by '6°B' in the image). The sample in Fig. 46(a) had a room temperature (RT) PL peak at 2.09 μm, while that in 46(b) had a peak at 2.485 μm. Since the PL peak shifts to longer wavelength (lower energy) as the InAs content in the GaInAsSb alloy increases, the sample in Fig. 46(b) was further in the miscibility gap than that in 46 (a) (see Figs. 33 and 34). Whereas there is minimal TEM diffraction contrast in the GaInAsSb epilayer at the shorter PL wavelength, the sample further in the miscibility gap

exhibits vertical striations similar to those shown in Fig. 36. The sample shown in Fig. 46(a) was grown under conditions that yield the highest-quality GaInAsSb epilayers, and exhibited the most homogeneous microstructure of all the samples studied in this thesis. The 4 K PL FWHM of this sample was 4.3 meV. The sample in Fig. 46(b) also had a narrow 4 K PL FWHM of 9.5 meV, despite the inhomogeneity of the microstructure.

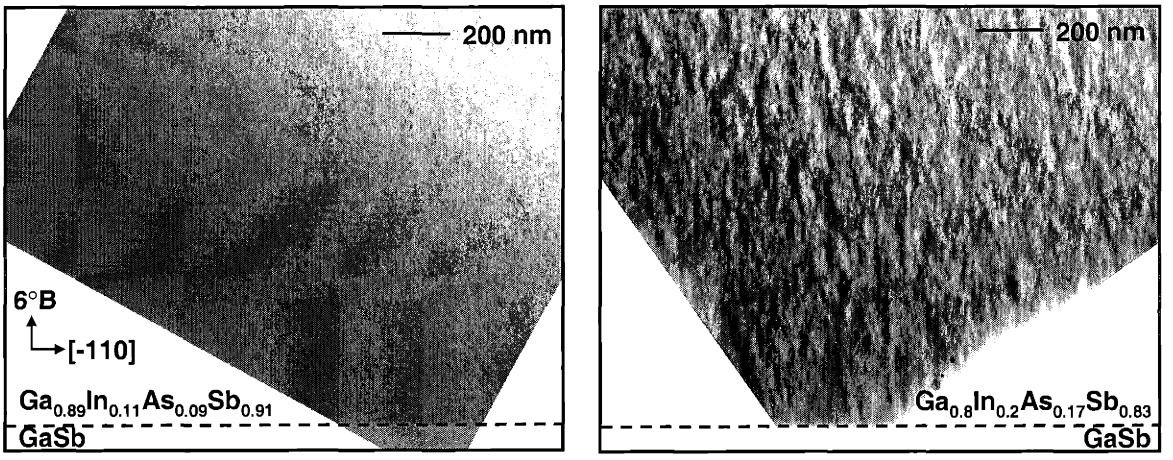

(a) (b)

Fig. 46. Bright field <110> x-sec TEM images of GaInAsSb grown at 525 °C on substrates oriented (001) 6° toward (1-11)B. The images are oriented so that the growth direction is straight up. The sample in (b) had a composition that was further into the miscibility gap than that in (a), and exhibited stronger spinodal-like contrast.

Two samples grown at 575 °C on substrates oriented (001) 6° toward (1-11)B are compared in Fig. 47. The micrographs are dark-field (DF), <110> x-secs. The sample in (a) had a RT PL peak at 2.082 μm, while that in (b) had a peak at 2.314 μm. Similar to the previous comparison, as the alloy composition went further into the miscibility gap the vertical striation contrast increased, although the difference was less dramatic in this case.

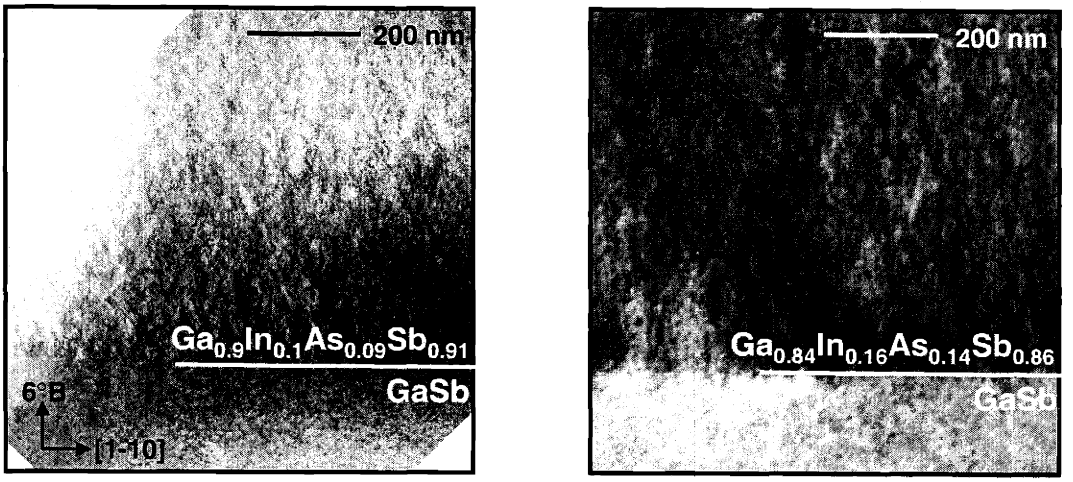

Fig. 47. Dark field <110> x-sec TEM images of GaInAsSb grown at 575 °C on substrates oriented (001) 6° toward (1-11)B. The sample in (b) was further into the miscibility gap than that in (a) and exhibited slightly stronger contrast.

Figure 48 compares two DF <110> x-sec images for samples grown at 575 °C on substrates oriented (001) 2° toward (1-11)B. The sample in Fig. 48(a) had a 300 K PL peak at 2.09 μm, while that in 48(b) had a peak at 2.44 μm. The sample further into the miscibility gap, shown in Fig. 48(b), exhibited stronger spinodal-decomposition-like contrast. There was not a dramatic difference between these two samples, since the (1-11)B step edge is very effective at incorporating adatoms. This is even more evident after comparing this example with the next two examples, which are for substrates oriented toward the (-1-11)A and (101).

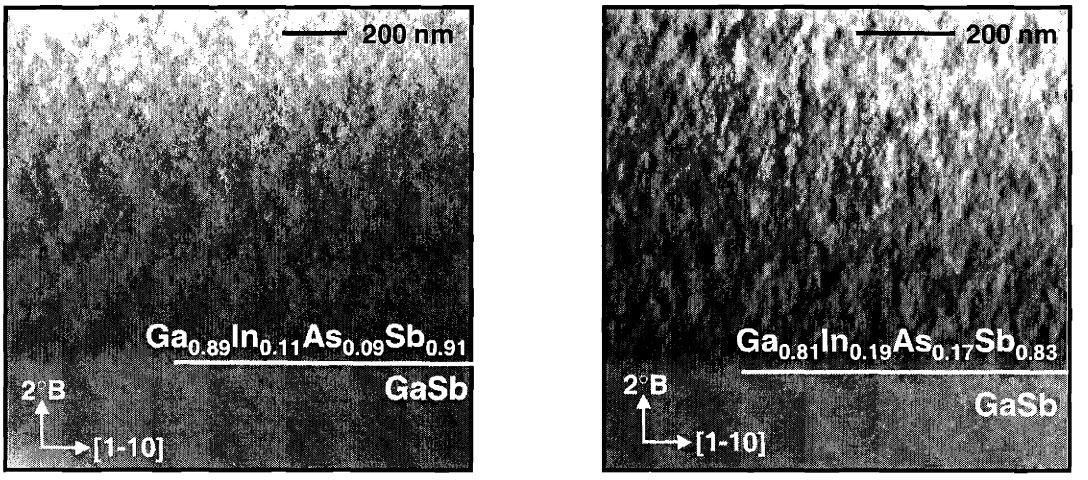

Fig. 48. Dark field <110> x-sec TEM images of GaInAsSb grown at 575 °C on substrates oriented (001) 2° toward (1-11)B. The sample in (b) was further into the miscibility gap than that in (a) and exhibited stronger spinodal-like contrast.

A comparison of samples grown at 575 °C on substrates oriented (001) 2° toward (-1-11)A is displayed in Fig. 49. These images are dark-field (DF), <1-10> x-secs. The samples in (a), (b), and (c) had RT PL peaks at 2.08 μm, 2.3 μm, and 2.45 μm, respectively. Again, as the alloy composition went further into the miscibility gap (from (a) to (c)), the GaInAsSb epilayer increasingly exhibited contrast in the form of vertical striations. The striations became stronger in contrast and larger in lateral length scale as the alloy went further into the miscibility gap. Higher magnification images of the samples shown in (b) and (c) are presented in (d) and (e), respectively. The striations formed immediately at the start of epilayer growth. Note that the striation contrast was stronger for these samples than for those shown in Figs. 46-48.

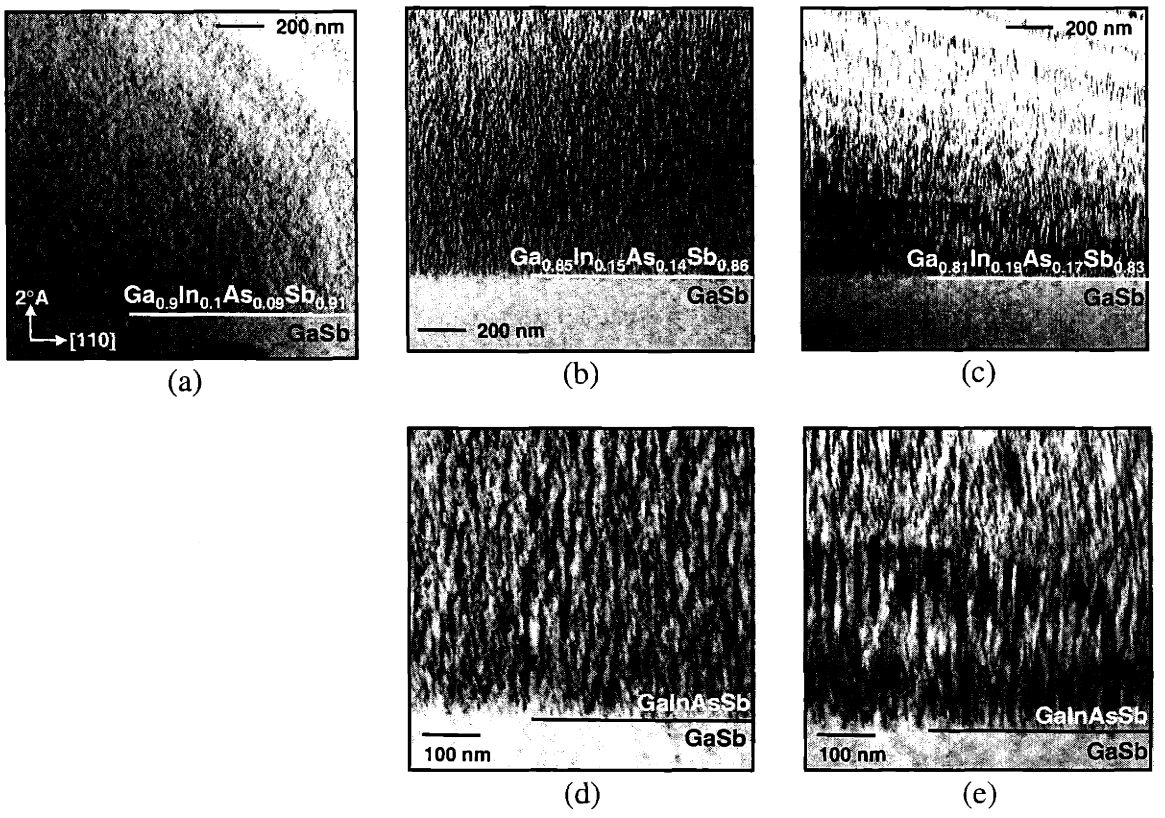

Fig. 49. DF <1-10> x-sec TEM images of GaInAsSb epilayers grown on GaSb substrates oriented (001) 2° toward (-1-11)A. The alloy composition was further into the miscibility gap going from (a) to (c). The images in (d) and (e) are higher magnifications of those in (b) and (c), respectively.

The last comparison examining the effect of alloy composition is given in Fig. 50, for samples grown at 575 °C on substrates oriented (001) 2° toward (101). These are DF <220> 2-beam images. The samples in (a), (b), and (c) had RT PL peaks at 2.088 μm, 2.235 μm, and 2.45 μm, respectively. The samples shown in (b) and (c) had markedly different microstructures than those of previous samples. The microstructures of these samples were dominated by the presence of large vertical slabs, similar to what was seen in InAlAs epilayers discussed in section 4.2.2. Figure 50(d) is a plan-view (PV) TEM of the sample shown in Fig. 50(b). Notice the striations that run along a <1-10> direction,

and have the same spacing as the lateral length scale of the slabs seen in Fig. 50(b). (For comparison, the PV TEM of a homogeneous sample like that shown in Fig. 46(a) exhibits almost no contrast.) In addition, the AFM image of the surface of this sample (displayed in Fig. 50(e)) indicated a morphology dominated by trenches running along the [1-10] direction, which correspond to the striations seen in Fig. 50(d). Energy dispersive x-ray (EDX) analysis of the surface of a similar sample indicated that the alloy composition in the trench area was slightly enriched in GaAs (on the order of 2-3 atomic percent), while that in the surrounding areas was slightly enriched in InSb [154] as discussed in section 4.3.2 above.

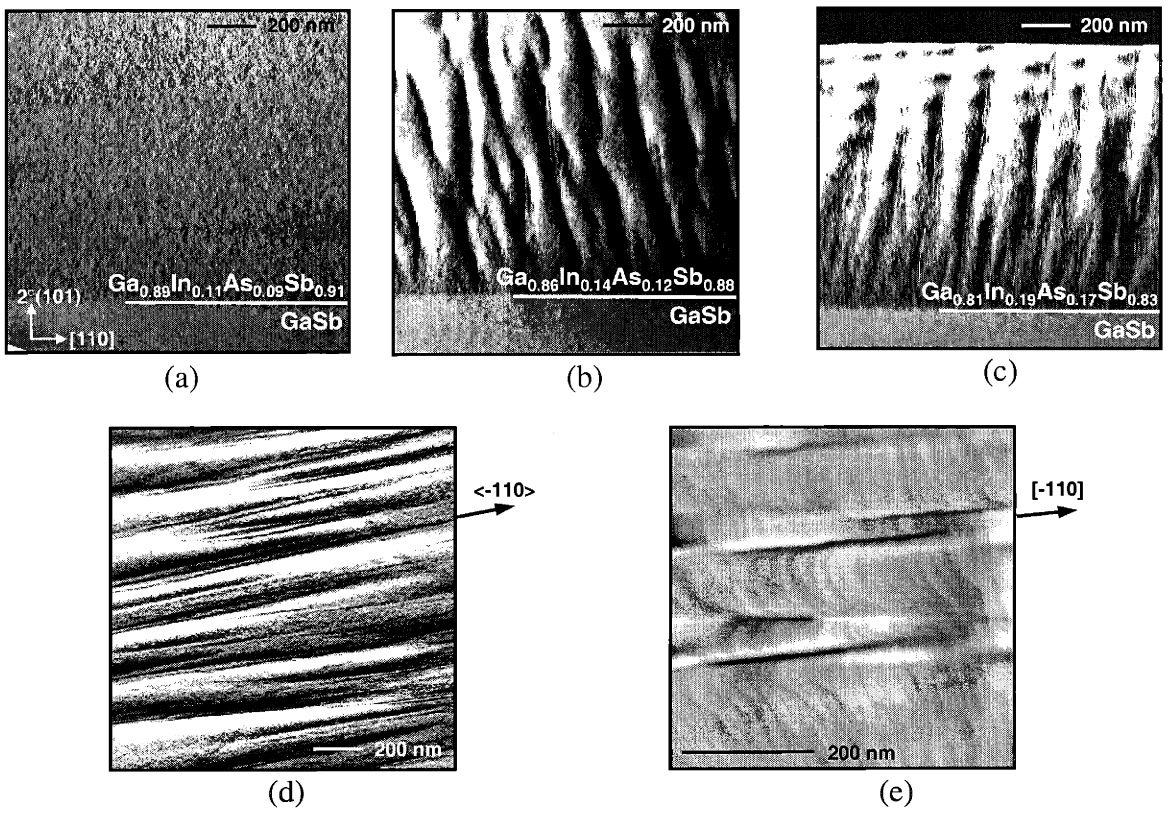

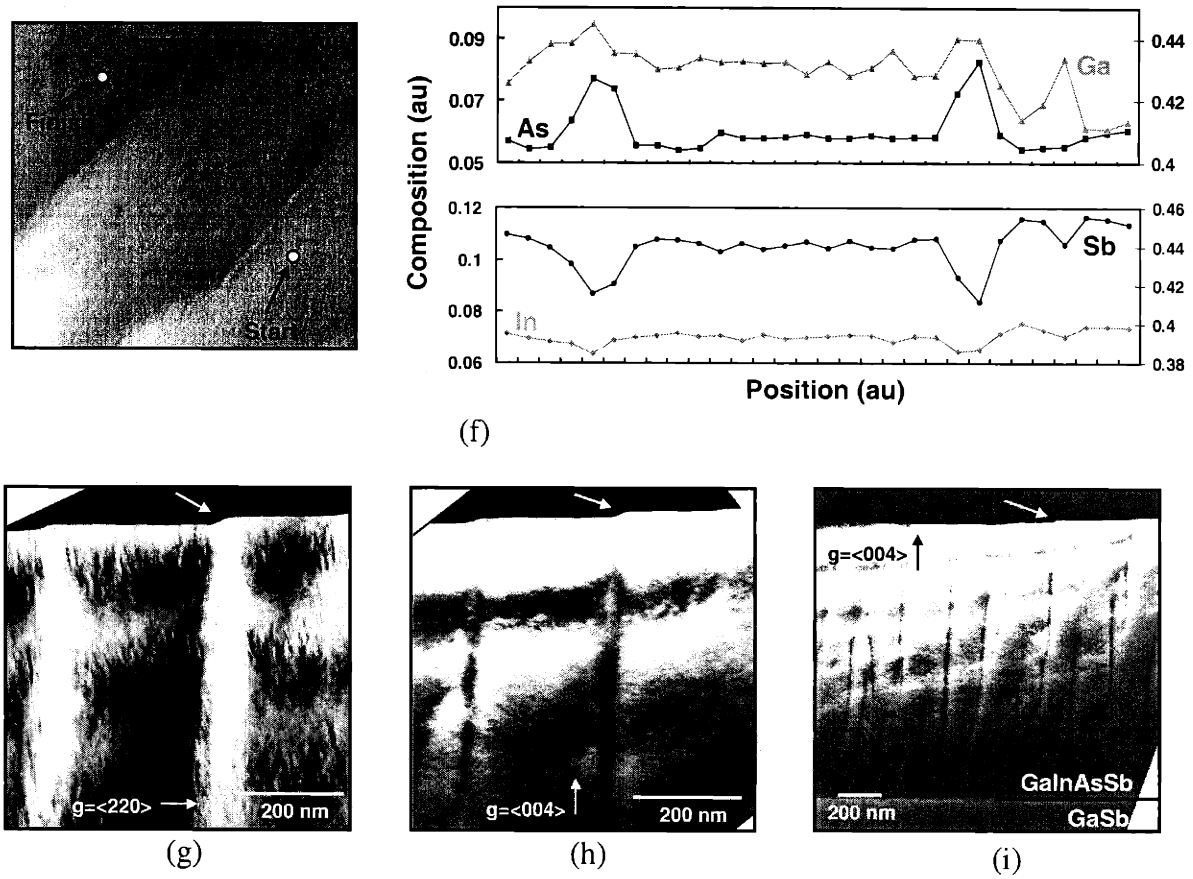

Fig. 50. X-sec TEM images of samples grown at 575 °C on substrates oriented (001) 2° toward (101). The samples were further into the miscibility gap going from (a) to (c). A PV TEM image of sample (b) is shown in (d); the corresponding AFM image is shown in (e). Notice the striations in both the PV TEM and AFM images that align along the [-110] direction and are correlated with the vertical slabs seen in the x-sec TEM image in (b). STEM/EDX analysis of this sample, shown in (f), indicated that the sample phase separated to GaAs- and InSb-rich phases. Higher magnification images of the sample shown in (c) are given in (g)-(i) and directly indicate that the GaAs-enriched phase aligned with surface trench features seen in the AFM of (e).

EDX analysis (VG, Model HB603 STEM) of the sample shown in Fig. 50(b) is presented in Fig. 50(f). Again, it is seen that the sample has phase separated into two regions: a smaller volume that is enriched in GaAs, and a larger volume that is enriched in InSb. The GaAs enrichment relative to the nominal composition is larger than the

InSb enrichment. This is in agreement with theoretical thermodynamic calculations discussed above that predict GaInAsSb alloys in the miscibility gap to phase separate to a small volume strongly enriched in GaAs, and a large volume slightly enriched in InSb. Of course, the kinetic limitations of the OMVPE growth process strongly inhibit the microstructure from achieving its equilibrium thermodynamic state, but the influence of the thermodynamic driving force for phase separation on the resulting microstructure is nonetheless clear.

A higher magnification x-sec TEM image of the top of the sample in Fig. 50(c) is shown in Fig. 50(g) and reveals a very interesting detail. The GaAs-enriched regions are aligned with features on the surface that resemble large step edges. (The epoxy layer above the top surface of the sample was still intact, indicating that the observed surface morphology was not an ion milling artifact but rather the true morphology.) These step edges are the trench features seen in the AFM image above. The same area is shown in Fig. 50(h) using DF <004> 2-beam conditions. This image more clearly indicates the spatial location of the phase-separated regions.[†] (A lower magnification using DF <004> 2-beam conditions is shown in Fig. 50(i).) These images provide experimental evidence of a coupling between compositional and morphological perturbations. This is in agreement with theoretical calculations that when an alloy phase separates, the associated strain energy from the lattice mismatch of the two phases can be partially relieved if the smaller-lattice-constant phase forms a valley on the surface and the larger-lattice-constant

[†] Based on structure factor calculations, the <004> 2-beam will be chemically sensitive to phase separation into GaAs- and InSb-enriched regions. <220> 2-beam conditions will also be chemically sensitive to this phase separation; however, this 2-beam is principally imaging the strain field associated with the phase separation. This strain field lies primarily in the <220> direction and not the <004> direction; therefore, the <004> 2-beam condition will more directly indicate the actual physical location of the phase separated regions.

phase forms a peak. In this case, the smaller-lattice-constant phase is the GaAs-enriched phase, and it is located in the trenches seen in the AFM images (which are the "step edges" seen in the x-sec TEM images). The larger-lattice-constant InSb-rich phase is located in the regions between these valleys.

Once the alloy phase separates and forms such a surface morphology, all subsequent epitaxial deposition is biased in the sense that the surface valleys preferentially incorporate GaAs-enriched alloy compositions, while the surrounding areas preferentially incorporate InSb-enriched compositions [107, 158, 167]. This "strain-locking" is what creates the vertical slabs in the microstructure: as each monolayer is deposited and phase separates, the GaAs-enriched region situates itself in the surface valley, directly above the previous GaAs-enriched region. Likewise, the InSb-enriched phase exhibits vertical registry from monolayer to monolayer. As a result, the final microstructure is not randomly phase separated, but rather forms aligned, orderly, self-organized slabs. This strain-locking effect is similar to that seen in the growth of multiple layers of quantum dots. It is often found that multiple layers of quantum dots align with one another along the vertical growth direction [168-170]. This is because the strain field from an underlying quantum dot layer influences where the quantum dots in the subsequently-deposited quantum layer locate themselves.

Although this microstructure was very different than any of the ones seen in Figs. 46-49, closer examination of the sample shown in Figs. 49(c) and (e) suggests that it may have been close to forming such a microstructure. Figure 51(a) shows a higher magnification image of this sample using DF <004> 2-beam conditions. Note the faint vertical striations that align with slight "pits" or valleys in the surface. (Again, the epoxy

above this surface was intact, indicating that these surface valleys were not ion milling artifacts.) This is similar to what was seen in Fig. 50(h), although the lateral length scale between the striations is much larger in Fig. 50(h). A DF <220> 2-beam image of the Fig. 51(a) sample, shown in Fig. 51(b), indicates that the spinodal-like contrast is quite coarse, and begins to resemble the contrast seen in Fig. 51(c). Figure 51(c) is a high magnification image of the substrate/epilayer interface of the sample shown in Fig. 50(c). It is interesting to note from this image that the large vertical slabs did not form immediately upon epilayer growth. Rather, the initial stages of growth displayed spinodal-like contrast, which developed into the slab microstructure as growth proceeded.

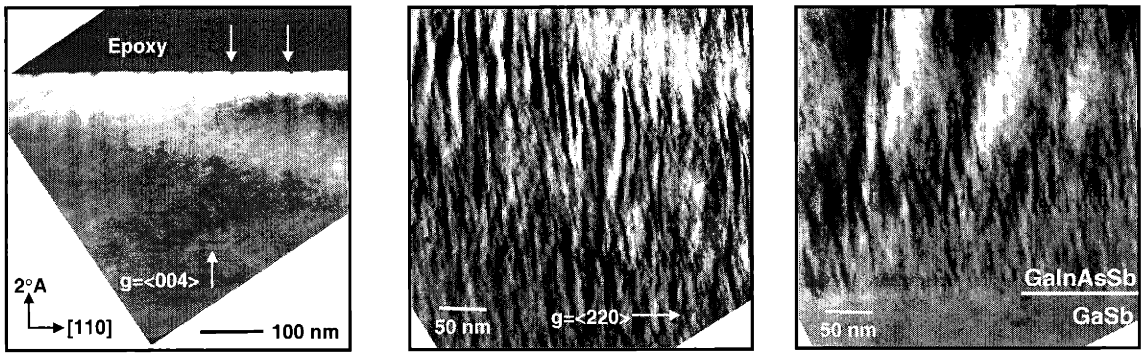

(a) (b) (c)

Fig. 51. (a) DF x-sec TEM image of the sample shown in Figs. 49(c) and (e). This <004> 2-beam indicates that the sample had a coupling between composition modulations and surface morphology features. The sample is shown in (b) using <220>-type 2-beam conditions. The sample in (c) is the same as that in Fig. 50(c), and illustrates that the early stages of growth were similar to the sample shown in (b).

In all five comparisons presented in this section, as the alloy composition went further into the miscibility gap, the GaInAsSb epilayer increasingly exhibited more contrast in TEM images. This is strongly suggestive that the contrast seen in these

images is due to phase separation. In fact, direct compositional analysis using EDX confirms that contrast seen in the least homogeneous (most phase separated) epilayer was due to a composition modulation. It is likely that this phase separation occurred strictly at the surface of the growing epilayer and not through bulk diffusion; therefore, the surface chemistry and morphology played extremely important roles in determining the resulting microstructure of the epilayer. This was directly seen in the images presented in Figs. 50 and 51 where the composition modulation was directly coupled to perturbations (features) in the surface morphology.

4.4.1.2 Effect of substrate miscut direction on GaInAsSb microstructure

The results of section 4.2.1 suggested that phase separation was enhanced at higher growth temperatures (i.e. 575 °C vs. 525 °C) and at smaller miscut angles (i.e. 2° vs. 6°) due to growth kinetics. Therefore, in this section all the samples that are compared were grown at 575 °C on substrates with a 2° miscut angle to exaggerate the differences between the various substrate misorientation directions. The first set of samples all had a nominal RT PL peak at 2.09 μm, while the second set had a nominal RT PL peak at 2.45 μm. Therefore, the effect of substrate misorientation direction as a function of alloy composition is also examined in this section.

Figures 49(a), 48(a), and 50(a) displayed three samples grown at 575 °C, all with a RT PL peak between 2.08 and 2.09 μm, indicating very similar alloy compositions. The substrates were all misoriented 2°, toward the (-1-11)A, (1-11)B, and (101), respectively. The GaInAsSb epilayer grown on the substrate misoriented 2° toward (1-11)B was the most homogenous, while that misoriented 2° toward (101) exhibited the

most contrast of the three samples. This suggests that GaSb substrates misoriented toward the (1-11)B surface yield the most homogeneous, highest-quality epilayers, in agreement with results presented in section 4.2.1. However, at this particular alloy composition, which is near or just outside the calculated miscibility gap, the effect of substrate misorientation is minimal. All three samples exhibited similar microstructures, and had similar PL and x-ray characteristics (not shown).

The result for samples grown at alloy compositions further into the miscibility gap was quite different. The samples compared here were all grown at 575 °C on substrates with a 2° miscut angle, and had 300 K PL peaks near 2.45 μm. The difference between these microstructures – simply caused by different substrate miscut directions – is striking. Sample #6, shown in Fig. 48(b), was grown on a substrate oriented (001) 2° toward (1-11)B, and had a 300 K PL peak at 2.44 μm. Samples #9 and #12 were grown on substrates oriented (001) 2° toward (-1-11)A and (101), respectively, with 300 K PL peaks at 2.44 and 2.45 μm. These samples were shown in Figs. 49(c), 49(e), 51(a), and 51(b) (for sample #9), and Figs. 50(c), 50(g)-(i), and 51(c) (for sample #12). The GaInAsSb epilayer grown on the substrate miscut toward the (1-11)B direction exhibited moderate contrast in the form of spinodal-like decomposition. This contrast was stronger, coarser, and more elongated in the growth direction for the sample grown on the substrate miscut toward the (-1-11)A direction. The sample grown on the (101) miscut substrate exhibited more extreme phase separation. It initially formed spinodal-like contrast, as seen near the substrate/epilayer interface. However, as growth proceeded, the homogeneity degraded and the sample phase separated to form vertical slabs through the epilayer, as discussed before in section 4.4.1.1.

It is again emphasized that all three of these samples were grown under the same conditions: the same temperature, growth rate, alloy composition, and miscut angle. The only difference was the substrate miscut direction, yet the resulting microstructures were dramatically different. This emphasizes the fact that the phase separation occurred strictly by surface diffusion – and not bulk diffusion – since the miscut direction only affected the surface thermodynamics and kinetics.

The results from this section are very interesting. For both sets of comparisons, GaInAsSb epilayers grown on substrates miscut toward the (1-11)B direction had the most homogeneous microstructures, while those miscut toward the (101) exhibited the least homogeneous microstructures. The effect was far more dramatic for the second set of samples, which had alloy compositions further into the miscibility gap. The surface chemistry – in particular, the chemistry and bonding at the step edge due to the substrate miscut direction – plays a critical role in determining the adatom surface lifetime. The longer the adatom lifetime, the easier it is for the alloy to approach its equilibrium microstructure. For alloy compositions inside a miscibility gap, the preferred microstructure is phase separated. It is apparent from these results that the adatom incorporation rate is greatest at a (1-11)B step edge, and lowest at a (101) step edge. Therefore, (1-11)B step edges present the greatest kinetic barrier to phase separation, and GaInAsSb alloys grown on substrates misoriented toward the (1-11)B exhibit the most homogeneous microstructure. In contrast, (101) step edges are the least effective at incorporating adatoms. Thus, GaInAsSb alloys grown on substrates misoriented toward

the (101) are closer to the thermodynamically preferred state, and therefore more phase separated.

It is not clear why the (1-11)B step edge is the most effective at incorporating adatoms, while the (101) step edge is the least effective and the (-1-11)A is in between. A simple examination (not shown here) of the crystallography of these three step edges and terraces suggests that the (1-11)B and (101) step edges provide preferred bonding incorporation for adatoms compared to their respective terraces, while the (-1-11)A step edge is no different than bonding conditions on the terrace. This would suggest that the (1-11)B and (101) step edges should be quite effective at incorporating adatoms, while the (-1-11)A step edge should be the least effective. This is not the case, however. This suggests that the actual bonding and chemistry present at the various step edges and terraces is more involved than simple crystallographic considerations, and is complicated by various reconstructions present at these sites. While terrace reconstructions are well-known for MBE samples, they are less well characterized in OMVPE. In addition, the bonding/reconstruction present at step edges on miscut substrates is even less well understood. If this information were available, it would provide insight into the relative ability of each step edge to incorporate adatoms into the crystal.

Another factor that needs to be taken into consideration is the asymmetry of the surface diffusivities. Since surface dimers typically align along the [110] or [-110] direction, the diffusivity along the [110] direction ($D_{[110]}$) will not be the same as that along the [-110] direction ($D_{[-110]}$). The exact reconstruction present on the epitaxial surface during OMVPE growth of the samples studied in this thesis is unknown. However, since the grossly-phase-separated sample shown in Fig. 50 formed trenches

along the [-110] direction, this implies that $D_{[110]}$ was greater than $D_{[-110]}$. If this were true, then adatoms on a substrate miscut toward the (101) would have a longer effective lifetime or diffusion length compared to those on a substrate miscut toward the (-1-11)A. This is because the (-1-11)A steps are perpendicular to the fast diffusion direction, but the (101) steps are at an angle of 45°. This might partially explain the slightly increased phase separation on substrates miscut toward the (101) compared to those miscut toward the (-1-11)A. Again, knowledge of the exact reconstruction present on the surfaces of these samples during epitaxial growth would provide great insight.

4.4.1.3 Effect of substrate miscut angle on GaInAsSb microstructure

Two sets of comparisons are examined in this section: a series of samples grown at 575 °C on substrates oriented 2, 4, or 6° toward the (1-11)B, all with a 300 K PL peak near 2.09 μm, and a series of samples grown at 575 °C on substrates oriented 2 or 6° toward the (101), with a 300 K PL peak near 2.25 μm. TEM images from the first set appeared similar. The sample grown on the 2° miscut substrate was shown in Fig. 48(a), while that grown on the 6° miscut substrate was shown in Fig. 47(a). Figure 52 is a DF [110] x-sec TEM image of the sample grown on the 4° miscut substrate. These DF [110] x-secs appear fairly similar to each other, suggesting that at this particular alloy composition and growth temperature the (1-11)B step edge is so effective at incorporating adatoms that little improvement is gained going from a 2° to a 6° miscut angle. Interestingly, though, the self-organized tilted superlattice (not shown here; discussed further in section 4.4.3) is present throughout the epilayer grown on the 2° miscut substrate, and is completely absent on the 6° miscut substrate. This can be

understood from the framework presented in section 4.4.3.3 as due to the increase in the kinetic barrier to surface diffusion going from a 2° to a 6° miscut angle. Therefore, even though the miscut angle had little effect on the spinodal-like contrast in this set of samples, it had a big impact on the presence of the tilted superlattice.

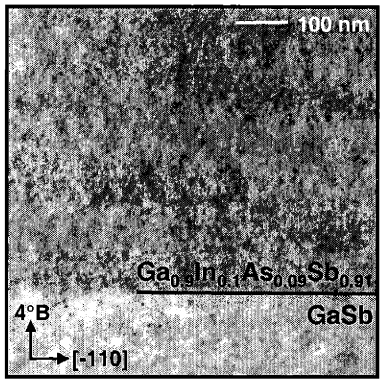

Fig. 52. DF x-sec TEM image of a GaInAsSb epilayer grown at 575 °C on a GaSb substrate oriented (001) 4° toward (1-11)B.

The second set of samples is shown in Fig. 53. The sample in Fig. 53(a) was grown at 575 °C on a substrate miscut 6° toward the (101), and had a 300 K PL peak near 2.26 μm, while that in Fig. 53(b) was grown at 575 °C on a substrate miscut 2° toward the (101), and had a 300 K PL peak near 2.24 μm. The sample shown in Fig. 53(b) was also shown in Figs. 50(b) and 50(d)-(f). The [1-10] DF images in Fig. 53 indicate that the epilayer homogeneity improved dramatically by increasing the miscut angle from 2 to 6°. It is expected that the adatom lifetime decreases as the miscut angle increases, because an adatom encounters more step edges in a given diffusion time as the miscut angle

increases. Therefore, the kinetic barrier to diffusion is increased – which should increase epilayer homogeneity – as the miscut angle is increased.

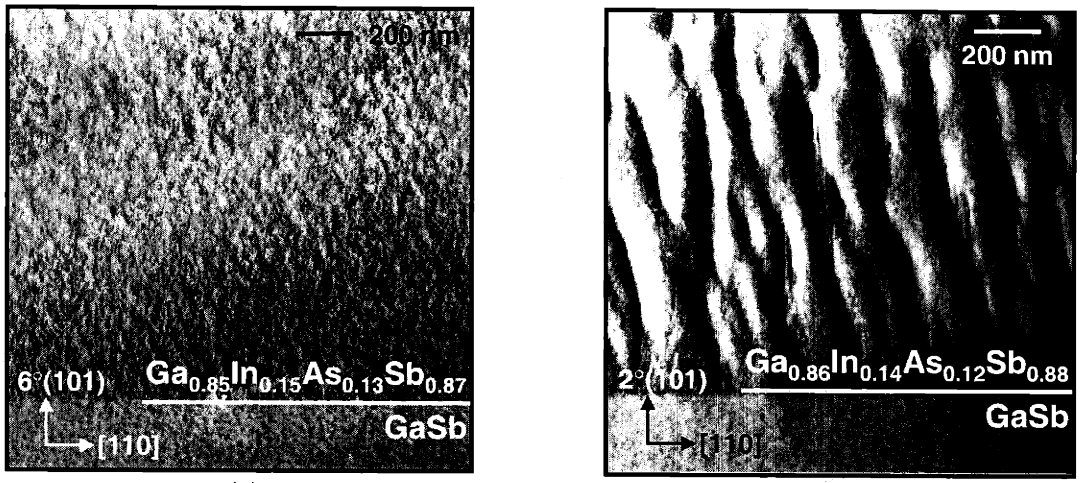

Fig. 53. X-sec TEM images illustrating the effect of miscut angle on epilayer homogeneity. The GaInAsSb epilayers were grown at 575 °C on substrates (a) 6° and (b) 2° toward the (101) and were of similar composition. The larger miscut angle in (a) created a larger barrier to surface diffusion, yielding a more homogenous epilayer.

This set of samples should be interpreted somewhat cautiously, however, because the 2° miscut substrate was etched in the bromine-based etch discussed in section 2.4.3, while the 6° miscut substrate was etched only in HCl. The bromine-based etch is known to roughen the GaSb surface, and this roughness can promote phase separation. An example of the influence of surface morphology on phase separation is given in section 4.4.3.2 below. Therefore, it is possible that some of the difference between these two samples was due to the starting substrate surface morphology, and some was due to the increased miscut angle. However, based on the PL, x-ray, and AFM results of Wang

given in the previous section, it is clear that epilayer homogeneity improves as the miscut angle increases, all other factors held constant.

4.4.2 Discussion of TEM microstructure results

The results presented in section 4.4.2 covered a range of alloy compositions (300 K PL peak from 2.08-2.49 μm), substrate miscut directions ((-1-11)A, (1-11)B, and (101)), substrate miscut angles (2-6°), and growth temperatures (525 and 575 °C). The observed GaInAsSb microstructures varied quite dramatically, from epilayers that exhibited almost no contrast – indicative of a homogeneous alloy, to epilayers that had strong contrast in the form of large vertical slabs – indicative of phase-separated material. The microstructures correlate well with data from other *ex situ* characterization techniques, including PL, x-ray, and AFM. All these techniques agree that the highest quality, most homogeneous GaInAsSb epilayers occur for alloys that:

- Have compositions further outside the calculated miscibility gap
- Are grown on GaSb substrates miscut toward the (1-11)B direction
- Are grown on GaSb substrates miscut 6°
- Are grown at 525 °C

While the alloy composition determines the thermodynamic driving force for phase separation, the actual extent of phase separation and resulting microstructure are strongly influenced by kinetic growth barriers. By increasing these kinetic barriers, the adatom lifetime is decreased and the alloy is inhibited from achieving the thermodynamic equilibrium microstructure. These kinetic barriers include the substrate misorientation angle and direction, growth temperature, and growth rate. All these factors are related to surface kinetics, which underscores the fact that the final microstructure is determined by surface processes. An additional observation emphasizing the importance of the surface

(1) Although the results from every sample will not be included, all GaInAsSb samples examined by x-sec TEM indicated the presence of a superlattice. These samples spanned the range of the most homogeneous to the most phase separated shown in section 4.4.2. In all cases, the superlattice was either tilted, parallel, or some combination of both. These two variants will be discussed in more detail in this section.

(2) For most samples, **g** = <222> or <111> 2-beam conditions were required to image the superlattice. Any of the four accessible <222> or 4 <111> conditions could be used, and gave the same results. The only difference between <222> and <111> conditions was that the <111> images typically had more thickness fringes, which obscured the superlattice. Therefore, <222> conditions were typically used. Both BF and DF could be used, although in most cases DF gave clearer images. In a few cases, the superlattice could be observed using **g** = <004> or <113> 2-beam conditions. Finally, it was noticed that the superlattice contrast increased (i.e. the superlattice became more noticeable) as the sample was tilted away from the <110> pole toward the <123> pole. The clearest images were obtained using **g** = <222> near the <123> pole.

(3) For samples which x-sec TEM, x-sec FE-SEM, and RSXRM all indicated the presence of a superlattice, the measured tilt angle (if any) and period of the superlattice was the same for all three techniques. This corroboration underscored the fact that the NSL was an actual feature in the microstructure, and not an artifact due to TEM sample preparation. In addition, examination of several samples indicated that TEM is the most sensitive to the presence of the NSL, while x-sec SEM is the least sensitive of the three techniques.

As mentioned in point (1) above, some sort of NSL was observed in every sample examined by x-sec TEM, using <222> 2-beam conditions. Table IV maps out the growth conditions for which a NSL was observed, either by TEM, FE-SEM, or RSXRM. A check mark indicates that a superlattice (parallel, tilted, or both) was observed. A gray box indicates growth conditions for which no samples were examined. It is expected that those samples also have a superlattice.

is the coupling between modulations in the alloy composition and perturbations in the surface morphology experimentally seen above.

These results suggest that for a given alloy composition, it is possible to "tune" the microstructure by varying the kinetic growth parameters. This type of epitaxial engineering may play an important role in future self-assembled micro- and nano-scale devices.

4.4.3 "Natural superlattice" formed in GaInAsSb

Section 4.3.3 illustrated the initial observation of vertical composition modulation in a GaInAsSb epilayer, which was seen using x-sec FE-SEM. The vertical composition modulation had the appearance of a natural superlattice (NSL). In that sample, the superlattice was inclined 10° with respect to the surface (epitaxial growth plane), and had a period of 20 nm. [110] x-sec TEM by Chen *et al.* also revealed the tilted superlattice in that sample, at an angle of 10° and period of 20 nm. <222> or <111> 2-beam conditions were required to image the superlattice using TEM. In addition, this tilted superlattice was also observed using reciprocal space x-ray mapping (RSXRM), as illustrated in Fig. 45(b).

Very few reports of vertical composition modulation forming a natural superlattice exist in the literature [114, 122, 133, 134, 165, 166, 121, 144, 162]. Most reported composition modulations form a lateral superstructure in the material, similar to the spinodal decomposition or vertical slabs discussed above. Since this vertical NSL is such an unusual phenomenon, it was studied in greater detail as part of this thesis. The results are presented in this section. Three interesting points are worth noting:

Table IV. Growth Conditions for which Natural Superlattice was Observed			
	525 °C	550 °C	575 °C
(001) 2° → (-1-11)A		✓	✓
(001) 6° → (-1-11)A		✓	
(001) 2° → (1-11)B		✓	✓
(001) 6° → (1-11)B	✓	✓	✓
(001) 2° → (1-11)B		✓	✓
(001) 6° → (1-11)B		✓	✓

Cross-section TEM images illustrating the superlattice in a variety of samples are displayed in Fig. 54. All of these images, except for (b) and (c), have been oriented so that the growth direction is straight up. The growth direction is indicated by a shorthand notation: for example, on a substrate oriented (001) 6° toward (1-11)B, the growth direction on the image is indicated as 6°B. Table V lists some parameters for each of these samples, and cross-references these samples to the ones listed in Table III. All the images were obtained using **g** = DF <222> ([-110] x-secs) or DF <2-22> ([110] x-secs) 2-beam conditions, except for images (e) and (i) which used BF conditions.

Table V. Parameter List for Samples in Fig. 54						
Fig. 54:	**Sample # in Table III**	**Growth Temp (°C)**	**300 K PL Peak λ (μm)**	**Substrate orientation**	**x-sec**	**Tilted or Parallel Superlattice**
(a)	2	525	2.485	6°(1-11)B	[110]	T + faint P
(b)	2	Same as (a) – higher magnification of epilayer/substrate interface				
(c)	2	Same as (a) – higher magnification of top of epilayer				
(d)	14	575	2.260	6° (101)	[110]	T
(e)	14	Same as (d) – higher magnification of epilayer				
(f)	10	575	2.088	2° (101)	[-110]	T
(g)	5	575	2.088	2° (1-11)B	[110]	T
(h)	4	575	2.314	6° (1-11)B	[110]	T + P
(i)	8	575	2.291	2° (-1-11)A	[-110]	P
(j)	7	575	2.08	2° (-1-11)A	[-110]	P
(k)	1	525	2.09	6° (1-11)B	[110]	P
(l)	13	575	2.076	4° (1-11)B	[110]	P
(m)	3	575	2.082	6° (1-11)B	[110]	P
(n)	9	575	2.444	2° (-1-11)A	[-110]	T + P
(o)	11	575	2.235	2° (101)	[-110]	P
(p)	12	575	2.450	2° (101)	[-110]	P
(q)	6	575	2.441	2° (1-11)B	[110]	P + rare T (T not seen in RSXRM)

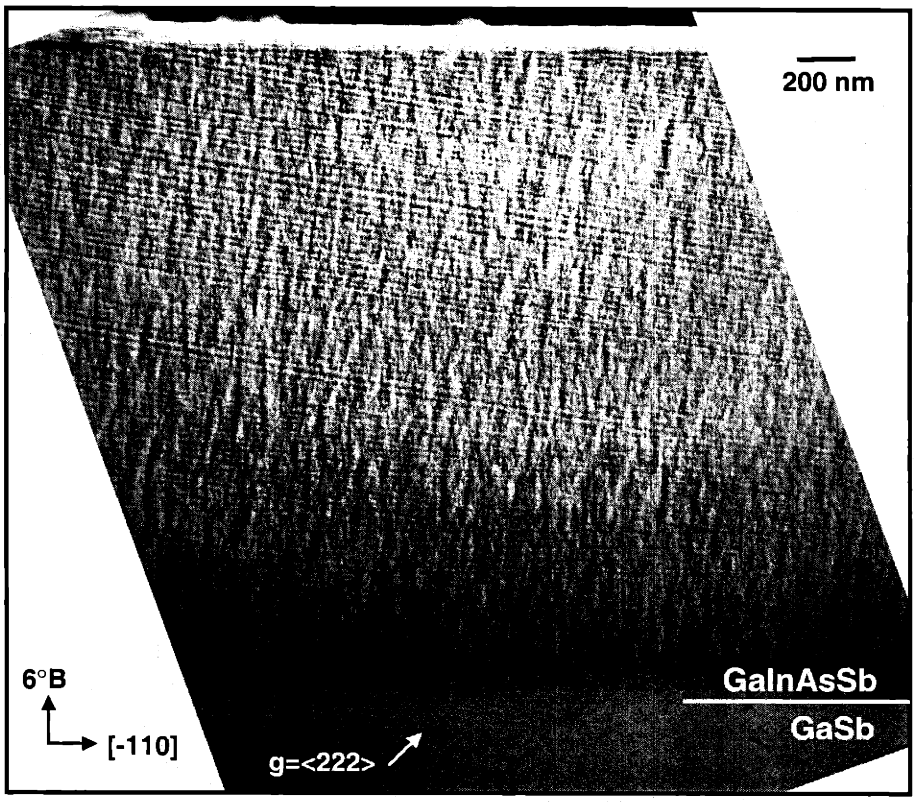
200 nm
6°B
[-110]
g=<222>
GaInAsSb
GaSb

(a)

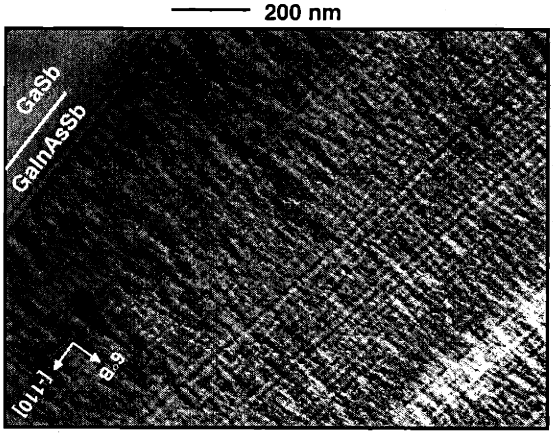
200 nm
GaSb
GaInAsSb
[-110]
g=g

(b)

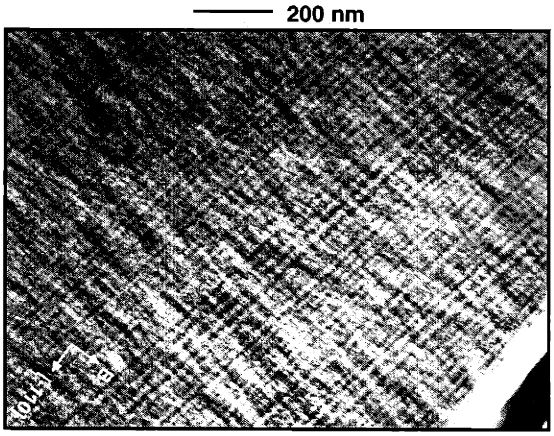
200 nm

(c)

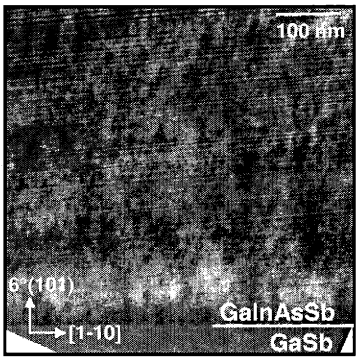

(d)

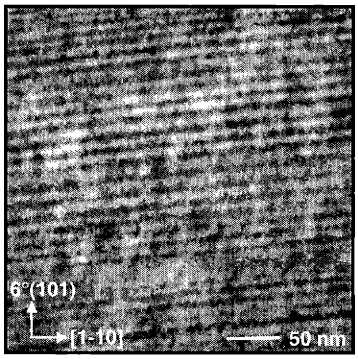

(e)

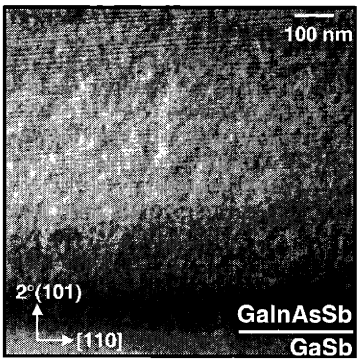

(f)

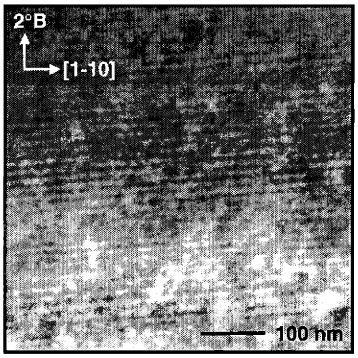

(g)

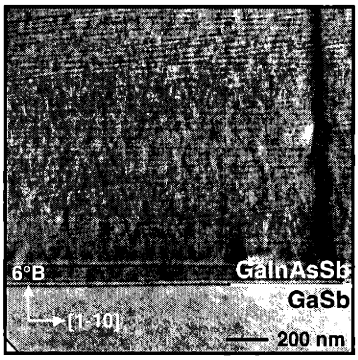

(h)

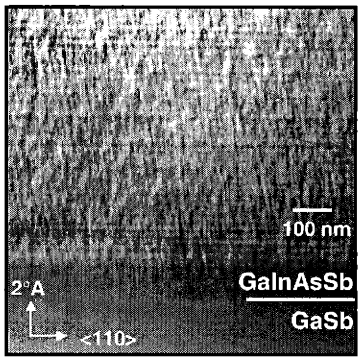

(i)

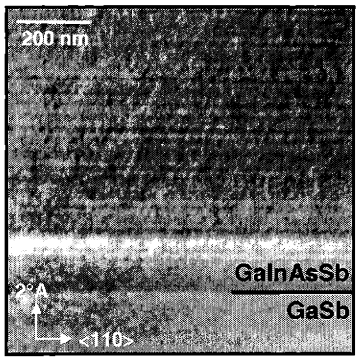

(j)

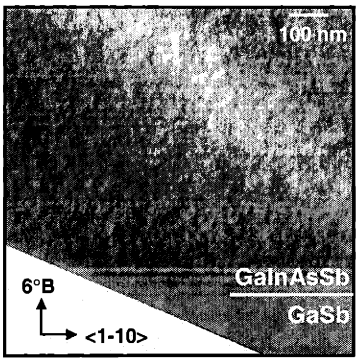

(k)

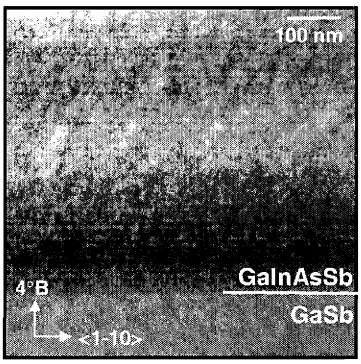

(l)

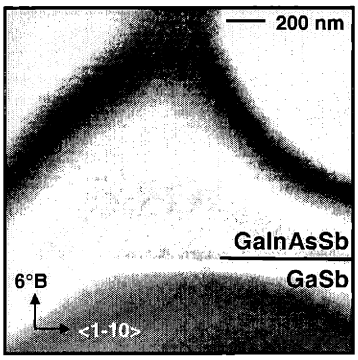

(m)

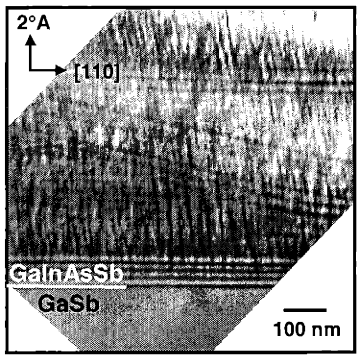

(n)

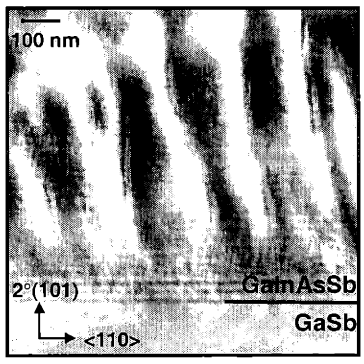

(o)

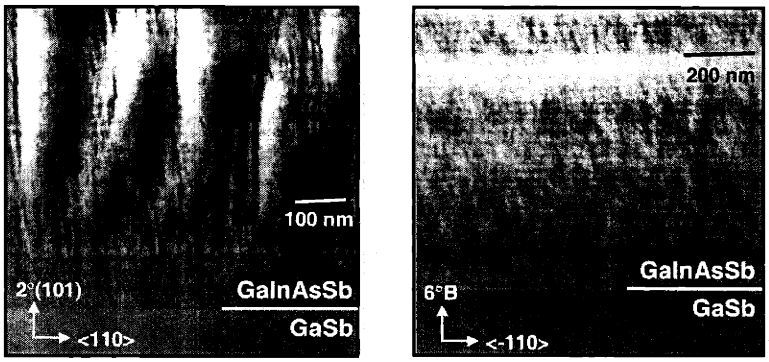

(p) (q)

Fig. 54. TEM images of superlattice obtained using **g** = <222> or <2-22> 2-beam conditions. The superlattice was present for a variety of growth conditions. Some form of superlattice – parallel, tilted, or both – was seen in every sample examined by TEM in this thesis. It is even easier to see the superlattice in these figures if the figures are viewed obliquely.

Figure 54 illustrates that the natural superlattice was present for a broad range of growth conditions.[†] The period of the superlattice in different samples varied from about 10 nm to 40 nm. The relationship of the period to various growth parameters, such as growth temperature, alloy composition, and substrate misorientation, is still unclear, and probably requires a larger data set for extensive analysis.

The figures indicate that the NSL can take the form of a purely tilted superlattice (with respect to the substrate surface normal), a purely parallel superlattice, or some combination of both (in particular figures (b), (h), and (n)). Note that it is even easier to see the superlattice in these figures if the figures are viewed obliquely, i.e. at a glancing incidence angle to the page. Surprisingly, even in the samples that exhibit the most phase

separation, a superlattice is still present (i.e. figures (o) and (p)). All of the samples in Fig. 54 were also shown in Figs. 46-53. However, the superlattice was not apparent in these samples until <222> 2-beam conditions were used.

The three immediate questions are: what is this superlattice, what causes the tilted variant, and what causes the parallel variant? As mentioned above, it is seen both theoretically and experimentally that GaInAsSb alloys with compositions inside the miscibility gap phase separate to GaAs- and InSb-rich regions. One possible explanation for the superlattice, therefore, is that it is a composition modulation into GaAs- and InSb-rich phases. This would explain why the superlattice was observable using TEM, RSXRM, and FE-SEM (after a brief stain etch). In addition, since GaAs and InSb have a large lattice constant difference ($\approx$ 14%), any phase separation into phases even slightly enriched in these two binaries will create large strain fields throughout the epilayer. Since TEM is very sensitive to strain fields, this might explain the high sensitivity of TEM to the superlattice, and the strong contrast in TEM images.

Unfortunately, EDX analysis of the superlattice did not yield any statistically significant composition modulation. However, this does not mean that the superlattice is not a composition modulation. In fact, it is unlikely that EDX would be able to measure a composition modulation associated with the superlattice for two reasons. First, the period of the superlattice was typically between 10 and 30 nm. Each "phase" was therefore between 5 and 15 nm. It is very difficult to achieve accurate EDX analysis at

---

[†] In most of these TEM images (particularly (a), (h), and (n)), several strong parallel bands are seen at interfaces between different epilayers, particularly at the substrate/epilayer interface. These bands are *not* part of the superlattice feature seen throughout the rest of the epilayer, and should be ignored. They are due to the fact that under the <222> 2-beam near the (123) pole, the interface is not aligned with the electron beam. This yields the fringes seen at the interface, similar to fringes for a stacking fault or planar defect.

this small nano-length scale, because of the probe size and the volume averaging of the probe throughout the sample. Second, the sensitivity limit of EDX is about one atomic percent, and it is expected that the composition modulation associated with the superlattice was no larger than one to two atomic percent. There are two reasons for this expectation. The first is that the reciprocal space x-ray maps (shown in Fig. 45(b)) typically required more than 24 hours integration time to resolve the presence of the superlattice, suggesting that the magnitude of the composition modulation was fairly small. Second, although the 4 K PL FWHM was broadened due to the superlattice, the effect was not as significant as in more grossly phase-separated samples. For example, the sample shown in Fig. 50(b) had phase separation on the order of 2-3 atomic percent as measured by EDX, and a 4 K PL FWHM of 50-60 meV. The highest-quality GaInAsSb epilayers had a 4 K PL FWHM of 4-5 meV. Samples like those shown in Fig. 54(a)-(c) had a 4 K PL FWHM of 8-10 meV. Since the sample with phase separation of 2-3 atomic percent had a FWHM of 50-60 meV, while samples which only had a superlattice had a FWHM of 8-10 meV, it is expected that the superlattice phases were only enriched in GaAs and InSb around one atomic percent.

Despite the inability of EDX to directly resolve a composition modulation, it is postulated that the superlattice seen in the above GaInAsSb epilayers is a composition modulation into phases slightly enriched (~1 atomic %) in GaAs and InSb. The transmission electron diffraction patterns of these epilayers indicate that the epilayers are not atomically ordered, and do not have stacking faults, twins, or other microstructural defects. A composition modulation is the only other microstructural feature that would

---

The extent (width) of these fringes scales with the sample thickness and angular difference between the electron beam and the interfacial plane between epilayers.

be observable by FE-SEM (after a brief stain etch), TEM, and RSXRM. Note that this composition modulation occurred concomitantly with other phase separation mechanisms in the epilayer, including the spinodal-decomposition-like vertical striations and large vertical slabs (seen in Figs. 50(b) and (c) for example). This underscores the extremely complicated nature of epitaxial growth.

The other two questions posed above relate to the origins of the tilted and parallel variants of the NSL. There have been reports in the literature of similar parallel natural superlattices, typically in epilayers grown by MBE. In many cases, this parallel superlattice has been explained as an artifact due to substrate rotation during epitaxial growth [117, 145]. This occurs because in many MBE reactors, the substrate is not axi-symmetric with respect to the effusion cells. Therefore, as the substrate rotates, the relative incorporation of the various elements in the alloy changes, creating an artificial superlattice with the period of the substrate rotation. Although the substrates studied in this thesis were rotated during epitaxial growth, this rotation cannot be the cause of the parallel superlattice seen in the GaInAsSb epilayers for two reasons. First, substrates are positioned axi-symmetric with respect to source gas flows in this OMVPE reactor, as seen in Fig. 2. Therefore, substrate rotation would not change the alloy composition of the epilayer. Second, the periods of the NSL and the substrate rotation are completely unrelated. Substrates were typically rotated at speeds between 40 and 250 RPM. Since the GaInAsSb was typically grown at a rate of 1.55 nm/s, this would suggest superlattice periods of 2.3 to 0.37 nm. However, the observed period of the parallel superlattice was far larger, typically between 20 and 40 nm.

It is also not expected that the superlattice formed as a result of bulk diffusion since the bulk diffusivities are too low at typical growth temperatures. The origin of the parallel superlattice is therefore unclear. To form the parallel superlattice, the growing epilayer must preferentially incorporate small additional amounts of either GaAs or InSb in an oscillatory fashion. A systematic oscillation in the output of a mass flow controller in the OMVPE reactor could cause such a superlattice. However, no evidence of such a systematic oscillation was observed. Another possibility for the parallel superlattice is that the epilayer preferentially incorporated GaAs- or InSb-enriched phases in an alternating fashion to accommodate strain. If an epilayer is globally in tension with respect to the GaSb substrate, it could relieve some of this strain if several monolayers of slightly InSb-enriched GaInAsSb are incorporated. If enough InSb-enriched GaInAsSb monolayers are incorporated, this would swing the strain state of the epilayer to compression, in which case it would preferentially incorporate slightly GaAs-enriched GaInAsSb for several monolayers. If this mechanism of oscillation between compressive- and tensile-strained states were self-sustaining, it would create a parallel superlattice. However, the presence of such a mechanism is purely speculative at this point, for which no experimental evidence exists. Given the tremendous difficulty in ascertaining the origin of the parallel superlattice variant, this thesis instead focused on the tilted variant of the superlattice.

4.4.3.1 Discussion of the tilted natural superlattice in GaInAsSb

In order to understand part of the mechanism that causes the tilted superlattice, an explanation of step-flow growth is necessary and is given here. All samples studied in this thesis were grown on offcut GaSb substrates. Nominally (001)-oriented GaSb boules

were misoriented 2, 4, or 6° toward the (-1-11)A, (1-11)B, or (101) by the manufacturer before being sawed into wafers. The various directions are diagrammed in Fig. 43 for clarity. This miscut produces a series of evenly-spaced atomic-height steps on the surface, creating a "vicinal" surface. The spacing between the steps (called the "terrace length") is dictated by the height of the step edge and the miscut angle. For example, a substrate misoriented 6° will have a terrace length of 1.4 nm for monolayer-height steps, and 2.9 nm for bi-layer-height steps. (Surface steps on silicon are typically monolayer-height, while on III-V surfaces it is often assumed that the surface is always terminated by the group V species, which produces bi-layer-height steps.) Depending on growth temperature and other conditions, these mono- or bi-layer height steps are either stable or unstable with respect to bunching. On step-bunched surfaces, individual steps coalesce to form periodic step bunches, which typically consist of 3-5 individual surface steps. Since the step bunches have a larger height than the individual steps, the terrace length must increase accordingly in order to preserve the miscut angle. For example, a GaSb substrate misoriented 6° that has step bunches comprised of 5 individual steps will have a step-bunch height of 1.5 nm and a terrace length of 5*2.9 nm = 14.5 nm.

Many crystal growers prefer miscut substrates because the epitaxial growth occurs in a step-flow mode, yielding very high-quality surfaces. In step-flow growth mode, adatoms preferentially incorporate at step edges or at kinks in the step edge rather than randomly on the terrace. Step-flow growth is therefore a far more orderly process than 2D (layer-by-layer) or 3D growth. This growth mode is sustainable as long as the terrace length is shorter than the adatom diffusion length.

For samples grown on substrates misoriented toward the (1-11)B that had a tilted superlattice, the tilt was only observable in [110]/[-1-10] cross-sections. On samples with tilted superlattices grown on substrates misoriented toward the (101), the tilt could be seen in any <110> cross-section. (<110>-type cross-sections were always used because these are the natural cleave planes for III-V zincblende semiconductors.) This observation strongly indicated that the tilted superlattice was directly related to the step-flow growth mode. The tilt angle could only be seen in cross-sections that were orthogonal to (or at least off angle from) the step-flow direction, whereas cross-sections that were parallel to the step-flow direction did not indicate any tilt. Examples of this are shown in Fig. 55. Figure 55(a) is a DF [-110] x-sec TEM (**g** = <222>) of the sample shown as a [110] x-sec in Figs. 54(a)-(c). Figure 55(b) is a BF [-110] x-sec TEM (**g** = <004>) of the sample shown as a [110] x-sec in Fig. 54(h). Both of the samples shown in Fig. 55 were grown on substrates misoriented toward the (1-11)B. Even though they have tilted superlattices (see Fig. 54), when they are viewed along the [-110], parallel to the step-flow direction, the tilt angle is no longer observable. This suggests that the microstructure of the tilted superlattice is a series of lamellae, only tilted in one direction as shown schematically in Fig. 44(b).

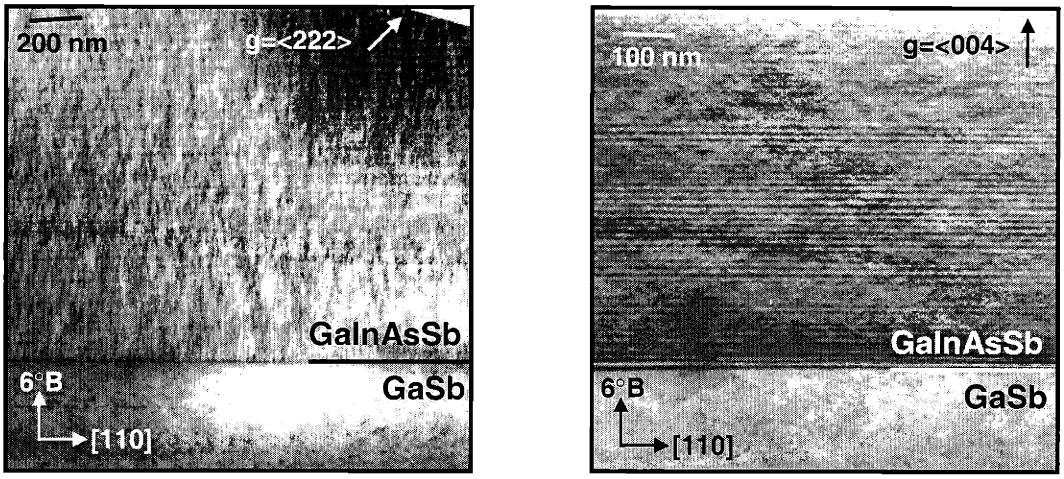

(a) (b)

Fig. 55. DF [-110] x-sec TEM images of the samples shown as [110] x-sec images (a) in Figs. 54(a)-(c), and (b) in Fig. 54(h). Even though both these samples have tilted superlattices, the superlattice appears parallel when viewed from a [-110] x-sec because of the direction of step-flow growth on substrates miscut toward the (1-11)B direction. This is illustrated by the schematic microstructure in Fig. 44(b).

Close examination of all tilted superlattices seen in this thesis revealed two interesting details. First, the angle of the tilt was always larger than the angle of the substrate miscut, both angles taken with respect to the growth direction. For example, the sample shown in Figs. 54(a)-(c) had a superlattice with a tilt angle of 10°, but was grown on a substrate ((001) 6° toward (1-11)B) with surface steps that had a 6° inclination with respect to the growth surface. This is schematically shown in Fig. 56. Second, the superlattice appeared to be extremely robust. While the period was not always constant throughout the epilayer (variations in the periodicity are clearly seen in Fig. 54(n) for example), the individual layers or lamella that comprised the superlattice continued uninterrupted throughout growth of the entire epilayer. Any particular dark or light band can be traced throughout the entire epilayer without interruption. This is absolutely

remarkable for a microstructural feature that is completely self-organized and naturally occurring.

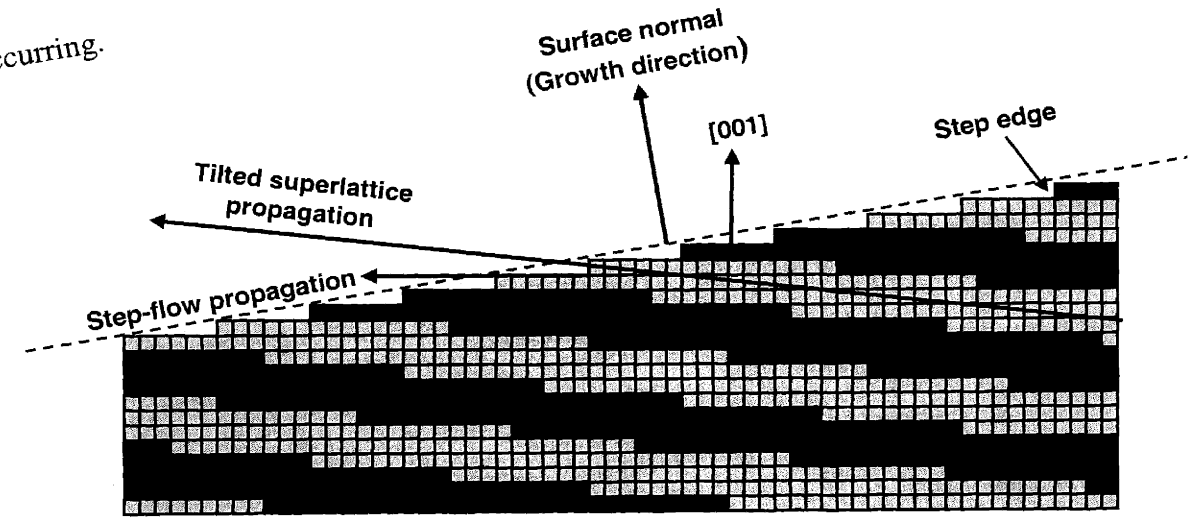

Fig. 56. Schematic illustration of the relationship between the growth direction (surface normal), [001] direction, step-flow direction, and superlattice propagation direction.

The two questions that need to be addressed therefore, are: (1) Why does the tilted variant of the superlattice have an additional tilt angle with respect to the substrate miscut angle, and (2) Why does the superlattice exhibit such continuity and robustness, even though it is a naturally occurring phenomenon?

Insight into these questions may be contained within a paper written by Venezuela *et al.* in 1999 [161]. This paper presented initial results on a model of epitaxial growth that predicted spontaneous superlattice formation during deposition on step-bunched surfaces. On step-bunched surfaces, the elastic strain field along the surface is not constant. In particular, the strain of the step at the top of the bunch is relatively tensile, while that at the base of the bunch is relatively compressive [160]. When a multi-element

alloy is deposited from the vapor, the larger atoms in the alloy preferentially incorporate at step edges in tension, while the smaller atoms preferentially incorporate at step edges in compression. As a result, even alloy systems that have no thermodynamic driving force to phase separate (i.e. no miscibility gap) could have lateral composition modulations along the surface due to component segregation at different steps within a step bunch. Essentially, alloy systems could phase separate to spontaneously form natural superlattices just because of strain considerations at the growing surface.[†]

One can visualize that as step-flow growth proceeded, a tilted superlattice (with the same tilt angle as the substrate miscut) would form throughout the epilayer as a result, with the period size equal to the height of the step-bunch. Interestingly, though, the model did not predict that the superlattice would have the same tilt angle as the substrate miscut. Rather, it predicted that the superlattice would have an additional tilt angle with respect to the substrate miscut – exactly what was seen experimentally in Figs. 54(a)-(h) and (n). The additional tilt angle would be on the order of the angle of the substrate miscut, again similar to what is seen for example in Figs. 54(a)-(c) where the substrate miscut is 6° and the additional tilt angle is 4° (giving a total superlattice tilt angle of 10°). The results of Venezuela's simulation are shown in Fig. 57(a). It can be seen that the superlattice has the same period as the step bunches, and that it has an additional tilt with respect to the substrate miscut angle.

[†] A term was also included to account for systems that had a thermodynamic driving force to phase separate. This tendency had little effect on the period of the superlattice – that was determined by the height of the step bunch. However, it did have an effect on the magnitude of the alloy decomposition – the amount of alloy decomposition became stronger as the thermodynamic driving force increased.

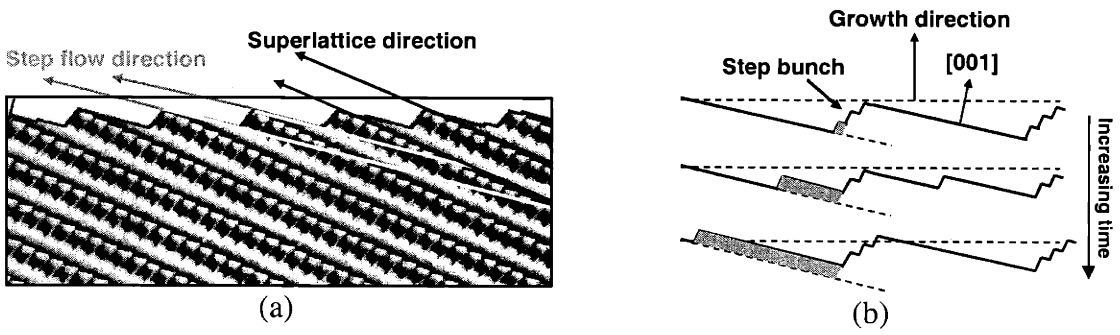

Fig. 57. (a) Results from simulation predicting formation of tilted superlattice with additional tilt angle (from ref. [161]). (b) Schematic illustration of step ejection/capture during epitaxial growth on step-bunched surfaces.

The reason for this additional tilt angle is the complex step-flow dynamics on a step-bunched surface. During epitaxial growth, if step bunches remained static – in other words, if the specific steps that comprised a step bunch were the same throughout growth of the entire epilayer – then the superlattice would not have an additional tilt angle. Rather, the superlattice would have exactly the same tilt angle as the steps. However, step-flow growth is more complicated than the simple model of static step-bunches. As Kandel and Weeks first postulated [171], during epitaxial growth on step-bunched surfaces, individual single steps are continually "ejected" from the base of one bunch and captured by the adjacent bunch. An illustration of this is shown schematically in Fig. 57(b). The implications of this step ejection and capture are very important: a step that is initially located at the base of a bunch will preferentially incorporate the smaller element in the alloy, since that step is in compression. However, after the step is ejected and captured by the adjacent bunch, it is now located at the top of the bunch, and so will switch its incorporation preference to the larger element in the alloy. This provides a mechanism for individual steps to toggle their adatom incorporation preference between

the various elements in the alloy during epilayer growth. Simple geometric considerations of the crystallography dictate that exactly such a mechanism must exist in order to achieve a superlattice that has an additional tilt angle with respect to the steps. Additional tilt requires that individual steps switch their adatom incorporation preference back and forth during epilayer growth. (This can be seen in Fig. 56 by tracing any particular step.) The rate at which this toggling occurs dictates the magnitude of the additional tilt – if steps are rapidly ejected from a bunch and therefore rapidly switch their adatom preference, the superlattice will have a large additional tilt angle. On the other hand, if the step-bunches are essentially static during growth and rarely eject individual steps, then the superlattice will have essentially the same tilt angle as the surface steps.

The results of this model were extremely impressive and of interest because they seemed to explain the origin of the additional tilt angle seen in Figs. 54(a)-(h) and (n). However, previous AFM studies of surface morphology by Wang revealed that samples that had a tilted superlattice were not always step-bunched. In particular, GaInAsSb grown at 525 °C is vicinal (single atomic steps) while that grown at 575 °C is step-bunched [157], but tilted superlattices occurred in both cases. In addition, the period of the tilted superlattice was typically 15-30 nm, much larger than the height of the step-bunches typically seen in GaInAsSb grown at 575 °C. Since the Venezuela model depends on alloy decomposition at step-bunches, it was unclear that the model was directly applicable to the results of this thesis. This suggested that it was not step-bunches, but rather another surface feature, that was directly related to the tilted superlattice.

Closer examination of the surface morphology of samples with a tilted superlattice discovered such a surface feature. AFM images revealed that undulations were present on the surface of all samples with a tilted superlattice. Examples of these undulations are shown in Fig. 58. The samples in Fig. 58 correspond to the samples in Fig. 54 as follows:

Fig. 58 (a) is a 3-D AFM image of sample #2 (shown in Figs. 54 (a)-(c))
Fig. 58 (b) is an overhead (2-D) AFM image of sample #5 (shown in Fig. 54 (g))
Fig. 58 (c) is a 2-D AFM image of sample #4 (shown in Fig. 54 (h))
Fig. 58 (d) is a 2-D AFM image of sample #14 (shown in Figs. 54 (d) and (e))
Fig. 58 (e) is a 3-D AFM image of sample #10 (shown in Fig. 54 (f))

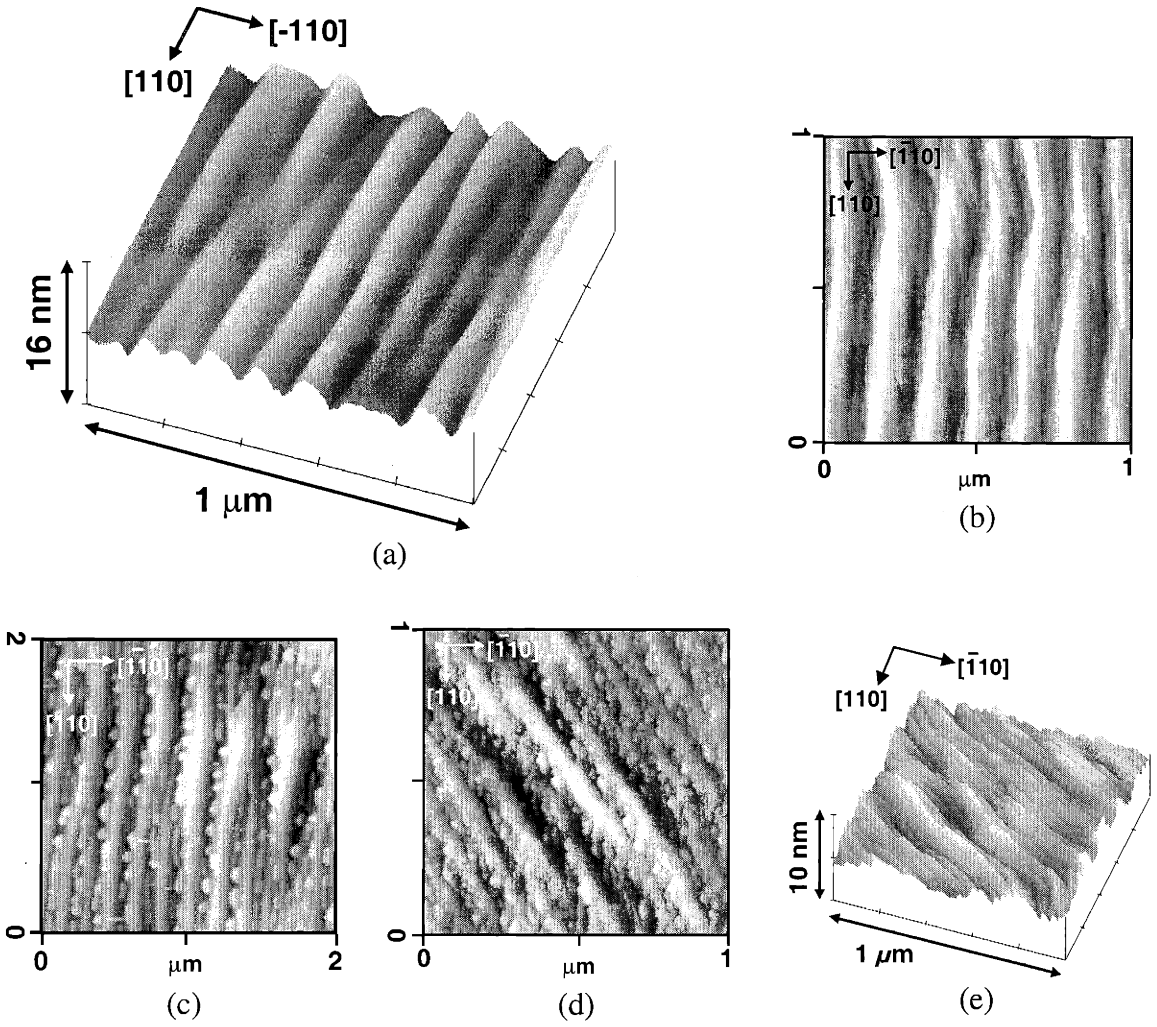

Fig. 58. AFM images of the surface undulations present on surfaces of samples with a tilted superlattice. These are the surfaces of the samples seen in: (a) Figs. 54(a)-(c), (b) Fig. 54(g), (c) Fig. 54(h), (d) Fig. 54(d)-(e), and (e) Fig. 54(f). The undulations were formed to relieve local strain associated with the lateral surface segregation due to the tilted superlattice.

Two characteristics of these undulations suggested that they were related to the tilted superlattice. The first is that the lateral period of these undulations was in good agreement with the lateral period of the tilted superlattice when it intersected the growth surface. As an example, consider Fig. 58(a) and Figs. 53(a)-(c). The AFM image indicates that the surface undulations had a lateral period of about 115 nm. The tilted

superlattice had a period of 20 nm, and a tilt angle of 10°. (The period was measured perpendicular to the direction of superlattice propagation, i.e. parallel to the direction of the composition modulation.) Simple geometry indicates that when a 20 nm period tilted at a 10° angle intersects the free surface, it will have a lateral period of: 20 nm / sin (10°) = 115 nm. Thus, the lateral period of the tilted superlattice and the surface undulations was the same. More examples of this correlation are given in Table VI.

Table VI. Correlation of Tilted Superlattice and Surface Undulations

Sample	SL Period	SL Tilt Angle	SL Lateral Period	AFM Period
Fig. 58(a)	20 nm	10°	115 nm	115 nm
Fig. 58(b)	14.6 nm	5.8°	144 nm	143 nm
Fig. 58(c)	30 nm	7.2°	239 nm	243 nm
Fig. 58(d)	11 nm	6.5°	97 nm	110 nm
Fig. 58(e)	13.8 nm	6.0°	132 nm	160 nm

In addition, AFM images, TEM images, and reciprocal space x-ray maps (not shown here) indicated that the amplitude of the surface undulations was related to the strength of the tilted superlattice. Taken together, the correlation of their lateral periods and strength (amplitude) suggests that the tilted superlattice and surface undulations were related phenomena. It is proposed that the surface undulations played a similar role to step-bunches in the Venezuela model. The qualitative model for development of the tilted superlattice is therefore as follows. During deposition of the first few monolayers of GaInAsSb, a random mix of Ga, In, As, and Sb adatoms was present on the surface of the GaSb substrate. This is shown schematically in Fig. 59(a). Due to the thermodynamic driving force of the miscibility gap, the adatoms segregated to form a lateral composition modulation along the surface. One phase (labeled "1" in Fig. 59(b))

was slightly enriched (~ one atomic percent) in InSb, while the other phase (phase "2") was slightly enriched in GaAs. Once such a lateral composition modulation existed, there was a large elastic strain field along the surface due to the lattice-mismatch between the two GaInAsSb phases enriched in GaAs and InSb. As Glas has recently shown theoretically [158], a surface with such a lateral composition modulation can effectively relieve its strain if the larger lattice constant phase (the InSb-rich phase in this case) forms peaks, while the smaller lattice constant phase (the GaAs-rich phase) forms valleys. The surface therefore formed a series of peaks and valleys, creating surface undulations as shown in Fig. 59(c). This explains the undulations seen in the AFM images of Fig. 58. This concept of coupled compositional and morphological perturbations was seen on a much stronger scale in samples #11 and 12, in sec. 4.4.2.

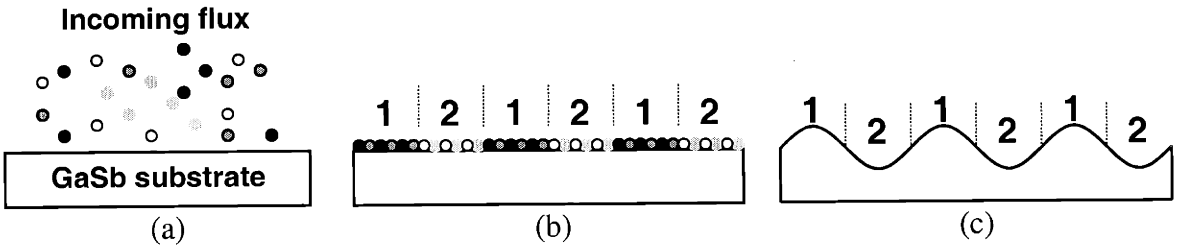

Fig. 59. Schematic illustration of the formation of the surface undulations associated with the tilted superlattice. (a) The random flux of incoming adatoms (b) laterally phase separated due to the miscibility gap. (c) The strain due to this lateral composition modulation was relieved by the larger-lattice-constant phase (InSb-rich) forming surface peaks, while the smaller-lattice-constant phase (GaAs-rich) forms surface valleys.

Once such undulations formed, all subsequent epitaxial deposition was biased in the sense that the surface peaks preferentially incorporated InSb-enriched GaInAsSb, while the surface valleys preferentially incorporated GaAs-enriched GaInAsSb. In other

words, when each successive monolayer was deposited and laterally phase separated, the InSb- and GaAs-rich regions were not randomly situated with respect to the underlying InSb- and GaAs-rich regions. Rather, the new InSb- and GaAs-rich regions were strain-locked to the underlying InSb- and GaAs-rich regions due to the strain field of the surface undulations [107, 158]. This strain-locking explains the robustness of the superlattice – why it is that any particular dark or light band seen in the TEM continues uninterrupted during growth of the entire epilayer. (This strain-locking effect is so strong it can actually force phase separation in an epilayer that does not normally do so. See section 4.4.3.2 for details.) Such strain-locking mechanisms due to surface strain are known to play important roles in other epitaxial phenomena. One example is the vertical registry of multiple layers of quantum dots, discussed previously in section 4.4.1.1. Another example is the atomic ordering (e.g. CuAu, CuPt) seen in many III-V ternary and quaternary compounds, which is now believed to be caused by surface reconstructions (dimers) [101]. The ordered microstructure is typically energetically unfavorable in the bulk based on theoretical calculations and experimental annealing experiments [101, 145]. However, the surface dimers create a strain field 2-3 monolayers below the surface such that group III elements will alternate along {110} or {111} planes to minimize surface strain energy. Thus, the effect of surface strain fields explains various phenomena seen in epitaxial microstructures, and also likely explains the continuity and robustness of the tilted natural superlattice in GaInAsSb.

The additional tilt of the superlattice with respect to the surface steps can be understood from a similar mechanism to that in the Venezuela model. Rather than ejection and capture of single steps from step bunches, in this case the additional tilt is

caused by ejection and capture of single steps from surface peak or valley regions. The lateral period of the undulations was typically 100-200 nm. Each peak or valley region was therefore 50-100 nm, and thus comprised on average 17-34 individual steps (for a 6° miscut) or 6-11 steps (for a 2° miscut). As epitaxial growth proceeded, if an individual step was ejected by a valley and captured by an adjacent peak, that step would switch its incorporation preference from GaAs-enrichment to InSb-enrichment. Similarly, that step would eventually be ejected from the peak and captured by the adjacent valley, switching its preference back to GaAs-enrichment. The magnitude of the additional tilt was dependent on the relative lateral velocities of the surface undulations and the individual steps that comprised those undulations.

4.4.3.2 Effect of surface strain fields on promoting phase separation: tilted superlattice example

Further proof of the importance of strain-locking and the impact of surface strain fields on epitaxial growth is given in Fig. 60. Figure 60(a) shows side-by-side DF <2-20> 2-beam images of a sample with the following structure:

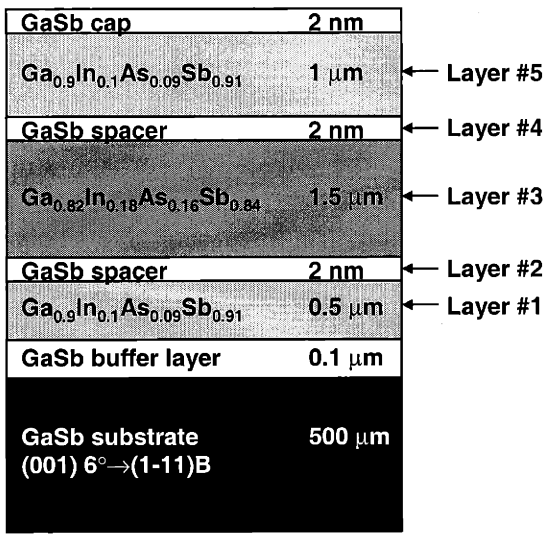

All layers were grown at 525 °C except for the buffer layer, which was grown at 550 °C.

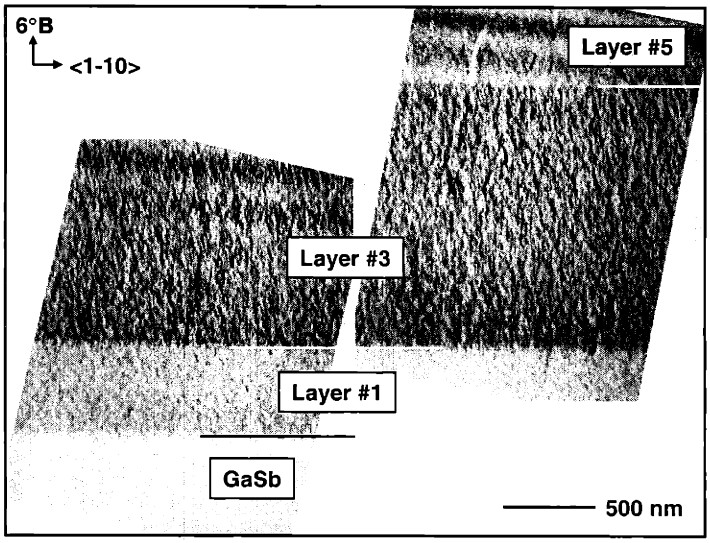
6°B
<1-10>
Layer #5
Layer #3
Layer #1
GaSb
500 nm

(a)

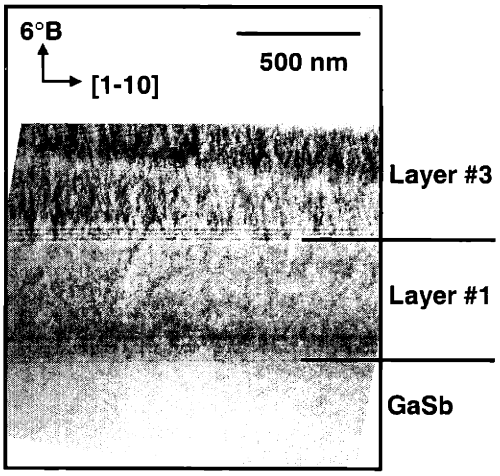
6°B
[1-10]
500 nm
Layer #3
Layer #1
GaSb

(b)

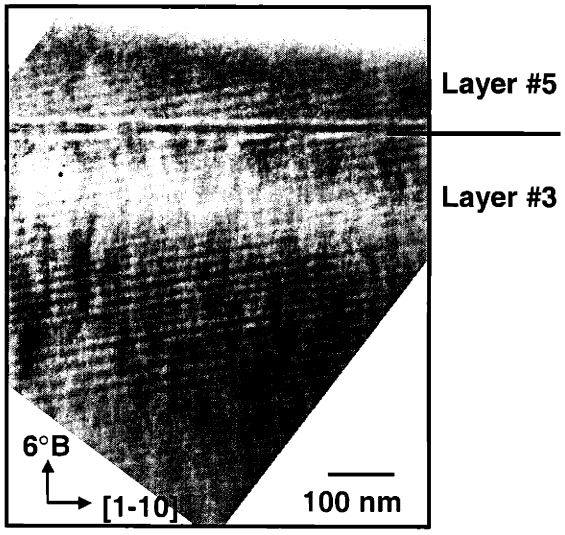
Layer #5
Layer #3
6°B
[1-10]
100 nm

(c)

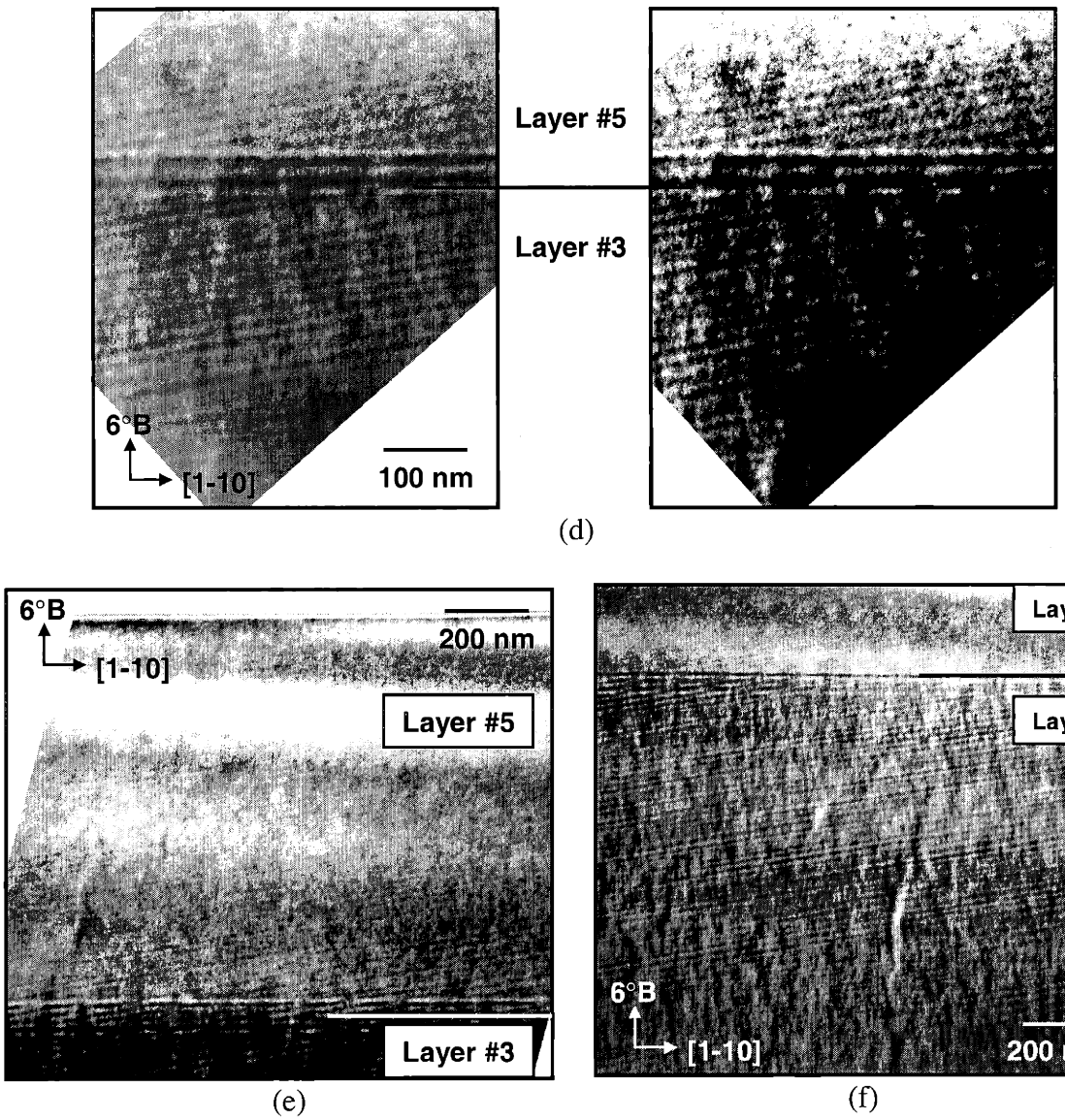

Fig. 60. TEM images illustrating the effect of a surface strain field on promoting phase separation. The epitaxial structure is shown in (a) using <220> 2-beam diffraction conditions. The <222> 2-beam image in (b) indicates that Layer #3 had a tilted superlattice, while Layer #1 did not, which was expected based upon previous growth runs. However, Layer #5 – which was exactly the same as Layer #1 – is seen to have had a tilted superlattice in (c)-(f). The superlattice was promoted in Layer #5 by the surface undulations present due to the tilted superlattice in Layer #3.

Layers #1 and 5 had exactly the same composition and growth conditions, and were very similar to sample #1 in section 4.4.1. The growth conditions and composition

of this alloy yield the highest-quality, most homogeneous epilayer studied in this thesis. Layer #3 was very similar to sample #2 in section 4.4.1, also shown in Fig. 54(a)-(c). Based on the characterization results of sample #2 in section 4.4.1, it was expected that layer #3 above would have strong spinodal-decomposition-like contrast, and a strong, uniform natural tilted superlattice throughout the epilayer. The surfaces of layers #3 and 4 were expected to have undulations associated with the tilted superlattice, as discussed in section 4.4.3.1 above. (It was known from previous experiments that the thin GaSb layer – layer #4 – would conform to the surface of layer #3, and would not planarize or change the morphology of layer #3.) The <2-20> image in Fig. 60(a) indicates that layer #3 did indeed exhibit strong spinodal-like contrast, while layers #1 and 3 barely exhibited more contrast than the GaSb substrate.

The interesting results from this sample are shown in the cross-section TEM images in Figs. 60(b)-(f). Figure 60(b) is a <2-22> 2-beam image of the substrate, buffer layer, and layers #1-3. As expected based on previous results, layer #3 exhibited a tilted superlattice (tilted at 10° with respect to the growth direction), while there was no superlattice in layer #1. However, there *was* a tilted superlattice in layer #5, as seen in Figs. 60(c)-(f). These <2-22> 2-beam images show layers #3-5. Figure 60(c) is a close-up of the interface between layers #3 and 5. The left panel of Fig. 60(d) is a higher magnification of this region, and is shown with increased contrast in the right panel. Figure 60(e) shows layer #5 completely. If this image is viewed obliquely (i.e. at a glancing incidence angle to the page), it can be seen that the tilted superlattice is present throughout the entire epilayer, although it appeared to weaken as growth proceeded. Finally, Fig. 60(f) is a lower magnification image of layers #3-5, from which the relative

strength of the tilted superlattice composition modulation between layers #3 and 5 can be discerned.

The tilted superlattice present in layer #3 was propagated into layer #5, even though the superlattice was not present in layer #1 and layers #1 and 5 were *exactly* the same! These images clearly illustrate the coupling of compositional and morphological perturbations. Even though layer #5 did not inherently want to phase separate to form a tilted superlattice, it did so because the surface undulations present from layer #3 created a surface strain field that continued to drive lateral surface segregation. This is in line with calculations of the Venezuela/Tersoff model mentioned earlier, which predicted phase separation for alloys grown on surfaces with modulated strain fields. In this case, the tilted superlattice from layer #3 created surface undulations, as discussed before. These undulations can be seen in Fig. 60(c) in layer # 4 (the thin GaSb spacer layer between layers #3 and 5). Regions where a dark band from layer #3 intersect layer #4 also appear dark, while light regions appear light. The lateral period of these dark and light regions in layer #4 is about 100 nm. This correlates with the tilted superlattice, which had a period of 17.2 nm and a tilt angle of 9.7°, yielding a lateral period of [17.2 nm / sin (9.7°)] = 102 nm. Therefore, layer #4 provides additional evidence that the tilted superlattice composition modulation is coupled to the surface undulations.

When layer #5 was deposited on the undulated surface of layer #4, it laterally phase separated and propagated as a tilted superlattice even though it did not inherently want to do so. The surface peaks continued to preferentially incorporate InSb-rich GaInAsSb, while the surface valleys preferentially incorporated GaAs-rich GaInAsSb. This provides direct evidence of the ability of surface strain / roughness to promote phase

separation. As growth proceeded, the strength of the tilted superlattice weakened in layer #5 because layer #5 was not grown under conditions that would inherently promote the tilted superlattice, and the surface undulations from layer #3 could not force this form of phase separation in layer #5 indefinitely.

4.4.3.3 Phase space framework for tilted superlattice

The qualitative model for self-organization of a tilted superlattice in GaInAsSb was given in section 4.4.3.1 as follows:

- A random mix of Ga, In, As, and Sb adatoms deposits from the vapor on the GaSb substrate and laterally phase separates to form slightly GaAs- and InSb-enriched phases due to a miscibility gap.
- The growth surface forms undulations to relieve the strain associated with this lateral phase separation. The InSb-rich phase forms peaks, while the GaAs-rich phase forms valleys.
- All subsequent epitaxial deposition and phase separation is strain-locked by the strain field of the surface undulations. Therefore, the continuity of the superlattice is very robust.
- Due to step-flow growth, the lateral phase separation propagates as a tilted superlattice throughout the epilayer. The additional tilt angle of the superlattice with respect to the surface steps depends on the relative lateral flow rates of the surface steps and surface undulations.

Since the tilted superlattice was only present for certain alloy compositions and growth conditions, it is of interest to understand what conditions promote or inhibit formation of the tilted superlattice. Examination of Fig. 54 and Table V does not immediately suggest any pattern for the formation of the tilted superlattice – it seems to be randomly present in samples of different alloy compositions, grown on different substrates and at different temperatures. The key to interpreting these results lies in the fact that the qualitative model discussed above clearly depends on the ability of the just-deposited surface adatoms to diffuse on the growth surface, and laterally phase separate in an orderly fashion to form InSb- and GaAs-rich phases. Therefore, the samples should be mapped

out in a framework based on the thermodynamic driving force for phase separation vs. the kinetic growth barrier to surface diffusion. At one extreme, if a sample has little or no thermodynamic driving force for phase separation, and is grown under conditions that impose large kinetic barriers to surface diffusion, that sample will be fairly homogeneous and exhibit minimal phase separation. At the other extreme, if a sample has a large driving force for phase separation and is grown under conditions that present only minimal barriers to surface diffusion, that sample will exhibit strong phase separation.

Neither of these conditions would be expected to promote the tilted superlattice. For the first case, surface diffusion is inhibited too greatly to enable the required lateral segregation. In the second case, the lateral segregation is not controlled well enough to result in the orderly phase separation required for the tilted superlattice. Examples of samples in both these categories were observed in this thesis. Samples #1 and 3 in Table III were essentially homogeneous with minimal phase separation, as evidenced by minimal contrast in TEM images, a narrow 4 K PL FWHM, a narrow x-ray FWHM, and a uniform, regular surface morphology. Samples #11 and 12 in Table III were at the other end of the spectrum and exhibited gross phase separation, as evidenced by broad inhomogeneities in TEM images, a broad 4 K PL FWHM, broad tilt/mosaicity in RSXRM, and perturbations in the surface morphology that coupled to the phase separation. Sample #6 was also fairly phase separated based on a broad 4 K PL FWHM and epilayer broadening in RSXRM due to tilt/mosaicity (not shown here).

The tilted superlattice was instead present for a third group of conditions, where the thermodynamic driving force for phase separation was balanced by the kinetic barrier to surface diffusion. This situation enabled the orderly surface segregation required to

form the tilted superlattice. Figure 61 shows the framework that maps out these three categories: minimal phase separation (PS); strong PS; and formation of a tilted superlattice. The thermodynamic driving force for phase separation increases along the x-axis, and is dependent on the alloy composition and growth temperature. As the alloy goes further into the miscibility gap (increasing fraction of InAs in GaInAsSb and longer PL peak wavelength), the thermodynamic driving force obviously increases. In addition, as the growth temperature is reduced the thermodynamic driving force for phase separation increases because of the increasing importance of enthalpic vs. entropic contributions (see section 4.1.1 above). The kinetic barrier to surface diffusion increases along the y-axis, and is dependent on the substrate miscut angle, miscut direction, and growth temperature. The growth rate would also be on this axis but is not included here because it was not one of the variables studied in this thesis. The TEM, PL, x-ray, and AFM results from the previous sections indicated that the kinetic barrier to surface diffusion increased as the miscut angle increased; on (1-11)B surface steps vs. (101) surface steps; and as the growth temperature decreased.

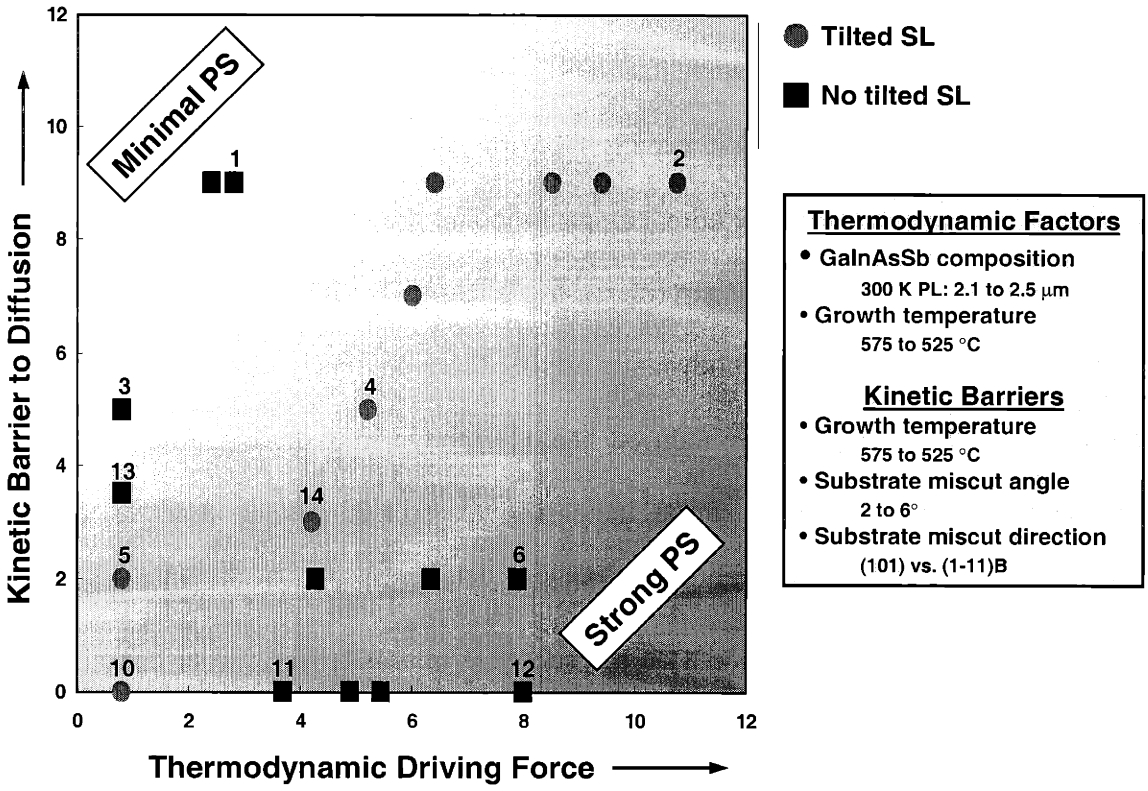

Fig. 61. Framework for formation of tilted superlattice (SL) and general extent of phase separation (PS).

This qualitative framework can be made semi-quantitative – and specific samples can be plotted on it – if quantitative "points" or values are assigned to each of the 5 parameters listed above. Table VII below lists values used for Fig. 61. This process is somewhat arbitrary and it is not suggested that these values have any physical meaning. However, the relative values are not completely arbitrary since estimates can be made based upon data from the previous sections. For example, it is expected that growth temperature will have a larger effect on the kinetic barrier to surface diffusion (due to the exponential temperature dependence of diffusion) than on the thermodynamic driving force for phase separation. This is in line with results that indicated that the phase

separation was more extensive for samples grown at higher temperatures. Therefore, the relative change in values along the y-axis for different temperatures should be larger than the change along the x-axis, as is the case in Table VII.

Sample numbers shown on the plot refer to the list in Table III. Other samples are also included in Fig. 61 that were not listed in Table III.

Table VII. "Points" System for Thermodynamic and Kinetic Parameters	
Thermodynamic Parameters (x-axis)	
300 K PL Peak Wavelength (μm)	**Points/Value**
2.0	0
2.1	2
2.2	4
2.3	6
2.4	8
2.5	10
Growth Temperature (°C)	**Points/Value**
525	1
550	0
575	-1
Kinetic Parameters (y-axis)	
Substrate Miscut Angle (°)	**Points/Value**
2	1
4	2.5
6	4
Substrate Miscut Direction	**Points/Value**
(101)	1
(1-11)B	3
Growth Temperature (°C)	**Points/Value**
525	2
550	0
575	-2

(In the table, the 300 K PL peak wavelength is used as a proxy for the actual GaInAsSb alloy composition. As the alloy goes further into the miscibility gap, the content of InAs increases, and the PL peak shifts to longer wavelengths.)

An example of how this table was used is as follows. Sample #2 in Table III had a 300 K PL peak at 2.485 μm and was grown at 525 °C on a substrate oriented (001) 6° toward (1-11)B. The thermodynamic driving force for a 2.485 μm PL peak equals 0.85*10 + 0.15*8 = 9.7 "points", while a growth temperature of 525 °C equals 1 "point". The total thermodynamic driving force was therefore 9.7 + 1 = 10.7. The kinetic barrier was similarly obtained as 4 (6° miscut angle) + 3 ((1-11)B miscut direction) + 2 (525 °C growth temperature) = 9. Therefore, sample #2 was plotted at (10.7,9), and it had a tilted superlattice.

It was seen that the samples in the upper left-hand corner of the framework exhibited minimal phase separation, because they had a very low thermodynamic driving force for phase separation in addition to a high kinetic barrier to surface diffusion. Samples in the bottom right-hand corner exhibited gross or coarse phase separation, since they had a large thermodynamic driving force to phase separate and a low kinetic barrier to surface diffusion. It was the samples in between these two cases, which had a balance between thermodynamics and kinetics, that exhibited the tilted superlattice. These samples lie along the diagonal from the lower left to the upper right corner. Samples in this region underwent orderly phase separation and could therefore form the tilted superlattice.

Although this chart and the points/values used to create it are not expected to be completely accurate, the general idea of the framework remains valid: that the tilted superlattice will be formed under conditions that balance the thermodynamic driving force to phase separate with the kinetic barriers to surface diffusion. Additional

parameters could also be included in the chart but were not studied in this thesis, such as epilayer growth rate and lattice mismatch (global epilayer strain).

4.5 Summary of phase separation in GaInAsSb

$Ga_{1-x}In_xAs_ySb_{1-y}$ alloys with ($0.1 < x < 0.2$) and ($0.09 < y < 0.18$) lie in or near the calculated bulk miscibility gap. Thermodynamic calculations predict phase separation into a smaller volume of strongly GaAs-enriched alloy and a larger volume of weakly InSb-enriched alloy. Although OMVPE growth conditions kinetically limit thermodynamic driving forces, the effect of these thermodynamic forces is clearly seen in the microstructures of GaInAsSb samples shown in section 4.4. Alloy compositions that lie furthest outside the miscibility gap exhibit very homogenous microstructures, with minimal contrast in TEM images, narrow 4 K PL FWHM, and smooth, regular surface morphologies. As the alloy composition goes further into the miscibility gap, the thermodynamic driving force for phase separation increases and the resulting microstructure is inhomogeneous. Interestingly, different forms of phase separation can co-exist in the same sample. Spinodal-like contrast was observed in every sample, with increasing contrast further in the miscibility gap. Simultaneously, a natural superlattice was also observed in every sample. Although the origin of the parallel variant is unclear, the tilted variant was explained as caused by lateral phase separation on the growing surface that propagated in a tilted fashion throughout the microstructure due to complex step-flow dynamics. Finally, in the most phase-separated samples, smaller-volume GaAs-rich vertical slabs were formed in the alloy, while the remainder of the material was slightly InSb-rich. Both these slabs and the tilted superlattice were observed to create and couple to perturbations in the surface morphology, providing experimental

evidence of such coupling theories advanced in the literature. Additional evidence of this coupling was given in section 4.4.3.2, where an example was shown of a GaInAsSb sample that does not inherently phase separate to form a tilted superlattice but was forced to do so by depositing it on the tilted superlattice template from an underlying sample. Since surface roughness and strain fields therefore promote phase separation, this presents another reason to eliminate the bromine-based etch from GaSb substrate preparation since it is known that this etchant roughens the GaSb surface.

It was also observed that the thermodynamic driving force for phase separation could be inhibited by varying kinetic growth parameters. These parameters included the direction of substrate miscut, angle of miscut, and growth temperature. That the miscut direction had a strong influence on the resulting phase-separated microstructure illustrates the important role of surface processes on the resulting microstructure. This balance between thermodynamics and kinetic barriers was mapped out in the framework of Fig. 61, and gave insight into the growth conditions for which a tilted superlattice could be expected to form in GaInAsSb. It was suggested that the main requirement, along with step-flow growth, is that the growth conditions are such that there is a balance between the thermodynamic driving force for phase separation and the kinetic barrier to surface diffusion. This map was helpful in interpreting the TEM microstructure results obtained in this thesis.

5. Conclusions

Antimonide-based epilayers are often used as the active layer in mid-IR devices such as lasers, detectors, and thermophotovoltaics (TPVs). However, these materials are not well characterized compared to other III-V semiconductors, such as the arsenides, phosphides, and nitrides. This thesis focused on characterizing GaSb, $Ga_{1-x}In_xAs_ySb_{1-y}$ ($0.1 < x,y < 0.2$), and $Al_xGa_{1-x}As_ySb_{1-y}$ ($0 < x < 1$, $0 < y < 0.08$) epilayers used in TPVs. Specifically, *in situ* reflectance was used to study the epitaxial growth characteristics, while *ex situ* TEM and AFM were used to characterize the microstructure and phase separation of GaInAsSb.

An *in situ* spectral reflectance monitor was designed and fitted to the organometallic vapor phase epitaxy (OMVPE) reactor. This reflectance system had a spectral range of 380-1100 nm. The advantage of spectral reflectance over single-wavelength reflectance was demonstrated in that the reflectance system can be optimized to observe various growth processes by selecting the wavelength that is most sensitive to a particular process. Quantitative curve-fitting of the reflectance oscillations to obtain epilayer growth rates was most successful at longer wavelengths (1000 nm) due to lower

optical absorption. The *in situ* reflectance oscillations were also curve fit to obtain the (growth temperature) refractive index of different epilayers. This parameter is typically only of interest in that it is related to the alloy composition. However, it was determined that an easier method of obtaining alloy compositions is to use *in situ* reflectance ratios. Specifically, the ratio of the *in situ* GaInAsSb baseline reflectance to that of the GaSb buffer layer was observed to correlate linearly with the 300 K photoluminescence peak wavelength of the GaInAsSb epilayer, yielding the following equation:

$$\text{300 K PL peak wavelength of GaInAsSb (nm)} = -16649*m + 18285 \qquad (12a)$$

where m is the reflectance ratio. This technique accurately determines the 300 K PL peak within 1% of the actual *ex situ* measurement, and is obviously faster than performing the *ex situ* PL measurement. In addition, since this technique relies on a reflectance ratio, it is highly accurate, and does not require calibration to absolute reflectance units. The reflectance can be measured using any arbitrary units, as long as it scales linearly with the absolute reflectance. This ratio is most sensitive near λ = 700 nm since the reflectance difference between GaSb and GaInAsSb is greatest at this wavelength.

A similar calibration was obtained for $Al_xGa_{1-x}As_ySb_{1-y}$ alloys. In this case, the reflectance ratio of the AlGaAsSb epilayer to the GaSb buffer was taken at λ = 500 nm. This was because the AlGaAsSb baseline reflectance in thin layers was easier to measure at 500 nm due to increased optical absorption at 500 nm vs. 700 nm. The following equations were determined:

$$\text{Al fraction 'x'} = -8.428*m + 8.795 \qquad (m < 0.986) \qquad (12b)$$
$$\text{Al fraction 'x'} = -34.149*m + 34.155 \qquad (m > 0.986) \qquad (12c)$$

Again, m was the reflectance ratio. There was a kink in the data at m = 0.986 (x = 0.48), and therefore two separate equations, due to the crossover from a direct to indirect

bandgap. The crossover at x = 0.48 (T = 550 °C) correlated very well with reported literature values of x = 0.45 at T = 25° C [52-54].

The *in situ* reflectance was also used to study GaSb substrate oxide desorption. Shorter wavelengths (500 and 633 nm) were more sensitive to this process. Various etch procedures were examined. Using *in situ* reflectance and *ex situ* AFM data, the following etch procedure was determined to yield the highest-quality, most reproducible GaSb substrate surfaces for epitaxial growth:

1. Solvent rinse (hot trichloroethylene, acetone, 2-propanol)
2. Etch/agitate in HCl (3-5 min)
3. 2-propanol rinse (10 times)
4. Sheet 2-propanol off substrate surface using N_2
5. Heat GaSb to any temperature between 525 and 575 °C for at least 600 s

It was also demonstrated how the *in situ* reflectance could be used to perform reactor/growth calibrations. For example, the minimum V/III ratio was quickly determined in one growth run using *in situ* reflectance at 500 nm. Additionally, the *in situ* reflectance was sensitive to the minimum organometallic source pre-flow time for equilibration, and to a loss of source material during a growth run.

Analytic functions were generated for GaSb, $Ga_{0.84}In_{0.16}As_{0.14}Sb_{0.86}$, and $Al_xGa_{1-x}AsSb$ ($0 < x < 1$) between 1 and 3 μm by curve-fitting second-, third-, and fourth-order polynomials to reported experimental data. The model for $Al_xGa_{1-x}AsSb$ was created using a linear interpolation between data for GaSb and $AlAs_{0.08}Sb_{0.92}$. This worked well since there is only minimal bowing between these two endpoints [52, 53]. Adachi's Model Dielectric Function [1, 2] was curve-fit to data for GaSb, GaAs, InAs, and InSb between 200 and 1000 nm. These analytic functions were helpful in

interpreting *in situ* reflectance data, and in designing distributed Bragg reflectors used as back surface reflectors in TPVs.

$Ga_{1-x}In_xAs_ySb_{1-y}$ alloy compositions ($0.1 < x,y < 0.2$) used for the active layers in TPVs lie in or near a calculated bulk miscibility gap. These layers are therefore expected to have a thermodynamic driving force to phase separate. Previous PL, AFM, and x-ray studies of phase separation in these epilayers by Wang demonstrated the importance of various growth parameters on kinetically inhibiting the extent of phase separation. This thesis focused on characterizing the microstructure and extent of phase separation using TEM and AFM. Epilayers were studied as a function of growth temperature (525 vs. 575 °C), alloy composition ($x,y = 0.1$ to $x,y = 0.2$), substrate miscut angle (2 to 6°), and substrate miscut direction ((-1-11)A vs. (1-11)B vs. (101)). A wide range of microstructures was observed, from nearly homogeneous to strongly phase separated. The microstructures correlated well with the previous characterization results from Wang. Specifically, alloys grown at 525 °C on substrates oriented (001) 6° toward (1-11)B with compositions further outside the miscibility gap exhibited the most homogeneous microstructures, and previously exhibited the narrowest 4 K PL FWHM and most uniform surface morphology. The extent of phase separation increased for higher growth temperatures, smaller miscut angles, (101) miscut direction, and alloy compositions further into the miscibility gap. For a given alloy composition and growth temperature, the microstructure was observed to be strongly dependent on the substrate miscut angle and direction. This result underscored the importance of surface thermodynamics and kinetics in epitaxial growth processes.

The most phase-separated samples formed vertical slabs (spaced about 100-200 nm apart) throughout the epilayer. Energy-dispersive x-ray measurements indicated that the material had phase separated to a smaller-volume phase enriched 2-3 atomic percent in GaAs, and a larger-volume phase slightly enriched in InSb. This was similar to previously reported results [154], and in line with reported thermodynamic calculations [92, 93, 149]. In addition, it was observed using x-sec TEM that the composition modulation created and coupled to perturbations in the surface morphology. This type of coupling is in agreement with theoretical models in the literature [107, 158].

One interesting manifestation of the phase separation was the spontaneous formation of a natural superlattice throughout the epilayer. Two variants of this superlattice were observed – one parallel to the growth surface, and one tilted with respect to the growth surface. The tilted variant had an additional tilt angle with respect to the substrate miscut angle and was studied in detail. This superlattice was likely a composition modulation into slightly (approximately one atomic percent) GaAs- and InSb-rich regions, since it could also be detected using reciprocal space x-ray mapping and field-emission scanning electron microscopy (after a brief stain etch). It was observed that all samples that had a tilted superlattice also had surface undulations. The lateral period of these undulations correlated with the lateral period of the tilted superlattice when it intersected the free surface. This suggested that the undulations were formed to relieve the local strain due to the composition modulation associated with the tilted superlattice, providing another example of the coupling between a composition modulation and features in the surface morphology. A qualitative model for the propagation of the tilted superlattice was proposed, wherein the robustness or continuity

of the superlattice was due to strain-locking by the surface undulations. The impact of this surface strain field was clearly demonstrated by its ability to promote the tilted superlattice in an epilayer that did not inherently form such a superlattice. These results were shown in Fig. 60. Additionally, it was proposed that the additional tilt angle of the superlattice with respect to the substrate miscut angle was due to individual step ejection and capture between adjacent peak and valley regions in the surface undulations. This is similar to the model proposed by Venezuela *et al.* [161], although alloy decomposition took place at step-bunches in their model which was different than these thesis results.

Finally, the samples studied by TEM were mapped out in a framework of thermodynamic driving force for phase separation vs. kinetic barrier to surface diffusion. Samples with minimal thermodynamic driving force and a high kinetic barrier to diffusion exhibited fairly homogeneous microstructures with minimal phase separation. Samples at the other extreme, with a large thermodynamic driving force to phase separate and minimal kinetic barrier to surface diffusion, exhibited inhomogeneous microstructures with stronger phase separation. The tilted superlattice was observed for samples that were in between these two domains, and had a balance between the thermodynamic driving force for phase separation and the kinetic barrier to surface diffusion.

6. Future Work

Results from the *in situ* reflectance system indicated that it was sensitive to both bulk optical properties (the interference growth oscillations) and surface optical properties (e.g. substrate oxide desorption). One important property for thin-film devices is the interface quality between epilayers, which depends on epilayer surface stability. The epilayer surface stability is important because crystal growers often use growth pauses during gas switching sequences between different epilayers. These pauses are designed to ensure that the gases from one epilayer are completely out of the reactor when the gases from the next epilayer are switched in, to obtain the most atomically abrupt interfaces possible. However, the quality of the interface between these epilayers will be compromised if the epilayer surface is not stable during this growth pause. If the *in situ* reflectance is sensitive to the epilayer surface stability, these growth pauses could be properly designed using *in situ* diagnostics to determine the most suitable procedure. Initial results (not presented in this thesis) suggested that the *in situ* reflectance is indeed sensitive to epilayer surface stoichiometry/stability. In particular, it was seen that the GaSb surface was relatively stable under a H_2 anneal, becoming only slightly non-

stoichiometric which could be corrected using a low flow of trimethylantimony (TMSb). The GaInAsSb surface, however, was less stable under a H_2 anneal. The difference between the GaInAsSb and GaSb surfaces was likely due to the higher volatility of As compared to Sb. A capping layer of Sb on the GaInAsSb surface seemed to improve its stability; however, this may have promoted an As/Sb exchange reaction at the surface [172]. It would be of great interest to conduct a detailed study of the sensitivity of the *in situ* reflectance to epilayer switching sequences, and correlate the results with *ex situ* characterization to determine the most suitable ambient and switching time to preserve epilayer surfaces and obtain high-quality epitaxial interfaces.

The TEM images of phase separation in GaInAsSb raised several interesting questions about the phase separation mechanisms, some of which remain unanswered. In particular, it would of interest to understand the initial formation stages of the tilted superlattice, and the mechanism that formed the parallel superlattice. The qualitative model presented in section 4.4.3 explained the propagation of the tilted superlattice throughout the epilayer once it formed. However, it is still unclear why and how the initial random adatom mixture phase separated laterally on the surface to form "stripes" aligned with the step edges, and with a period of 100-200 nm. One possibility is that there was some feature on the starting substrate surface that promoted this phase separation. However, it is hard to discern such a feature in the AFM images presented in section 2.4.3. This length scale seems to be common to other forms of phase separation. For example, the vertical slabs seen in grossly-phase-separated samples (see Figs. 50(b) and (c)) were spaced about 100-200 nm apart. Additionally, the coarse-contrast basket-weave pattern seen in LPE-grown InGaAsP samples (see section 4.2.1) typically had a

period of 100-200 nm. It is still unclear why the adatoms segregated in these particular patterns.

Initial results also indicated that the additional tilt angle of the tilted superlattice was typically 4° on samples that were not extensively phase separated. The exact origin of the 4° is not clear, as well as how (and whether) this additional tilt angle can be changed by altering various growth parameters.

It would also be of interest to ascertain whether the tilted superlattice could be promoted by pre-patterning the substrate surface. Results in section 4.4.3.2 indicated that the tilted superlattice could be forced to form in an epilayer that would not inherently due so by growing it on the surface of an epilayer that did form the tilted superlattice. However, it is not clear whether the tilted superlattice in the upper layer was promoted just by the morphology of the underlying epilayer, or whether the strain field associated with that morphology promoted the tilted superlattice. A pre-patterned substrate, created by lithography for example, would clarify this point, since it would have a morphological undulation with no associated strain field. Additionally, the period of this undulation could be very well defined using lithography, which would result in a very uniform tilted superlattice. A uniform, tilted superlattice might be of interest for certain devices.

It is also of interest to study the parallel variant of the superlattice in more detail. The process by which this superlattice formed is unclear, although it may be related to a global epilayer strain-oscillation mechanism. Finally, it would be of interest to understand the relationship between the various forms of phase separation observed in the epilayers: spinodal-like contrast, tilted superlattice, parallel superlattice, and coarse

vertical slabs. The fact that several of these phase separation forms could be observed in the same epilayer underscores the complicated nature of epitaxial growth.

Appendix A. TEM Specimen Preparation Procedure

Since GaSb and GaInAsSb are soft materials, the following procedure is recommended to minimize sample damage when preparing specimens for transmission electron microscopy (TEM).

1.0 Cleaving plan-view specimens

1.1 Cleave a 4 mm x 4 mm square from the wafer

1.2 Skip to section 3.0

2.0 Cleaving cross-section specimens

2.1 Cleave a section from the wafer that is 4 mm wide, and at least 10 mm long. **Note the orientation of the cleave**

2.2 Cleave this piece in half, yielding two pieces each at least 4 mm wide by 5 mm long

2.3 Cleave two pieces of scrap GaSb of the same size for supports

2.4 Apply M-Bond 610 (2-part liquid epoxy) to the top (growth) face of each of the two pieces cleaved in section 2.2

2.5 Glue these two pieces together, growth face to growth face

2.6 Apply M-Bond 610 to the top face of one of the support GaSb pieces. Glue it to the backside of one of the pieces of the sandwich formed in 2.5

2.7 Apply M-Bond 610 to the top face of the other GaSb support piece. Glue it to the backside of the other piece of the sandwich formed in 2.5

2.8 Place this 4-piece sandwich between the tips of Teflon-coated reverse-action tweezers. Make sure the pieces of the sandwich remain relatively well-aligned with one another—use another pair of normal tweezers to align the pieces if necessary.

2.9 Lightly squeeze the tips of the reverse-action tweezers to ensure that all the pieces are in intimate contact. Brush a little additional M-Bond 610 along all four edges of the sandwich. The pieces will uptake any additional necessary epoxy through capillary action.

2.10 Place the tweezers with sandwich into an oven. Bake at 150 °C for 1.5 hours.

2.11 After 1.5 hours, turn the oven off and allow the sandwich to cool in the oven for about 30 minutes. The sandwich is then ready to be sawed.

2.12 Mount the sandwich, long edge down, onto the aluminum block using black wax. Heat the hot plate to 150 °C (a setting of "4" on the dial) to melt the wax. Quench the block in a water beaker when ready.

2.13 Mount the aluminum block in the wire saw. Rotate the chuck so that the sandwich is aligned perpendicular to the wire blade.

2.14 Saw pieces about 0.75 to 1 mm thick. These will form one of the two orthogonal <110> cross-sections. Make sure to leave at least 3-4 mm of length on the un-sawed part for the other cross-section. Each full rotation of the saw handle translates the sample by 1 mm. Make sure to use diamond-impregnated wire saw blades, and continuously squirt water onto the saw blade/sandwich so that the saw is never dry-cutting the sandwich. Also squirt water onto the pulleys to keep them moistened.

2.15 Place the aluminum mount on the hot plate. Allow the black wax to soften for a minute or so, then remove the sawed pieces from the aluminum mount. Delicately trim any excess black wax off the sample with a scalpel.

2.16 The sawed pieces can now be ground down and polished as per section 3.0

2.17 The un-sawed piece of the sandwich, which will be used for the other cross-section, is too thick (4 mm) to be directly ground. It can be rotated and remounted (backside [001] face down) and sawed into 4 pieces each 1 mm thick.

3.0 Mounting and polishing

3.1 Measure height of glass or metal mounting stub of Gatan hand polisher using digital micrometer. Zero the reading when the stub height is being measured.

3.2 Place glass or metal mounting stub of Gatan hand polisher on hot plate. Heat to 150 °C (setting "4" on dial)

3.3 For plan-view sample, mount sample top (growth) face down, into the wax. For a cross-section sample, mount either side face down. Gently apply pressure to the sample with a toothpick so that the sample lies flat.

3.4 Using tongs, quench the mounting stub in water in a beaker.

3.5 Measure the height of the sample using the digital micrometer. For a plan-view sample, the height is typically 510-530 μm, depending on the substrate thickness. The thickness of a cross-section sample depends on how thick the pieces were saw cut.

3.6 Mount the stub in the Gatan hand polisher. Rotate the dial counter-clockwise to lower the sample into the hand polisher, until the top of the sample is flush with the metal face of the hand polisher. You can test for flushness by running a glass slide over the metal face – the slide should not catch on the sample. Zero the dial.

3.7 For a plan-view sample, grind sample down to a thickness of 100 μm using 600 grit wet/dry SiC sandpaper, advancing the sample in 25 μm increments. Do NOT apply additional downward pressure to the hand polisher!! Loosely grab the hand polisher, and allow the weight of it to provide the downward pressure on the sample. You can measure the sample thickness with the digital micrometer occasionally, although the micrometer dial of the Gatan hand polisher is fairly accurate. Grind back and forth in a straight line parallel to one edge of the sample. Each time you advance the micrometer 25 μm, rotate your grip on the hand polisher 180° so that you thin the sample evenly. Keep the sandpaper wet at all times. Occasionally rinse the sample with a water squirt bottle. Skip to 3.9.

3.8 For a cross-section sample, grind off about 150 μm of material using 600 grit wet/dry SiC sandpaper, advancing the sample in 25 μm increments. You can measure the sample thickness with the digital micrometer occasionally, although the micrometer dial of the Gatan hand polisher is fairly accurate. Grind back and forth in a straight line parallel to the sandwich interfaces. Each time you advance the micrometer 25 μm, rotate your grip on the hand polisher 180° so that you thin the sample evenly. Keep the sandpaper wet at all times. Occasionally rinse the sample with a water squirt bottle. Check that the surface looks reasonable using the optical microscope before skipping to 3.10.

3.9 For a plan-view sample, continue to grind down to 30 μm thickness using 10 μm increments and 2000 grit wet/dry sandpaper. Grind the sample back and forth in a straight line perpendicular to the direction used for the 600 grit sandpaper. Again, rotate your grip on the hand polisher 180° each time you advance the micrometer. Keep the sandpaper and sample wet as before. When you get to 30 μm, make sure that the polish lines from the 600 grit sandpaper are completely removed, and replaced by polish lines from the 2000 grit sandpaper. Skip to 3.11.

3.10 For a cross-section sample, grind the sample perpendicular to the sandwich interfaces on 2000 grit wet/dry sandpaper using 10 μm increments until all the polish lines from the 600 grit sandpaper are replaced by those from the 2000 grit sandpaper. This

typically occurs after removing 60 μm of material. Observe the surface quality using the optical microscope. Again, rotate your grip on the hand polisher 180° each time you advance the micrometer. Keep the sandpaper and sample wet as before.

3.11 For both plan-view and cross-sections, advance the micrometer 5-6 μm, and polish the sample on P4000 grit (circular) sandpaper, in the same direction used for the 600 grit. Continue to polish until the polish lines from the 2000 grit are replaced by those from the P4000 grit. You do not need to continually advance the micrometer for this step. Keep the sandpaper and sample wet.

3.12 Dry polish the sample on the felt pad with 0.05 μm Al_2O_3 particles. Polish the sample by moving somewhat rapidly in a figure eight motion or circular motion. After 30-60 seconds, check the surface under the optical microscope. Most of the polish lines should be removed, and the surface should be a dull black. It should look mirror smooth under ordinary light. For plan-view samples, skip to 3.14.

3.13 For cross-sections, remove the mounting stub from the hand polisher and squirt off the excess alumina polish with DI water. Place the stub in DI water in an ultrasonic bath for 5 minutes to clean off all the alumina polish. Put the stub on the hot plate at 150 °C, allow the wax to soften, grab the sample by the edges using Teflon-coated tweezers, and flip the sample over so that the polished face is wax mounted to the stub. Be careful not to damage the polished face. Gently apply pressure to the back of the sample with a toothpick to ensure a good mount. Quench the mount in water. Place the mounting stub in the hand polisher, and **proceed to grind/polish the backside as if the sample were a plan-view sample (starting at step 3.7)**. A hint for when you get back to step 3.9: on cross-section samples, when you get down to about 30-35 μm thick, the edges of the sample will begin to grind away, and the sample will no longer be square. Be careful not to grind away too much material from the edges.

3.14 Your sample should be about 30 μm thick now. Remove the mounting stub from the hand polisher, and squirt sample clean with DI water. Mix a small drop of 5 minute, 2-part epoxy. Using a toothpick, apply a thin, even coating of epoxy to the backside of a copper grid. Gently grab the grid by the edges using fine tweezers, and drop/mount the grid onto the sample. For cross-sections, make sure that the center interface between the two epilayers is centered along the slot of the copper grid. For plan-view samples, the orientation of the grid on the sample does not matter. (However, it is helpful to mount the grid so that about 0.5 mm hangs off the edge of the sample. This will be helpful to handle the grid later without cracking the sample.) Under the optical

microscope, you can observe the alignment of the grid on the sample. You can gently move it around using the tweezers. Be careful not to poke the sample!! If you don't like the position of the grid or you have too much epoxy, you can remove it with acetone and start again. **Allow the epoxy to set for at least 2 hours.**

NOTE: The copper grids are 3 mm in diameter. If one dimension of your sample is less than 3 mm, and your sample is very thin (< 20 μm), there is a possibility that the epoxy on the grid may glue your grid to the mounting stub. One way to avoid this is to ensure that the wax spot to which the sample is mounted is wider than 3 mm. Then any overhang of the copper grid will mount to the wax, which will be dissolved away later.

3.15 Remove the wax from the mounting stub by swirling the stub in a beaker of acetone for about 20 seconds. Observe sample surface under the optical microscope to check for wax removal. Using a scalpel, gently cut away the excess sample so that there is no material extending beyond the 3 mm copper grid. This is important because the ion miller and TEM sample holders both have exactly 3 mm diameter recesses to mount your sample. If you have any additional material overhang, the sample will not sit properly in either the ion miller or TEM mounts. Swirl the stub in acetone to clean the sample.

3.16 Place the mounting stub on the hot plate at 150 °C. Allow the wax to soften for about one minute. Using a toothpick, GENTLY push the edge of the copper grid so that the sample and grid slide toward the edge of the mounting stub. Push the sample about half off the mounting stub. Using fine tweezers, gently grab the edge of the copper grid and lift the sample off the stub. Dip the sample into a beaker of acetone and swirl gently for about 30 seconds to remove excess wax from the back of the sample. Check the sample under the optical microscope to make sure the wax is removed (keep holding the grid in the tweezers at all times). Place the sample into a sample holder.

NOTE: When you grab the copper grid between the tweezer tips, if you also grab part of the sample it might cleave because it is so thin and delicate at this stage. You want to avoid touching the sample with the tweezers if possible, and grab ONLY the copper grid. For cross-section samples, this is easy because the width of the copper grid is 3 mm, while the width of the sandwich is only 2 mm (4 pieces, each 500 μm thick, yields 2 mm total width). Therefore, on cross-section samples, since you mount the grid centered along the center interface, there will automatically be 0.5 mm of copper grid overhang on either side of the sandwich where you can grab only the grid and avoid touching the sample. For plan-view samples, you can achieve this by mounting the

grid so that at least 0.5 mm overhangs the sample and leaves you a spot to grab the copper grid without touching the sample. This makes handling the sample far easier. If the backside of the copper grid is completely covered by sample and there is no clean area to grab, then handle the specimen as delicately as possible. Try to grab near an edge so that if a cleave is formed, it will not run through the center of the sample.

3.17 You are now ready to ion mill!

Ion Mill Instructions for TEM Specimens

1. GaSb-based materials are VERY soft and so must be ion milled under delicate conditions to avoid substantial ion mill damage. These guidelines will minimize ion mill damage to your samples.
2. Use a Gatan DuoMill with a liquid nitrogen cold stage.
3. Mount the sample in the appropriate sample holder. Make sure you use the holders for the cold stage!
4. Fill the cold trap with liquid nitrogen. Mount the sample in the DuoMill, pump down, and lower the Whisperlok into the liquid nitrogen dewar. Allow the sample to cool to liquid nitrogen temperature for 20-30 minutes.
5. Adjust the mill angle to 11°. For cross-sections, turn on both guns. **For plan-view specimens, only turn on the top gun so that you are milling from the substrate back-side, and not through the epilayer!**
6. Set the guns to 3.75 kV, and 0.2 mA per gun. (Note: According to Gatan you can use their high kV guns at any kV, but below 4 kV the efficiency is greatly reduced.) For a plan-view sample, you can set the single gun to 0.4 mA.
7. Set the specimen rotation to 10 RPM. (This control is under the front panel.)
8. For samples that are 30 μm thick, these mill conditions will usually mill through the sample in about 10-15 hours. You can use the terminator for plan-view specimens. Raise the Whisperlok and check the sample every few hours using the light microscope. Towards the end check the sample more frequently—every 30 to 60 minutes. Typically, when the sample is very thin and about to have a mill hole, you will see some bright fringes near the thin area with the microscope. This means you are about 30-60 minutes away from completion. At this

point, decrease the gun voltages to 3.5 kV, and currents to 0.15 mA/gun. (0.3 mA for plan-view samples.)

9. Once you have a small hole in your sample, you are done. Stop the mill as soon as you have even the smallest hole! Raise the Whisperlok, remove the liquid nitrogen dewar, lower the Whisperlok, and allow the sample to warm up for at least 30 minutes before checking in the TEM. If the sample is still too thick to see anything in the TEM, you can continue to mill for 30-60 more minutes at 3.5 kV and 0.15 mA/gun.

NOTES: If you completely fill the cold trap with liquid nitrogen, it will last about 6-8 hours. You must always keep liquid nitrogen in the cold trap during ion milling, otherwise all the contaminants in the chamber will adsorb to your sample!

During milling, part of the copper grid will mill and adsorb onto the sample. You will see a thin ring of metal along the inner edge of the sample. This is normal, and due to the shallow 11° incidence angle.

Since samples take so long to mill, it is helpful to initiate milling at night. Set the ion miller for 8-9 hours and allow it to mill overnight. Then, you will only need a few more hours to finish milling it in the morning. (This means that during your final hour or two of milling overnight, the liquid nitrogen cold trap will be dry. So you must mill for at least another 30 minutes the following day using the cold trap to remove any adsorbed contaminants.)

Bibliography

1. Adachi, S., *Physical Properties of III-V Semiconductor Compounds*. 1992, New York: John Wiley & Sons. 318.
2. Adachi, S., "Optical dispersion relations for GaP, GaAs, GaSb, InP, InAs, InSb, $Al_xGa_{1-x}As$, and $In_{1-x}Ga_xAs_yP_{1-y}$." *Journal of Applied Physics*, 1989. **66**(12). p. 6030-6040.
3. Munoz, M., Wei, K., Pollak, F.H., Freeouf, J.L., and Charache, G.W., "Spectral ellipsometry of GaSb: Experiment and modeling." *Physical Review B*, 1999. **60**(11). p. 8105-8110.
4. Munoz, M., Wei, K., Pollak, F.H., Freeouf, J.L., Wang, C.A., and Charache, G.W., "Optical constants of $Ga_{1-x}In_xAs_ySb_{1-y}$ lattice matched to GaSb (001): Experiment and modeling." *Journal of Applied Physics*, 2000. **87**(4). p. 1780-1787.
5. Palik, E.D., Glembocki, O.J., and Takarabe, K., *Aluminum Arsenide (AlAs)*, in *Handbook of Optical Constants of Solids II*, E.D. Palik, Editor. 1991, Academic Press, Inc.: Boston. p. 489-499.
6. Edwards, D.F., and White, R.H., *Aluminum Antimonide (AlSb)*, in *Handbook of Optical Constants of Solids II*, E.D. Palik, Editor. 1991, Academic Press, Inc.: Boston. p. 501-511.
7. Palik, E.D., ed. *Handbook of Optical Constants of Solids*. 1985, Academic Press: Orlando. 804.
8. Palik, E.D., ed. *Handbook of Optical Constants of Solids II*. 1991, Academic Press: Boston. 1096.
9. Herman, I.P., *Optical Diagnostics for Thin Film Processing*. 1996, New York: Academic Press. 783.
10. Pickering, C., *In situ Optical Studies of Epitaxial Growth*, in *Handbook of Crystal Growth*, D.T.J. Hurle, Editor. 1994, Elsevier Science. p. 817-878.
11. Bertness, K.A., "Smart pyrometry for combined sample temperature and reflectance measurements in molecular-beam epitaxy." *Journal of Vacuum Science and Technology B*, 2000. **18**(3). p. 1426-1430.
12. Leveque, G., and Nouaoura, M., "Temperature measurements by optical pyrometry during the epitaxial growth of semiconductors." *The European Journal Applied Physics*, 1998. **4**. p. 227-233.
13. Pidduck, A.J., Robbins, D.J., Cullis, A.G., Gasson, D.B., and Glasper, J.L., "In Situ Laser Light Scattering: I. Detection of Defects Formed during Silicon Molecular Beam Epitaxy." *Journal of the Electrochemical Society*, 1989. **136**(10). p. 3083-3088.
14. Lavoie, C., Johnson, S.R., Mackenzie, J.A., Tiedje, T., and van Buuren, T., "Diffuse optical reflectivity measurements on GaAs during molecular-beam

epitaxy processing." *Journal of Vacuum Science and Technology A*, 1992. **10**(4). p. 930-933.
15. Chason, E., Sinclair, M., Floro, J.A., Hunter, J.A., and Hwang, R.Q., "Spectroscopic light scattering for real-time measurements of thin film and surface evolution." *Applied Physics Letters*, 1998. **72**(25). p. 3276-3278.
16. Celii, F.G., Kao, Y.C., Liu, H.-Y., Files-Sesler, L.A., and Beam, E.A.I., "Laser light scattering detection of InGaAs strained layer relaxation during molecular-beam epitaxial growth." *Journal of Vacuum Science and Technology B*, 1993. **11**(3). p. 1014-1017.
17. Bertness, K.A., Kramer, C., Olson, J.M., and Moreland, J., "In Situ Observation of Surface Morphology of InP Grown on Singular and Vicinal (001) Substrates." *Journal of Electronic Materials*, 1994. **23**(2). p. 195-200.
18. Aspnes, D.E., Quinn, W.E., Tamargo, M.C., Pudensi, M.A.A., Schwarz, S.A., Brasil, M.J.S.P., Nahory, R.E., and Gregory, S., "Growth of $Al_xGa_{1-x}As$ parabolic quantum wells by real-time feedback control of composition." *Applied Physics Letters*, 1992. **60**(10). p. 1244-1246.
19. Roth, J.A., Chow, D.H., Olson, G.L., Brewer, P.D., Williamson, W.S., and Johs, B., "Real-time control of the MBE growth of InGaAs on InP." *Journal of Crystal Growth*, 1999. **201/202**. p. 31-35.
20. Beaudoin, M., Grassi, E., Johnson, S.R., Ramaswamy, K., Tsakalis, K., Alford, T.L., and Zhang, Y.-H., "Real-time composition control of InAlAs grown on InP using spectroscopic ellipsometry." *Journal of Vacuum Science and Technology B*, 2000. **18**(3). p. 1435-1438.
21. Kuo, C.-H., Boonzaayer, M., DeHerrera, M., Kyong, T., Zhang, Y.-H., Johs, B., and Hale, J.S., "Real time in situ composition control of InGaAs lattice matched to InP by an 88-wavelength ellipsometer." *Journal of Vacuum Science and Technology B*, 1998. **16**(3). p. 1484-1488.
22. Lee, J.-S., and Masumoto, Y., "Real-time monitoring of ellipsometry monolayer oscillations during metalorganic vapor-phase epitaxy." *Journal of Crystal Growth*, 2000. **221**. p. 111-116.
23. Beresford, R., Yin, J., Tetz, K., and Chason, E., "Real-time measurements of stress relaxation in InGaAs/GaAs." *Journal of Vacuum Science and Technology B*, 2000. **18**(3). p. 1431-1434.
24. Floro, J.A., Chason, E., and Lee, S.R., *Real time measurement of epilayer strain using a simplified wafer curvature technique*, in *Diagnostic Techniques for Semiconductor Materials Processing II. Symposium Mater. Res. Soc. 1996*, S.W. Pang, et al., Editors. 1996: Pittsburgh. p. 491-496.
25. Kobayashi, N., and Horikoshi, Y., "Optical Investigation on the Growth Process of GaAs during Migration-Enhanced Epitaxy." *Japanese Journal of Applied Physics*, 1989. **28**(11). p. L1880-L1882.
26. Dietz, N., Rossow, U., Aspnes, D.E., and Bachmann, K.J., "Real-time optical monitoring of heteroepitaxial growth processes on Si under pulsed chemical beam epitaxy." *Applied Surface Science*, 1996. **102**. p. 47-51.
27. Klipstein, P.C., Lyapin, S.G., Mason, N.J., and Walker, P.J., "In situ characterisation of MOVPE by surface photoabsorption. II. Interface monitoring." *Journal of Crystal Growth*, 1998. **195**. p. 168-173.

28. Allwood, D.A., Mason, N.J., and Walker, P.J., "In situ characterisation of III-V substrate oxide desorption by surface photoabsorption in MOVPE." *Materials Science & Engineering B*, 1999. **B66**(1-3). p. 83-87.
29. Aspnes, D.E., Harbison, J.P., Studna, A.A., and Florez, L.T., "Optical-Reflectance and Electron-Diffraction Studies of Molecular-Beam-Epitaxy Growth Transients on GaAs (001)." *Physical Review Letters*, 1987. **59**(15). p. 1687-1690.
30. Meyne, C., Gensch, M., Peters, S., Pohl, U.W., Zettler, J.-T., and Richter, W., "In situ monitoring of ZnS/GaP and ZnSe/GaAs metalorganic vapor phase epitaxy using reflectance anisotropy spectroscopy and spectroscopic ellipsometry." *Thin Solid Films*, 2000. **364**. p. 12-15.
31. Ebert, M., Bell, K.A., Yoo, S.D., Flock, K., and Aspnes, D.E., "In situ monitoring of MOVPE growth by combined spectroscopic ellipsometry and reflectance-difference spectroscopy." *Thin Solid Films*, 2000. **364**. p. 22-27.
32. Tanaka, H., Colas, E., Kamiya, I., Aspnes, D.E., and Bhat, R., "*In situ* determination of free-carrier concentrations by reflectance difference spectroscopy." *Applied Physics Letters*, 1991. **59**(26). p. 3443-3445.
33. Fuoss, P.H., Kisker, D.W., Renaud, G., Tokuda, K.L., Brennan, S., and Kahn, J.L., "Atomic nature of organometallic-vapor-phase-epitaxial growth." *Physical Review Letters*, 1989. **63**(21). p. 2389-2392.
34. Brennan, S., Stephenson, G.B., Fuoss, P.H., Kisker, D.W., Lavoie, C., and Evans-Lutterodt, K.L., "Silicon-induced faceting of vicinal GaAs(001)." *Journal of Applied Physics*, 2000. **88**(6). p. 3367-3376.
35. Farrell, T., Armstrong, J.V., and Kightley, P., "Dynamic optical reflectivity to monitor the real-time metalorganic molecular beam epitaxial growth of AlGaAs layers." *Applied Physics Letters*, 1991. **59**(10). p. 1203-1205.
36. Breiland, W.G., and Killeen, K.P., "A virtual interface method for extracting growth rates and high temperature optical constants from thin semiconductor films using *in situ* normal incidence reflectance." *Journal of Applied Physics*, 1995. **78**(11). p. 6726-6736.
37. Killeen, K.P., and Breiland, W.G., "In Situ Spectral Reflectance Monitoring of III-V Epitaxy." *Journal of Electronic Materials*, 1994. **23**(2). p. 179-183.
38. Lum, R.M., McDonald, M.L., Bean, J.C., Vandenberg, J., Pernell, T.L., Robertson, A., and Karp, A., "*In situ* reflectance monitoring of InP/InGaAsP films grown by metalorganic vapor phase epitaxy." *Applied Physics Letters*, 1996. **69**(7). p. 928-930.
39. Sankur, H., Southwell, W., and Hall, R., "In Situ Optical Monitoring of OMPVE Deposition of AlGaAs by Laser Reflectance." *Journal of Electronic Materials*, 1991. **20**(12). p. 1099-1104.
40. Bajaj, J., Irvine, S.J.C., Sankur, H.O., and Svoronos, S.A., "Modeling of In Situ Monitored Laser Reflectance During MOCVD Growth of HgCdTe." *Journal of Electronic Materials*, 1993. **22**(8). p. 899-906.
41. Bean, J.C., Peticolas, L.J., Lum, R., and McDonald, M.L., "Simple equipment tolerant reflectometry for monitoring of molecular beam epitaxy and metalorganic chemical vapor deposition growth." *Journal of Vacuum Science and Technology A*, 1996. **14**(3). p. 946-951.

42. Ng, T.-B., Han, J., Biefeld, R.M., and Weckwerth, M.V., "In-Situ Reflectance Monitoring During MOCVD Growth of AlGaN." *Journal of Electronic Materials*, 1998. **27**(4). p. 190-195.
43. Vineis, C.J., Wang, C.A., Jensen, K.F., and Breiland, W.G., "In situ monitoring of GaSb, GaInAsSb, and AlGaAsSb." *Journal of Crystal Growth*, 1998. **195**. p. 181-186.
44. Bertness, K.A., Hickernell, R.K., Hays, S.P., and Christensen, D.H., "Noise reduction in optical *in situ* measurements for molecular beam epitaxy by substrate wobble normalization." *Journal of Vacuum Science and Technology B*, 1998. **16**(3). p. 1492-1496.
45. Macleod, H.A., *Thin-Film Optical Filters*. 2nd ed. 1986, New York: Macmillan Publishing Company. 519.
46. Azzam, R.M.A., and Bashara, N.M., *Ellipsometry and Polarized Light*. Paperback ed. 1987, New York: North-Holland. 539.
47. Aspnes, D.E., "Real-time optical diagnostics for epitaxial growth." *Surface Science*, 1994. **307-309**. p. 1017-1027.
48. Urban, F.K.I., and Tabet, M.F., "Virtual interface method for in situ ellipsometry of films grown on unknown substrates." *Journal of Vacuum Science and Technology A*, 1992. **11**(4). p. 976-980.
49. Aspnes, D.E., *Journal of the Optical Society of America*, 1993. **10**. p. 974.
50. Private communication. Breiland, W.G. 2000.
51. Vineis, C.J., Wang, C.A., and Jensen, K.F., "In-situ reflectance monitoring of GaSb substrate oxide desorption." *Journal of Crystal Growth*, 2001. **in press**.
52. Adachi, S., "Band gaps and refractive indices of AlGaAsSb, GaInAsSb, and InPAsSb: Key properties for a variety of the 2-4-um optoelectronic device applications." *Journal of Applied Physics*, 1987. **61**(10). p. 4869-4876.
53. Alibert, C., Joullie, A., Joullie, A.M., and Ance, C., "Modulation-spectroscopy study of the $Ga_{1-x}Al_xSb$ band structure." *Physical Review B*, 1983. **27**(8). p. 4946-4954.
54. Di Lernia, S., Geddo, M., Guizzetti, G., Patrini, M., Bosacchi, A., Franchi, S., and Magnanini, R., *Optical characterization of $Al_xGa_{1-x}Sb/GaSb$ epitaxial layers*, in *Diagnostic Techniques for Semiconductor Materials Processing II. Symp. Mater. Res. Soc. Proc. 406*, S.W. Pang, et al., Editors. 1996: Pittsburgh. p. 389-394.
55. Pidduck, A.J., Robbins, D.J., Gasson, D.B., Pickering, C., and Glasper, J.L., "In Situ Laser Light Scattering: II. Relationship to Silicon Surface Topography." *Journal of the Electrochemical Society*, 1989. **136**(10). p. 3088-3094.
56. Pidduck, A.J., Robbins, D.J., Young, I.M., Cullis, A.G., and Martin, A.S.R., "The Formation of Dislocations and their In-situ Detection During Silicon Vapour Phase Epitaxy at Reduced Temperature." *Materials Science & Engineering B*, 1989. **B4**. p. 417-422.
57. Pickering, C., "Correlation of in situ ellipsometric and light scattering data of silicon-based materials with post-deposition diagnostics." *Thin Solid Films*, 1991. **206**. p. 275-282.
58. Smith, G.W., Pidduck, A.J., Whitehouse, C.R., Glasper, J.L., Keir, A.M., and Pickering, C., "Surface topography changes during the growth of GaAs by molecular beam epitaxy." *Applied Physics Letters*, 1991. **59**(25). p. 3282-3284.

59. Smith, G.W., Pidduck, A.J., Whitehouse, C.R., Glasper, J.L., and Spowart, J., "Real-time laser-light scattering studies of surface topography development during GaAs MBE growth." *Journal of Crystal Growth*, 1993. **127**. p. 966-971.
60. Nissen, M.K., Lavoie, C., Eisebitt, S., Pinnington, T., and Tiedje, T., "Light scattering and electron microscopy study of the surface morphology of GaAs films grown by molecular beam epitaxy." *Scanning Microscopy*, 1994. **8**(4). p. 935-942.
61. Ritchie, S., Johnson, S.R., Lavoie, C., Mackenzie, J.A., Tiedje, T., and Streater, R., "Semiconductor substrate cleaning and surface morphology in molecular beam epitaxy." *Surface Science*, 1997. **374**. p. 418-426.
62. Allwood, D.A., Mason, N.J., and Walker, P.J., "In situ characterisation of MOVPE by surface photoabsorption. I. Substrate oxide desorption." *Journal of Crystal Growth*, 1998. **195**(1-4). p. 163-167.
63. Allwood, D.A., Grant, I.R., Mason, N.J., Palmer, R.A., and Walker, P.J., "In situ characterisation of epiready III-V substrates for MOVPE." *Journal of Crystal Growth*, 2000. **221**. p. 160-165.
64. Allwood, D.A., Carline, R.T., Mason, N.J., Pickering, C., Tanner, B.K., and Walker, P.J., "Characterization of oxide layers on GaAs substrates." *Thin Solid Films*, 2000. **364**. p. 33-39.
65. Allwood, D.A., Klipstein, P.C., Mason, N.J., Nicholas, R.J., and Walker, P.J., "GaAs High Temperature Optical Constants and Application to Optical Monitoring within the MOVPE Environment." *Journal of Electronic Materials*, 2000. **29**(1). p. 99-105.
66. Da Silva, F.W.O., Raisin, C., Silga, M., Nouaoura, M., and Lassabatere, L., *Semiconductor Science and Technology*, 1989. **4**. p. 565.
67. Mizokawa, Y., Komoda, O., and Miyase, S., *Thin Solid Films*, 1988. **156**. p. 127.
68. Barman, P., and Basu, S., *Applied Surface Science*, 1992. **55**. p. 173.
69. Mizokawa, Y., Komoda, O., Iwasaki, S., and Nakamura, S., *Japanese Journal of Applied Physics*, 1984. **23**. p. L257.
70. Wilmsen, C.W., *Physics and Chemistry of III-V Compound Semiconductor Surfaces*. 1985, New York: Plenum Press.
71. Schwartz, G.P., Gualtieri, G.J., Griffiths, J.E., Thurmond, C.D., and Schwartz, B., *Journal of the Electrochemical Society*, 1980. **127**. p. 2488.
72. Gomez Zazo, L.J., Montojo, M.T., Castano, L.J., and Piqueras, J., *Journal of the Electrochemical Society*, 1989. **136**. p. 1480.
73. Kodama, M., *Advanced Materials for Optics and Electronics*, 1994. **4**. p. 319.
74. Lu, Z., Jiang, Y., Wang, W.I., Teich, M.C., and Osgood, R.M.J., *Journal of Vacuum Science and Technology B*, 1992. **10**. p. 1856.
75. in *CRC Handbook of Chemistry and Physics*, D.R. Lide, Editor. 1992, CRC Press: Boca Raton. p. 4-41.
76. Wang, C.A., "OMVPE growth of GaInAsSb in the 2-2.4 mu m range." *Journal of Crystal Growth*, 1998. **191**(4). p. 631-640.
77. Wang, C.A., Salim, S., Jensen, K.F., and Jones, A.C., "Characteristics of GaSb growth using various gallium and antimony precursors." *Journal of Crystal Growth*, 1997. **170**. p. 55-60.

78. Wang, C.A., "Organometallic vapor phase epitaxial growth of AlSb-based alloys." *Journal of Crystal Growth*, 1997. **170**. p. 725-731.
79. Zollner, S., Garriga, M., Humlicek, J., Gopalan, S., and Cardona, M., "Temperature dependence on the dielectric function and the interband critical-point parameters of GaSb." *Physical Review B*, 1991. **43**(5). p. 4349-4360.
80. Alibert, C., Skouri, M., Joullie, A., Benouna, M., and Sadiq, S., "Refractive indices of AlSb and GaSb-lattice-matched $Al_xGa_{1-x}As_ySb_{1-y}$ in the transparent wavelength region." *Journal of Applied Physics*, 1991. **69**(5). p. 3208-3211.
81. Adachi, S., "Optical Properties of Al(x)Ga(1-x)As alloys." *Physical Review B*, 1988. **38**(17). p. 12345-12352.
82. Adachi, S., "Excitonic effects in the optical spectrum of GaAs." *Physical Review B*, 1990. **41**(2). p. 1003-1013.
83. Aspnes, D.E., and Studna, A.A., "Dielectric functions and optical parameters of Si, Ge, GaP, GaAs, GaSb, InP, InAs, and InSb from 1.5 to 6.0 eV." *Physical Review B*, 1983. **27**(2). p. 985-1009.
84. Logothetidis, S., Vina, L., and Cardona, M., "Temperature dependence of the dielectric function and the interband critical points of InSb." *Physical Review B*, 1985. **31**(2). p. 947-957.
85. Kamlet, L.I., Terry, F.L., Jr., and Maracas, G.N., "A temperature-dependent model for the complex dielectric function of GaAs." *Journal of Electronic Materials*, 1997. **26**(12). p. 1409-1416.
86. Lautenschlager, P., Garriga, M., Logothetidis, S., and Cardona, M., "Interband critical points of GaAs and their temperature dependence." *Physical Review B*, 1987. **35**(17). p. 9174-9189.
87. Aspnes, D.E., Olson, C.G., and Lynch, D.W., "Electroreflectance of GaSb from 0.6 to 26 eV." *Physical Review B*, 1976. **14**(10). p. 4450-4458.
88. Varshni, Y.P., "Temperature Dependence of the Energy Gap in Semiconductors." *Physica (Utrecht)*, 1967. **34**. p. 149-154.
89. Miyazaki, T., and Adachi, S., "Model Dielectric Constants of InSb." *Physica Status Solidi B*, 1991. **163**. p. 299-310.
90. Abid, H., Rezki, M., and Aourag, H., "Electronic structure and optical properties of the quaternary alloy $Ga_{1-x}Al_xAs_ySb_{1-y}$." *Materials Science & Engineering B*, 1996. **B41**. p. 314-321.
91. DeWinter, J.C., Pollack, M.A., Srivastava, A.K., and Zyskind, J.L., "Liquid phase epitaxial $Ga_{1-x}In_xAs_ySb_{1-y}$ lattice-matched to (100) GaSb over the 1.71 to 2.33 um wavelength range." *Journal of Electronic Materials*, 1985. **14**(6). p. 729-747.
92. Cherng, M.J., Jen, H.R., Larsen, C.A., Stringfellow, G.B., Lundt, H., and Taylor, P.C., "MOVPE growth of GaInAsSb." *Journal of Crystal Growth*, 1986. **77**(1-3). p. 408-417.
93. Onabe, K., "Unstable Region in Quaternary $In_{1-x}Ga_xAs_{1-y}Sb_y$ Calculated Using Strictly Regular Solution Approximation." *Japanese Journal of Applied Physics*, 1982. **21**(6). p. 964.
94. Tournie, E., Pitard, F., Joullie, A., and Fourcade, R., "High temperature liquid phase epitaxy of (100) oriented GaInAsSb near the miscibility gap boundary." *Journal of Crystal Growth*, 1990. **104**. p. 683-694.

95. Nakajima, K., Osamura, K., Yasuda, K., and Murakami, Y., "The pseudoquaternary phase diagram of the Ga-In-As-Sb system." *Journal of Crystal Growth*, 1977. **41**. p. 87-92.
96. Porter, D.A., and Easterling, K.E., *Phase Transformations in Metals and Alloys.* 2nd ed. 1992, London: Chapman & Hall. 514.
97. Stringfellow, G.B., "Calculation of regular solution interaction parameters in semiconductor solid solutions." *Journal of Physics and Chemistry of Solids*, 1973. **34**. p. 1749-1751.
98. Stringfellow, G.B., "Calculation of ternary and quaternary III-V phase diagrams." *Journal of Crystal Growth*, 1974. **27**. p. 21-34.
99. Stringfellow, G.B., "Spinodal decomposition and clustering in III/V alloys." *Journal of Electronic Materials*, 1982. **11**(5). p. 903-918.
100. Stringfellow, G.B., "Miscibility gaps in quaternary III/V alloys." *Journal of Crystal Growth*, 1982. **58**. p. 194-202.
101. Stringfellow, G.B., *Organometallic Vapor-Phase Epitaxy: Theory and Practice.* 2nd ed. 1999, San Diego: Academic Press. 572.
102. Cahn, J.W., "On spinodal decomposition." *Acta Metallurgica*, 1961. **9**. p. 795-801.
103. Cahn, J.W., "On spinodal decomposition in cubic crystals." *Acta Metallurgica*, 1962. **10**. p. 179-183.
104. Cahn, J.W., and Hilliard, J.E., "Spinodal decomposition: a reprise." *Acta Metallurgica*, 1971. **19**. p. 151-161.
105. Quillec, M., Daguet, C., Benchimol, J.L., and Launois, H., "$In_xGa_{1-x}As_yP_{1-y}$ alloy stabilization by the InP substrate inside an unstable region in liquid phase epitaxy." *Applied Physics Letters*, 1982. **40**(4). p. 325-326.
106. Srolovitz, D.J., "On the stability of surfaces of stressed solids." *Acta Metallurgica*, 1989. **37**(2). p. 621-625.
107. Glas, F., "Elastic state and thermodynamical properties of inhomogeneous epitaxial layers: application to immiscible III-V alloys." *Journal of Applied Physics*, 1987. **62**(8). p. 3201-3208.
108. Ipatova, I.P., Malyshkin, V.G., and Shchukin, V.A., "On spinodal decomposition in elastically anisotropic epitaxial films of III-V semiconductor alloys." *Journal of Applied Physics*, 1993. **74**(12). p. 7198-7210.
109. Schlenker, D., Miyamoto, T., Pan, Z., Koyama, F., and Iga, K., "Miscibility gap calculation for Ga(1-x)In(x)N(y)As(1-y) including strain effects." *Journal of Crystal Growth*, 1999. **196**. p. 67-70.
110. Karpov, S.Y., "Suppression of phase separation in InGaN due to elastic strain." *MRS Internet Journal of Nitride Research*, 1998. **3**(16). p. 1-5.
111. Lin, C., and Li, A.Z., "The effect of strain on the miscibility gap in Ga-In-Sb ternary alloy." *Journal of Crystal Growth*, 1999. **203**. p. 511-515.
112. Asomoza, R., Elyukhin, V.A., and Pena-Sierra, R., "Spinodal decomposition in the $A_xB_{1-x}C_yD_{1-y}$ quaternary alloys." *Journal of Crystal Growth*, 2001. **222**. p. 58-63.
113. Williams, D.B., and Carter, C.B., *Transmission Electron Microscopy: A Textbook for Materials Science.* Vol. 3. Imaging. 1996, New York: Plenum Press.

114. Follstaedt, D.M., Schneider, R.P., Jr., and Jones, E.D., "Microstructures of (In,Ga)P alloys grown on GaAs by metalorganic vapor-phase epitaxy." *Journal of Applied Physics*, 1995. **77**(7). p. 3077-3087.
115. Ueda, O., Takechi, M., and Komeno, J., "Generation of strong composition-modulated structures and absence of ordered structures in InGaP crystals grown on (110) GaAs substrates by metalorganic chemical vapor deposition." *Applied Physics Letters*, 1989. **54**(23). p. 2312-2314.
116. Okuda, H., Kondo, M., Kato, K., and Nakajima, K., "X-ray observation of composition modulation caused by phase decomposition in GaInP ternary alloys." *Applied Physics Letters*, 1990. **56**(4). p. 337-339.
117. Wang, J., Steeds, J.W., and Hopkinson, M., *The study of MBE grown (001) $In_xGa_{1-x}P/GaAs$ strained layer heterostructures by TEM and CL*, in *Microscopy of Semiconducting Materials 1993.*, A.G. Cullis, A.E. Staton-Bevan, and J.L. Hutchison, Editors. 1993: Oxford. p. 295-300.
118. Kiriakidis, G., Stoemenos, J., Ginoudi, A., Tsagaraki, K., Dimoulas, A., Maurell, P., and Garcia, J.C., "Structural study of In(x)Ga(1-x)P/GaAs interfaces grown by MOMBE." *Semiconductor Science and Technology*, 1992. **7**. p. A127-A130.
119. Seong, T.-Y., Booker, G.R., and Norman, A.G., *TEM and TED studies of fine scale contrasts in InGaAs layers grown by metalorganic chemical vapour deposition*, in *Microscopy of Semiconducting Materials 1993.*, A.G. Cullis, A.E. Staton-Bevan, and J.L. Hutchison, Editors. 1993: Oxford. p. 301-304.
120. Peiro, F., Cornet, A., and Morante, J.R., *On the occurrence of phase separation in InGaAs/InP systems*, in *Microscopy of Semiconducting Materials 1993.*, A.G. Cullis, A.E. Staton-Bevan, and J.L. Hutchison, Editors. 1993: Oxford. p. 291-294.
121. Hartmann, A., Dieker, C., Hollfelder, M., Hardtdegen, H., Forster, A., and Luth, H., "Spontaneous formation of a tilted AlGaAs/GaAs superlattice during AlGaAs growth." *Applied Surface Science*, 1998. **123/124**. p. 704-709.
122. Chin, A., Lin, H.Y., and Hsieh, K.Y., "Strong enhancement of the optical and electrical properties, and spontaneous formation of an ordered superlattice in (111)B AlGaAs." *Journal of Crystal Growth*, 1995. **150**. p. 436-440.
123. Takeuchi, M., Shiba, K., Huang, H.K., Sato, K., Inoue, K., Maehashi, K., and Nakashima, H., "Structural analysis of AlGaAs quantum wires on vicinal (110) GaAs by transmission electron microscopy and energy dispersive X-ray spectroscopy." *Journal of Crystal Growth*, 1995. **150**. p. 441-445.
124. Cremades, A., Albrecht, M., Krinke, J., Dimitrov, R., Stutzmann, M., and Strunk, H.P., "Effects of phase separation and decomposition on the minority carrier diffusion length in $Al_xGa_{1-x}N$ films." *Journal of Applied Physics*, 2000. **87**(5). p. 2357-2362.
125. Doppalapudi, D., Basu, S.N., Ludwig, K.F., and Moustakas, T.D., "Phase separation and ordering in InGaN alloys grown by molecular beam epitaxy." *Journal of Applied Physics*, 1998. **84**(3). p. 1389-1395.
126. El-Masry, N.A., Piner, E.L., Liu, S.X., and Bedair, S.M., "Phase separation in InGaN grown by metalorganic chemical vapor deposition." *Applied Physics Letters*, 1998. **72**(1). p. 40-42.
127. Suemune, I., Morooka, N., Uesugi, K., Ok, Y.-W., and Seong, T.-Y., "Formation of wire-like surfaces and lateral composition modulation in GaAsN grown by

metalorganic molecular-beam epitaxy." *Journal of Crystal Growth*, 2000. **221**. p. 546-550.

128. Biefeld, R.M., Baucom, K.C., Kurtz, S.R., and Follstaedt, D.M., "The growth of $InP_{1-x}Sb_x$ by metalorganic chemical vapor deposition." *Journal of Crystal Growth*, 1993. **133**. p. 38-46.
129. Duncan, W.J., Ali, A.S.M., Marsh, E.M., and Spurdens, P.C., "Metalorganic vapour phase epitaxy growth of InPAsSb alloys lattice matched to InAs." *Journal of Crystal Growth*, 1994. **143**. p. 155-161.
130. Cho, H.K., Lee, J.Y., Kwon, M.S., Lee, B., Baek, J.-H., and Han, W.S., "Observation of phase separation and ordering in the InAlAs epilayer grown on InP at the low temperature." *Materials Science & Engineering B*, 1999. **B64**. p. 174-179.
131. Grenet, G., Gendry, M., Oustric, M., Robach, Y., Porte, L., Hollinger, G., Marty, O., Pitaval, M., and Priester, C., "Surface spinodal decomposition in low temperature $Al_{0.48}In_{0.52}As$ grown on InP(001) by molecular beam epitaxy." *Applied Surface Science*, 1998. **123/124**. p. 324-328.
132. Georgakilas, A., Michelakis, K., Halkias, G., Becourt, N., Peiro, F., and Cornet, A., "Potential use of the tendency of III-V alloys to separate for fabrication of low dimensionality structures." *Microelectronic Engineering*, 1998. **41/42**. p. 583-586.
133. Ferguson, I.T., Norman, A.G., Joyce, B.A., Seong, T.-Y., Booker, G.R., Thomas, R.H., Phillips, C.C., and Stradling, R.A., "Molecular beam epitaxial growth of InAsSb strained layer superlattices. Can nature do it better?" *Applied Physics Letters*, 1991. **59**(25). p. 3324-3326.
134. Norman, A.G., Seong, T.-Y., Ferguson, I.T., Booker, G.R., and Joyce, B.A., "Structural studies of natural superlattices in group III-V alloy epitaxial layers." *Semiconductor Science and Technology*, 1993. **8**. p. S9-S15.
135. Cherng, M.J., Cherng, Y.T., Jen, H.R., Harper, P., Cohen, R.M., and Stringfellow, G.B., "OMVPE growth of the metastable III/V alloy $GaAs_{0.5}Sb_{0.5}$." *Journal of Electronic Materials*, 1986. **15**(2). p. 79-85.
136. Henoc, P., Izrael, A., Quillec, M., and Launois, H., "Composition modulation in liquid phase epitaxial $In_xGa_{1-x}As_yP_{1-y}$ layers lattice matched to InP substrates." *Applied Physics Letters*, 1982. **40**(11). p. 963-965.
137. Ueda, O., Isozumi, S., and Komiya, S., "Composition-modulated structures in InGaAsP and InGaP liquid phase epitaxial layers grown on (001) GaAs substrates." *Japanese Journal of Applied Physics*, 1984. **23**(4). p. L241-L243.
138. Norman, A.G., and Booker, G.R., "Transmission electron microscope and transmission electron diffraction observations of alloy clustering in liquid-phase epitaxial (001) GaInAsP layers." *Journal of Applied Physics*, 1985. **57**(10). p. 4715-4720.
139. Chu, S.N.G., Nakahara, S., Strege, K.E., and Johnston, W.D.J., "Surface layer spinodal decomposition in $In_{1-x}Ga_xAs_yP_{1-y}$ and $In_{1-x}Ga_xAs$ grown by hydride transport vapor-phase epitaxy." *Journal of Applied Physics*, 1985. **57**(10). p. 4610-4615.
140. McDevitt, T.L., Mahajan, S., Laughlin, D.E., Bonner, W.A., and Keramidas, V.G., "Two-dimensional phase separation in $In_{1-x}Ga_xAs_yP_{1-y}$ epitaxial layers." *Physical Review B*, 1992. **45**(12). p. 6614-6622.

141. LaPierre, R.R., Okada, T., Robinson, B.J., Thompson, D.A., and Weatherly, G.C., "Spinodal-like decomposition of InGaAsP/(100) InP grown by gas source molecular beam epitaxy." *Journal of Crystal Growth*, 1995. **155**. p. 1-15.
142. Okada, T., and Weatherly, G.C., "The role of strain and composition on the morphology of InGaAsP layers grown on <001> InP substrates." *Journal of Crystal Growth*, 1997. **179**. p. 339-348.
143. Chen, G.S., Wang, T.Y., and Stringfellow, G.B., "Transmission electron microscope characterization of AlGaInP grown by organometallic vapor phase epitaxy." *Applied Physics Letters*, 1990. **56**(15). p. 1463-1465.
144. Gomyo, A., Hotta, H., Miyasaka, F., Tada, K., Fujii, H., Fukagai, K., Kobayashi, K., and Hino, I., "Step-bunching in $(Al_xGa_{1-x})_{0.5}In_{0.5}P$ layers on misoriented (001) GaAs substrates grown by metalorganic vapor phase epitaxy." *Journal of Crystal Growth*, 1994. **145**. p. 126-132.
145. Gavrilovic, P., Dabkowski, F.P., Meehan, K., Williams, J.E., Stutius, W., Hsieh, K.C., Holonyak, N.J., Shahid, M.A., and Mahajan, S., "Disordering of the ordered structure in MOCVD-grown GaInP and AlGaInP by impurity diffusion and thermal annealing." *Journal of Crystal Growth*, 1988. **93**. p. 426-433.
146. Okada, T., LaPierre, R.R., Mullan, C., Weatherly, G.C., Robinson, B.J., and Thompson, D.A., *Transmission electron microscopy and photoluminescence studies of $In_{1-x}Ga_xAs_yP_{1-y}$ films grown on <100> InP substrates*, in *Microscopy of Semiconducting Materials*. 1995, IOP Publishing Ltd.: Oxford. p. 253-256.
147. Glas, F., *Composition variations, clustering and composition fluctuations in III-V alloys*, in *Microscopy of Semiconducting Materials 1993.*, A.G. Cullis, A.E. Staton-Bevan, and J.L. Hutchison, Editors. 1993: Oxford. p. 269-278.
148. Vul', A.Y., *Gallium Antimonide (GaSb)*, in *Handbook Series on Semiconductor Parameters*, M. Levinshtein, S.L. Rumyanstev, and M. Shur, Editors. 1996, World Scientific: New Jersey. p. 125-145.
149. Dutta, P.S., and Miller, T.R., "Engineering Phase Formation Thermo-Chemistry for Crystal Growth of Homogeneous Ternary and Quaternary III-V Compound Semiconductors from Melts." *Journal of Electronic Materials*, 2000. **29**(7). p. 956-963.
150. Wang, C.A., Choi, H.K., Turner, G.W., Spears, D.L., Manfra, M.J., and Charache, G.W., *Lattice-matched epitaxial GaInAsSb/GaSb thermophotovoltaic devices*, in *Thermophotovoltaic Generation of Electricity. Third NREL Conference. AIP Conf. Proc. #401.* 1997: Colorado Springs. p. 75-87.
151. Wang, C.A., Choi, H.K., Oakley, D.C., and Charache, G.W., "Recent progress in GaInAsSb thermophotovoltaics grown by organometallic vapor-phase epitaxy." *Journal of Crystal Growth*, 1998. **195**(1-4). p. 346-355.
152. Wang, C.A., Choi, H.K., Oakley, D.C., and Charache, G.W., *Substrate misorientation effects on epitaxial GaInAsSb*, in *Infrared Applications of Semiconductors II. Symp. Mater. Res. Soc. 1998*, D.L.J. McDaniel, et al., Editors. 1988: Boston. p. 37-44.
153. Wang, C.A., Choi, H.K., Oakley, D.C., and Charache, G.W., *Extending the cutoff wavelength of lattice-matched GaInAsSb/GaSb thermophotovoltaic devices*, in *Thermophotovoltaic Generation of Electricity. Fourth NREL Conference*. 1999: Denver. p. 256-265.

154. Wang, C.A., Choi, H.K., Ransom, S.L., Charache, G.W., Danielson, L.R., and DePoy, D.M., "High-quantum-efficiency 0.5 eV GaInAsSb/GaSb thermophotovoltaic devices." *Applied Physics Letters*, 1999. **75**(9). p. 1305-1307.
155. Wang, C.A., Choi, H.K., and Charache, G.W., "Epitaxial growth of GaInAsSb for thermophotovoltaic devices." *IEE Proceedings Optoelectronics*, 2000. **147**(3). p. 193-198.
156. Wang, C.A., "Correlation between surface step structure and phase separation in epitaxial GaInAsSb." *Applied Physics Letters*, 2000. **76**(15). p. 2077-2079.
157. Wang, C.A., "Step structure of GaInAsSb grown by organometallic vapor phase epitaxy." *Journal of Electronic Materials*, 2000. **29**(1). p. 112-117.
158. Glas, F., "Thermodynamic and kinetic instabilities of lattice-matched alloy layers: Compositional and morphological perturbations." *Physical Review B*, 2000. **62**(11). p. 7393-7401.
159. Glas, F., "Coupling of the morphological and compositional instabilities in a stressed alloy with a free surface." *Applied Surface Science*, 1998. **123/124**. p. 298-302.
160. Tersoff, J., "Stress-Driven Alloy Decomposition during Step-Flow Growth." *Physical Review Letters*, 1996. **77**(10). p. 2017-2020.
161. Venezuela, P., Tersoff, J., Floro, J.A., Chason, E., Follstaedt, D.M., Liu, F., and Lagally, M.G., "Self-organized growth of alloy superlattices." *Nature*, 1999. **397**. p. 678-681.
162. Chen, Y.-C., Bucklen, V., Rajan, K., Wang, C.A., Charache, G.W., Nichols, G., Freeman, M., and Sander, P., *Self-organized composition modulation in OMVPE $Ga_{1-x}In_xAs_ySb_{1-y}$/GaSb epitaxial heterostructures*, in *Self-Organized Processes in Semiconductor Alloys*, A. Mascarenhas, et al., Editors. 2000, Materials Research Society: Warrendale. p. 367-373.
163. Kaspi, R., Barnett, S.A., and Hultman, L., "Growth of InGaAsSb layers in the miscibility gap: Use of very-low-energy ion irradiation to reduce alloy decomposition." *Journal of Vacuum Science and Technology B*, 1995. **13**(3). p. 978-987.
164. Wang, C.A., Vineis, C.J., Calawa, D.R., and Nitishin, P.M. "Observation of Spontaneous Vertical Composition Modulation in Epitaxial GaInAsSb." in *2000 Fall MRS Symposium*. 2000. Boston, MA.
165. Simon, L., Faure, J., Kubler, L., and Schott, M., "Stress driven spontaneous mesoscopic alloy decomposition and ordering along step bunches during epitaxial Si(1-y)C(y) alloy growth on Si." *Journal of Crystal Growth*, 1997. **180**. p. 185-197.
166. Simon, L., Kubler, L., Bischoff, J.L., Bolmont, D., Faure, J., Claverie, A., and Balladore, J.L., "Epitaxial growth of $Si_{1-y}C_y$ alloys characterized as self-organized, ordered, nanometer-sized C-rich aggregates in monocrystalline Si." *Physical Review B*, 1996. **54**(15). p. 10559-10564.
167. Malyshkin, V.G., and Shchukin, V.A., "Development of composition inhomogeneities in layer-by-layer growth of an epitaxial film of a solid solution of III-V semiconductors." *Semiconductors*, 1993. **27**(11-12). p. 1062-1068.

168. Tersoff, J., Teichert, C., and Lagally, M.G., "Self-Organization in Growth of Quantum Dot Superlattices." *Physical Review Letters*, 1996. **76**(10). p. 1675-1678.
169. Zhang, Y.W., Xu, S.J., and Chiu, C.-h., "Vertical self-alignment of quantum dots in superlattice." *Applied Physics Letters*, 1999. **74**(13). p. 1809-1811.
170. Yao, J.Y., Andersson, T.G., and Dunlop, G.L., "The interfacial morphology of strained epitaxial $In_xGa_{1-x}As/GaAs$." *Journal of Applied Physics*, 1991. **69**(4). p. 2224-2230.
171. Kandel, D., and Weeks, J.D., "Simultaneous Bunching and Debunching of Surface Steps: Theory and Relation to Experiments." *Physical Review Letters*, 1995. **74**(18). p. 3632-3635.
172. Collins, D.A., Wang, M.W., Grant, R.W., and McGill, T.C., "Reflection high energy electron diffraction observation of anion exchange reactions on InAs surfaces." *Journal of Applied Physics*, 1994. **75**(1). p. 259-262.